Application de la microtomographie par rayons X à l'étude des dépôts de tsunamis

Simon Falvard

▶ **To cite this version:**

Simon Falvard. Application de la microtomographie par rayons X à l'étude des dépôts de tsunamis. Sciences de la Terre. Université Blaise Pascal - Clermont-Ferrand II, 2016. Français. NNT : 2016CLF22686 . tel-01487053

HAL Id: tel-01487053

https://theses.hal.science/tel-01487053v1

Submitted on 10 Mar 2017

HAL is a multi-disciplinary open access archive for the deposit and dissemination of scientific research documents, whether they are published or not. The documents may come from teaching and research institutions in France or abroad, or from public or private research centers.

L'archive ouverte pluridisciplinaire **HAL**, est destinée au dépôt et à la diffusion de documents scientifiques de niveau recherche, publiés ou non, émanant des établissements d'enseignement et de recherche français ou étrangers, des laboratoires publics ou privés.

Numéro d’ordre : D.U. 2686

UNIVERSITÉ BLAISE PASCAL

U.F.R. Sciences et Technologies

ÉCOLE DOCTORALE DES SCIENCES FONDAMENTALES

N° 862

Laboratoire Magmas et Volcans

THÈSE

Présentée pour obtenir le grade de

DOCTEUR D’UNIVERSITÉ

Spécialité : Volcanologie

par

Simon FALVARD

Titulaire du Master 2 Recherche « Géoenvironnement »

Application de la microtomographie par rayons X à l’étude des dépôts de tsunamis.

Soutenue publiquement le 1er avril 2016 devant la commission d’examen composée de :

Jean-Luc Schneider	Professeur, Université de Bordeaux	Rapporteur
Witold Szczuciński	Chercheur, Université de Poznań	Rapporteur
Christian Beck	Professeur, Université de Savoie	Examinateur
Lucia Gurioli	Physicienne, Université Blaise Pascal, Clermont-Fd.	Examinateur
Paolo Marco de Martini	Chercheur, INGV, Rome	Examinateur
Patrick Wassmer	Professeur, Université de Strasbourg	Examinateur
Raphaël Paris	Chargé de Recherche, UBP, Clermont-Ferrand	Directeur de thèse

«Nature uses only the longest threads to weave her patterns, so each small piece of her fabric reveals the organization of the entire tapestry. »

Richard P. Feynman, *The Character of Physical Law*, 1965

RÉSUMÉ GÉNÉRAL

L'étude des dépôts de tsunamis est une science relativement jeune, et si de nombreux progrès ont été faits, en particulier au cours des trois dernières décennies, les techniques disponibles à l'heure actuelle ne permettent pas l'étude exhaustive des dépôts, que ce soit à cause de problèmes de conservation, fréquemment rencontrés, ou de limites liées aux techniques analytiques elles-mêmes. En effet, leur résolution spatiale s'avère insuffisante pour les dépôts fins (fractions sableuses et inférieures), soit par leur principe même (absence de visualisation en trois dimensions sur des lames minces, par exemple), soit à cause des techniques d'échantillonnage dont elles dépendent.

Ce travail a permis d'explorer les applications d'une technique analytique jusqu'à présent inutilisée dans ce domaine, la microtomographie par rayons X, appliquée à trois dépôts de tsunamis : les dépôts du tsunami de Lisbonne en 1755 sur les côtes Andalouses, ceux d'un tsunami causé en 1996 dans le Lac Karymskoye au Kamchatka, et un potentiel dépôt de tsunami datant de l'Holocène à Ninety Mile Beach, sur le littoral ouest de l'Australie. Les problématiques liées aux techniques d'échantillonnage et au traitement des données brutes et à leur exploitation sont passées en revue et les solutions retenues sont exposées. Les résultats obtenus sont comparés à ceux obtenus par l'utilisation de techniques analytiques dont la pertinence et l'utilité ont été démontrées lors de précédentes études.

Cette technique se révèle extrêmement utile pour les analyses structurales (organisation interne des dépôts), texturales (distributions de tailles de grains, fabrique sédimentaire et dynamiques d'écoulements), ainsi que les analyses de composition (abondances en bioclastes et en minéraux lourds par exemple).

Le croisement des études structurales et texturales du dépôt du tsunami de 1755 mettent en avant des dynamiques de mise en place allant parfois à l'encontre des scenarii généralement admis et offre un nouveau point de vue sur les dépôts de tsunami.

Mots clés *: dépôts de tsunamis, tomographie par rayons X, fabrique sédimentaire, distribution de tailles de grains, anisotropie de la susceptibilité magnétique, semelles de traction, minéraux lourds, bioclastes.*

ABSTRACT

The study of tsunami deposits is a relatively young science, and even if substantial progress has been made (especially during the last three decades) the techniques available at present day do not allow exhaustive studies of the deposits, weither poor conservation of the deposits, which is a common problem, is to blame, or because of limitations of the techniques themselves. Their spatial resolution often appears to be insufficient for fine deposits (sand size fractions and finer) because of their working principle (lack of three dimensional visualisation of structures on thin sections for instance) or because of the sampling techniques they depend on.

This work allowed exploring the applications of an analytic technique, X-ray computed microtomography, which had to this day never used before for the study of tsunami deposits. Three distinct case studies have been made: deposits from the 1755 Lisbon tsunami on the western coast of Spain (Andalusia), deposits from the 1996 tsunami triggered in Karymskoye Lake, and a potential mid-Holocene tsunami deposit at Ninety Mile Beach, western Australia. Problematic linked to sampling techniques and raw data processing and exploitation are addressed. Chosen solutions are exposed. The results are compared to those obtained using techniques whose relevance and usefulness have been proven in previous studies.

This technique proves to be extremely useful for structural (deposits inner organisation), textural (grain size distribution, sedimentary fabrics and flow dynamics), and composition (bioclasts and heavy minerals abundances) analyses.

Crossing structural and textural analysis of the 1755 Lisbon tsunami deposit unravels deposition modes which go against the usually admitted scenario and offers a new point of view on tsunami deposits.

***Keywords** : tsunami deposits, X-ray microtomography, sedimentary fabrics, anisotropy of magnetic susceptibility, grain size distribution, heavy minerals, bioclasts.*

REMERCIEMENTS

Trois ans, c'est bien trop court pour réussir à faire tout ce qu'on voudrait, et bien trop long pour réussir à s'en tirer tout seul. Je tiens à remercier ici celles et ceux qui m'ont aidé à aller jusqu'ici sans (trop d') encombre(s).

A tout seigneur tout honneur, je commence par Raphaël, sans qui évidemment rien ne se serait fait et qui a réussi l'exploit de me faire m'intéresser à la sédimentologie (qui l'eût cru ?!) et m'a fait confiance pour mener à bien ce travail. Si je suis un peu moins mauvais sédimentologue c'est pour la plus grande partie grâce à toi ! J'ai également eu la chance d'avoir un directeur de thèse disponible tout le temps, compétent, ultra impliqué et au sens de l'humour douteux, et ça compte vraiment ! Merci également de m'avoir permis de travailler sur un sujet qui nécessite qu'on aille à la plage (pour d'évidentes raisons) !

Je remercie également Stéphanie Cuven, qui s'est partagé la tâche de m'encadrer avec Raphaël pendant le master 2, et qui outre ses précieuses explications sur un sujet que je ne maîtrisais à l'époque pas du tout nous a laissé une somme de données plus qu'utiles pour développer notre méthode.

Je tiens à remercier Simon Matthias May, pour la confiance inconditionnelle qu'il nous a accordée à Raphaël et moi en nous invitant à participer à son étude sur les dépôts de Ninety Mile Beach, qui aura consisté en une sorte d'épreuve du feu pour une technique dont certains points étaient encore en plein développement. Vielen Dank für diese Mitarbeit !

J'adresse mes remerciements aux personnes et sociétés qui m'ont permis d'avoir accès à des scanners et/ou m'ont permis d'en apprendre plus sur la technique, en particulier Eric Badel (INRA), Paul Tafforeau (ESRF), Elisabeth Miot-Noirault (INSERM), RX Solution SAS et Carl Zeiss AG. Merci également à Jérôme Bascou pour son aide précieuse concernant l'anisotropie de susceptibilité magnétique.

Un grand merci à Richard Ketcham dont le petit logiciel (Blob3D) a tout simplement permis à un pan entier de cette thèse d'exister. Un grand merci également à Wayne Rasband qui

a eu un jour l'idée de créer une suite de traitement d'image libre d'accès (ImageJ), et aux milliers de contributeurs qui l'ont rendue si indispensable !

Il me reste à remercier tous ceux qui ont eu à me supporter de près ou de loin pendant ces trois ans et ont pu à l'occasion me donner un coup de pouce. Je commence par les « vieux », en particulier Yannick pour… Pour bien trop de choses pour faire tenir ça en peu de lignes (et c'est peu dire !)… Brest, whisky, Matlab, Vic-sur-Aisne, Miss Yahourt, un nombre incalculable de pintes… bref, trop de choses. Et Oscar, qui heureusement pour lui n'a pas eu à me supporter bien longtemps dans l'open space. Sache que ta thèse m'est plus utile que tu ne pourrais croire ☺

Et également Angélie (merci pour les cours de physique et les balades géophysiques sur le Pariou !), Marine (merci pour les cours de Matlab !), Séb et sa machine magique à compter les grains de sable (et surtout les soirées !), Lola et Baptiste (merci pour l'Ouzo, même si ces remerciements commencent à plus ressembler à une carte de bar qu'autre chose !), Coco et ses billes de verre (et les rugby touch, auxquels mon assiduité aura hélas été scandaleusement inexistante), Lydie (Gree cookie !), Nina et son costume de pingouin, Mathias (parce qu'entre géotech' on se comprend !), Mélo et sa bande de cailloux, Vincent Nougaro, Asmaa et Manu pour les soirées jeux ; Camille, victime attitrée en son temps du lance-roquettes usb (encore désolé ☺), Marina (« Je sais pas du tout ce que c'est tes p'tits smarties colorés mais c'est joli ! »), Juliette et ses stylos de 10000 couleurs (plus utile qu'on ne pense au premier abord), Giacomo (« Oh yeah I'm so f****g late too ! »), Manon et le beaume du tigre, Gaby (directrice de communication de la presqu'il de Crozon), Marie-Anne, Sylvia, Alejandra et tous les petits nouveaux…

Un gros merci également à toutes les personnes de l'administration, en particulier Audrey, Marie-Christine et Cécile, qui m'ont largement facilité la vie pendant ces trois ans !

Merci aussi à Moustique, qui a donné de son temps sans compter pendant trois mois pour tenter de m'apprendre à faire des photos à peu près potables. Je ne m'y attendais pas mais ça m'a été plus qu'utile pour cette thèse !

Place, pour finir, à ceux qui ont eu à subir cette thèse de plein fouet, à savoir mes parents et les frangins, qui ont entendu parler de sable et d'histoires de labo bien plus que de raison au

cours de ces trois ans et qui n'ont pas trop mal respecté la sacro-sainte règle du « On ne demande pas « Et sinon ça sert à quoi ? » » ! Et pour finir le paragraphe pour finir, un grand merci à Lucie, pour tout un paquet de paquets de raisons, et en particulier pour s'être montrée d'une patience à toute épreuve !

Ces travaux ont bénéficié d'un financement de la part de la Région Auvergne (programme TSUNAMIX, dans lequel cette thèse s'inscrit), ainsi que de financements de la part de trois programmes : ANR-08-RISKNAT MAREMOTI (travaux sur les dépôts du tsunami de 1755) et ANR 08-JCJC-0042 VITESSS (travaux sur les dépôts du Lac Karymskoye) et le programme européen ASTARTE (mission d'échantillonnage sur Ios). Le Conseil Régional d'Auvergne et l'équipe de Volcanologie du Laboratoire Magmas et Volcans ont chacun pris en charge la participation à un congrès.

TABLE DES MATIÈRES

INTRODUCTION 14
I. Définition et sources des tsunamis 15
II. Caractérisation mécanique d'un tsunami. 17
III. Conséquences géomorphologiques. 19
IV. Identification et caractérisation des dépôts de tsunami 20
1. Techniques et méthodes d'analyse 20
2. Caractéristiques connues 27
V. Apports potentiels de la microtomographie par rayons X 30
1. Tomographie par rayons X : principe 30
2. Applications potentielles à l'étude des dépôts de tsunami 33
Références 33
CHAPITRE 1 : Etude des dépôts de tsunamis – techniques conventionnelles. 48
High-resolution analysis of a tsunami deposit: case-study from the 1755 Lisbon tsunami in southwestern Spain 49
Abstract 49
1. Introduction 50
2. Materials and methods 51
3. Results 53
4. Discussion and perspectives 73
5. Conclusion 78
Acknowledgements 79
References 79
CHAPITRE 2 : Tomographie par rayons X – méthodologie et étude de cas : le dépôt de tsunami de 1755 à Los Lances, Andalousie. 90
X-ray tomography of tsunami deposits: towards a new depositional model of tsunami deposits 91
Abstract 91
1. Introduction 92
2. X-ray computed tomography 94
3. Methods 96
4. Results 105
5. Discussion 113
6. Conclusions and perspectives 122
Acknowledgments 123
References 123
CHAPITRE 3 : Etude de cas – Analyse des minéraux lourds sur un transect de dépôts de tsunami - 1996 Lac Karymskoye, Kamchatka, Russie. 139

Structure and distribution of heavy minerals in tsunami deposits inferred from X-ray tomography – case of the 1996 volcanic tsunami in Karymskoye Lake, Kamchatka. 140
Introduction 140
1996 eruption and tsunamis in Karymskoye Lake 141
Methods 146
Results 148
Discussion 158
Conclusion 160
Acknowledgments 161
References 161
CHAPITRE 4 : Identification d'un paléotsunami et caractérisation de la fabrique sédimentaire par tomographie aux rayons X (Ouest Australie). 164
A mid-Holocene candidate tsunami deposit from the NW Cape (Western Australia) 166
ABSTRACT 166
1. INTRODUCTION 167
2. PHYSICAL SETTING 168
3. METHODS 170
4. SEDIMENTOLOGY 180
5. DATA INTERPRETATION AND DISCUSSION 182
6. CONCLUSIONS 185
ACKNOWLEDGMENTS 186
REFERENCES 186
CONCLUSION 193
ANNEXES 196
Annexe 1 : Traitement des scans, extraction et traitement des données. 196
Optimisation des images : ajustement des contrastes et traitement du bruit 197
2D : Séparation et mesure du diamètre intermédiaire des grains 198
2D : cartographie des tailles de grains 200
2D : mesures quantitatives, statistiques 202
3D : fabrique sédimentaire 204
1D : comptage des bioclastes 207
Annexe 2 : codes 208
Macro Filtre à trous (ImageJ) : 208
Grainmap : 209
Grainstat : 210
Bioclast : 214

INTRODUCTION

Les tsunamis d'ampleur parfois exceptionnelle qui ont eu lieu au cours de la dernière décennie (en particulier en Indonésie en 2004 et 2006 (Chagué-Goff et al., 2011; Cummins et al., 2009; Dunbar and McCullough, 2011, p. 201; Goff and Dominey-Howes, 2011; Hawkes et al., 2007; Moore et al., 2011; Paris et al., 2009), dans le Pacifique Sud en 2009 (Chagué-Goff et al., 2011; Dunbar and McCullough, 2011; Goff and Dominey-Howes, 2011; Jaffe et al., 2011; McAdoo et al., 2011), ou encore sur la côte Est du Japon en 2011 (Chagué-Goff et al., 2012, 2012; Goto et al., 2012a; Jagodziński et al., 2012; Nakamura et al., 2012; Naruse et al., 2012; Pilarczyk et al., 2012, p. 2012; Richmond et al., 2012; Tappin et al., 2012) et leurs conséquences socio-économiques démontrent l'utilité d'évaluer précisément les risques liés à l'aléa tsunami, en particulier dans un contexte de littoralisation de la population mondiale et d'accélération de l'augmentation du niveau moyen des océans (Gehrels et al., 2005; Nakada and Inoue, 2005). Ils mettent en lumière le fait que certains processus liés aux causes de tsunamis mais aussi à leurs effets ne sont compris et anticipés que de manière lacunaire, principalement parce que l'étude des tsunamis au sens large est une discipline jeune (Bourgeois, 2009) et que de nombreux progrès restent à faire tant dans la compréhension des évènements contemporains que dans le traçage et l'interprétation des évènements anciens, ainsi que dans la modélisation des futurs tsunamis (Bridge, 2008; Cuven et al., 2013; Goff et al., 2012; Jaffe and Gelfenbaum, 2007).

Nous n'aborderons pas ici les développements récents et les incertitudes demeurant quant aux processus de génération de tsunamis, aussi bien liés à l'activité sismique qu'aux instabilités gravitaires ou aux éruptions volcaniques. Si l'on se restreint aux effets morpho-sédimentaires d'un tsunami, force est de constater que très peu de techniques de modélisation prennent actuellement en compte les processus de transport de sédiments ou les informations tirées des dépôts de tsunamis. Quand les algorithmes sont conçus pour en tenir compte, d'importantes simplifications ou postulats doivent être faits. Jaffe et Gelfenbaum (2007) et Jaffe et al. (2012) considèrent par exemple uniquement les dépôts caractérisés par un granoclassement normal, et une mise en place du dépôt régie par la décantation simple des particules. Moore et al. (2007) évaluent la contrainte de cisaillement nécessaire pour mettre en mouvement les plus gros grains présents dans le dépôt. Soulsby et al. (2007) calculent des valeurs de distances d'inondation, de hauteur de vague et de vélocité à la côte en partant de la supposition qu'il existe une relation linéaire entre la diminution de la taille de grain moyenne

du dépôt et l'augmentation de la distance à la côte mais admettent que ces variables n'évoluent dans les cas réels pas de manière parfaitement linéaire. Pritchard et Dickinson (2008) modélisent numériquement le transport de sédiments en suspension ou par charge de fond par différents types de vagues non déferlantes de grande longueur d'onde, mais doivent pour ce faire ne considérer que le cas d'une plage de pente uniforme, sans tenir compte de la topographie. L'utilisation de telles simplifications est dictée par le manque de compréhension concernant les mécanismes complexes de mise en place des dépôts par les tsunamis. Le but de cette thèse aura donc été de tenter de developper une technique analytique permettant, au moins en partie, de combler certaines de ces lacunes, en particulier en ce qui concerne les dynamiques de mise en place des dépôts et plus précisément d'étudier l'organisation d'un dépôt de tsunami à des échelles millimétriques voire inframillimétriques qui n'ont jusqu'à présent que très peu été étudiées en deux dimensions, et jamais en trois dimensions.

I. Définition et sources des tsunamis

On retiendra dans le cadre de ce travail la définition donnée par (Sugawara, 2008) : « Un tsunami est un train de vagues transitoire formé dans un océan ou un bassin fermé par divers phénomènes à l'exclusion des phénomènes atmosphériques (météorologiques)». Cette définition n'est pas la seule proposée (ex. Tinti et al., 2004) mais elle présente l'avantage de ne définir le tsunami qu'en termes de sources et de mode de propagation sans en limiter le siège au seul milieu marin, ce qui nous semble être le point de vue le plus pertinent dans le cadre de la présente étude. En effet, outre le milieu marin, des tsunamis ont été rapportés et étudiés en milieu lacustre (ex. Belousov et al., 2000; Schnellmann et al., 2002).

Un tsunami peut être généré par quatre mécanismes principaux (Sugawara, 2008) :

- L'activité sismique sous-marine est à l'origine de nombreux tsunamis étudiés, contemporains, historiques ou préhistoriques (Atwater, 1987; Baptista et al., 2003; Fujiwara et al., 2000; Mastronuzzi et al., 2007; Minoura et al., 1996; Paris et al., 2007; Pinegina et al., 2003; Ramírez-Herrera et al., 2012; Richmond et al., 2011; Shi et al., 1995; Sugawara et al., 2012), dont la grande majorité se situe au niveau de zones de subductions. Le déplacement relatif de deux plaques au niveau de la faille sismogénique est répercuté au niveau de la masse liquide, qui a son tour se déplace sous la forme d'un train de vagues. D'après Sugawara

(2008), les séismes peu profonds (profondeur de l'hypocentre inférieure à 70 km) et couvrant de grandes surfaces sont responsables de la majorité des tsunamis d'origine sismique, et Kanamori (1972) note que les séismes les plus susceptibles de causer des tsunamis ne présentent pas nécessairement une magnitude élevée mais des moments sismiques élevés aux longues périodes, une caractéristique expliquée par le comportement visco-élastique du matériel constituant par exemple le prisme d'accrétion sédimentaire.

- Les glissements de terrain sous-marins constituent un autre mécanisme efficace dans la génération d'un tsunami. L'entrée dans l'eau d'un glissement de terrain (ou le déplacement sous l'eau d'une masse déjà imergée) entraîne le déplacement de la masse d'eau adjacente et la propogation d'une onde de choc. Un des glissements tsunamigénique les plus connus est le complexe de glissements de Storegga, en mer du Nord (Bugge et al., 1987; Dawson et al., 1988), dont des dépôts ont été retrouvés sur les côtes norvégiennes (Bondevik et al., 2005a, 2003, 1997), écossaises (Dawson et al., 1988; Dawson et Smith, 2000; Smith, 2004), les îles Shetland (Bondevik et al., 2005b, 2003) et les îles Feroé (Grauert et al., 2001).

Masson et al. (2006) décrivent plusieurs facteurs permettant la mise en place de glissements sous marins et les séparent en deux classes : les facteurs liés aux caractéristiques géologiques du matériel mobilisé (ex. les phénomènes de surpression intersticielle) et les facteurs externes, tels que les éruptions volcaniques (Nishimura and Miyaji, 1995), les séismes (Imamura et al., 1995), etc. Cette diversité des causes rend les glissements sous-marins communs dans toutes les régions du globe (p.ex. Alaska dans la baie Lituya (Miller, 1960) ou à Skagway Harbor (Kulikov et al., 1996), Grands Bancs de Terre-Neuve (Fine et al., 2005), Indonésie (Imamura et al., 1995, p. 95), Papouasie Nouvelle Guinée (Tappin et al., 1999, 2001, 2008; Bardet et al., 2003)) et entraîne une grande disparité quant à la taille relative des tsunamis engendrés (Masson et al., 2006).

- Plusieurs processus associés à l'activité volcanique peuvent être à l'origine de tsunamis (Latter, 1981; Paris et al., 2014a), que ce soit à la suite des ondes sismiques générées par l'éruption (Latter, 1981), l'effondrement de l'édifice (p. ex. l'éruption de Santorin en 3500 BP (Cita et Aloisi, 2000), le blast d'une éruption sous marine (Belousov et al., 2000), des avalanches de débris ou des coulées pyroclastiques (Paris et al., 2014a). Dans plusieurs cas le phénomène lié à la mise en place du train de vagues n'est pas clairement défini et sujet à controverse (Paris et al., 2014a)

- Quoique marginales en termes d'occurrences connues et de traitement par la littérature, les chutes de météorites sont susceptibles d'être un mécanisme déclencheur de tsunamis, suite au déplacement d'eau potentiellement conséquent qu'entraîne l'arrivée dans l'eau d'un bolide. Un cas est majoritairement traité dans la littérature, celui du tsunami causé par la chute d'un bolide d'un diamètre d'environ 10 km il y a 65 Ma dans la péninsule du Yucatán (Alvarez et al., 1980; Hildebrand et al., 1991). Bourgeois et al. (1988) sont à l'origine d'un travail pionnier dans l'identification des dépôts sédimentaires liés aux tsunamis et décrit dans le golfe du Mexique un dépôt gréseux présentant des structures typiques d'un courant de haute énergie (base érosive, présence de fragments de coquilles, de clastes roulés de mudstone issus du niveau sous-jacent…). Ils proposent comme mécanisme de mise en place de ces dépôts un tsunami dont la hauteur de vague aurait atteint entre 50 et 100 m. Ces observations ont été recoupées au Brésil (Albertão et Martins Jr., 1996) et au nord de l'île de Cuba (Goto et al., 2008; Tada et al., 2003).

II. Caractérisation mécanique d'un tsunami.

Les différents modes de génération des tsunamis et leurs caractéristiques de propagation leur confèrent généralement, malgré les différentes configurations possibles, un comportement de vagues longues, dont la longueur d'onde de l'ordre de plusieurs dizaines à centaines de km est nettement supérieure à la profondeur de la lame d'eau dans laquelle ils se déplacent (Wu, 1981; Sugawara, 2008) et dont l'amplitude en haute mer ne dépasse pas quelques dizaines de cm (Wu, 1981).

Le déplacement d'un tsunami en haute mer peut être décrit par le système d'équations suivant (Sugawara, 2008) :

$$\frac{\partial \eta}{\partial t} = -h\frac{\partial u}{\partial x}$$

$$\frac{\partial u}{\partial t} = -g\frac{\partial \eta}{\partial x}$$

où u représente la vitesse du courant, η l'élévation de l'eau par rapport à son niveau au repos, h la profondeur de l'eau, x la distance parcourue et g l'accélération de la pesanteur.

On peut déduire en éliminant u de ce système la vitesse C de l'onde qui peut être évaluée par la formule :

$$C = \sqrt{gh}$$

On en déduit également :

$$u = \pm\eta\sqrt{\frac{g}{h}}$$

On constate que si la vitesse de propagation de l'onde est proportionnelle à la profondeur d'eau, la vitesse du courant est inversement proportionnelle à celle-ci. Ces relations entraînent un ralentissement de l'onde lorsque l'épaisseur de la lame d'eau diminue, et une augmentation de la hauteur de la vague.

Sugawara (2008) propose 5 paramètres physiques permettant de caractériser un tsunami :

- La hauteur du tsunami, définie par la différence d'altitude entre le crête ou le creux de la vague et un niveau de référence de l'eau. La hauteur du tsunami est donc différente de la hauteur de la vague, définie par la différence d'altitude entre la crête et le creux de la vague.

- La période du tsunami, définie par la durée nécessaire au passage de 2 crêtes de vagues en un point fixe (période de l'onde).

- L'altitude atteinte par l'eau à l'intérieur des terres définit la hauteur du *run-up*, et peut être significativement différente de la hauteur de la vague.

- La magnitude m du tsunami est définie dans le cas d'un tsunami d'origine sismique en lien avec les dimensions du déplacement du fond marin, et est proportionnelle à la magnitude du séisme. Elle est définie par Iida (1963), par la formule empirique suivante :

$$m = 2{,}61M - 18{,}44$$

où M est la magnitude locale du séisme.

Sugawara (2008) précise que la magnitude du tsunami peut également être définie par la hauteur du tsunami mesurée à la côté ou par un marégraphe. Papadopoulos (2003), présente la magnitude du tsunami définie par sa hauteur sous la forme :

$$Mt = a.logH + b.log\Delta + D$$

où H est l'amplitude maximale du tsunami en mètres, Δ est la distance du site d'observation par rapport à l'épicentre en kilomètres et a, b et D sont des constantes.

- L'intensité du tsunami est une évaluation des effets du tsunami. Papadopoulos et Imamura (2001) ont proposé une échelle permettant de classer l'intensité d'un tsunami selon trois critères : ses conséquences sur les humains, sur les objets (véhicules compris) et sur le bâti, permettant une caractérisation précise du phénomène. Cette évaluation reste cependant subjective, l'évaluation de l'importance relative de chaque critère ne bénéficiant pas de standards et de caractéristiques fixes.

III. Conséquences géomorphologiques.

L'accélération du courant à l'approche des côtes a pour conséquence une augmentation de la contrainte de cisaillement à l'interface eau/fond marin qui peut si les conditions mécaniques sont réunies (vitesse du courant, cohésion du sédiment, taille des particules, etc.) se traduire par la mise en mouvement et le transport de matériel sédimentaire (Hjulström, 1935).

Cette caractéristique confère aux tsunamis : (1) un fort potentiel érosif au niveau du plateau continental et à l'intérieur des terres tant que la vitesse du courant est suffisante, puis (2) un potentiel sédimentaire proportionnel à la quantité de matériel mobilisé (Bondevik et al., 1997; Bourgeois, 2009; Dawson et al., 1996; Etienne et al., 2011; Minoura et al., 1997, 1996; Moore et al., 2007; Naruse et al., 2012; Paris et al., 2009; Richmond et al., 2012; Shi et al., 1995; Szczuciński et al., 2012). De ce fait, les caractéristiques associées aux dépôts sédimentaires mis en place dans les terres par un tsunami sont étroitement liées, non seulement à la topographie locale et aux caractéristiques du matériel disponible (Goff et al., 2012; Goto et al., 2012a; Jaffe and Gelfenbaum, 2007; Paris et al., 2007) mais aussi aux

caractéristiques physiques de l'écoulement (Bondevik et al., 2005a; Jaffe and Gelfenbaum, 2007; Minoura et al., 1997). Toutefois, les relations reliant ces dernières aux dépôts ne sont actuellement pas encore parfaitement appréhendées. Morton et al. (2008) insistent donc sur la nécessité de mener des campagnes d'analyse visant à caractériser le plus finement possible les caractéristiques structurales et géographiques des dépôts, qui constituent des données essentielles au calibrage des modèles numériques.

De ce fait, l'étude des dépôts sédimentaires de tsunamis a connu depuis la fin des années 80 un engouement particulier non seulement dans le but de détecter d'anciens évènements peu ou pas référencés dans les archives historiques (Atwater, 1992, p. 19, 1987; Bondevik et al., 1997; Bourgeois et al., 1988; Bugge et al., 1987; Dawson et al., 1988; Dunbar and McCullough, 2011; Grauert et al., 2001; Pinegina et al., 2003), mais également pour obtenir des informations quantitatives sur leur texture (Goff et al., 2012; Imamura et al., 1995; Jaffe and Gelfenbaum, 2007; Morton et al., 2008; Smith et al., 2007).

Cependant, la dépendance aux sources des dépôts ainsi que plusieurs problèmes de conservation (Cuven et al., 2013; Paris et al., 2009; Szczuciński, 2012; Szczuciński et al., 2007) et le fait que d'autres processus de haute énergie, tels que les tempêtes, peuvent entraîner la mise en place de formations sédimentaires aux caractéristiques assez proches, compliquent sensiblement l'identification et la caractérisation des dépôts de tsunami (Chagué-Goff et al., 2011; Cuven et al., 2013; Dawson et al., 2008; Goff et al., 2012, 2004; Kelletat, 2008; Kortekaas and Dawson, 2007; Nanayama et al., 2000). Pour pallier à ces problèmes, plusieurs angles d'approche ont été abordés au cours du temps dans le but de multiplier au maximum les critères d'identification et d'obtenir une description aussi complète que possible (Chagué-Goff et al., 2011; Goff et al., 2012).

IV. Identification et caractérisation des dépôts de tsunami

1. Techniques et méthodes d'analyse

i. Analyse de taille des grains et indice de tri

L'analyse de la taille des grains (granulométrie) constitutifs du dépôt et de ses variations verticales, latérales et longitudinales est une technique très fréquemment utilisée (Bondevik et al., 2005b; Chagué-Goff et al., 2002; Cuven et al., 2013; Iliev et al., 2005; Imamura et al., 1995; Jaffe and Gelfenbaum, 2007; Minoura et al., 1997, 1996; Moore et al.,

2007; Morton et al., 2008; Naruse et al., 2012; Pilarczyk et al., 2012; Szczuciński et al., 2012). Les principaux intérêts de cette technique classique sont, par comparaison du matériel du dépôt avec les différents stocks sédimentaires présents à proximité, de pouvoir définir le ou les stock(s) source(s) (Szczuciński et al., 2012), d'estimer les caractéristiques physiques du flux nécessaire à leur mise en place (principe du problème inverse ; ex : Jaffe et Gelfenbaum, 2007), et de séparer différentes phases au cours de l'évènement par l'identification de niveaux sédimentaires de caractéristiques distinctes (Minoura et al., 1997; Moore et al., 2007; Szczuciński et al., 2012). L'analyse de l'indice de tri (*sorting*) ainsi que des coefficients de dissymétrie (*skewness*) et d'aplatissement (*kurtosis*) des distributions de tailles de grains apporte des informations complémentaires quant à la nature du stock source et aux conditions de mise en place (Minoura et al., 1997; Paris et al., 2007; Ramírez-Herrera et al., 2012; Szczuciński et al., 2012).

Ces analyses sont menées en laboratoire sur des échantillons prélevés de différentes manières : le pas d'échantillonnage peut être défini sur le terrain, en fonction de la stratigraphie apparente (Cuven et al., 2013; Jagodziński et al., 2012; Moore et al., 2007; Pilarczyk et al., 2012; Szczuciński et al., 2012), technique qui semble être la plus utilisée, même si de nombreuses publications n'exposent pas les techniques de prélèvement utilisées. L'échantillonnage peut également être réalisé par carottage (Bondevik et al., 2005b; Cuven et al., 2013; Moore et al., 2007; Ramírez-Herrera et al., 2012; Szczuciński et al., 2012), auquel cas le sous-échantillonnage est réalisé en laboratoire. Dans les deux cas, le sous-échantillonnage est réalisé soit à pas fixe (par exemple tous les centimètres) soit en suivant la stratigraphie visible.

La dépendance des dépôts de tsunami aux stocks sédimentaires disponibles est à l'origine d'une très grande disparité entre différents dépôts et parfois au sein d'un seul dépôt. Ainsi, si dans de nombreux cas un dépôt de tsunami est caractérisé par une couche sableuse (Bondevik et al., 2005b; Bourgeois et al., 1988; Dawson et al., 2008, 1996, 1988; Long et al., 1989; Minoura et al., 1997, 1996; Moore et al., 2007; Paris et al., 2007; Shi et al., 1995; Szczuciński et al., 2012; Wright and Mella, 1963), toutes les tailles de grain peuvent être trouvées, des clastes et/ou couches argileuses (*rip-up* et/ou *mud drapes cf*. p. ex. Bondevik et al., 2005b; Cuven et al., 2013; Szczuciński et al., 2012; Takashimizu and Masuda, 2000) aux blocs plurimétriques (Etienne et al., 2011; Goto et al., 2010, 2012b), parfois en association avec des fractions sédimentaires fines (Paris et al., 2010b).

Dans de nombreux cas, un granoclassement normal est observé, accompagné d'une diminution de l'épaisseur et de la taille de grain moyenne du dépôt vers l'intérieur des terres (*landward thinning & fining* ; p. ex. Bondevik et al., 2005b; Gelfenbaum and Jaffe, 2003; Goff et al., 2004; Minoura et al., 1997, 1996; Shi et al., 1995), mais certains dépôts ou certains niveaux au sein d'un dépôt peuvent présenter un granoclassement inverse (p. ex. Bondevik et al., 2005b; Moore et al., 2007; Naruse et al., 2012). De plus, un épaississement du dépôt est parfois constaté vers l'intérieur des terres, en particulier parce que la topographie locale joue un rôle parfois prépondérant sur les processus de sédimentation (p. ex. Morton et al., 2008; Paris et al., 2007). Si les niveaux à granoclassement normal sont souvent associés à un épisode de dépôt de particules en suspension dans un écoulement dont l'énergie diminue au cours du temps (p. ex Dawson et al., 1988; Shi et al., 1995; Szczuciński et al., 2012), les épisodes de dépôt à granoclassement inverse semblent plutôt traduire des épisodes de transport sédimentaire en charge de fond, durant lesquels la friction intergranulaire est un facteur de dépôt plus efficace que la seule gravité sans pour autant annuler l'action de cette dernière (Moore et al., 2011, 2007; Szczuciński et al., 2012).

ii. Anisotropie de susceptibilité magnétique et fabrique sédimentaire

L'anisotropie de susceptibilité magnétique exploite les caractéristiques magnétiques des minéraux du dépôt sédimentaire pour en déduire leur orientation (Rees, 1965). Un échantillon exposé à un champ magnétique H présentera un moment magnétique induit M tel que

$$M = kH$$

où k représente la susceptibilité magnétique de l'échantillon (Wassmer et al., 2010). Rees (1965) confirme l'applicabilité de cette technique aux dépôts silteux et sableux mais note que les caractéristiques magnétiques de ce type de sédiment sont généralement très largement définies par sa teneur en minéraux ferromagnétique, et en particulier en magnétite. De ce fait, la valeur de susceptibilité magnétique mesurée dans une direction sera celle de la fraction ferromagnétique du dépôt, et sera directement dictée par sa répartition spatiale dans l'échantillon ainsi que par l'orientation de ses grains. La mesure dans plusieurs directions de l'espace d'un échantillon donné se traduit par la définition d'un ellipsoïde, dont la géométrie dépend donc directement de l'orientation des grains (Rees, 1965).

Cette technique a été utilisée dans plusieurs contextes sédimentaires (p. ex. Liu et al., 2001; Park et al., 2000; Rees and Woodall, 1975; Tarling and Hrouda, 1993) mais son application dans le cadre de l'étude des dépôts de tsunamis est très récente et encore peu représentée (Wassmer et al., 2010; Goff et al., 2012; Cuven et al., 2013; Paris et al., 2014b; Schneider et al., 2014).

Wassmer et al. (2010), Cuven et al. (2013) et Schneider et al. (2014) utilisent pour le prélèvement d'échantillons des cubes de polystyrène de 2 cm de côté enfoncés dans le sédiment pour le prélever à l'emporte-pièce. Cette technique permet d'assurer un minimum de remaniement de la texture du dépôt, et conditionne directement la précision maximale de la mesure, qui ne peut être inférieure aux dimensions de l'échantillon.

Wassmer et al. (2010) déduisent des mesures d'AMS l'évolution hydrodynamique du tsunami du 26 décembre 2004 dans la région de Banda Aceh, grâce à l'observation de l'évolution des orientations préférentielles des particules du dépôt, qui révèle le passage d'une mise en place sous de fortes contraintes cisaillantes à la base du dépôt à une mise en place dominée par la décantation. Wassmer et al. (2010) notent également que l'orientation préférentielle des grains dépend non seulement des contraintes cisaillantes (*i.e.* la vitesse du courant) mais également de la granulométrie du dépôt ainsi que de la topographie locale qui influe directement et notablement sur la direction et l'énergie du courant. Ces observations sont corroborées par Schneider et al. (2014), qui notent également l'importance de l'étude du facteur de forme de l'ellipsoïde de susceptibilité magnétique, en particulier pour l'analyse des fluctuations de vitesse du courant. Cuven et al. (2013) parviennent également à obtenir grâce aux données d'ASM des informations sur la direction et l'énergie du courant du tsunami de Lisbonne de 1755 malgré la rareté des éléments ferro et paramagnétiques et de faibles valeurs de susceptibilité magnétique.

D'autres techniques d'analyse texturale sont employées mais de manière très marginale, comme les prélèvements à la résine (*resin peels*, p. ex. Naruse et al., 2012) qui permettent le prélèvement d'une fine couche de sédiment en assurant un minimum de perturbation au niveau de l'orientation des grains. On note cependant que la nature de ces prélèvements ne permet pas, contrairement à l'anisotropie de susceptibilité magnétique, d'évaluer la fabrique sédimentaire dans les trois dimensions de l'espace.

iii. Signature chimique du tsunami

Un tsunami en milieu marin se traduit par l'apport à l'intérieur des terres de quantités conséquentes d'eau de mer, dont la signature chimique diffère de l'eau douce. Minoura and Nakaya (1991) sont ainsi les premiers à mettre en évidence des traces d'inondation par d'importantes quantités d'eau salée d'origine marine, via l'analyse des ions du chlore, du calcium et du magnésium dont la concentration augmente dans les eaux interstitielles au sein du dépôt. Ils détectent également une diminution du rapport Mg^{2+}/Ca^{2+} dans les niveaux sableux du dépôt par rapport à l'encaissant argileux.

La technique a depuis été développée et peut passer par l'analyse de prélèvements sédimentaires (Chagué-Goff, 2010; Chagué-Goff et al., 2012; Cuven et al., 2013; Goff & Chagué-Goff, 1999; Ramírez-Herrera et al., 2012) ou de l'eau interstitielle (Chagué-Goff, 2010). Les analyses peuvent concerner les éléments majeurs par spectrométrie d'émission atomique (ICP-AES, Chagué-Goff et al., 2012 ; Cuven et al., 2013), les ions hydrosolubles par titrage (Szczuciński et al., 2005) ou chromatographie ionique (Chagué-Goff et al., 2012a), les métaux en traces par spectrométrie d'adsorption atomique (AAS, Szczuciński et al., 2005, Chagué-Goff et al., 2012) ou la composition élémentaire totale de l'échantillon par spectrométrie de fluorescence des rayons X (XRF, Goff et Chagué-Goff, 1999 ; Ramírez-Herrera et al., 2012, Cuven et al., 2013).

Goff et Chagué Goff (1999) considèrent les augmentations de concentrations du fer et du soufre comme des marqueurs de paléosalinité dans un dépôt de tsunami. Szczuciński et al. (2005) trouvent d'importantes quantités de sels (Na^+, K^+, $Ca2^+$, $Mg2^+$, Cl^-, SO_4^{2-}) et de cadmium, cuivre, zinc, plomb et arsenic au sein d'un dépôt mis en place par le tsunami de décembre 2004 en Thaïlande. Chagué-Goff et al. (2012b) utilisent le chlore et le sodium comme marqueurs de paleosalinité, en particulier en association avec le brome, moins sujet au lessivage. Pilarczyk et al. (2012) utilisent les mesures du carbone organique total (TOC) et du $\delta^{13}C$ pour évaluer l'origine de la matière organique de dépôts terrestres et marins et observe une augmentation du $\delta^{13}C$ et une diminution du TOC au sein d'un dépôt de tsunami. Cuven et al. (2013) utilisent le strontium et le baryum comme marqueurs d'inondation d'origine marine et identifie également les dépôts du tsunami de Lisbonne grâce aux rapports Si/Al et Si/Ti, associés à une augmentation de la teneur en quartz du sédiment mis en place par le tsunami par rapport à la base pré-tsunami et aux dépôts post tsunami argilo-silteux.

Chagué-Goff (2010) souligne que les marqueurs chimiques associés à un tsunami sont susceptibles d'être retrouvés dans l'intégralité de la zone d'inondation, ce qui n'est pas le cas des dépôts sédimentaires, dont la limite d'avancée dans les terres ne correspond généralement pas à la limite d'inondation.

Cependant, si cette technique est susceptible de révéler un épisode d'inondation, et si certains marqueurs chimiques (Ti, Zr…) peuvent renseigner sur l'énergie relative du courant lors de mises en place des dépôts, elle n'apporte que peu voire pas de renseignements sur les caractéristiques hydrodynamiques précises de l'évènement, et ne permet généralement pas d'identifier la nature du phénomène (tsunami, tempête, typhon…), d'où la nécessité de croiser les résultats des analyses chimiques avec ceux d'autres techniques analytiques (Chagué-Goff et al., 2010).

iv. Analyse des marqueurs biologiques

Suivant le stock sédimentaire mobilisé, les dépôts de tsunamis sont susceptibles de contenir du matériel marin lacustre et terrestre, dont la faune et la flore diffèrent sensiblement (Goff et al., 2012). La provenance des dépôts peut donc être potentiellement identifiée grâce à son contenu biologique, macroscopique et microscopique, et certaines indications sur la profondeur, la salinité du milieu, etc. peuvent être précisément définies, permettant de définir l'origine du stock sédimentaire. Outre certains bioclastes « accessoires » (bois, plantes, squelettes de petits animaux), les tests de macroorganismes tels que les ostracodes (Bony et al., 2012; Naruse et al., 2012, Tanaka et al., 2012) ou les mollusques (Minoura et al., 1996) sont utilisés, ainsi que certains microorganismes, parmi lesquels les diatomées (Bondevik et al., 1997; Dawson, 2007; Ramírez-Herrera et al., 2012; Szczuciński et al., 2012), les foraminifères (Bondevik et al., 1997; Dominey-Howes et al., 1999; Pilarczyk et al., 2012; Ramírez-Herrera et al., 2012) ou les nannolithes (Paris et al., 2010a; Szczuciński et al., 2012).

Dans la majorité des cas, les dépôts de tsunamis sont associés à des concentrations en bioclastes élevées par rapport aux niveaux sédimentaires sus et sous-jacents (Bondevik et al., 1997 ; Naruse et al., 2012 ; Paris et al., 2010 ; Pilarczyk et al., 2012 ; Ramírez-Herrera et al., 2012 ; Tanaka et al., 2012). Cependant, la présence de bioclastes dans les dépôts semble ne pas toujours correspondre à une origine marine *per se* mais peut parfois simplement traduire le remaniement de matériel sédimentaire contenant ces marqueurs (Pilarczyk et al., 2012). A l'opposé, Szczuciński et al. (2012) constatent la quasi absence de bioclastes marins dans les

dépôts du tsunami de 2011 du Tohoku-Oki et associent cette particularité à l'absence de sédiments d'origine profonde (fonds marins) dans les dépôts du tsunami. Les concentrations plus élevées de bioclastes typiques d'eaux douces et/ou saumâtres vont également dans le sens du remaniement de sédiments issus en grande majorité de la plage et des dunes. À l'opposé, Paris et al. (2009) attribuent à plus de 75% du volume des sédiments déposés à Lhok Nga (Sumatra, Indonésie) par le tsunami du 26 décembre 2004 une origine marine, et Gelfenbaum et Jaffe (2003) estiment qu'au moins deux tiers des dépôts du tsunami de Papouasie Nouvelle Guinée de 1998 proviennent du large.

Les marqueurs palynologiques peuvent également être utilisés pour définir l'impact écologique d'un évènement et/ou la provenance du matériel sédimentaire d'un dépôt. Minoura et al. (1996) note ainsi des indices de modification des populations végétales suite à l'inondation de la côte d'Ust'-Kamchatsk par le tsunami mis en place lors du séisme de 1923.

Comme toutes les particules, les bioclastes sont sujets à d'éventuelles remobilisation post dépôt et phénomènes de dissolution, en particulier les microorganismes, facilement déplacés par les phénomènes de lessivage ou de bioturbation (Paris et al., 2010a; Pilarczyk et al., 2012).

v. Marqueurs structuraux (structures sédimentaires)

L'analyse de la morphologie des dépôts, sur le terrain ou en laboratoire, permet d'obtenir plusieurs informations sur les caractéristiques hydrodynamiques de l'écoulement. D'un point de vue structural, les dépôts de tsunamis peuvent se présenter sous la forme de lamines (Moore et al., 2007; Morton et al., 2008; Naruse et al., 2012; Szczuciński et al., 2012) qui peuvent parfois être associées à une phase précise de l'évènement (*uprush*, *backwash*, phases de stagnation… *cf.* p. ex. Moore et al., 2007; Morton et al., 2008; Naruse et al., 2012), ou au contraire de niveaux massifs, sans structuration apparente à l'œil nu (Bondevik et al., 2005b).

Si l'étude des structures sédimentaires de taille plurimillimétrique et supérieure est suffisamment commune pour être traitée de manière routinière, les structures de taille millimétrique et inférieure n'ont à ce jour bénéficié que d'une attention mineure. Kilfeather et al. (2007) est à l'origine de la première publication dédiée à l'étude de la micromorphologie des dépôts de tsunamis, et démontre que les dépôts de tsunamis présentent à l'échelle

millimétrique et inframillimétrique des caractéristiques structurales et texturales complexes insoupçonnables à l'œil nu (laminations fines, micro *rip-ups*, contacts érosifs, alignements minéraux ou encore granoclassements microscopiques) et dont l'étude détaillée est susceptible d'apporter des renseignements à même de compléter l'interprétation des conditions de mise en place du dépôt.

L'étude de Kilfeather et al. (2007) s'appuie sur un échantillonnage continu par carottage et la réalisation de lames minces recouvrant l'intégralité de la stratigraphie du dépôt. On note cependant que ce type d'échantillon ne permet (après préparation) qu'une étude approfondie dans deux dimensions de l'espace, et ne permet donc pas de quantifier la texture du sédiment. De plus, la méthode d'imprégnation du sédiment par de la résine époxyde et plus particulièrement la déshydratation par échange eau/acétone est à l'origine de la formation de craquelures horizontales et verticales dans l'échantillon, avec des conséquences évidentes sur la structure du dépôt, en particulier aux échelles considérées.

2. Caractéristiques connues

L'ensemble des techniques développées dans l'étude des dépôts de tsunamis a permis la mise en place progressive d'une liste de critères d'identification assez conséquente, dont l'application dans différents contextes a permis de reconnaître des caractéristiques communes à la majorité des dépôts (Bourgeois, 2009 ; Chagué-Goff et al., 2011 ; Goff et al., 2012). On note aussi qu'à l'heure actuelle l'intégralité des techniques expérimentales n'a pas été mise en œuvre dans le cadre d'une seule et même étude, plusieurs recoupements sont permis par la diversité des sites étudiés et l'exhaustivité croissante des études. De ce fait, les caractéristiques suivantes peuvent être considérées comme représentatives des dépôts de tsunamis, sans pour autant leur être forcément exclusives.

- Dans la mesure où les dépôts formés par les tsunamis sont directement dépendants du stock sédimentaire disponible, toutes les fractions granulométriques peuvent être représentées, des silts et argiles aux blocs plurimétriques, toutes les classes granulométriques pouvant apparaître dans un seul et même dépôt.

- Le plancher du dépôt est généralement caractérisé par une base érosive et un dépôt en discordance, caractéristiques qui peuvent également apparaître au sein du dépôt entre différentes couches successives. La présence de clastes de substratum (p. ex. clastes de sol arraché ou *rip-ups*, idem avec de la boue…) est fréquente, en particulier en base de dépôt ou au sein du dépôt au dessus de couches cohérentes.

- Le dépôt est souvent stratifié, avec une structuration interne qui, dans certains cas, n'est pas sans rappeler les séquences turbiditiques telles que définies par Bouma (1964) et Lowe (1976).

- La structuration interne du dépôt est souvent complexe à l'échelle micromorphologique même dans le cas où la séquence semble simple en première observation. Les microstructures déjà observées suggèrent une mise en place complexe, et complètent généralement les données macrostructurales sans les contredire.

- Chaque vague est susceptible de mettre en place une ou plusieurs couches de sédiments, sans que le nombre de vagues puisse toujours être relié aux nombre de couches retrouvées dans le dépôt. Les phases d'érosion intermédiaires rendent le rapport entre le nombre de couches et le nombre de vagues encore plus difficile à établir, dans la mesure où la séquence compte fréquemment des lacunes plus ou moins importantes et difficiles (voire impossibles) à estimer.

- Le dépôt tend généralement à perdre en épaisseur, et la taille des grains à diminuer en direction de l'intérieur des terres. La topographie locale influence cependant la configuration du dépôt, parfois de manière très marquée (on constate fréquemment un épaississement du dépôt dans les dépressions par exemple, ou au pied d'obstacles).

- Les figures d'imbrications et les orientations préférentielles des grains, ainsi que certains objets charriés ou déplacés (arbres, poteaux, etc.) indiquent généralement des courants orientés vers l'intérieur des terres (phase d'inondation ou *uprush*) ou vers la mer (phase de retrait ou *backwash*). Là encore la topographie locale peut jouer un rôle prépondérant dans l'orientation du courant.

- Le dépôt présente souvent un granoclassement globalement normal (à l'échelle du dépôt), mais chaque strate présente cependant fréquemment un classement individuel, normal ou inverse.

- Les structures sédimentaires retrouvées dans les dépôts peuvent être très variées : laminations, dunes, stratifications obliques, convolutions voire même ressemblant à des anti-dunes (p. ex. lorsque l'écoulement est canalisé, typiquement lors des phases de *backwash*).

- Le dépôt peut présenter des marqueurs de phases de décantation entre vagues successives, sous la forme de passées argileuses succédant plus ou moins progressivement à un niveau plus grossier (*mudlines*) ou nappant le niveau inférieur (*mud drapes*).

- Les enrichissements en minéraux lourds de certains dépôts peuvent permettre de tracer les stocks sédimentaires mobilisés par le tsunami et sont souvent concentrés dans des lamines, ce qui peut permettre de contraindre les conditions hydrodynamiques du flux durant leur mise en place.

- Les dépôts peuvent présenter, quand elle est conservée, une signature géochimique, généralement marine (p. ex. Cl, Br, Na ; Ca dans le cas de bioclastes marins) et de haute énergie (p. ex. Ti, Zr), mais des indices d'influence continentale peuvent également être retrouvés (Al ou Ti par exemple). On note cependant que certains éléments très solubles se conservent mal dans les dépôts (p. ex. Na, Cl, S).

- Le contenu biologique des dépôts (pollen, bois, mais surtout bioclastes carbonatés) donnent fréquemment des informations importantes sur la provenance du sédiment. Les bioclastes marins sont fréquents (mais pas toujours présents) et constituent une source de renseignements importante. Les fragments de plantes et de bois peuvent permettre une datation du dépôt. Un âge précis peut cependant s'avérer difficile à obtenir, l'origine exacte des fragments végétaux et leur état quand ils ont été mobilisés par le tsunami n'étant pas forcément simple à définir.

L'ensemble de ces critères permet une identification et une caractérisation relativement précise des dépôts de tsunami, cependant il est fréquent que plusieurs d'entre eux ne puissent être étudiés ou soient absents de la séquence considérée, réduisant d'autant la précision de

l'analyse. On note souvent une grande variabilité non seulement longitudinale mais aussi latérale dans les caractéristiques des dépôts, parfois sur des distances relativement courtes (quelques mètres). De plus, les conditions météorologiques, les activités anthropiques et biologiques diverses (bioturbation par les animaux fouisseurs, les plantes...) font que le dépôt peut parfois se dégrader très rapidement, entraînant l'altération voire la perte de plusieurs marqueurs. Dans ce contexte, il reste essentiel de développer de nouvelles techniques d'analyse permettant de compléter la "boîte à outils" actuelle afin d'exploiter un maximum des renseignements préservés au sein du dépôt (Goff et al., 2001; Etienne et al., 2011; Ramírez-Herrera et al., 2012; Cuven et al., 2013). De plus, si les analyses micromorphologiques ont montré qu'à l'heure actuelle de nombreux détails restaient dans l'ombre faute d'observations suffisamment précises, elles n'ont pour l'instant été que très peu exploitées. Enfin, beaucoup de techniques analytiques utilisées actuellement sont basées sur des échantillonnages discrets, par pas régulier ou généralement défini sur le terrain en fonction de la structuration visible sur le terrain. Ce mode de prélèvement et d'exploitation des données introduit de nombreux biais liés à l'opérateur et à la précision des mesures. La mise en place de techniques basées sur un échantillonnage et un mode d'analyse continu permettrait l'obtention de données plus pertinentes, en particuliers concernant des structures fines mais essentielles à la compréhension précise de l'évènement (p.ex. mudlines, fines lamines, formes d'érosion…). Les mesures de répartition de tailles de grain et de fabrique sédimentaire gagneraient également en pertinence en étant menées individuellement sur chaque structure du dépôt, hors les techniques actuelles ne permettent pas toujours une telle précision. Il apparaît donc intéressant d'exploiter des techniques regroupant ces critères de continuité, de haute précision et de non destructivité.

V. Apports potentiels de la microtomographie par rayons X

1. Tomographie par rayons X : principe

La tomographie par rayons X assistée par ordinateur (*X-ray Computed Tomography*, ou *X-CT*) est dérivée de la radiographie par rayons X qui repose sur le principe d'absorption partielle d'un flux de rayons X (10^{-11}nm < λ < 10^{-8}nm) par un matériau de coefficient d'absorption linéaire μ. L'intensité initiale du faisceau I_0 est reliée à l'intensité transmise I par la formule :

$$I = I_0 e^{-\mu x}$$

où x représente l'épaisseur traversée par le faisceau.

Hamblin (1962) a mis en évidence les intérêts de l'utilisation de l'imagerie par rayons X dans le cadre de la géologie, en démontrant son potentiel à permettre la visualisation de structures invisibles à l'œil nu sur des échantillons rocheux opaques et d'aspect homogène. Les radiographies réalisées montrent clairement une structuration interne parfois complexe, et facilitent largement l'interprétation des conditions de mise en place du sédiment. Cependant, cette technique nécessite une préparation méticuleuse de l'échantillon et sa destruction partielle dans la mesure où une variation de l'épaisseur de l'échantillon augmente son pouvoir d'absorption. La réalisation de lames ou de plaquettes est donc nécessaire dan le cadre de la radiographie par rayons X.

Le principe de la radiographie est repris par Hounsfield (1962) qui conçoit un appareil capable de combiner informatiquement plusieurs radiographies d'un même objet sous plusieurs angles différents afin d'obtenir une série d'images en deux dimensions (« tranches » d'objet, plus communément appelées *slices*) qui une fois concaténées permettent une visualisation de son volume et de sa structuration interne en trois dimensions.

Cette technique d'imagerie permet ainsi de visualiser les variations d'absorption de l'objet. L'absorption de l'échantillon étant fonction de sa composition atomique et de la longueur d'onde du rayonnement, la technique permet d'en détecter les variations de densité interne. Un des principaux intérêts de cette technique étant de permettre la visualisation de la structure interne d'un échantillon de manière non destructive, elle est utilisée de manière extensive dans le milieu médical (scanners) et le contrôle industriel des matériaux (détection d'imperfections, de défauts de cristallisation, etc.).

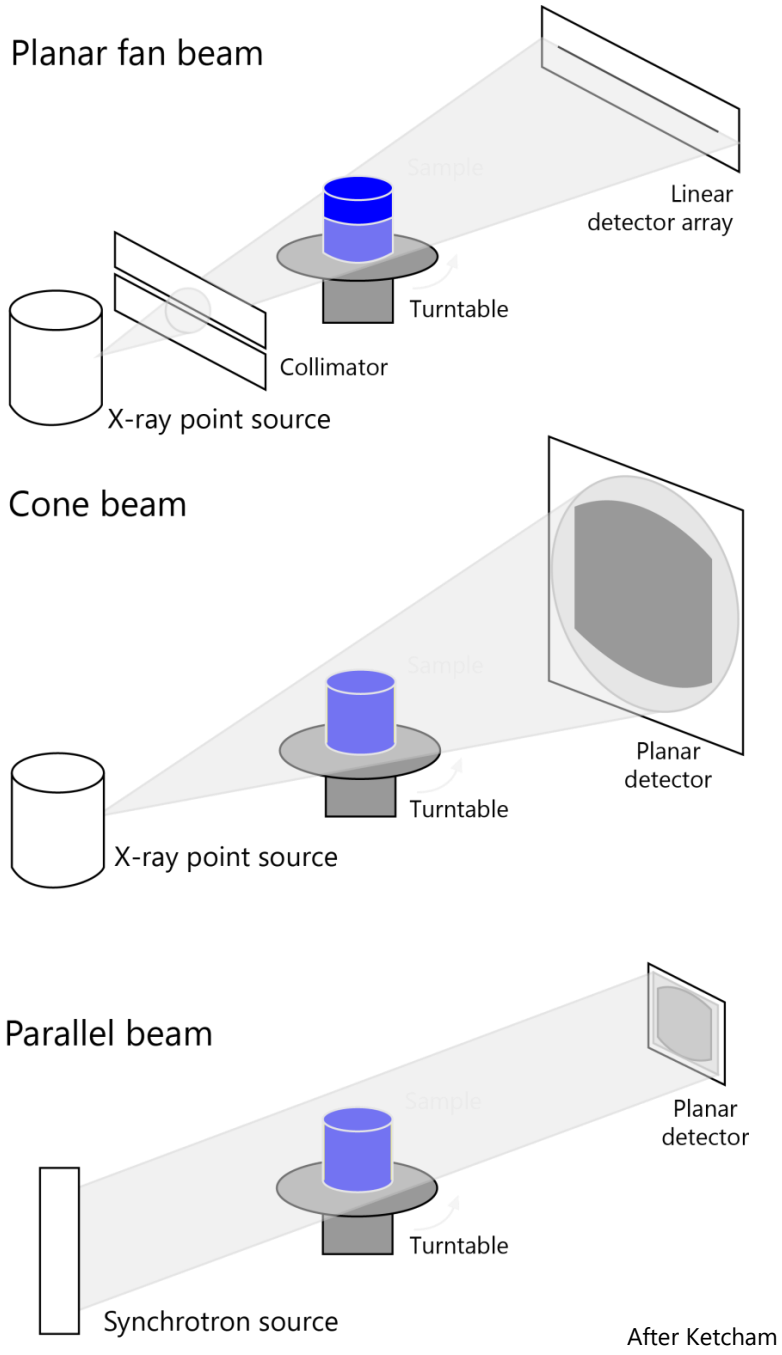

Fig. 1 : principe de fonctionnement de la tomographie par rayons X. L'échantillon (en bleu) est traversé par les rayons X émis à la source du tomographe. Un capteur à l'autre bout du dispositif mesure l'atténuation par l'échantillon du flux de rayons X. Plusieurs scans de l'échantillon sont réalisés afin de l'analyser sur 360° (rotation) et sur toute sa hauteur (translation verticale si nécessaire). La forme du faisceau dépend généralement de l'utilisation pour laquelle le scanner est conçu : faisceau en éventail pour les scanners à usages médicaux, en cône pour les scanners à usage industriel ou scientifique. Les faisceaux parallèles sont produits par les synchrotrons et quelques scanners scientifiques très spécifiques. Cette géométrie du faisceau permet de s'affranchir plus aisément d'un certain nombres d'artefacts durant la reconstruction des volumes.

2. Applications potentielles à l'étude des dépôts de tsunami

Dans le milieu des sciences de la Terre, la tomographie par rayons X a été utilisée dans plusieurs domaines (Mees et al., 2003), comme les analyses texturales et structurales (p. ex. Denison et al., 1997; Jerram and Higgins, 2007), les analyses minéralogiques (p. ex. Friese et al., 2013), les analyses de morphologie et de taille de grains (p. ex. Higgins, 2000) ou encore de porosité de pyroclastes (p. ex. Giachetti et al., 2011). Ces études ont démontré la pertinence de l'analyse en trois dimensions couplées aux hautes précisions permises par la technologie actuelle.

Si la radiographie par rayons X a déjà été utilisée de manière assez marginale afin d'analyser la structure des dépôts de tsunamis (p. ex. (Bondevik et al., 2005b; Chagué-Goff et al., 2012; Minoura et al., 1996), le potentiel de la visualisation en trois dimensions des structures et textures des dépôts n'a pas encore été exploité (Cuven et al., 2013). Hors, les technologies actuelles sont en mesure de permettre des analyses à des échelles micrométriques (Giachetti et al., 2011; Ketcham and Carlson, 2001) et sont donc susceptibles de permettre des analyses microstructurales, micromorphologiques et texturales poussées, et d'apporter un complément novateur à l'étude des dépôts tsunamis.

Références

Albertão, G.A., Martins Jr., P.P., 1996. A possible tsunami deposit at the Cretaceous-Tertiary boundary in Pernambuco, northeastern Brazil. Sedimentary Geology 104, 189–201.

Alvarez, L.W., Alvarez, W., Asaro, F., Michel, H.V., 1980. Extraterrestrial Cause for the Cretaceous-Tertiary Extinction. Science 208, 1095–1108.

Atwater, B.F., 1987. Evidence for great Holocene earthquakes along the outer coast of Washington State. Science 236, 942–944.

Atwater, B.F., 1992. Geologic evidence for earthquakes during the past 2000 years along the Copalis River, southern coastal Washington. Journal of Geophysical Research: Solid Earth 97, 1901–1919.

Babu, N., Babu, D.S.S., Das, P.N.M., 2007. Impact of tsunami on texture and mineralogy of a major placer deposit in southwest coast of India. Environ Geol 52, 71–80.

Baptista, M.A., Miranda, J.M., Chierici, F., Zitellini, N., 2003. New study of the 1755 earthquake source based on multi-channel seismic survey data and tsunami modeling. Natural Hazards and earth System Science 3, 333–340.

Bardet, J.-P., Synolakis, C.E., Davies, H.L., Imamura, F., Okal, E.A., 2003. Landslide Tsunamis: Recent Findings and Research Directions, in: Bardet, J.-P., Imamura, F., Synolakis, C.E., Okal, E.A., Davies, H.L. (Eds.), Landslide Tsunamis: Recent Findings and Research Directions, Pageoph Topical Volumes. Birkhäuser Basel, 1793–1809.

Belousov, A., Voight, B., Belousova, M., Muravyev, Y., 2000. Tsunamis Generated by Subaquatic Volcanic Explosions: Unique Data from 1996 Eruption in Karymskoye Lake, Kamchatka, Russia. Pure appl. geophys. 157, 1135–1143.

Bondevik, S., Svendsen, J.I., Mangerud, J., 1997. Tsunami sedimentary facies deposited by Storegga tsunami in shallow marine basins and coastal lakes, western Norway. Sedimentology 44, 1115-1131.

Bondevik, S., Mangerud, J., Dawson, S., Dawson, A., Lohne, Ø., 2003. Record-breaking height for 8000-year-old tsunami in the North Atlantic. Eos, Transactions American Geophysical Union 84, 289–293.

Bondevik, S., Løvholt, F., Harbitz, C., Mangerud, J., Dawson, A., Inge Svendsen, J., 2005a. The Storegga Slide tsunami—comparing field observations with numerical simulations. Marine and Petroleum Geology 22, 195–208.

Bondevik, S., Mangerud, J., Dawson, S., Dawson, A., Lohne, Ø., 2005b. Evidence for three North Sea tsunamis at the Shetland Islands between 8000 and 1500 years ago. Quaternary Science Reviews 24, 1757–1775.

Bony, G., Marriner, N., Morhange, C., Kaniewski, D., Perinçek, D., 2012. A high-energy deposit in the Byzantine harbour of Yenikapı, Istanbul (Turkey). Quaternary International 266, 117–130.

Bouma, A.H., 1964. Turbidites. Developments in Sedimentology 3, 247-256.

Bourgeois, J., Hansen, T.A., Wiberg, P.L., Kauffman, E.G., 1988. A Tsunami Deposit at the Cretaceous-Tertiary Boundary in Texas. Science 241, 567–570.

Bourgeois, J., 2009. Geologic effects and records of tsunamis. The sea 15, 55–91.

Bridge, J.S., 2008. Discussion of articles in "Sedimentary features of tsunami deposits". Sedimentary Geology 211, 94.

Bugge, T., Befring, S., Belderson, R.H., Eidvin, T., Jansen, E., Kenyon, N.H., Holtedahl, H., Sejrup, H.P., 1987. A giant three-stage submarine slide off Norway. Geo-Marine Letters 7, 191–198.

Chagué-Goff, C., Dawson, S., Goff, J.R., Zachariasen, J., Berryman, K.R., Garnett, D.L., Waldron, H.M., Mildenhall, D.C., 2002. A tsunami (ca. 6300 years BP) and other Holocene environmental changes, northern Hawke's Bay, New Zealand. Sedimentary Geology 150, 89–102.

Chagué-Goff, C., 2010. Chemical signatures of palaeotsunamis: A forgotten proxy? Marine Geology 271, 67–71.

Chagué-Goff, C., Schneider, J.-L., Goff, J.R., Dominey-Howes, D., Strotz, L., 2011. Expanding the proxy toolkit to help identify past events — Lessons from the 2004 Indian Ocean Tsunami and the 2009 South Pacific Tsunami. Earth-Science Reviews 107, 107–122.

Chagué-Goff, C., Andrew, A., Szczuciński, W., Goff, J., Nishimura, Y., 2012. Geochemical signatures up to the maximum inundation of the 2011 Tohoku-oki tsunami — Implications for the 869 AD Jogan and other palaeotsunamis. Sedimentary Geology 282, 65–77.

Cita, M.B., Aloisi, G., 2000. Deep-sea tsunami deposits triggered by the explosion of Santorini (3500y BP), eastern Mediterranean. Sedimentary Geology 135, 181–203.

Cummins, P.R., Kong, L.S.L., Satake, K., 2009. Introduction to “Tsunami Science Four Years After the 2004 Indian Ocean Tsunami, Part I: Modelling and Hazard Assessment”. Pure and Applied Geophysics 165, 1983–1989.

Cuven, S., Paris, R., Falvard, S., Miot-Noirault, E., Benbakkar, M., Schneider, J.-L., Billy, I., 2013. High-resolution analysis of a tsunami deposit: Case-study from the 1755 Lisbon tsunami in southwestern Spain. Marine Geology 337, 98–111.

Dawson, A.G., Long, D., Smith, D.E., 1988. The Storegga Slides: Evidence from eastern Scotland for a possible tsunami. Marine Geology 82, 271–276.

Dawson, A.G., Shi, S., Dawson, S., Takahashi, T., Shuto, N., 1996. Coastal sedimentation associated with the June 2nd and 3rd, 1994 tsunami in Rajegwesi, Java. Quaternary Science Reviews 15, 901–912.

Dawson, S., Smith, D.E., 2000. The sedimentology of Middle Holocene tsunami facies in northern Sutherland, Scotland, UK. Marine Geology 170, 69–79.

Dawson, S., 2007. Diatom biostratigraphy of tsunami deposits: Examples from the 1998 Papua New Guinea tsunami. Sedimentary Geology 200, 328–335.

Dawson, A.G., Stewart, I., Morton, R.A., Richmond, B.M., Jaffe, B.E., Gelfenbaum, G., 2008. Reply to Comments by Kelletat (2008) comments to Dawson, A.G. and Stewart, I. (2007) tsunami deposits in the geological record [Sedimentary Geology, 200, 166–183]. Sedimentary Geology 211, 92–93.

Denison, C., Carlson, W.D., Ketcham, R.A., 1997. Three-dimensional quantitative textural analysis of metamorphic rocks using high-resolution computed X-ray tomography: Part I. Methods and techniques. Journal of Metamorphic Geology 15, 29–44.

Dominey-Howes, D., Dawson, A., Smith, D., 1999. Late Holocene coastal tectonics at Falasarna, western Crete: a sedimentary study. Geological Society, London, Special Publications 146, 343–352.

Dunbar, P., McCullough, H., 2011. Global tsunami deposits database. Natural Hazards 63, 267–278.

Etienne, S., Buckley, M., Paris, R., Nandasena, A.K., Clark, K., Strotz, L., Chagué-Goff, C., Goff, J., Richmond, B., 2011. The use of boulders for characterising past tsunamis: Lessons from the 2004 Indian Ocean and 2009 South Pacific tsunamis. Earth-Science Reviews 107, 76–90.

Fine, I.V., Rabinovich, A.B., Bornhold, B.D., Thomson, R.E., Kulikov, E.A., 2005. The Grand Banks landslide-generated tsunami of November 18, 1929: preliminary analysis and numerical modeling. Marine Geology 215, 45–57.

Friese, K.-I., Cichy, S.B., Wolter, F.-E., Botcharnikov, R.E., 2013. Analysis of tomographic mineralogical data using YaDiV—Overview and practical case study. Computers & Geosciences 56, 92–103.

Fujiwara, O., Masuda, F., Sakai, T., Irizuki, T., Fuse, K., 2000. Tsunami deposits in Holocene bay mud in southern Kanto region, Pacific coast of central Japan. Sedimentary Geology 135, 219–230.

Gehrels, W.R., Kirby, J.R., Prokoph, A., Newnham, R.M., Achterberg, E.P., Evans, H., Black, S., Scott, D.B., 2005. Onset of recent rapid sea-level rise in the western Atlantic Ocean. Quaternary Science Reviews 24, 2083–2100.

Gelfenbaum, G., Jaffe, B., 2003. Erosion and Sedimentation from the 17 July, 1998 Papua New Guinea Tsunami. Pure and Applied Geophysics 160, 1969-1999.

Giachetti, T., Burgisser, A., Arbaret, L., Druitt, T.H., Kelfoun, K., 2011. Quantitative textural analysis of Vulcanian pyroclasts (Montserrat) using multi-scale X-ray computed microtomography: comparison with results from 2D image analysis. Bulletin of Volcanology 73, 1295–1309.

Goff, J.R., Chagué-Goff, C., 1999. A late Holocene record of environmental changes from coastal wetlands: Abel Tasman National Park, New Zealand. Quaternary International 56, 39–51.

Goff, J., Chagué-Goff, C., Nichol, S., 2001. Palaeotsunami deposits: a New Zealand perspective. Sedimentary Geology 143, 1–6.

Goff, J., McFadgen, B.G., Chagué-Goff, C., 2004. Sedimentary differences between the 2002 Easter storm and the 15th-century Okoropunga tsunami, southeastern North Island, New Zealand. Marine Geology 204, 235–250.

Goff, J., Dominey-Howes, D., 2011. The 2009 South Pacific Tsunami. Earth-Science Reviews 107, v–vii.

Goff, J., Chagué-Goff, C., Nichol, S., Jaffe, B., Dominey-Howes, D., 2012. Progress in palaeotsunami research. Sedimentary Geology 243–244, 70–88.

Goto, K., Tada, R., Tajika, E., Iturralde-Vinent, M.A., Matsui, T., Yamamoto, S., Nakano, Y., Oji, T., Kiyokawa, S., García Delgado, D.E., Díaz Otero, C., Rojas Consuegra, R., 2008. Lateral lithological and compositional variations of the Cretaceous/Tertiary deep-sea tsunami deposits in northwestern Cuba. Cretaceous Research 29, 217–236.

Goto, K., Kawana, T., Imamura, F., 2010. Historical and geological evidence of boulders deposited by tsunamis, southern Ryukyu Islands, Japan. Earth-Science Reviews 102, 77–99.

Goto, K., Chagué-Goff, C., Goff, J., Jaffe, B., 2012a. The future of tsunami research following the 2011 Tohoku-oki event. Sedimentary Geology 282, 1–13.

Goto, K., Sugawara, D., Ikema, S., Miyagi, T., 2012b. Sedimentary processes associated with sand and boulder deposits formed by the 2011 Tohoku-oki tsunami at Sabusawa Island, Japan. Sedimentary Geology 282, 188–198.

Grauert, M., Björck, S., Bondevik, S., 2001. Storegga tsunami deposits in a coastal lake on Suouroy, the Faroe Islands. Boreas 30, 263–271.

Hamblin, W.K., 1962. X-ray radiography in the study of structures in homogeneous sediments. Journal of Sedimentary Research 32, 201–210.

Hawkes, A.D., Bird, M., Cowie, S., Grundy-Warr, C., Horton, B.P., Shau Hwai, A.T., Law, L., Macgregor, C., Nott, J., Ong, J.E., Rigg, J., Robinson, R., Tan-Mullins, M., Sa, T.T., Yasin, Z., Aik, L.W., 2007. Sediments deposited by the 2004 Indian Ocean Tsunami along the Malaysia–Thailand Peninsula. Marine Geology 242, 169–190.

Higgins, M.D., 2000. Measurement of crystal size distributions. American Mineralogist 85, 1105–1116.

Hildebrand, A.R., Penfield, G.T., Kring, D.A., Pilkington, M., Z, A.C., Jacobsen, S.B., Boynton, W.V., 1991. Chicxulub Crater: A possible Cretaceous/Tertiary boundary impact crater on the Yucatán Peninsula, Mexico. Geology 19, 867–871.

Hjulström, F., 1935. Studies of the morphological activity of rivers as illustrated by the river Fyris. Bull. Geol. Inst. Uppsala 25, 221–527.

Hounsfield, G.N., 1962. Computerized transverse axial scanning (tomography): Part 1. Description of system. British Journal of Radiology 46 (552), 1016-1022.

Iida, K., 1963. Magnitude, energy and generation mechanisms of tsunamis and a catalogue of earthquakes associated with tsunamis, in: Pros. Tsunami Meetings 10th Pacific Sci Congr., IUGG Monogr. pp. 7–18.

Iliev, A.Y., Kaistrenko, V.M., Gretskaya, E.V., Tikhonchuk, E.A., Razjigaeva, N.G., Grebennikova, T.A., Ganzey, L.A., Kharlamov, A.A., 2005. Holocene tsunami traces on Kunashir Island, Kurile subduction zone, in: Tsunamis. Springer, pp. 171–192.

Imamura, F., Gica, E., Takahashi, T., Shuto, N., 1995. Numerical Simulation of the 1992 Flores Tsunami: Interpretation of Tsunami Phenomena in Northeastern Flores Island and Damage at Babi Island, in: Imamura, D.F., Satake, D.K. (Eds.), Tsunamis: 1992–1994, Pageoph Topical Volumes. Birkhäuser Basel, pp. 555–568.

Jaffe, B.E., Gelfenbaum, G., 2007. A simple model for calculating tsunami flow speed from tsunami deposits. Sedimentary Geology 200, 347–361.

Jaffe, B., Buckley, M., Richmond, B., Strotz, L., Etienne, S., Clark, K., Watt, S., Gelfenbaum, G., Goff, J., 2011. Flow speed estimated by inverse modeling of sandy sediment deposited by the 29 September 2009 tsunami near Satitoa, east Upolu, Samoa. Earth-Science Reviews 107, 23–37.

Jagodziński, R., Sternal, B., Szczuciński, W., Lorenc, S., 2009. Heavy minerals in 2004 tsunami deposits on Kho Khao Island, Thailand. Polish Journal of Environmental Studies 18, 103–110.

Jagodziński, R., Sternal, B., Szczuciński, W., Chagué-Goff, C., Sugawara, D., 2012. Heavy minerals in the 2011 Tohoku-oki tsunami deposits—insights into sediment sources and hydrodynamics. Sedimentary Geology 282, 57–64.

Jerram, D.A., Higgins, M.D., 2007. 3D analysis of rock textures: quantifying igneous microstructures. Elements 3, 239–245.

Kanamori, H., 1972. Mechanism of tsunami earthquakes. Physics of the Earth and Planetary Interiors 6, 346–359.

Kelletat, D., 2008. Comments to Dawson, A.G. and Stewart, I. (2007), Tsunami deposits in the geological record. — Sedimentary Geology 200, 166–183. Sedimentary Geology 211, 87–91.

Ketcham, R.A., Carlson, W.D., 2001. Acquisition, optimization and interpretation of X-ray computed tomographic imagery: applications to the geosciences. Computers & Geosciences 27, 381–400.

Kilfeather, A.A., Blackford, J.J., Meer, J.J.M. van der, 2007. Micromorphological Analysis of Coastal Sediments from Willapa Bay, Washington, USA: A Technique for Analysing Inferred Tsunami Deposits. Pure appl. geophys. 164, 509–525.

Kortekaas, S., Dawson, A.G., 2007. Distinguishing tsunami and storm deposits: An example from Martinhal, SW Portugal. Sedimentary Geology 200, 208–221.

Kulikov, E.A., Rabinovich, A.B., Thomson, R.E., Bornhold, B.D., 1996. The landslide tsunami of November 3, 1994, Skagway Harbor, Alaska. Journal of Geophysical Research: Oceans 101, 6609–6615.

Latter, J.H., 1981. Tsunamis of volcanic origin: Summary of causes, with particular reference to Krakatoa, 1883. Bull Volcanol 44, 467–490.

Liu, B., Saito, Y., Yamazaki, T., Abdeldayem, A., Oda, H., Hori, K., Zhao, Q., 2001. Paleocurrent analysis for the Late Pleistocene–Holocene incised-valley fill of the Yangtze delta, China by using anisotropy of magnetic susceptibility data. Marine Geology 176, 175–189.

Long, D., Smith, D.E., Dawson, A.G., 1989. A Holocene tsunami deposit in eastern Scotland. Journal of Quaternary Science 4, 61–66.

Lowe, D.R., 1976. Subaqueous liquefied and fluidized sediment flows and their deposits. Sedimentology 23 (3), 285-308.

Masson, D.G., Harbitz, C.B., Wynn, R.B., Pedersen, G., Lovholt, F., 2006. Submarine landslides: processes, triggers and hazard prediction. Philosophical Transactions of the Royal Society A: Mathematical, Physical and Engineering Sciences 364, 2009–2039.

Mastronuzzi, G., Pignatelli, C., Sansò, P., Selleri, G., 2007. Boulder accumulations produced by the 20th of February, 1743 tsunami along the coast of southeastern Salento (Apulia region, Italy). Marine Geology 242, 191–205.

McAdoo, B.G., Ah-Leong, J.S., Bell, L., Ifopo, P., Ward, J., Lovell, E., Skelton, P., 2011. Coral reefs as buffers during the 2009 South Pacific tsunami, Upolu Island, Samoa. Earth-Science Reviews 107, 147–155.

Mees, F., Swennen, R., Geet, M.V., Jacobs, P., 2003. Applications of X-ray computed tomography in the geosciences. Geological Society, London, Special Publications 215, 1–6.

Miller, D.J., 1960. The Alaska Earthquake of July 10, 1958: Giant wave in Lituya Bay. Bulletin of the Seismological Society of America 50, 253-266.

Minoura, K., Nakaya, S., 1991. Traces of tsunami preserved in inter-tidal lacustrine and marsh deposits: some examples from northeast Japan. Journal of Geology 99, 265–287.

Minoura, K., Gusiakov, V.G., Kurbatov, A., Takeuti, S., Svendsen, J.I., Bondevik, S., Oda, T., 1996. Tsunami sedimentation associated with the 1923 Kamchatka earthquake. Sedimentary Geology 106, 145–154.

Minoura, K., Imamura, F., Takahashi, T., Shuto, N., 1997. Sequence of sedimentation processes caused by the 1992 Flores tsunami: Evidence from Babi Island. Geology 25, 523–526.

Moore, A., Goff, J., McAdoo, B.G., Fritz, H.M., Gusman, A., Kalligeris, N., Kalsum, K., Susanto, A., Suteja, D., Synolakis, C.E., 2011. Sedimentary Deposits from the 17 July 2006 Western Java Tsunami, Indonesia: Use of Grain Size Analyses to Assess Tsunami Flow Depth, Speed, and Traction Carpet Characteristics. Pure Appl. Geophys. 168, 1951–1961.

Moore, A.L., McAdoo, B.G., Ruffman, A., 2007. Landward fining from multiple sources in a sand sheet deposited by the 1929 Grand Banks tsunami, Newfoundland. Sedimentary Geology 200, 336–346.

Morton, R.A., Goff, J.R., Nichol, S.L., 2008. Hydrodynamic implications of textural trends in sand deposits of the 2004 tsunami in Sri Lanka. Sedimentary Geology 207, 56–64.

Nakada, M., Inoue, H., 2005. Rates and causes of recent global sea-level rise inferred from long tide gauge data records. Quaternary Science Reviews 24, 1217–1222.

Nakamura, Y., Nishimura, Y., Putra, P.S., 2012. Local variation of inundation, sedimentary characteristics, and mineral assemblages of the 2011 Tohoku-oki tsunami on the Misawa coast, Aomori, Japan. Sedimentary Geology 282, 216–227.

Nanayama, F., Shigeno, K., Satake, K., Shimokawa, K., Koitabashi, S., Miyasaka, S., Ishii, M., 2000. Sedimentary differences between the 1993 Hokkaido-nansei-oki tsunami and the 1959 Miyakojima typhoon at Taisei, southwestern Hokkaido, northern Japan. Sedimentary Geology 135, 255–264.

Naruse, H., Arai, K., Matsumoto, D., Takahashi, H., Yamashita, S., Tanaka, G., Murayama, M., 2012. Sedimentary features observed in the tsunami deposits at Rikuzentakata City. Sedimentary Geology 282, 199–215.

Nichol, S.L., Goff, J.R., Devoy, R.J.N., Chagué-Goff, C., Hayward, B., James, I., 2007. Lagoon subsidence and tsunami on the West Coast of New Zealand. Sedimentary Geology 200, 248–262.

Nishimura, Y., Miyaji, N., 1995. Tsunami deposits from the 1993 southwest Hokkaido earthquake and the 1640 Hokkaido Komagatake eruption, northern Japan. Pure and Applied geophysics 144, 719–733.

Papadopoulos, G.A., Imamura, F., 2001. A proposal for a new tsunami intensity scale. Proc. Int. Tsunami Sym. 5, 569–577.

Papadopoulos, G.A., 2003. Quantification of Tsunamis: A Review, in: Yalçiner, A.C., Pelinovsky, E.N., Okal, E., Synolakis, C.E. (Eds.), Submarine Landslides and Tsunamis, NATO Science Series. Springer Netherlands, pp. 285–291.

Paris, R., Lavigne, F., Wassmer, P., Sartohadi, J., 2007. Coastal sedimentation associated with the December 26, 2004 tsunami in Lhok Nga, west Banda Aceh (Sumatra, Indonesia). Marine Geology 238, 93–106.

Paris, R., Wassmer, P., Sartohadi, J., Lavigne, F., Barthomeuf, B., Desgages, E., Grancher, D., Baumert, P., Vautier, F., Brunstein, D., Gomez, C., 2009. Tsunamis as geomorphic crises: Lessons from the December 26, 2004 tsunami in Lhok Nga, West Banda Aceh (Sumatra, Indonesia). Geomorphology 104, 59–72.

Paris, R., Cachão, M., Fournier, J., Voldoire, O., 2010a. Nannoliths abundance and distribution in tsunami deposits: example from the December 26, 2004 tsunami in Lhok Nga (northwest Sumatra, Indonesia). Géomorphologie : relief, processus, environnement 109–118.

Paris, R., Fournier, J., Poizot, E., Etienne, S., Morin, J., Lavigne, F., Wassmer, P., 2010b. Boulder and fine sediment transport and deposition by the 2004 tsunami in Lhok Nga (western Banda Aceh, Sumatra, Indonesia): A coupled offshore–onshore model. Marine Geology 268, 43–54.

Paris, R., Switzer, A.D., Belousova, M., Belousov, A., Ontowirjo, B., Whelley, P.L., Ulvrova, M., 2014a. Volcanic tsunami: a review of source mechanisms, past events and hazards

in Southeast Asia (Indonesia, Philippines, Papua New Guinea). Nat Hazards 70, 447–470.

Paris, R., Wassmer, P., Lavigne, F., Belousov, A., Belousova, M., Iskandarsyah, Y., Benbakkar, M., Ontowirjo, B., Mazzoni, N., 2014b. Coupling eruption and tsunami records: the Krakatau 1883 case study, Indonesia. Bulletin of Volcanology 76 (4): 814.

Park, C.-K., Doh, S.-J., Suk, D.-W., Kim, K.-H., 2000. Sedimentary fabric on deep-sea sediments from KODOS area in the eastern Pacific. Marine Geology 171, 115–126.

Pilarczyk, J.E., Horton, B.P., Witter, R.C., Vane, C.H., Chagué-Goff, C., Goff, J., 2012. Sedimentary and foraminiferal evidence of the 2011 Tōhoku-oki tsunami on the Sendai coastal plain, Japan. Sedimentary Geology 282, 78–89.

Pinegina, T.K., Bourgeois, J., Bazanova, L.I., Melekestsev, I.V., Braitseva, O.A., 2003. A millennial-scale record of Holocene tsunamis on the Kronotskiy Bay coast, Kamchatka, Russia. Quaternary Research 59, 36–47.

Pritchard D, Dickinson L (2008) Modelling the sedimentary signature of long waves on coasts: implications for tsunami reconstruction. Sed Geol 206:42–57.

Ramírez-Herrera, M.-T., Lagos, M., Hutchinson, I., Kostoglodov, V., Machain, M.L., Caballero, M., Goguitchaichvili, A., Aguilar, B., Chagué-Goff, C., Goff, J., Ruiz-Fernández, A.-C., Ortiz, M., Nava, H., Bautista, F., Lopez, G.I., Quintana, P., 2012. Extreme wave deposits on the Pacific coast of Mexico: Tsunamis or storms? — A multi-proxy approach. Geomorphology 139–140, 360–371.

Rees, A.I., 1965. The Use of Anisotropy of Magnetic Susceptibility in the Estimation of Sedimentary Fabric1. Sedimentology 4, 257–271.

Rees, A.I., Woodall, W.A., 1975. The magnetic fabric of some laboratory-deposited sediments. Earth and Planetary Science Letters 25, 121–130.

Richmond, B., Szczuciński, W., Chagué-Goff, C., Goto, K., Sugawara, D., Witter, R., Tappin, D.R., Jaffe, B., Fujino, S., Nishimura, Y., Goff, J., 2012. Erosion, deposition and

landscape change on the Sendai coastal plain, Japan, resulting from the March 11, 2011 Tohoku-oki tsunami. Sedimentary Geology 282, 27–39.

Richmond, B.M., Buckley, M., Etienne, S., Chagué-Goff, C., Clark, K., Goff, J., Dominey-Howes, D., Strotz, L., 2011. Deposits, flow characteristics, and landscape change resulting from the September 2009 South Pacific tsunami in the Samoan islands. Earth-Science Reviews 107, 38–51.

Schneider, J.-L., Chagué-Goff, C., Bouchez, J.-L., Goff, J., Sugawara, D., Goto, K., Jaffe, B., Richmond, B., 2014. Using Magnetic Fabric to Reconstruct the Dynamics of Tsunami Deposition on the Sendai Plain, Japan — The 2011 Tohoku-Oki Tsunami. Marine Geology 358, 89-106.

Schnellmann, M., Anselmetti, F.S., Giardini, D., McKenzie, J.A., Ward, S.N., 2002. Prehistoric earthquake history revealed by lacustrine slump deposits. Geology 30, 1131–1134.

Shi, S., Dawson, A.G., Smith, D.E., 1995. Coastal Sedimentation Associated with the December 12th, 1992 Tsunami in Flores, Indonesia, in: Imamura, D.F., Satake, D.K. (Eds.), Tsunamis: 1992–1994, Pageoph Topical Volumes. Birkhäuser Basel, pp. 525–536.

Smith, D., 2004. The Holocene Storegga Slide tsunami in the United Kingdom*1. Quaternary Science Reviews 23, 2291–2321.

Smith, D.E., Foster, I.D.L., Long, D., Shi, S., 2007. Reconstructing the pattern and depth of flow onshore in a palaeotsunami from associated deposits. Sedimentary Geology 200, 362–371.

Soulsby RL, Smith DE, Ruffman A (2007) Reconstructing tsunami run-up from sedimentary characteristics— a simple mathematical model. Sixth International Symposium on Coastal Processes—coastal sediments'07 coasts, Oceans, Ports and River Institute (COPRI) of the American Society of Civil Engineers, May 13–17, New Orleans, Louisiana Vol. 2, pp 1075–1088.

Sugawara, D., 2008. Tsunamis and Tsunami Sedimentology, in: Tsunamiites. Elsevier, pp. 9–49.

Sugawara, D., Goto, K., Imamura, F., Matsumoto, H., Minoura, K., 2012. Assessing the magnitude of the 869 Jogan tsunami using sedimentary deposits: Prediction and consequence of the 2011 Tohoku-oki tsunami. Sedimentary Geology 282, 14–26.

Szczuciński, W., Niedzlieski, P., Rachlewicz, G., Sobczyński, T., Zioła, A., Kowalski, A., Lorenc, S., Siepak, J., 2005. Contamination of tsunami sediments in a coastal zone inundated by the 26 December 2004 tsunami in Thailand. Environmental Geology 49, 321-331.

Szczuciński, W., Niedzielski, P., Kozak, L., Frankowski, M., Zioła, A., Lorenc, S., 2007. Effects of rainy season on mobilization of contaminants from tsunami deposits left in a coastal zone of Thailand by the 26 December 2004 tsunami. Environ Geol 53, 253–264.

Szczuciński, W., 2012. The post-depositional changes of the onshore 2004 tsunami deposits on the Andaman Sea coast of Thailand. Natural Hazards 60, 115–133.

Szczuciński, W., Kokociński, M., Rzeszewski, M., Chagué-Goff, C., Cachão, M., Goto, K., Sugawara, D., 2012. Sediment sources and sedimentation processes of 2011 Tohoku-oki tsunami deposits on the Sendai Plain, Japan — Insights from diatoms, nannoliths and grain size distribution. Sedimentary Geology 282, 40–56.

Tada, R., Iturralde-Vinent, M.A., Matsui, T., Tajika, E., Oji, T., Goto, K., Nakano, Y., Takayama, H., Yamamoto, S., Kiyokawa, S., others, 2003. K/T boundary deposits in the Paleo-western Caribbean basin. The circum-Gulf of Mexico and the Caribbean 582–604.

Takashimizu, Y., Masuda, F., 2000. Depositional facies and sedimentary successions of earthquake-induced tsunami deposits in Upper Pleistocene incised valley fills, central Japan. Sedimentary Geology 135, 231–239.

Tanaka, G., Naruse, H., Yamashita, S., Arai, K., 2012. Ostracodes reveal the sea-bed origin of tsunami deposits. Geophysical Research Letters 39 (5), *L05406*

Tappin, D.R., Matsumoto, T., Watts, P., Satake, K., McMurtry, G.M., 1999. Sediment Slump likely caused 1998 Papua New Guinea tsunami. Eos 80 (30), 329-344.

Tappin, D.R., Watts, P., McMurtry, G.M., Lafoy, Y., Matsumoto, T., 2001. The Sissano, Papua New Guinea tsunami of July 1998 - Offshore evidence on the source mechanism. Marine Geology 175, 1-23.

Tappin, D.R., Watts, P., Grilli, S.T., 2008. The Papua New Guinea tsunami of 17 July 1998: anatomy of a catastrophic event. Natural Hazards and Earth System Sciences 8, 243-266.

Tappin, D.R., Evans, H.M., Jordan, C.J., Richmond, B., Sugawara, D., Goto, K., 2012. Coastal changes in the Sendai area from the impact of the 2011 Tōhoku-oki tsunami: Interpretations of time series satellite images, helicopter-borne video footage and field observations. Sedimentary Geology 282, 151–174.

Tarling, D., Hrouda, F., 1993. Magnetic Anisotropy of Rocks. Springer.

Tinti, S., Maramai, A., Graziani, L., 2004. The New Catalogue of Italian Tsunamis. Natural Hazards 33, 439–465.

Wassmer, P., Schneider, J.-L., Fonfrège, A.-V., Lavigne, F., Paris, R., Gomez, C., 2010. Use of anisotropy of magnetic susceptibility (AMS) in the study of tsunami deposits: Application to the 2004 deposits on the eastern coast of Banda Aceh, North Sumatra, Indonesia. Marine Geology 275, 255–272.

Wright, C., Mella, A., 1963. Modifications to the soil pattern of South-Central Chile resulting from seismic and associated phenomenona during the period May to August 1960. Bulletin of the Seismological Society of America 53, 1367–1402.

Wu, T.Y., 1981. Long Waves in Ocean and Coastal Waters. Journal of Engineering Mechanics 107, 501–522.

CHAPITRE 1 : Etude des dépôts de tsunamis – techniques conventionnelles.

Un prérequis indispensable à l'évaluation de la pertinence de la tomographie par rayons X dans le cadre de l'étude des dépôts de tsunamis a été de constituer un jeu de données complet en utilisant les techniques d'échantillonnage et d'analyse qualifiées ici de "conventionnelles" afin de comparer leurs résultats à ceux obtenus par X-CT (chapitre 2). L'étude qui suit a été menée de 2010 à 2013 dans le cadre de l'ANR Maremoti. Ma contribution s'est faite en deux temps : (1) campagne d'échantillonnage et descriptions stratigraphiques *in situ* et analyses conventionnelles (analyses granulométriques par diffraction laser, comptages de bioclastes, anisotropie de la susceptibilité magnétique, analyse des éléments majeurs par ICP-AES, observations structurales sur lames minces et radiographies) au cours d'un stage de master 2 Recherche sous la conduite de Raphaël Paris et Stéphanie Cuven ; (2) puis en début de thèse, premières analyses basées sur les données d'X-CT fraîchement acquises.

Le chapitre 1 est basé sur un article publié en 2013 dans Marine Geology ; article qui reprend l'intégralité des données obtenues sur un des sites d'étude (tsunami de 1755 en Andalousie) et permettra de faire le lien entre l'analyse des dépôts par X-CT et les données apportées par les techniques « conventionnelles » (chapitre 2). Les interprétations et conclusions présentées dans ce premier article concernant les dépôts de tsunami et leur mode de mise en place ont en effet servi de référence ou ont pu être discutées, voire critiquées en fonction des résutats obtenus par l'X-CT.

High-resolution analysis of a tsunami deposit: case-study from the 1755 Lisbon tsunami in southwestern Spain

Stéphanie Cuven[1,3], Raphaël Paris[2,4,5], Simon Falvard[1,3], Elisabeth Miot-Noirault[6], Mhammed Benbakkar[2,4,5], Jean-Luc Schneider[7], Isabelle Billy[7]

(1) Clermont Université, Université Blaise Pascal, GEOLAB, BP 10448, F-63000 Clermont-Ferrand

(2) Clermont Université, Université Blaise Pascal, Laboratoire Magmas et Volcans, BP 10448, F-63000 Clermont-Ferrand

(3) CNRS, UMR 6042, GEOLAB, F-63057 Clermont-Ferrand

(4) CNRS, UMR 6524, LMV, F-63038 Clermont-Ferrand

(5) IRD, R 163, LMV, F-63038 Clermont-Ferrand

(6) Clermont Université, Université d'Auvergne, INSERM UMR 990, F-63005 Clermont-Ferrand

(7) Université Bordeaux 1, CNRS-UMR 5805 EPOC, Avenue des Facultés, BP 184, F-33405 Talence

Abstract

A multi-proxy approach using trench sediment analysis on the southwestern coast of Spain (Los Lances Bay, Andalusia) provides a high-resolution record of the 1755 Lisbon tsunami and offers new means to interpret tsunami deposits. A combination of sedimentological (grain size, sorting, AMS), micromorphological (X-ray tomography and radiography, thin sections) and geochemical analysis (X-ray microfluorescence, ICP-AES) combines to provide a comprehensive reconstruction of the different phases of tsunami deposition and flow dynamics. Vertical variations in sediment texture, fabric and composition of the 1755 tsunami deposits in Los Lances are then discussed with reference to existing literature on diagnostic criteria commonly used for identifying and interpreting tsunami deposits. Finally possible leads for future investigation are proposed.

Keywords: 1755 Lisbon tsunami, tsunami deposits, grain size distribution, X-ray fluorescence, X-ray tomography, anisotropy of magnetic susceptibility

1. Introduction

Seven years after the 2004 Indian Ocean tsunami, the sedimentary record of palaeotsunamis is becoming increasingly well documented worldwide, and scientists now have access to a more varied proxy toolkit, including sedimentological, micropalaeontological, geochronological and geochemical methods (Dawson and Stewart, 2007; Bourgeois, 2009; Chagué-Goff, 2010; Goff et al., 2012; Keating et al., 2011). Kilfeather et al. (2007) tested the feasibility of using micromorphology (on thin sections) as a diagnostic tool to identify and improve interpretation of tsunami deposits. This multidisciplinary approach also allows the palaeoenvironments before, during and after the tsunami to be investigated, even if one or more proxies cannot be applied due to local conditions. Despite considerable progress in palaeotsunami research, distinguishing tsunami from storm deposits is still complex, and reconstructing a past tsunami event from its deposits remains difficult (e.g. Jaffe and Gelfenbaum, 2007; Pritchard and Dickinson, 2008; Jaffe et al., 2012; Paris et al., 2012). Information from grain size distribution, palaeontological and geochemical analyses of bulk samples from onshore tsunami deposits can be limited by (1) the subjectivity and low resolution of manual sampling in the field, and (2) the poor preservation potential of sedimentary structures in these unconsolidated sediments. Indeed, the structure and vertical grain size trends of tsunami deposits are rapidly modified by bioturbation, as demonstrated by Szczuciński (2012).

In this study, we couple sedimentological and geochemical proxies, using both destructive and non-destructive methods, to carry out high resolution characterisation of the 1 November, 1755 Lisbon tsunami deposits in southwestern Spain (Fig. 1). The results include two- and three-dimensional X-ray imagery and X-ray microfluorescence analysis (µXRF) of previously studied tsunami deposits. We surveyed several sites where the tsunami deposits were well preserved and already studied (Luque et al., 2001, 2004; Gracia et al., 2006; Reicherter et al., 2010; Lario et al., 2011). Deposits of the 1755 tsunami are particularly well preserved at the coastal plain of Los Lances, located 25 km SW of Algeciras, near the city of

Tarifa (Gibraltar Strait). Four washover fans breaching all Holocene ridges, including the Late Medieval ridge, were interpreted as evidence of the 1755 tsunami (Gracia et al., 2006). Based on historical reports, a bridge which was built at the beginning of the eighteenth century was partly destroyed by the 1755 tsunami (Fig. 2). Numerous bricks from the bridge can be found in the washover fan deposits. Reicherter et al. (2010) found tsunami deposits up to 700 m inland (~4 m a.s.l.). According to historical sources (Campos, 1991), the 1755 tsunami waves were 11 m high in Los Lances and the inundation distance reached more than 1.5 km. Boulder imbrications are found up to 5 m a.s.l. at Trafalgar Cape (Whelan and Kelletat, 2005). East of the Gibraltar Strait tsunami wave heights were considerably lower (< 2 m in Gibraltar and Ceuta; Baptista et al., 1998).

The geomorphic impact of storms along the southwestern Spanish coast is limited to littoral spits, beaches and seaward dune slopes, despite MWH (mean wave height) often exceeding 5 m (Rodríguez-Ramírez et al., 2003).

2. Materials and methods

The field survey along the southern coast of Andalusia (Spain) was carried out in October 2010 and resulted in a comprehensive sedimentological data set of the 1755 tsunami deposits. Sedimentary descriptions of the deposits were recorded in situ along trenches. Intact sedimentary structures from the tsunami deposit were sampled in plastic boxes, 18 cm-long carbon tubes and 50 cm-long half-cores. Bulk samples were also collected along trenches for grain size and geochemical analyses. We focussed our investigations on the Los Lances Bay because the sediments were less disturbed than elsewhere and the flat topography of the bay reduces the complexity of flow dynamics and preserves the sedimentary record.

Sedimentary fabrics were identified at high resolution using several non-destructive approaches: (1) visual description and photographs of the cores using a Nikkor 105 mm VR lens at a resolution of 24.8 megapixels (Nikon D3X); (2) two-dimensional X-ray imagery of the cores (resolution 125 µm) using the SCOPIX device (EPOC laboratory, Bordeaux; Migeon et al. 1999); (3) three-dimensional imagery of carbon tubes by X-ray tomography (CT-scan) using an Explore CT-120 GE Healthcare (INSERM Clermont-Ferrand, 1 voxel = 100 µm); (4) three-dimensional X-ray imagery of plastic boxes using a Siemens SOMATOM

Sensation 16 (CHU Bordeaux, 1 voxel = 350 µm). Thin-sections were made for each box sample using dehydration by water-acetone-epoxy-exchange (e.g. Zaragosi et al., 2006).

The magnetic susceptibility (MS) analysis (4 mm resolution) was carried out at the EPOC laboratory on half-cores using a Bartington Instruments Multisus File with a MS2E1 sensor. The anisotropy of magnetic susceptibility (AMS) was analysed using a Kappabridge KLY-2. Samples were collected in 2 cm-sided boxes pressed into the half-cores, as described in Wassmer et al. (2010). Each sample was analysed in 15 directions to determine the magnitude and directions of the maximum, intermediate, and minimum AMS axes.

Grain size analyses were performed using (1) a Laser Coulter (2 mm to 50 µm) on bulk samples and (2) a Malvern Mastersize S (878.67-0.06 µm) on samples from the half-cores (sampling step = 1 cm). Prior to grain size analysis, samples were heated in a hydrogen peroxide solution to dissolve organic material. Summary statistics presented here include geometric mean grain size (µm), sand content (%), mud content (%), sorting (Φ), skewness (Φ), and kurtosis (Φ).

Non-destructive chemical analyses were performed on half-cores using an Avaatech X-ray Fluorescence (XRF) core scanner (EPOC laboratory, Bordeaux). Therefore, high-resolution chemical element variations from fresh sediment were captured at the sediment surface every 1 mm with ionization energies of 10, 30 and 50 kv. Additionally, bulk samples were subjected to (1) inductively coupled plasma-atomic emission spectrometry (ICP-AES) analyses using a Jobin-Yvon ULTIMA C instrument, and (2) loss on ignition (LOI) analyses to estimate organic and carbonate content following the method described in Heiri et al. (2001).

Examination of XRF profiles (31 elemental profiles from Al to Ba) and comparison with ICP-AES and LOI results helped select significant elemental profiles or elemental ratios. We focused on Al, Si, P, S, K, Ca, Ti, Mn, Fe, Rb, Sr and Ba because they are in sufficient concentration to be detected by an Avaatech system. Cl, Na, Mg and I were either out of range or not of sufficient concentration in the sediment to be detected by an XRF device.

3. Results

3.1. Log stratigraphy, sedimentary facies and composition

We present here the results obtained on core LL1bis, sampled close to the bridge in Los Lances Bay which was partially destroyed by the 1755 tsunami (Fig. 2). Core LL1 is affected by bioturbation, but the stratigraphy is identical (with small variations in subunit thicknesses). The two cores also display the same stratigraphy as described by Reicherter et al. (2010). The 1755 tsunami deposit is found at a depth of between 29 and 54 cm, with a diffuse upper boundary to greyish to brownish clays, and a clear lower contact with underlying grey clays (Fig. 3; 54 cm deep). The pre-tsunami sediments are dark grey clays (dg-c 1) affected by intense bioturbation, and contain shells of brackish-water bivalves. The contact between the clays and the tsunami deposit is sharp and horizontal, but micromorphological observations reveal scouring of the pre-tsunami underlying clays and important bulking at the base of the tsunami deposit.

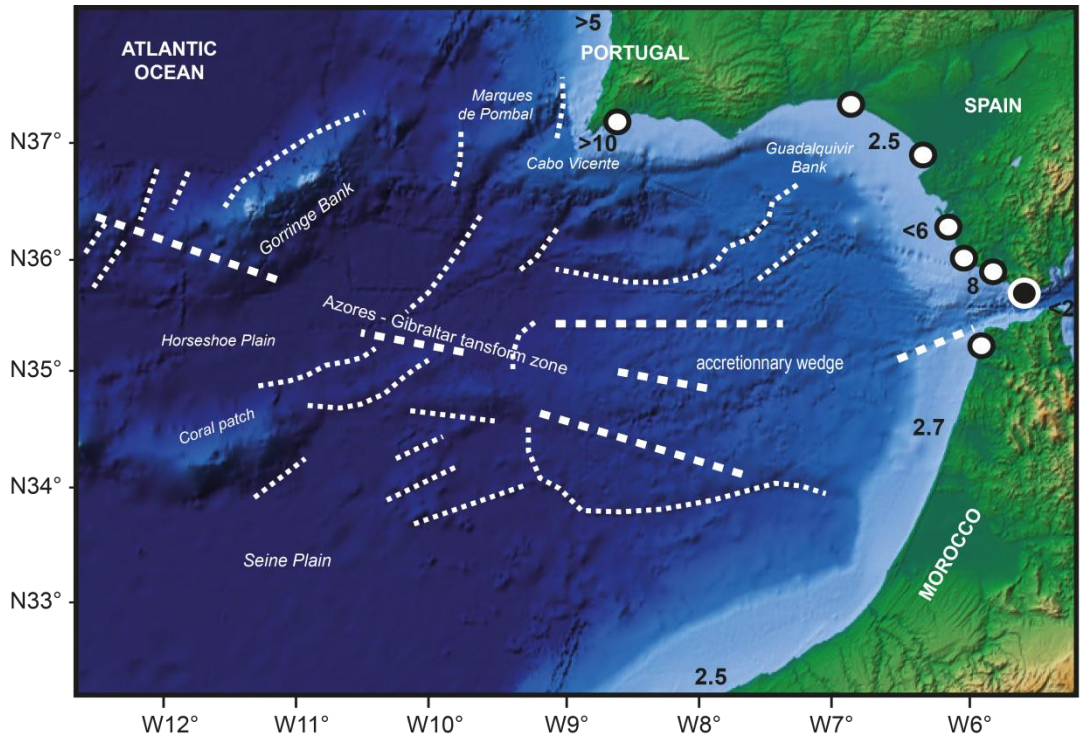

Figure 1: General tectonic setting of the Eurasia (Iberia)–Africa (Nubia) plate boundary. White bold dotted lines: faults; White dotted lines: tectonic lineaments; white dots: observed wave height; black dot: location of the Los Lances Bay.

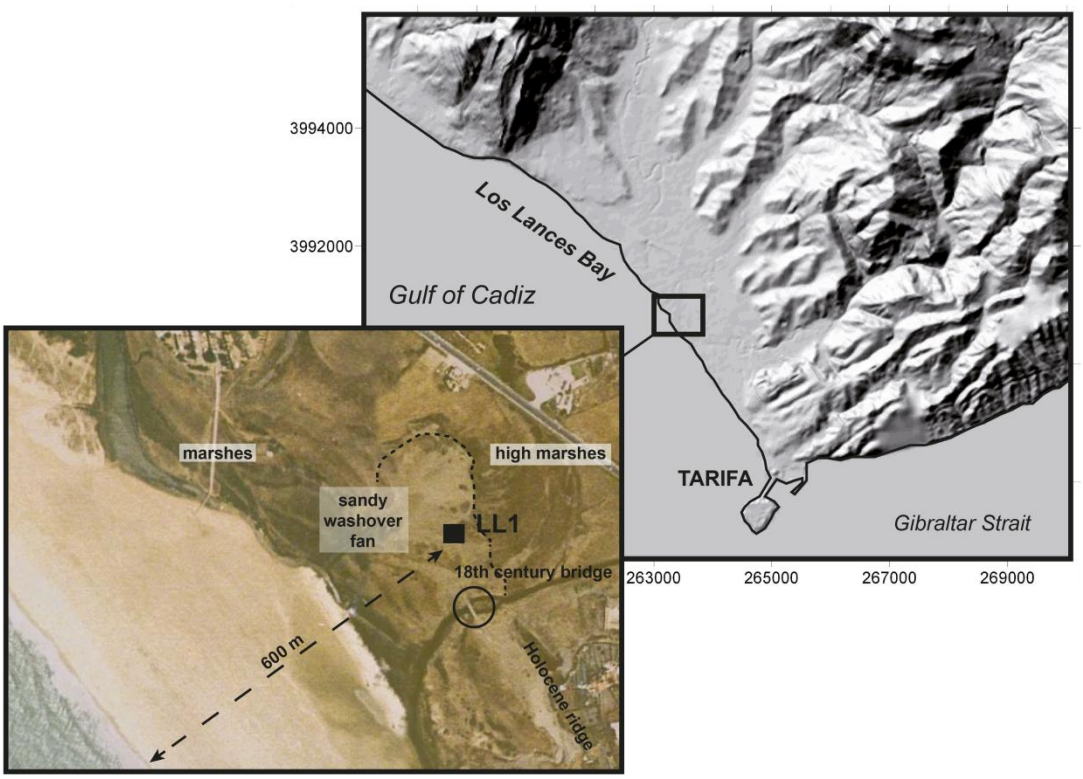

Figure 2: Location map and satellite view of the study area. Cores LL1 and LL1bis were retrieved from the 1755 sandy washover fan (Gracia et al., 2006; Reicherter et al., 2010). The bridge was constructed at the beginning of the eighteenth century and partially destroyed by the 1755 tsunami.

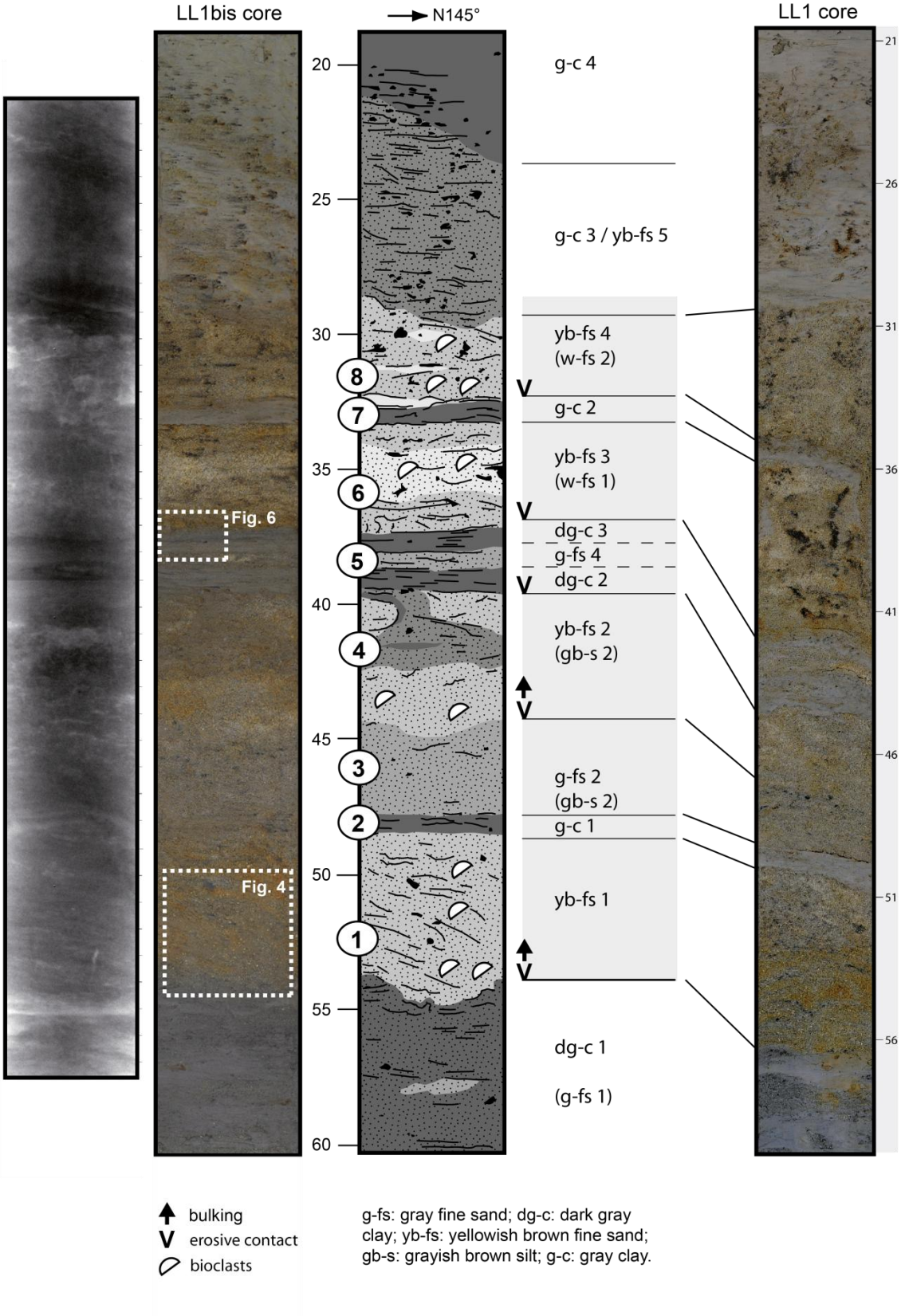

Figure 3: Log stratigraphy of cores LL1bis and LL1 (Los Lances Bay) and X-radiography (SCOPIX). The 1755 Lisbon tsunami deposit contains 8 subunits (numbers) between the depths of 54 and 29 cm.

The 1755 tsunami deposit is internally subdivided into 8 subunits (Fig. 3).

1. Subunit 1 (54-49cm): basal yellowish-brown fine sands (yb-fs 1) containing oblique injections (Fig. 4) and rip-up clasts of the underlying dark grey clay and dark brown organic matter (OM), and numerous marine bioclasts (very fine shell fragments of bivalves, gastropods, diatoms, and foraminifers).

2. Subunit 2 (49-48 cm): at a depth of 48 cm, this sand is capped by a discontinuous thin layer of greyish clay (mud line g-c 1).

3. Subunit 3 (48-44.5 cm): grey fine sands (g-fs 2) in a grey clayey matrix, roughly laminated, with very few bioclasts. The upper part of this subunit is enriched in rip-up clasts of OM.

4. Subunit 4 (44.5-39.5 cm): yellowish-brown fine sands (yb-fs 2) mixed with grey fine sands (g-fs 3), with a basal erosive contact with subunit 3. Many marine bioclasts are found in the lower part of the subunit. The structure of the upper half of subunit 4 is complex, showing convolute bedding of grey brown silts and clays (g-bs 1). Numerous wood fragments were found near the top of the subunit.

5. Subunit 5 (39.5-37 cm): subunit 4 is overlain by two horizontal mud lines (dg-c 2 & 3), less than 1 cm thick and made of laminated dark grey clay. A thin layer of grey fine sands (g-fs 4) is intercalated between the two mud lines (Fig. 5).

6. Subunit 6 (37-33 cm): another erosive contact is found between subunit 6 (yb-fs 3) and the underlying mud line (dg-c 3), characterized by injections of mud into the overlying sand (Fig. 6). Subunit 6 displays poorly defined horizontal laminations and stretched rip-up clasts of OM. It consists mainly of yellowish-brown fine sand (yb-fs 3), with a central band of white fine sand (w-fs 1) rich in marine bioclasts.

7. Subunit 7 (33-32.5 cm): mud line of grey clay (g-c 2) eroded by subunit 8.

8. Subunit 8 (32.5-29 cm): yellowish-brown sand (yb-fs 4) particularly rich in rip-up clasts of soil, wood fragments and marine bioclasts.

9. Tsunami subunit 8 is overlain by alternating clay (g-c 3) and sand (yb-fs 5) rich in rip-up clasts of OM. The clay is then massive from 20 cm to the surface (g-c 4).

When observed with the binocular microscope (bulk samples) and polarising microscope (thin sections), the tsunami deposit is mostly composed of subangular to subrounded quartz grains (60-90%) from Miocene sandstones (*areniscas de Aljibe*: ITGE, 1990), together with subrounded orthopyroxenes (5-30%) and other heavy minerals (<10%). Charred wood (charcoal) represents up to 5% of the particles, specifically in the clay-rich horizons (Table 1). Numerous marine bioclasts were identified: fragments of shells (gastropods, bivalves), benthic foraminifers, diatoms, sponge spicules, rhodophyta calcareous algae, echinoderms (sea-urchin radiols). The proportion of pyroxene crystals and marine bioclasts varies vertically. Subunits 1 and 8 are particularly rich in bioclasts, whereas the central part of the tsunami deposit (from subunit 3 to subunit 6) has few to no bioclasts. This composition is similar to other 1755 Lisbon tsunami deposit outcrops from the Gulf of Cadiz (Gutiérrez-Mas et al., 2009; Hindson et al., 1996; Hindson and Andrade, 1999; Luque et al., 2002; Morales et al., 2008, 2011; Pozo et al., 2010; Reicherter et al., 2010).

3.2. Grain size distribution

3.2.1. Grain size distribution from laser diffractometry

Grain size distribution (GSD) for the tsunami deposit confirms a high proportion of sand (> 40%) at depths of 54-39.5 cm (subunits 1, 3 and 4), 37-33 cm (subunit 6) and 29-32 cm (subunit 8), and predominantly silt (60-80%) and clay (10%) in other subunits (Fig. 7). The geometric mean grain size (mGS) shows high variability within the interval 54-29 cm, which perfectly delineates the tsunami deposit, compared to the homogeneous fine-grained sediments overlying and underlying the tsunami deposit (Fig. 7).

GSD is unimodal in the coarsest grained facies (e.g. depths of 46-42 cm in subunits 3-4, 36-33 cm in subunit 6, and 32-30 cm in subunit 8), and plurimodal in the finest grained facies (e.g. depths of 51-50 cm in subunit 1, 48-47 cm in subunit 2, and 40-39 cm in subunit 5) of the tsunami deposit sequence. The tsunami deposit is very poorly sorted, except in the coarse grained subunit 6, where it is poorly sorted. Kurtosis is lower than 1.5 for subunits 1 to 4 (mesokurtic to leptokurtic) and higher than 2 for subunits 5 to 8 (very leptokurtic). The tsunami deposit is also characterised by fine skewed GSD (Fig. 8), except for mud lines of subunits 5 and 7 which have the same symmetrical form as the overlying and underlying

clays. The mGS is positively correlated with the skewness (R^2=0.98). Subunit 3 is inversely graded, whereas subunits 4 and 8 are normally graded (Fig. 7).

3.2.2. GSD and elemental analyses

A normality test revealed that the GSD series was non-normal, so we used a Spearman coefficient to test the correlations between the GSD and elemental analyses. Correlation between SiO_2 (Table 2: ICP-AES) and GSD is positive in the very fine sand fraction ($r = 0.86$; $p < 0.0025$; $n = 9$) and becomes negative in the very coarse silt fraction ($r = -0.81$; $p < 0.0072$; $n = 9$). Al_2O_3, Ti_2O_3 and K_2O are negatively correlated with mGS ($r = -0.91$; $p < 0.0005$; $n = 9$; $r = -0.97$; $p < 0.00002$; $n = 9$; and $r = -0.9$; $p < 0.0009$; $n = 9$; respectively) and positively correlated with the mud fraction ($r = 0.92$, $p < 0.0005$, $n = 9$; $r = 0.92$, $p < 0.0005$, $n = 9$; and $r = 0.90$; $p < 0.0009$; $n = 9$; respectively). Fe_2O_3, CaO and Sr, as determined by ICP-AES, are independent of GSD.

We have tested relationships between sediment composition and GSD by examining the following elemental ratios: Si/Ti, Si/Al, Si/Rb, Zr/K, Ti/Zr and K/Si (from XRF analysis). Since grain size could affect the relative abundance of an element in XRF data, ratios are used to eliminate any analytical bias (e.g. Croudace et al., 2006). Si, Ti and Al are used for grain size normalization because of their lithogenic nature and resistance to chemical weathering, and their concentration in major sources (e.g. Calvert et al., 2001). As suggested by the correlations between GSD and ICP-AES data, Si/Ti and Si/Al ratios reflect the GSD of the tsunami deposit ($r = 0.84$; $p < 0.00000$; $n = 49$; and $r = 0.78$; $p < 0.00000$; $n = 49$ respectively). The tsunami deposit is characterised by high Si/Al values, and peaks of Si/Al closely match sand-rich horizons (Fig. 7). Si-normalized aluminium generally represents quartz (Bertrand et al., 2012; Calvert et al., 2001), which is indeed the main component of the tsunami deposit (Table 1).

Figure 4: Photograph of core LL1bis, showing oblique injections and rip-up clasts of pre-tsunami dark grey clay in tsunami subunit 1 (54-49cm: basal yellowish-brown fine sands yb-fs 1, cf. fig. 3).

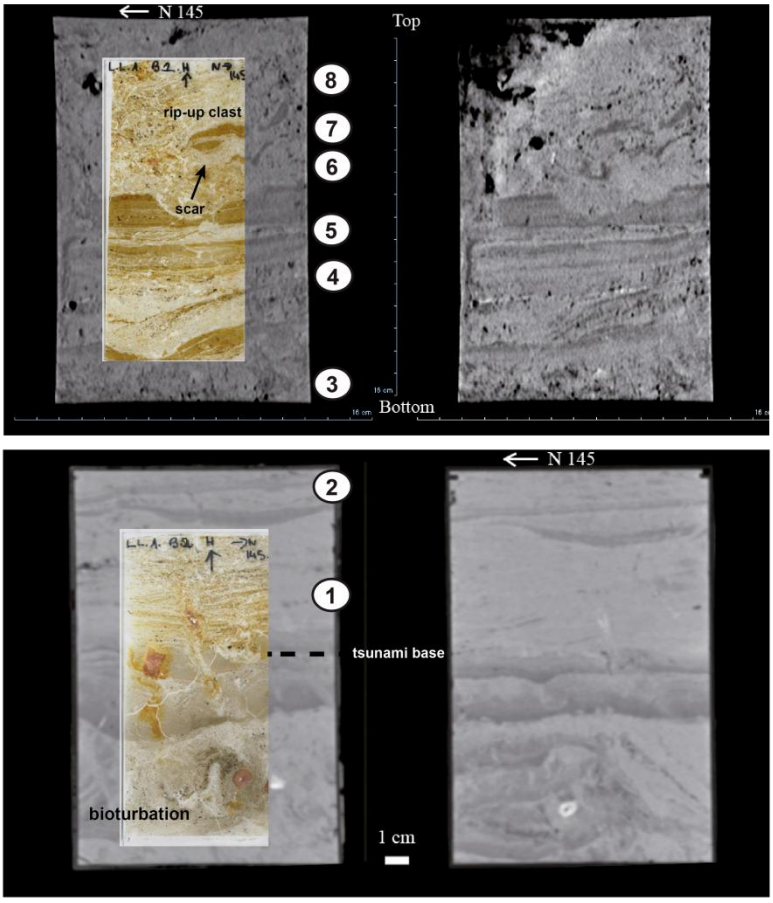

Figure 5: X-ray topograms (Siemens SOMATOM Sensation 16, CHU Bordeaux) and thin sections of the 1755 tsunami deposits in Los Lances. Numbers refer to tsunami subunits (Fig. 3). The pre-tsunami clay displays evidence of bioturbation. Note the scar and rip-up clast of clay (mud line, subunit 5, cf. fig. 3) incorporated in subunit 6.

Figure 6: Erosive contact between subunit 5 (mud line dg-c 3) and subunit 6 (yb-fs 3), characterized by injections of mud in the overlying fine sand. The mud line is suborganised in horizontal laminae with varying grain size.

Depth	Subunit	Qz	Opx	Other minerals*	Marine bioclasts	Wood**
31 cm	8	77	13	4	4	3
32 cm	8	75	5	8	7	5
35 cm	6	86	6	4	2	2
37 cm	6	82	8	9	0	1
39 cm	4	76	12	6	1	5
41 cm	4	79	12	5	0	5
43 cm	4	77	14	3	1	4
47 cm	3	87	9	3	0	1
51 cm	1	81	11	2	2	4
53 cm	1	61	31	2	4	2

* mostly heavy minerals

** including charcoals

Table 1 – Composition of the 1755 tsunami deposits in Los Lances in % (thin sections observed through a polarising microscope). Depths and subunits refer to core LL1bis. Qz: quartz; Opx: orthopyroxene.

The positive correlation between Rb and GSD ($r = 0.82$; $p < 0.0000$; $n = 49$) suggests that Rb-based ratios could represent the muddy fraction of the sediment, as proposed by

Croudace et al. (2006). K/Si also increases with mud proportion ($r = 0.74$; $p < 0.00000$; $n = 49$), whereas Si/Rb reflects variations in the proportion of sand ($r = 0.83$; $p < 0.0000$; $n = 49$). Since K/Si is less affected by mud proportion variability in the pre- and post-tsunami deposits (Fig. 7) it can be used to delineate the base and top of the tsunami deposit.

Zr resides mainly in zircon, a heavy mineral that is generally concentrated in the fine sand fraction (Ganeshram et al., 1999). When a coarse grain of zircon lies directly under the XRF beam, it obviously produces a high amplitude peak (Cuven et al., 2010). Considering that K is predominantly in the muddy fraction (clay minerals), Zr/K is potentially a useful grain size indicator. Note that most of these observations are suitable for quartz-dominated tsunami deposits, but would not apply to carbonate-dominated deposits.

3.3. Sedimentary fabric

3.3.1. X-ray absorption and magnetic susceptibility

High compaction, low porosity and presence of heavy minerals create denser material, resulting in high grey values in X-ray imagery (grey values represent X-ray absorption). The contact between the clayey substratum and the tsunami deposit (Fig. 3 at 54 cm deep) is marked by high grey values (Fig. 8: mean grey value of 180/255 on an 8-bit scale SCOPIX image). Clay- and OM-rich sediments such as mud lines (e.g. subunits 5 and 7), oblique injections of clay into sands (e.g. subunit 1) and rip-up clasts of soil (e.g. subunit 8) appear in dark grey (Fig. 9). Only the coarsest bioclasts (e.g. shells) could be detected as small spots of high grey value (e.g. subunit 1).

Bulk magnetic susceptibility (MS) is generally used as an indicator of the net contribution of ferromagnetic (magnetite, hematite, etc.) or paramagnetic (amphibole, pyroxene, etc.) minerals in the sediment (e.g. Bertrand et al., 2012; Sandgren and Snowball, 2001). In our case, MS would increase with the proportion of orthopyroxenes and other heavy minerals in the tsunami deposit (Table 1), thus resulting in higher grey values (Fig. 8). Nevertheless, it is difficult to correlate the data given the different resolutions of sampling: one bulk value every 4 mm for MS, and one mean grey value every 125 µm for X-ray absorption (SCOPIX). An intermediate scale is provided by XRF profiles of Fe and Ti (Fig. 8). MS, Fe and Ti decrease with sediment sorting (e.g. subunit 6). When sorting increases,

settling is less turbulent and particle density plays a significant role in deposition processes. Thus, heavy minerals are concentrated in pockets or laminae, as described in recent tsunami deposits (e.g. Morton et al., 2007; Higman and Bourgeois, 2008; Srinivasalu et al., 2008; Jagodziński et al., 2009, 2012; Switzer et al., 2012). These concentrations of heavy minerals are clearly identifiable in thin section (Fig. 10) and correspond to peaks of MS, Fe, Ti and X-ray absorption (Fig. 8 and 9: high grey values). Note that laminae of heavy minerals often occur near the base and top of the mud lines (subunits 2, 5 and 7).

3.3.2. Anisotropy of magnetic susceptibility

Wassmer et al. (2010) demonstrated that AMS applied to unconsolidated tsunami deposits can give information on sediment fabrics and depositional processes. The anisotropy of each sample (i.e. each cubic box) can be visualised by a triaxial ellipsoid (the maximum, intermediate and minimum axes corresponding to principal eigenvectors). The calculation of AMS parameters such as the corrected degree of anisotropy (Pj), magnetic lineation (L) and foliation (F), alignment parameter (Fs) and shape parameter (T) allow evaluating relationships between magnetic fabrics and depositional processes to be investigated. The alignment parameter represents the development of a linear fabric and thus increases with bottom current strength. The shape parameter describes the geometry of the AMS ellipsoid, which is oblate for $T>0$ (settling mode) or prolate for $T<0$ (traction mode). It has been demonstrated that the mean orientation of the grain's long axis (and thus the maximum tensor axis, K_{max}), is parallel to flow direction for moderate currents and settling from suspension. For stronger currents with dominant traction (bed load), the long axis of prolate particles (K_{max}) tends to be orientated perpendicular to flow direction (see review in Wassmer et al., 2010).

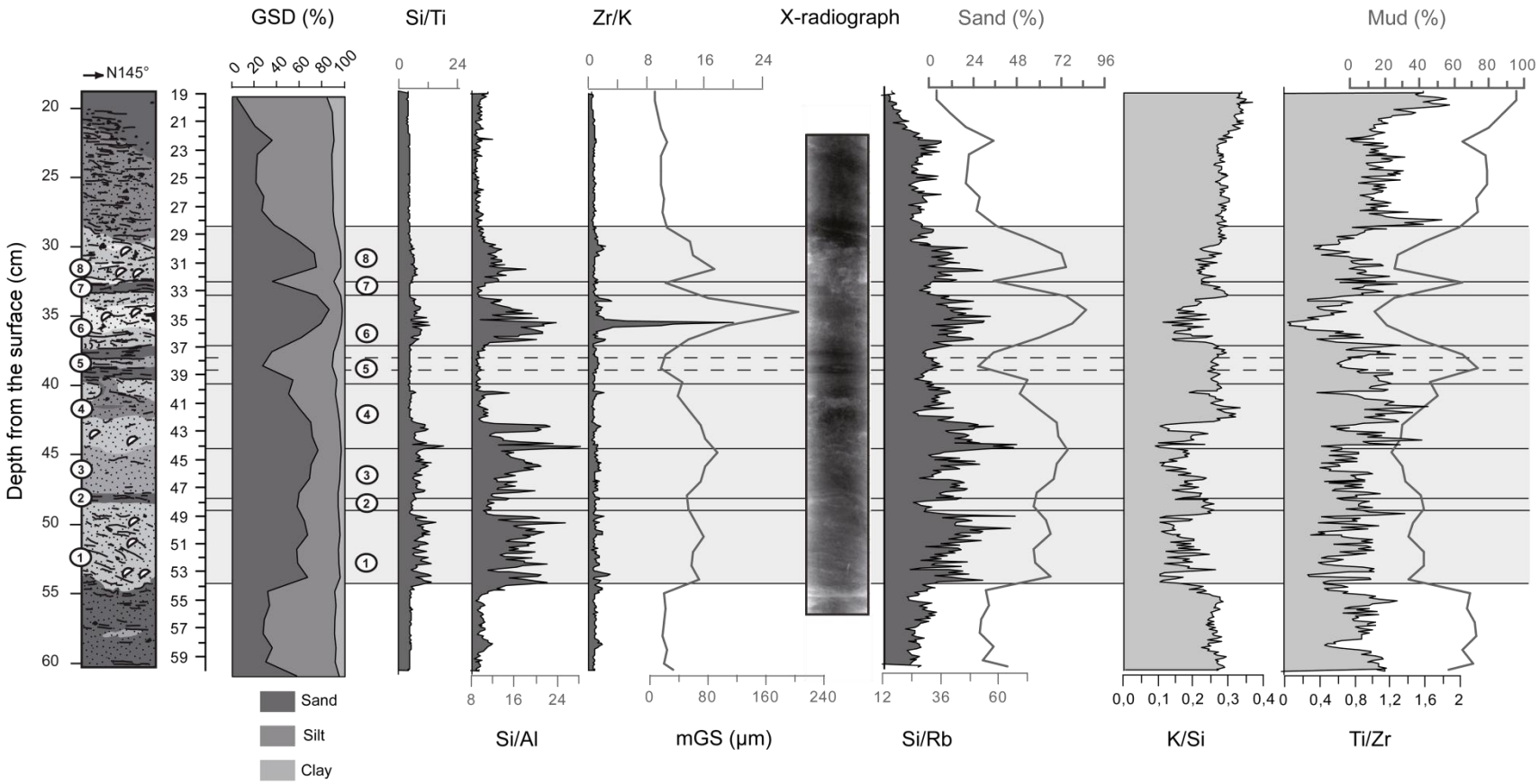

Figure 7: Sediment texture of core LL1bis based on grain size distribution (Malvern Mastersize S), X-radiography (SCOPIX,), and elemental ratios (Avaatech XRF). Shaded area covers the 1755 tsunami deposit.

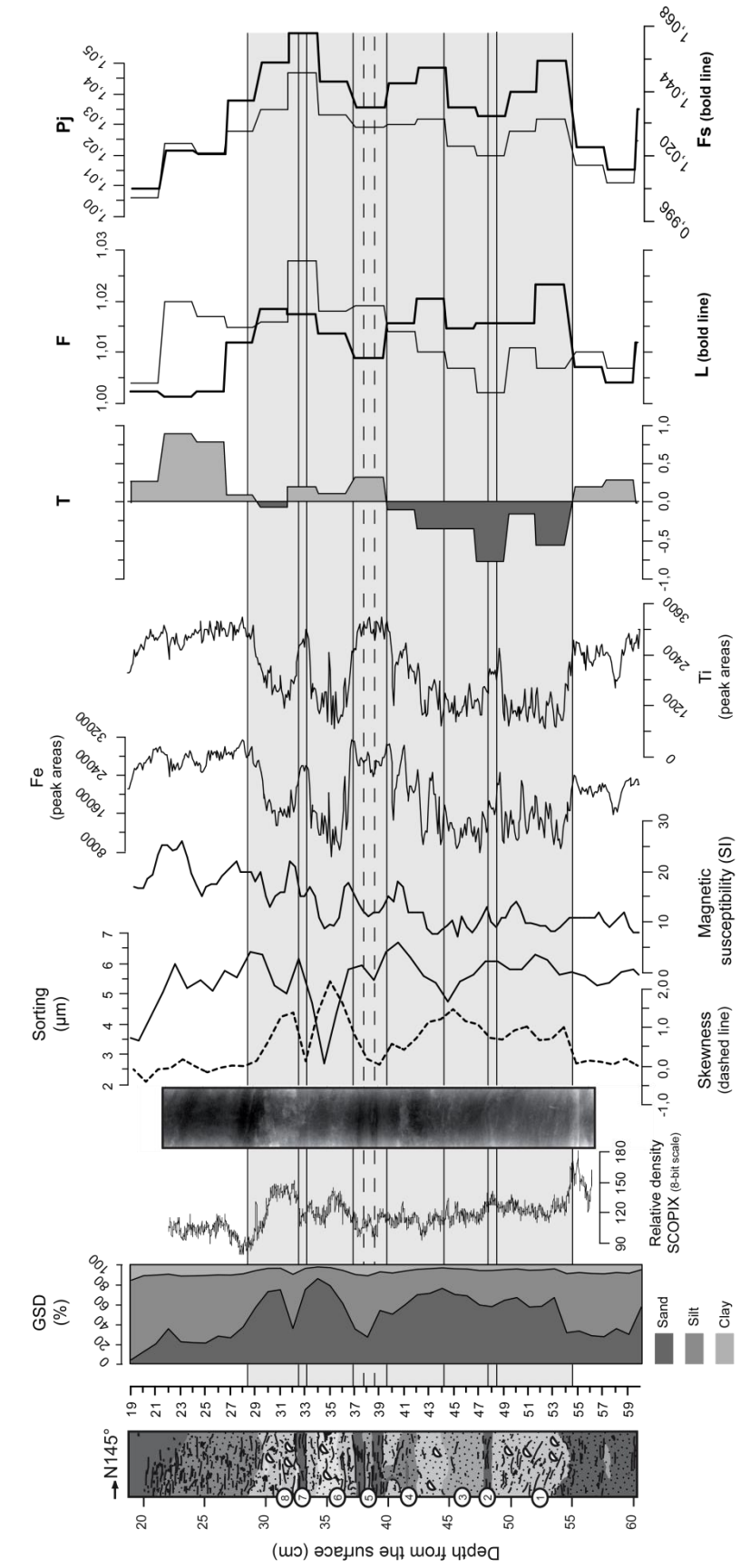

Figure 8: Sedimentary fabrics and sorting documented by relative density (mean grey values of laser absorption averaged line by line, SCOPIX), sorting, skewness, magnetic susceptibility, anisotropy of magnetic susceptibility (AMS), Fe and Ti (XRF). T: AMS ellipsoid shape parameter (oblate if T>0, prolate if T<0); Pj: corrected degree of anisotropy; Fs: alignment parameter; F: magnetic foliation; L: magnetic lineation. Note that more variability appears in the profile of relative density due to a higher analytical precision (0.125 mm) compared to XRF (1mm), MS (4 mm), sorting (10 mm) and AMS data (20 mm).

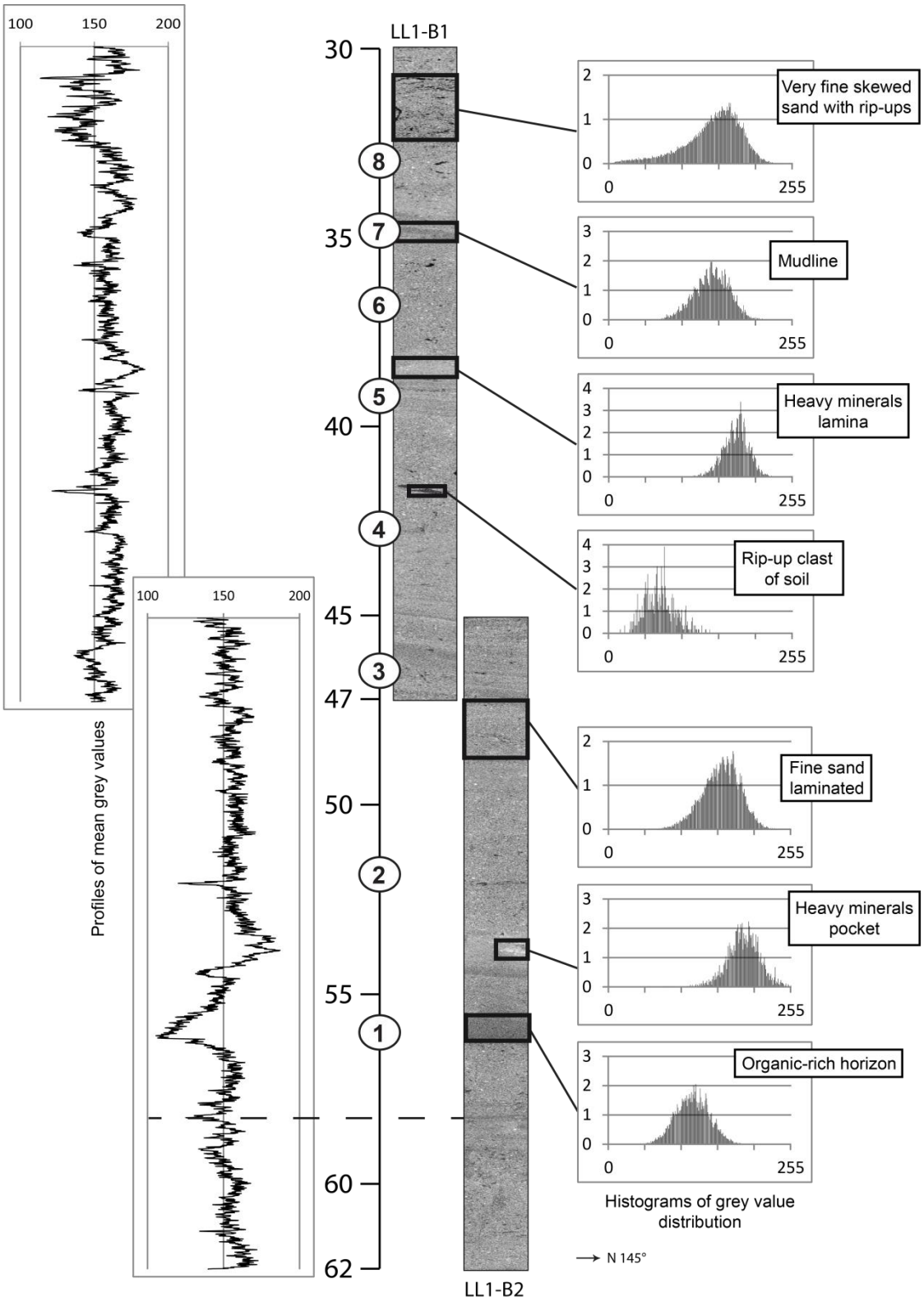

Figure 9: X-ray topograms of carbon tubes (Explore CT-120 GE Healthcare, INSERM Clermont-Ferrand), mean grey value profiles (line by line averaged values), histograms of grey value distribution of different sedimentary facies and features (e.g. rip-up clasts, mud lines, concentrations of heavy minerals).

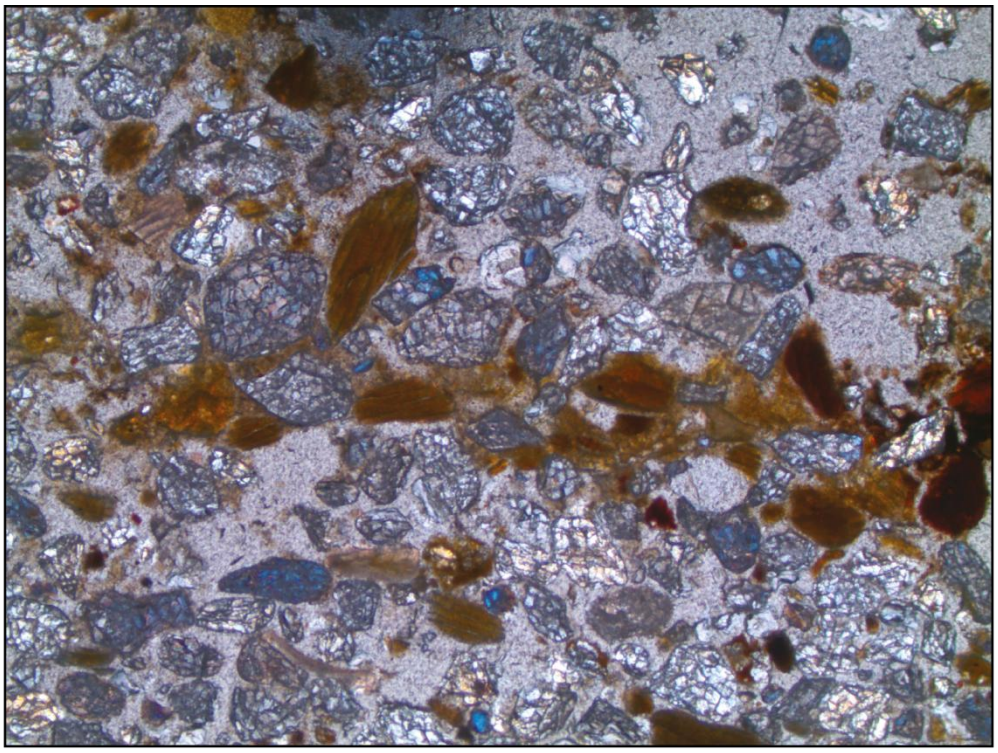

Figure 10: Photomicrograph of a thin section from subunit 1 in cross-polarised light. The concentration of heavy minerals in the central part (orthopyroxenes and other dark minerals) corresponds to a peak of MS (Fig. 8 at 51 cm deep) and high values of X-ray absorption (Fig. 9 at 54 cm deep). Other grains are quartz.

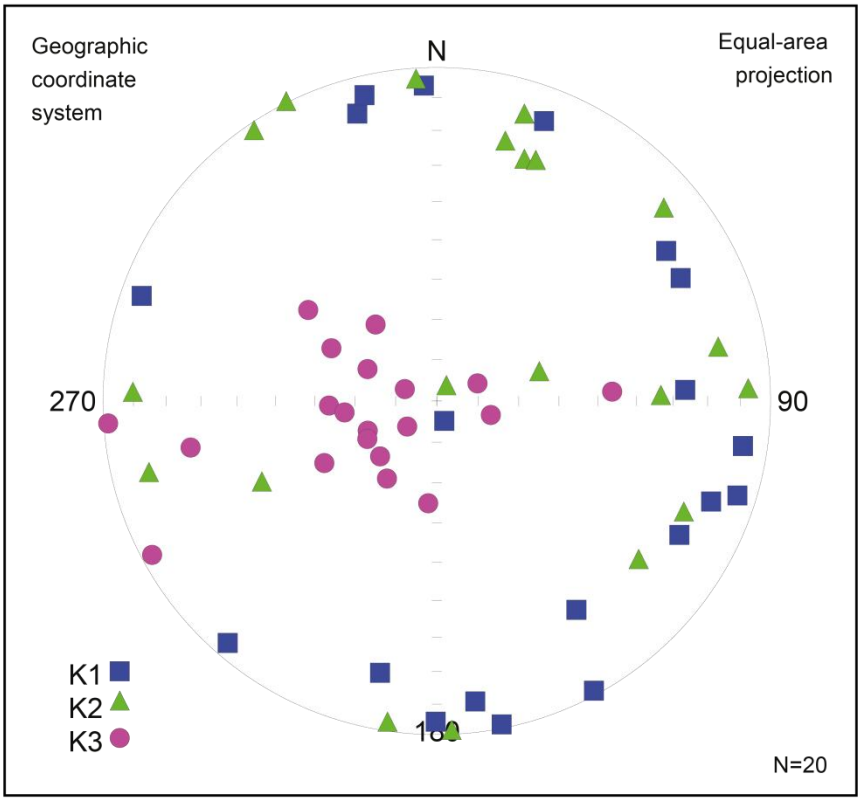

Figure 11: Projections of AMS (anisotropy of magnetic susceptibility) tensor axes onto a diagram of the lower hemisphere equal areas. K1, K2 and K3 represent the Kmax, Kint and Kmin tensor axes, respectively.

Clayey sediments underlying and overlying the 1755 tsunami deposit in Los Lances (LL1bis core) are characterized by low degrees of anisotropy (Pj) and oblate shape (T>0). The magnetic fabric of the tsunami horizon is characterized by prolate ellipsoids from -52 to -39 cm (subunits 1 to 4), spherical-oblate ellipsoids from -39 to -32 cm (subunits 5 to 7), and spherical-prolate from -32 to -29 cm (subunit 8). There is a positive correlation between the vertical variations of anisotropy and alignment (R^2=0.93), showing successive pulses. Subunit 2 is too narrow (< 5 mm) to be sampled for AMS analysis. Traction dominates the lower part of subunits 1 and 4, but settling may be present in their upper part (Fig. 8). Subunit 3 displays weak foliation, a decrease in alignment and anisotropy, but a clear prolate ellipsoid. The dark grey clays (mud lines) of subunit 5 are characterized by an oblate ellipsoid, a decrease in traction and increasing settling from suspension (weak magnetic lineation, strong foliation**)**. Sands of subunit 6, which are better sorted than the other sandy units, were mostly deposited by settling. Subunit 7 (mud line) is clearly dominated by settling. Subunit 8 is characterized by renewed traction, but the ellipsoid is nearly spherical. These trends are concordant with the previous observations on sorting and magnetic susceptibility.

The projections of AMS tensor axes onto a diagram of the lower hemisphere equal areas (Fig. 11) give information on the influence of currents on the preferential orientation of the long axes of particles (grains). The K_{max} of subunits 1 to 4 are oriented NNW-SSE (declination). Given that transport was by traction for these subunit deposits, this dominant orientation is thus perpendicular to a current oriented WSW-ESE. The mud lines of subunit 5 were deposited by settling in a flow oriented NE-SW (parallel to the declination of the K_{max}). These results are concordant with waves coming from the SW to WSW, the shoreline of Los Lances being oriented NNW-SSE. Palaeocurrent reconstruction of subunits 6 to 8 is less easy because the ellipsoids are almost spherical.

In traction mode, K_{max} declination is perpendicular to the inferred current and significant inclination of the K_{int} might signal the presence of particles imbrication (e.g. K_{int} inclination >40° in subunits 1 and 3). In settling mode, particles imbrication is less developed, thus resulting in a lower K_{max} inclination (the K_{max} declination being parallel to flow orientation).

3.4. Sediment source

3.4.1. Sr and Ba as proxies for marine inundation

Sr and Ba are important components of marine biota, and play an important role in the marine biogeochemical cycle (e.g. Gonneea and Paytan, 2006). Sr is related to the marine sedimentation processes and mainly originates from marine calcic biota (e.g. Chagué-Goff, 2010; Rubio et al., 2000). Therefore, strontium has been used as a proxy for marine inundation due to its higher concentration in seawater. Both XRF and ICP-AES Sr profiles display a rapid increase in Sr concentration at the base of the tsunami deposit (subunit 1), followed by a progressive decrease upwards (Fig. 12). The lowest concentrations of Sr are found in subunits 6 and 8, even lower than in the clays below and above the tsunami deposit.

Barium is commonly associated with various phases in marine sediments, such as the phase related to biological activity (carbonates, organic matter, opal and barite), but it is also sometimes associated with ferromanganese oxyhydroxides and terrestrial material (Gonneea and Paytan, 2006; Schroeder et al., 1997). In fact, Ba occurs in higher concentrations in estuarine than in marine sediments (Wedepohl, 1971). Another hypothesis is that the excess Ba represents the non- terrigenous Ba component, as found by normalizing against Al or Ti (Murray et al., 2000). Therefore Ba/Ti is often used to reconstruct marine biological productivity. In our case, Ba/Ti delineates the tsunami deposits, and peaks are associated with coarse-grained sediments (Fig. 12). Ti and Fe are sometimes used as indicators of the terrestrial origin of sediments (e.g. Ramírez-Herrera et al., 2012). Indeed, vertical variations of Ti and Fe through core LL1bis display lower concentrations in the tsunami deposits than in the underlying and overlying clays, but intra-tsunami variations are mostly controlled by the distribution of heavy minerals.

3.4.2. Calcium and carbonates

Observations of tsunami sediments with a polarising microscope confirm that the main source of Ca is marine bioclasts (biogenic Ca in shells and foraminifers). High Ca concentrations are detected in subunits 1 and 4, and low concentrations in the mud lines (subunit 2). The base of the tsunami deposit is also marked by an increase in carbonates, as

estimated by LOI at 950°C (Fig. 12). Observations with the binocular microscope confirm the absence of marine bioclasts in subunit 3 (Table 1).

There is an apparent discrepancy between Ca concentrations (XRF), carbonates (LOI at 950°C) and binocular microscope observations in the uppermost part of the tsunami deposit (subunit 8). XRF profiles show very low Ca concentrations from subunits 5 to 8 (40-29 cm deep), whereas marine bioclasts represent up to 7% of the clasts within subunit 8 (Table 2). Observations of the sediments in thin section and using X-ray tomography (resolution 100 µm) reveal that shell fragments are larger in the lower part of the tsunami (subunits 1 and 4) than in the upper part (subunits 6 and 8). Thus the biogenic Ca might be underestimated by the 4-mm wide beam of the XRF core scanner. This observation could explain the low Ca detected by XRF in the upper part of the tsunami deposit, smaller shells being less concentrated within the 4-mm wide beam of the XRF core scanner.6

Complementary information is provided by Ca/Al. Al-based elemental ratios are chosen to represent the silicate part of the sediment that resides exclusively in the lithogenic fraction. Therefore, an increase in the Ca/Al ratio may illustrate an increase of carbonates and their biogenic fraction. Amplification of the Ca/Al profile shows significant increase in subunits 6 and 8, and a clear decrease in subunit 5 (mud lines). Intervals of negative Spearman coefficient of correlation between Ca and Al may characterise sediments dominated by marine sources (~subunits 1, 2 and 4), and positive intervals of sediments dominated by continental sources (subunits 3 and 5 to 8). This hypothesis is supported by a decrease in Sr concentration upwards. Peaks of organic matter, as represented by LOI at 550°C, correspond to sediments enriched in rip-up clasts of soil (subunits 4 and 8).

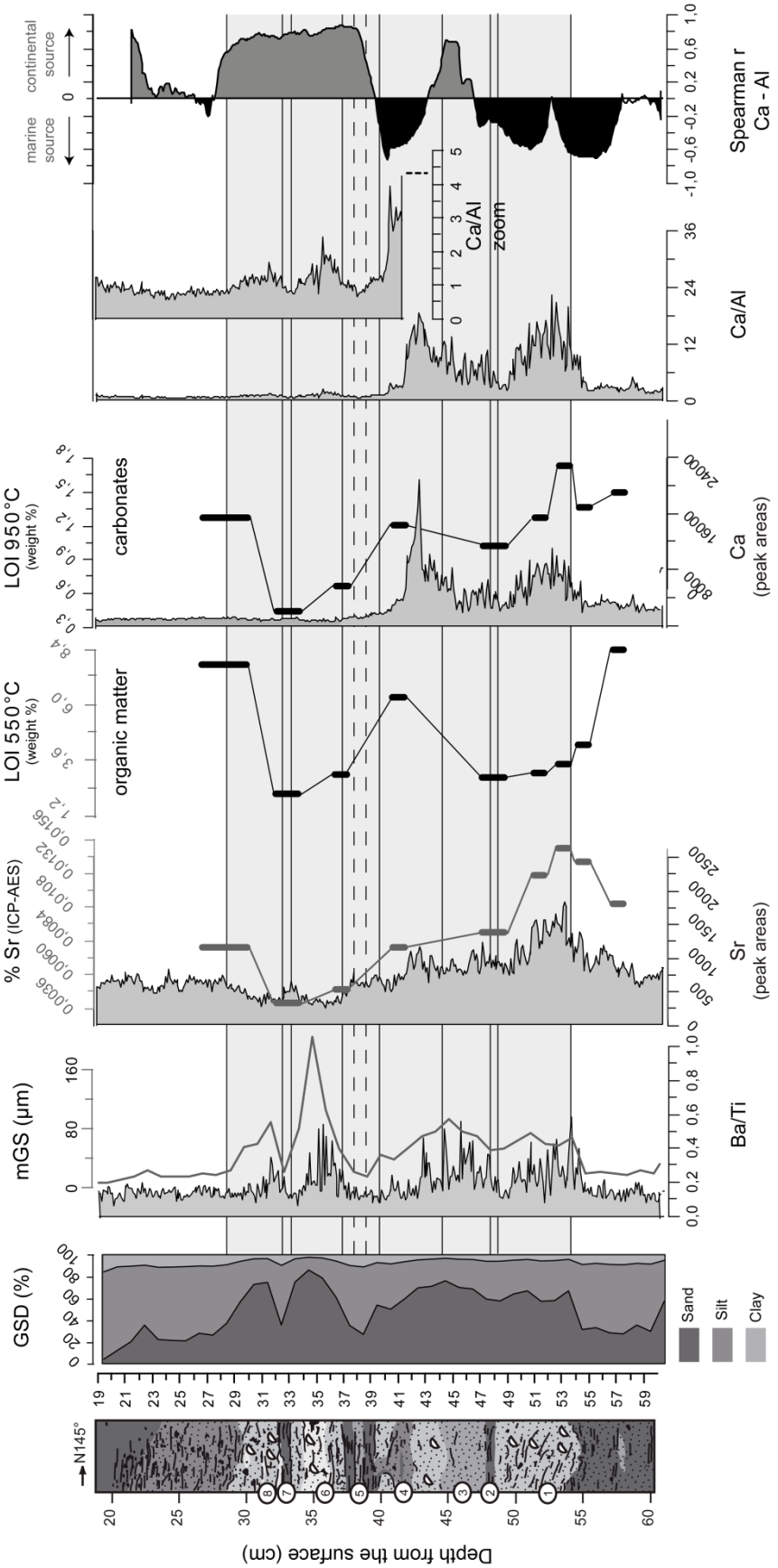

Figure 12: Sediment sources documented by XRF (step-size of 1 mm), ICP-AES and LOI data (loss on ignition at 550°C and 950°C).

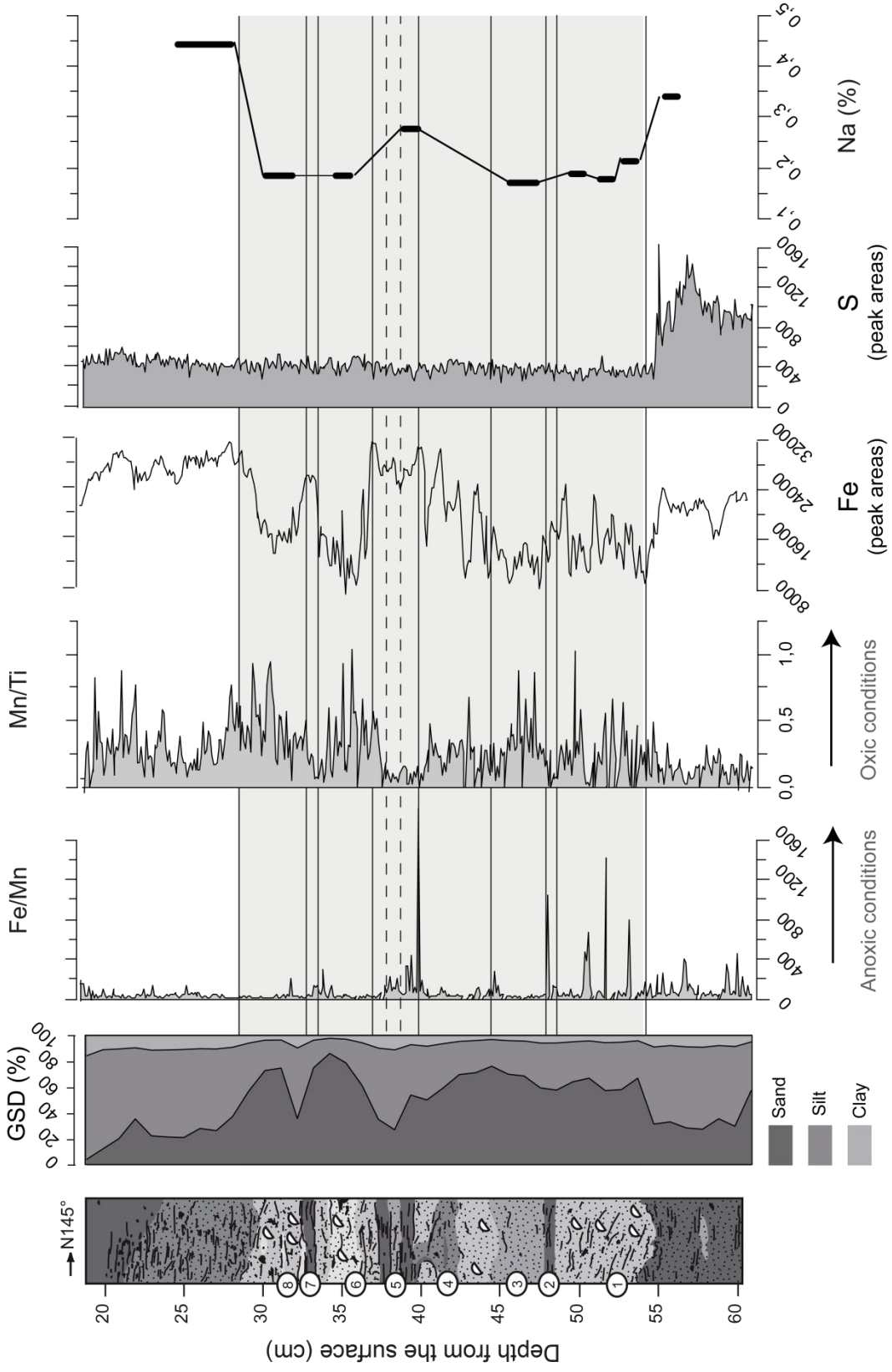

Figure 13: Post-depositional processes highlighted by XRF (step-size of 1 mm). Na was out of detection range of the Avaatech XRF core scanner, so the Na profile here is from ICP-AES.

Depth (cm)	22-26	31-33	39-40	42-43	45-47	50-51	53-54	55-56	57-58
Oxide (wt.%)									
SiO_2	66,39	87,65	83,93	71,45	84,27	83,93	80,85	79,04	65,27
Al_2O_3	12,37	4,32	5,54	10,61	4,72	4,66	4,11	5,24	12,69
Fe_2O_3	5,69	2,45	3,41	4,67	2,29	2,44	5,15	4,49	5,33
MgO	1,47	0,55	0,70	1,30	0,59	0,64	0,65	0,82	1,57
CaO	0,32	0,20	0,20	0,98	1,65	2,17	2,85	2,27	1,27
Na_2O	1,20	0,50	0,50	0,75	0,46	0,51	0,48	0,57	0,92
K_2O	1,37	0,65	0,68	1,15	0,67	0,66	0,62	0,70	1,51
TiO_2	0,76	0,26	0,40	0,68	0,27	0,29	0,24	0,33	0,73
MnO	0,12	0,06	0,04	0,05	0,03	0,10	0,03	0,02	0,04
P_2O_5	0,20	0,09	0,12	0,18	0,09	0,09	0,20	0,19	0,20
Ba	0,015	0,016	0,016	0,015	0,013	0,016	0,018	0,019	0,017
Sr	0,008	0,004	0,005	0,008	0,009	0,013	0,015	0,014	0,011
H_2O+	3,98	0,80	1,11	2,85	1,01	0,85	0,85	1,11	3,21
H_2O-	5,44	1,88	2,74	4,95	3,12	3,51	3,51	4,71	7,02
Total	*99,32*	*99,43*	*99,40*	*99,63*	*99,18*	*99,86*	*99,57*	*99,54*	*99,79*
LOI 550°	7,77	2,22	3,03	6,34	2,91	3,08	3,51	4,32	8,37
LOI 950°	1,27	0,45	0,67	1,21	1,03	1,28	1,74	1,36	1,50

Table 2 - Major element compositions and loss on ignition (LOI) of bulk samples from the 1755 tsunami deposits in Los Lances (ICP-AES, Jobin-Yvon ULTIMA C, Clermont-Ferrand). LOI at 550° and 950° represent the organic carbon and carbonate contents, respectively.

3.5. Post-depositional processes

Based on the assumption that Mn (in the MnS state) is redox sensitive, the lower redox potential of Fe compared to Mn implies that Fe precipitates before Mn during oxic conditions. Therefore we used Fe/Mn as a palaeo-redox indicator (Davison, 1993; Schmidt et al., 2008). Anoxic conditions are revealed from the analyses of the pre-tsunami clay and tsunami mud lines (Fig. 13). Post-depositional oxidation is revealed by Mn/Ti (Croudace et al., 2006). Maximal values of Mn/Ti are recorded in the coarse-grained tsunami subunits and in the post-tsunami sediments (Fig. 13).

S is often related to post-depositional diagenetic processes in brackish/marine depositional environments of peat, but S and Fe can be used together as indicators of palaeosalinity and flooding frequency (Chagué-Goff, 2010). Figure 13 shows that the S is

highly concentrated in the underlying layer of the tsunami deposit. S is highly mobile and generally subject to dissolution by meteoritic waters (e.g. Chagué-Goff et al., 2012a). Elemental sulphur easily moves from the sand-dominated tsunami deposits down to the underlying clayey sediments. The high concentration of S accumulated in the pre-tsunami clay might thus result from post-tsunami flushing of salt by rainfalls. Na is also highly soluble and its concentration, as estimated by ICP-AES, is lower in the tsunami deposit than in underlying and overlying clays (Fig. 13).

4. Discussion and perspectives

4.1. A tentative tsunami scenario

The 1755 events were recently discussed by Blanc (2008, 2011) who proposed the following scenario for Cadiz, 80 km NW of the Los Lances Bay (this is the nearest place for which a detailed chronology is available). The 1755 tsunami in Cadiz consisted of 6 successive waves, with a progressively decreasing period from 20 to 40 minutes. Observations gathered by Blanc (2008) ascribe a decrease in wave "force" and "violence", especially after 1:00 PM (i.e. for the fifth and sixth waves). The tsunami scenario may have been slightly different in Los Lances, depending on the offshore bathymetry and coastal morphology.

Due to reworking and erosion during the tsunami itself, the sedimentary record has to be considered as being incomplete. Nevertheless, the coupling of high-resolution textural and geochemical analysis allows us to propose a comprehensive reconstruction of the different phases of tsunami deposition. The organisation of the Los Lances sequence into distinct subunits, the description of bedforms and sediment fabrics, vertical variations of texture and composition can all be used as evidence that the 1755 tsunami event was associated with changes in flow conditions and depositional mechanisms.

- Subunit 1 can be interpreted as the result of the first wave uprush, characterised by an impulse of sand-size sediments mostly composed of quartz (60-80%), heavy minerals (13-33%) and marine bioclasts (2-4%). The sudden transition from pre-tsunami dark grey clays to the coarser, silicate-dominated tsunami deposits is marked by increases in Si-based elemental ratios (Fig. 7), Sr and Ca (Fig. 12: presence of marine bioclasts). Erosion of the underlying

clay is shown by numerous rip-up clasts. Subunit 1 is very poorly sorted and dominated by traction (Fig. 8).

- The fine mud line (subunit 2) capping subunit 1 is interpreted as emplaced during a decantation phase between the first and second wave uprushes. The limited thickness of subunit 2 makes it difficult to sample directly, but it is well documented by µXRF and X-ray imagery (Fig. 7 and 8). All mud lines (subunits 2, 5 and 7) are characterised by low grey values for X-ray absorption, decreasing Si, Ba, Sr and Ca (which correspond in our case to marine indicators) and increasing K (mud proportion), settling and decreasing current strength (Fig. 8: AMS). Thin sections and X-ray imagery confirm the occurrence of thin laminae of heavy minerals (mostly orthopyroxenes) above and below the mud lines, thus explaining abrupt changes of Fe and magnetic susceptibility on the profiles of Fig. 8.

- Subunit 3 probably corresponds to a second wave uprush, but its characteristics differ slightly from subunit 1 in terms of composition (few marine bioclasts), texture (inverse grading) and sediment source (rip-up clasts of OM in the upper part of the subunit).

- The distinction between subunits 3 and 4 is not discernible by all the proxies, and there is evidence in subunit 4 of reworked subunit 3 material (bulking). Subunit 4 is richer in wood (5%) and heavy minerals (17-18%) and is not vertically graded (convolute bedding).

- After (at least) three successive wave uprushes, a second phase of settling is marked by two mud lines separated by a very thin layer of fine grey sand (subunit 5). The intermediate fine sand could be the result of a new, small-amplitude incoming wave, or a refracted wave. It is tempting to link this episode with the 1:00 PM reduction in the wave's violence (Blanc, 2008).

- The upper surface of the second mud line of subunit 5 is eroded by a new impulse of sand-sized sediments. This subunit 6 may correspond to another wave uprush, but it has a fine skewed GSD, is better sorted than the previous uprushes (subunits 1, 3 and 4) and is dominated by turbulent settling. This is also concordant with observations reported by Blanc (2008).

- After a third settling phase (mud line: subunit 7), subunit 8 might be interpreted as the result of the backwash (outflow phase). Compared to uprush subunits, it is characterised by abundant small-size marine bioclasts, numerous rip-up clasts of soil and wood, renewed

traction (Fig. 8: T<0), higher mud content (Fig. 7: K and K/Si profiles), lower Si and Ba concentrations (Fig. 12), and higher values of X-ray absorption (Figs. 8 and 9).

4.2. New insights into the key features of tsunami deposits and perspectives

Trench-scale diagnostic characteristics of tsunami deposits are listed (e.g. Dawson and Stewart 2007; Bourgeois 2009; Chagué-Goff et al. 2011; Keating et al. 2011; Goff et al. 2012) and discussed below, with reference to the main results from this high-resolution case-study:

All size fractions may be present, from clay to plurimetric boulders, depending on the sediment sources (offshore sediments, beach and dunes, riverbeds, soils). This is exactly the case for the 1755 Lisbon tsunami deposits in Los Lances, where all grain size fractions from fine sands to clays are present (Fig. 7). Some subunits arecomposed almost exclusively of sand (e.g. >80% in subunit 6), and others of silts (typically 60% for the mud lines). Grain size distributions are fine skewed, except for the mud lines.

A tsunami wave train generates a cycle of erosion-deposition processes, leading to the emplacement of successive fining-upwards subunits or subsequences. Nevertheless, a constant problem when interpreting a tsunami sequence is the uncertainty due to erosion of underlying deposits by each new wave, thus truncating the record, especially if wave amplitude increases during the event. The 1755 deposits generally display 8 subunits in Los Lances, but there is no fining upwards of the overall sequence. Normal grading is often reported for tsunami deposits, especially in their upper part (e.g. Bondevik et al., 1997; Minoura et al., 1997; Gelfenbaum and Jaffe, 2003; Hori et al., 2007; Paris et al., 2007; Choowong et al., 2008; Wagner and Srisutam, 2011). Inverse or no grading is typical of the lower part of tsunami deposits (e.g. Shi et al., 1995; Paris et al., 2007; Higman and Bourgeois, 2008; Moore et al., 2011), but is less common than normal grading. In our case, normal grading is observed in subunits 4 and 8, and inverse grading in subunit 3 (Fig. 7). Subunit 6 is divided into three parts: the central white fine sand is intercalated between yellowish-brown, very fine sands. Detailed analysis of cores and X-ray imagery reveal that the vertical grain size trends are more complex than observed in the field, and these small-scale (subcentimetric) grain size variations are of great interest when interpreting a sedimentary sequence. Thus visual observations and bulk sampling of the sediments alone may lead to an incomplete record and false interpretations.

Short settling phases are marked by mud lines and mud drapes. Three settling phases were identified in the 1755 tsunami deposits in Los Lances (mud lines of subunits 2, 5 and 7). Note that only subunit 5 was detected in the field, the other mud lines being identified by careful analysis of the cores in the lab, using thin sections, X-ray imaging and XRF. Mud lines of subunit 5 are clearly subdivided into horizontal laminae with varying grain size. The upper surface of the mud lines shows evidence of erosion and entrainment of mud by the lowermost sands of the following wave uprush (Fig. 6).

Erosion of the substratum by the tsunami floodwaters is attested by scour-and-fill features and rip-up clasts (of soil for example). We were able to find evidence for erosion of the clayey substratum in subunit 1 of the 1755 tsunami deposit in Los Lances, and four other erosive discontinuities were identified within the tsunami sequence (Fig. 3). Rip-up clasts of clay or soil (from the substratum or mud lines) may grade into stretched rip-ups, discontinuous laminae or convolute bedding. The abundance of rip-up clasts of organic matter increases upwards. Modelling these erosional microforms would be very useful for the reconstruction of flow dynamics.

Some units or layers are enriched in heavy minerals. In our case, heavy minerals (mostly orthopyroxenes) represent 12 to 33% of the grains observed with the binocular microscope. In a deposit dominated by quartz grains, the distribution of heavy minerals (mostly orthopyroxene) is not random. Vertical profiles of magnetic susceptibility and Fe, peaks of X-ray aborption and thin section analysis revealed zones or laminae enriched in heavy minerals, especially adjacent to the mud lines. Further investigations are needed to improve understanding of the spatial distribution of different populations of grains, in terms of density and shape, and their relationship to sediment sorting. For instance, Jagodziński et al. (2009) noted that higher mica concentrations occurred towards the upper part of the 2004 tsunami deposits in Thailand, with mica flakes found more commonly in the finest-grained sediment samples. The distribution of heavy minerals in tsunami deposits is thus a promising indicator of flow dynamics, even if they are source-dependent. The 2011 Tohuku-oki tsunami deposits in Sendai are particularly rich in heavy minerals, but no vertical trends could be detected with 1 cm- interval sampling (Jagodziński et al., 2012). X-ray microtomography at the grain-scale (e.g. synchrotron source) would be very useful for identifying heavy minerals and characterising their spatial distribution.

Marine bioclasts are used as indicators of sediment sources (diatoms, foraminifers, nannoliths, corals). Numerous marine bioclasts were identified in the 1755 tsunami deposits: fragments of shells (gastropods, bivalves), benthic foraminifers, diatoms, sponge spicules, rhodophyta calcareous algae, echinoderms (sea-urchin radiols). Their proportion and size vary vertically from 0 to 7% (Table 1). The proportion can be indirectly estimated by LOI at 950°C, or by scanning XRF analysis (Fig. 12). Observations of the sediments in thin section and X-ray tomography provide better estimates of the vertical variations of proportion and size of the marine bioclasts. For instance, shell fragments are larger in the lower part than in the upper part of the 1755 tsunami deposit in Los Lances. In addition to indicating sediment sources, the vertical distribution of specific bioclasts such as diatoms, foraminifers or nannoliths may provide information about changes in flow conditions (e.g. Sawai et al., 2009; Paris et al., 2010).

Sedimentary features such as laminations, convolutions, dunes, and even antidunes attest to a change in flow dynamics during a single event. Thanks to X-ray imaging and thin sections, we were able to identify oblique and horizontal laminations (subunits 1 and 3), and convolutions (subunit 4), but not dunes or antidunes. Further investigations using X-ray microtomography would provide better characterization of these features.

Clast fabrics indicate both landward (uprush) and seaward (backwash) currents. Characterising clast fabrics in silty to sandy size deposits is challenging. AMS appears to give information for inferring palaeo-current direction in unconsolidated sediments, if the transport mode is defined (Wassmer et al., 2010). In our case, the NNW-SSE declination of traction-dominated subunits 1, 3 and 4 indicates a flow oriented WSW-ENE. Mud lines of subunit 5 were deposited by settling in a flow oriented SW-NE. The palaeocurrent reconstruction of subunits 6 to 8 is only tentative because the anisotropy ellipsoids are almost spherical. We cannot characterise clast imbrication by AMS so it is difficult to distinguish between seaward and landward currents.

The geochemical signature shows an increase in indicators of marine inundation and high-energy environment. Compared to their substratum, deposits from high-energy coastal events are often characterized by an increase of Fe, S, Ti, Sr, Ba, Na, Ca, Cl, I or Br concentrations (e.g. Minoura et al., 1994; Chagué-Goff et al., 2002, 2012a; Goff et al., 2004; Schlichting and Peterson, 2006; Nichol et al., 2007; Abrantes et al., 2008). The main limitations to elemental approaches are: (1) geochemical trend variations from one site to

another, depending on the climatic, geomorphological and geological environment; (2) the dependence of some elements on the grain size distribution of the sediment. When using XRF data, selected elemental ratios are chosen in preference to single element concentrations in order to eliminate any bias due to grain size. Preparing thin sections of the tsunami deposits and identifying minerals using the polarising microscope is also a necessary step before interpreting vertical geochemical trends through a core.

We agree that the results of this study might be applicable only to: (1) silicate-dominated, (2) sand-size tsunami deposits, (3) preserved for the last ~250 years in the clayey sediments of, (4) a Mediterranean coastal marsh. In our case, the tsunami deposit is marked by high Si/Al (Fig 7) and Ba/Ti (Fig. 12) ratios compared to overlying and underlying clayey sediments. The discontinuity between the tsunami deposit and its substratum is also marked by a rapid increase in Ca (or Ca/Al) and Sr concentrations, followed by a progressive decrease upwards (Fig. 12). Na and S were leached from the 250 year-old fine-sand tsunami deposit and accumulated in the underlying clay (Fig. 13). Na is a good proxy for saltwater (seawater has higher content of Na than freshwater), but is not reliable in terms of preservation due to its high solubility, especially in peat or in a tropical climate (Chagué-Goff, 2010, 2012b). Deposits left by the 2004 Indian Ocean tsunami in Thailand were characterized by an increase in Na, Ca, Mg, Cl and SO_4 concentrations (Szczucińsky et al., 2005; Srinivasalu et al., 2008). After one rainy season, however, dissolution and washing out of finer fractions from the tsunami deposits significantly reduced the concentrations of water-soluble salts (Szczucińsky et al., 2007).

5. Conclusion

Onshore palaeotsunami deposits are often used to estimate earthquake recurrence intervals in seismic areas (Atwater, 1987; Minoura and Nakaya, 1991; Shennan et al., 1996; Pinegina et al., 2003; Cisternas et al., 2005; Williams et al., 2005), such as the south-western Iberian margin (Luque et al., 2001; Lario et al., 2011). On the other hand, many studies attempt to reconstruct past earthquakes by testing different rupture scenarios, modelling the subsequent tsunami propagation and comparing the model with observations or historical reports (e.g. for the 1755 tsunami: Baptista et al., 1998, 2011; Barkan et al., 2008; Omira et al., 2009; Lima et al., 2010; Roger et al., 2010). However, selecting an appropriate rupture

scenario, even based on a careful analysis and interpretation of sediment cores, is challenging. Nevertheless, reproducing the methodology presented in this paper on other tsunami cores all around the Gulf of Cadiz should help in increasing our understanding of the 1755 tsunami inundation, and in constraining the earthquake source.

Kilfeather et al. (2007) carried out pioneering work on the micromorphology of tsunami deposits. Five years on, there is still room for improvement in terms of linking tsunami flow characteristics to the sedimentary record. For instance, the relationships between sediment sorting, fabrics, anisotropy of magnetic susceptibility and X-ray absorption would be better documented by X-ray microtomography at a higher resolution (i.e. grain scale). Such studies also have the potential to define new criteria for distinguishing between storm and tsunami deposits.

Acknowledgements

This study was funded by the French National Research Agency, project ANR-08-RISKNAT MAREMOTI whose leader is Hélène Hébert (CEA), and Conseil Régional d'Auvergne, project TSUNAMIX. The authors are particularly grateful to Jérôme Bascou (LMV, St-Etienne: AMS), Bernard Martin (EPOC, Bordeaux: impregnation of the boxes and thin-sections), Gérard Chabaud (EPOC, Bordeaux: Malvern grain size analysis), Dr Eric Laffon, (Université Bordeaux 2, CHU du Haut-Lévêque, Service de Médecine Nucléaire), Michel Morales and Olivier Baris (CHU Bordeaux, Service d'Imagerie Médicale), and Fran Van Wyk de Vries (English revision). Catherine Chagué-Goff and an anonymous reviewer are thanked for their detailed and constructive comments. This is Laboratory of Excellence *ClerVolc* contribution n°57.

References

Abrantes, F., U. Alt-Epping, Lebreiro, S., Voelker, A., Schneider, R., 2008. Sedimentological record of tsunamis on shallow-shelf areas: The case of the 1969 AD and 1755 AD tsunamis on the Portuguese Shelf off Lisbon. Marine Geology 249 (3-4), 283-293.

Atwater, B.F., 1987. Evidence for great Holocene earthquakes along outer coast of Washington State. Science 236, 942-944.

Baptista, M. A., Heitor, S., Miranda, J.M., Miranda, P., Mendes Victor, L., 1998. The 1755 Lisbon tsunami: evaluation of the tsunami parameters. Journal of Geodynamics 25 (1-2), 143-157.

Baptista, M., Omira, R., Matias, L., Miranda, J.M., Annunziato, A., Carrilho, F., Kaabouben, F., 2011. On the Need for a Tsunami Warning System in the North East Atlantic Area (Gulf of Cadiz), in: Mörner, N.A. (Ed.), The tsunami threat – Research and Technology. InTech, pp. 13-28.

Barkan, R., ten Brink, U., Lin, J., 2008. Far field tsunami simulations of the 1755 Lisbon earthquake: Implications for tsunami hazard to the U.S. East Coast and the Caribbean. Marine Geology 264, 109-122.

Bertrand, S., Hughen, K.A., Sepúlveda, J., Pantoja, S., 2012. Geochemistry of surface sediments from the fjords of Northern Chilean Patagonia (44–47°S): Spatial variability and implications for paleoclimate reconstructions. Geochimica et Cosmochimica Acta 76, 125-146.

Blanc, P.-L., 2008. The tsunami in Cadiz on 1 November 1755: A critical analysis of reports by Antonio de Ulloa and by Louis Godin. Comptes Rendus Geosciences 340 (4), 251-261.

Blanc, P.-L., 2011, The Atlantic Tsunami on November 1st, 1755: World Range and Amplitude According to Primary Documentary Sources, in: Mörner, N.A. (Ed.), The tsunami threat – Research and Technology. InTech, pp. 423-446.

Bondevik, S., Svendsen, J.I., Mangerud, J., 1997. Tsunami sedimentary facies deposited by the Storegga tsunami in shallow marine basins and coastal lakes, western Norway. Sedimentology 44, 1115-1131.

Bourgeois, J., 2009. Geologic effects and records of tsunamis, in: Robinson, A.R., Bernard, E.N., (Eds.), The Sea, volume 15: Tsunamis. Harvard University Press, pp. 53-91.

Calvert, S.E., Pedersen, T.F., Karlin, R.E., 2001. Geochemical and isotopic evidence for post-glacial palaeoceanographic changes in Saanich Inlet, British Columbia. Marine Geology 174 (1), 287-305.

Campos, M.L., 1991. Tsunami hazards on the Spanish coasts of the Iberian Peninsula. Science of Tsunami Hazards 9 (1), 83-90.

Chagué-Goff, C., Dawson, S., Goff, J.R., Zachariensen, J., Berryman, K., Garnett, D., Waldron, H., Mildenhall, D., 2002. A tsunami (ca. 6300 years BP) and other Holocene environmental changes, northern Hawkes Bay, New Zealand. Sedimentary Geology 150, 89-102.

Chagué-Goff, C., 2010. Chemical signature of palaeotsunamis: a forgotten proxy? Marine Geology 271, 67-71.

Chagué-Goff, C., Schneider, J.L., Goff, J.R., Dominey-Howes, D., Strotz, L., 2011. Expanding the proxy toolkit to help identify past events – Lessons from the 2004 Indian Ocean Tsunami and the 2009 South Pacific Tsunami. Earth-Science Reviews 107, 107-122.

Chagué-Goff, C., Andrew, A., Szczuciński, W., Goff, J., Nishimura, Y., 2012a. Geochemical signatures up to the maximum inundation of the 2011 Tohoku-oki tsunami – implications for the 869 AD Jogan and other palaeotsunamis. Sedimentary Geology 282, 65-77.

Chagué-Goff, C., Niedzielski, P., Wong, H.K.Y., Szczuciński, W., Sugawara, D., Goff, J., 2012b. Environmental impact assessment of the 2011 Tohoku-oki tsunami on the Sendai plain. Sedimentary Geology 282, 175-187.

Choowong, M., Murakoshi, N., Hisada, K., Charusiri, P., Charoentitirat, T., Chutakositkanon, V., Jankaew, K., Kanjanapayont, P., Phantuwongraj, S., 2008. 2004 Indian Ocean tsunami inflow and outflow at Phuket, Thailand. Marine Geology 248, 179-192.

Croudace, I.W., Rindby, A., Rothwell, R.G., 2006. ITRAX: description and evaluation of a new multi-function X-ray core scanner. Geological Society, Special Publications 267, 51-63.

Cuven, S., Francus, P., Lamoureux, S.F., 2010. Estimation of grain size variability with micro X-ray fluorescence in laminated lacustrine sediments, Cape Bounty, Canadian High Arctic. Journal of Paleolimnology 44, 803-817.

Davison, W., 1993. Iron and Manganese in Lakes. Earth-Science Reviews 34, 119-163.

Dawson, A.G., Stewart, I., 2007. Tsunami deposits in the geological record. Sedimentary Geology 200, 166-183.

Ganeshram, R.S., Calvert, S.E., Pedersen, T.F., Cowie, G.L., 1999. Factors controlling the burial of organic carbon in laminated and bioturbated sediments off NW Mexico: implications for hydrocarbon preservation. Geochimica et Cosmochimica Acta 63 (11), 1723-1734.

Gelfenbaum, G., Jaffe, B., 2003. Erosion and sedimentation from the 17 July, 1998 Papua New Guinea tsunami. Pure and Applied Geophysics 160, 1969-1999.

Goff, J.R., Wells, A., Chagué-Goff, C., Nichol, S.L., Devoy, R.J.N., 2004. The elusive AD 1826 tsunami, South Westland, New Zealand. New Zealand Geographer 60 (2), 28-39.

Goff, J.R., Chagué-Goff, C., Nichol, S.L., Jaffe, B., Dominey-Howes, D., 2012. Progress in palaeotsunami research. Sedimentary Geology 243-244, 70-88

Gonneea, M.E., Paytan, A., 2006. Phase associations of barium in marine sediments. Marine Chemistry 100, 124-135.

Gracia, I. J., Alonso, C., Benavente, J., Anfuso, G., Del Rio, L., 2006. The Different Coastal Records of the 1755 Tsunami Waves along the south Atlantic Spanish Coast. Zeitschrift für Geomorphologie Suppl. Vol. 146, 195-220.

Gutiérrez-Mas, J.M., Juan, C., Morales, J.A., 2009. Evidence of high-energy events in shelly layers interbedded in coastal Holocene sands in Cadiz Bay (south-west Spain). Earth Surface Processes and Landforms 34, 810-823.

Heiri, O., Lotter, A.F., Lemcke, G., 2001. Loss on ignition as a method for estimating organic and carbonate content in sediments: reproducibility and comparability of results. Journal of Paleolimnology 25 (1), 101-110.

Hindson, R.A., Andrade, C., Dawson, A.G., 1996. Sedimentary processes associated with the tsunami generated by the 1755 Lisbon earthquake on the Algarve coast, Portugal. Physics and Chemistry of The Earth 21 (1-2), 57-63.

Hindson, R.A., and Andrade, C., 1999 Sedimentation and hydrodynamic processes associated with the tsunami generated by the 1755 Lisbon earthquake Quaternary International 56, 27-38.

Higman, B., Bourgeois, J., 2008. Deposits oft he 1992 Nicaragua tsunami. In: Shiki, T., Tsuji, Y., Yamazaki, T., Minoura, K. (Eds.), Tsunamiites – features and implications. Elsevier, pp. 81-103.

Hori, K., Kuzumoto, R., Hirouchi, D., Umitsu, M., Janjirawuttikul, N., Patanakanog, B., 2007. Horizontal and vertical variations of 2004 Indian tsunami deposits: an example of two transects along the western coast of Thailand. Marine Geology 239, 163-172.

Jaffe, B.E., Gelfenbaum, G., 2007. A simple model for calculating tsunami flow speed from tsunami deposits. Sedimentary Geology 200, 347-361.

Jaffe, B.E., Goto, K., Sugawara, D., Richmond, B., Fujino, S., Nishimua, Y., 2012. Flow speed estimated by inverse modelling of sandy tsunami deposits: results from the 11 March 2011 tsunami on the coastal plain near the Sendai airport, Honshu, Japan. Sedimentary Geology 282, 90-109.

Jagodziński, R., Sternal, B., Szczuciński, W., Lorenc, S., 2009. Heavy minerals in 2004 tsunami deposits on Kho Khao Island, Thailand. Polish Journal of Environmental Studies 18, 103–110.

Jagodziński, R., Sternal, B., Szczuciński, W., Chagué-Goff, C., Sugawara, D., 2012. Heavy minerals in the 2011 Tohoku-oki tsunami deposits – insights into sediment sources and hydrodynamics. Sedimentary Geology 282, 57-64.

Keating, B.H., Helsley, C.E., Wanink, M., Walker, D., 2011. Tsunami deposit research: fidelity of the tsunami record, ephemeral nature, tsunami deposits characteristics, remobilization of sediments by later waves, and boulder movement, in: Mörner, N.A. (Ed.), The tsunami threat – Research and Technology. InTech, pp. 389-4224.

Kilfeather, A., Blackford, J.J., van der Meer, J.J.M., 2007. Micromorphological analysis of coastal sediments from Willapa Bay, Washington, USA: a technique for analysing inferred tsunami deposits. Pure and Applied Geophysics 164, 509-525.

Lario, J., Zazo, C., Goy, J.L., Silva, P.G., Bardaji, T., Cabero, A., Dabrio, C.J., 2011. Holocene palaeotsunami catalogue of SW Iberia. Quaternary International 242, 196-200.

Lima, V.V., Miranda, J.M., Baptista, M.A., Catalão, J., Gonzalez, M., Otero, L., Olabarrieta, M., Alvarez-Gómez, J.A., Carreño, E., 2010. Impact of a 1755-like tsunami in Huelva, Spain. Natural Hazards and Earth System Science 10, 139-148.

Luque, L., Lario, J., Zazo, C., Goy, J.L., Dabrio, C.J., Silva, P.G., 2001. Tsunami deposits as paleoseismic indicators: examples from the Spanish coast. Acta Geologica Hispanica 36 (3-4), 197-211.

Luque, L., Lario, J., Civis, J., Silva, P.G., Zazo, C., Goy, J.L., Dabrio, C.J., 2002. Sedimentary record of a tsunami during Roman times, Bay of Cadiz, Spain. Journal of Quaternary Science 17 (5-6), 623-631.

Luque, L., Zazo, C., Lario, J., Goy, J.L., Civis, J., González, F.M., Silva, P.G., Dabrio, C.J., 2004. El efecto del tsunami del año 1755 en el litoral de Conil de la Frontera (Cádiz), in = Baquedano, E., Rubio, S. (Eds.), Miscelánea en Homenaje a Emiliano Aguirre, vol. I – Geología. Zona Arqueológica, 4, Alcalá de Henares, pp. 73-82.

ITGE, 1990. Mapa geológico de España, 1:50.000, Tarifa 1077.

Migeon, S., Weber, O., Faugères, J.C., Saint-Paul, J., 1999. SCOPIX: a new imaging system for core analysis. Geo-Marine Letters 18, 251–255.

Minoura, K., Nakaya, S., 1991. Traces of tsunami deposits preserved in intertidal lacustrine and marsh deposits: some examples from Northeast Japan. Journal of Geology 99, 265-287.

Minoura, K., Nakaya, S., Uchida, M., 1994. Tsunami deposits in a lacustrine sequence of the Sanriku coast, Northeast Japan. Sedimentary Geology 89, 25-31.

Minoura, K., Imamura, F., Takahashi, T., Shuto, N., 1997. Sequence of sedimentation processes caused by the 1992 Flores tsunami: Evidence from Babi Island. Geology 25 (6), 523-526.

Moore, A., Goff, J., McAdoo, B.G., Fritz, H.M., Gusman, A., Kalligeris, N., Kalsum, K., Susanto, A., Suteja, D., Synolakis, C.E., 2011. Sedimentary deposits from the 17 July 2006 Western Java tsunami, Indonesia: use of grain size analyses to assess tsunami flow depth, speed, and traction carpet characteristics. Pure and Applied Geophysics 167 (11), 1951-1961.

Morales, J.A., Borrego, J., San Miguel, E.G., López-González, N., Carro, B., 2008. Sedimentary record of recent tsunamis in the Huelva Estuary (southwestern Spain). Quaternary Science Reviews 27 (7-8), 734-746.

Morales, J.A., Gutiérrez Mas, J.M., Borrego, J., Rodríguez-Ramírez, A., 2011. Sedimentary Characteristics of the Holocene Tsunamigenic Deposits in the Coastal Systems of the Cadiz Gulf (Spain), in: Mörner, N.A. (Ed.), The tsunami threat – Research and Technology. InTech, pp. 237-258.

Morton, R.A., Gelfenbaum, G., Jaffe, B.E., 2007. Physical criteria for distinguishing sandy tsunami and storm deposits using modern examples. Sedimentary Geology 200, (3-4), 184-207.

Murray, R.W., Knowlton, C., Leinen, M., Mix, A.C., Polsky, C.H., 2000. Export production and terrigenous matter in the Central Equatorial Pacific Ocean during interglacial oxygen isotope Stage 11. Global and Planetary Change 24, 59-78.

Nichol, S.L., Goff, J.R., Devoy, R., Chagué-Goff, C., Hayward, B., James, I., 2007. Lagoon subsidence and tsunami on the West Coast of New Zealand. Sedimentary Geology 200, 248-262.

Omira, R., Baptista, M.A., Matias, L., Miranda, J.M., Catita, C., Carrilho, F., Toto, E., 2009. Design of a sea-level tsunami detection network for the Gulf of Cadiz. Natural Hazards and Earth System Science 9, 1327-1338.

Paris, R., Lavigne, F., Wassmer, P., Sartohadi, J., 2007. Coastal sedimentation associated with the December 26, 2004 in Lhok Nga, west Banda Aceh (Sumatra, Indonesia). Marine Geology 238, 93-106.

Paris, R., Cachão, M., Fournier, J., Voldoire, O., 2010. Nannoliths abundance and distribution in tsunami deposits: example from the December 26, 2004 tsunami Lhok Nga (northwest Sumatra, Indonesia). Géomorphologie : Relief, Processus, Environnement 2010 (1), 109-118.

Paris, R., Nandasena, N.A.K., Fournier, J., 2012. Comment on 'Reconstructing tsunami run-up from the characteristics of tsunami deposits on the Thai Andaman Coast' by Srisutam and Wagner (2010). Coastal Engineering 61, 53-55.

Pinegina, T.K., Bourgeois, J., Bazanova, L.I., Melekestsev, I.V., Braitseva, O.A., 2003. A millenial-scale record of Holocene tsunamis on the Kronotskiy Bay coast, Kamchatka, Russia. Quaternary Research 59, 36-47.

Pozo, M., Ruiz, F., Carretero, M.I., Vidal, J.R., Caceres, L.M., Abad, M., Gonzalez-Regalado, M.L., 2010. Mineralogical assemblages, geochemistry and fossil associations of Pleistocene-Holocene complex siliciclastic deposits from the Southwestern Donana National Park (SW Spain): A palaeoenvironmental approach. Sedimentary Geology 225 (1-2), 1-18.

Pritchard, D., Dickinson, L., 2008. Modelling the sedimentary signature of long waves on coasts: implications for tsunami reconstruction. Sedimentary Geology 206, 42-57.

Ramírez-Herrera, M.T., Lagos, M., Hutchinson, I., Kostoglodov, V., Machain, M.L., Caballero, M., Giguitchaichvili, A., Aguilar, B., Chagué-Goff, C., Goff, J., Ruiz-Fernández, A.C., Ortiz, M., Nava, H., Bautista, F., Lopez, G.I., Quintana, P., 2012. Extreme wave deposits on the Pacific coast of Mexico: tsunamis or storms? – A multi-proxy approach. Geomorphology 139-140, 360-371.

Reicherter, K., Vonberg, D., Koster, B., Fernández-Steeger, T., Grützner, C., Mathes-Schmidt, M., 2010. The sedimentary inventory of the 1755 Lisbon tsunami along the southern Gulf of Cádiz (southwestern Spain). Zeitschrift für Geomorphologie 54, Suppl. 3, 147-173.

Rodríguez-Ramírez, A., Ruiz, F., Cáceres, L.M., Rodríguez-Vidal, J., Pino, R., Muñoz, J.M., 2003. Analysis of the recent storm record in the southwestern Spanish coast: implications for littoral management. The Science of the Total Environment 303 (3), 189-201.

Roger, J., Allgeyer, S., Hébert, H., Baptista, M.A., Loevenbruck, A., Schindelé, F., 2010. The 1755 Lisbon tsunami in Guadeloupe Archipelago: source sensitivity and investigation of resonance effects. The Open Oceanography Journal 4, 58-70.

Rubio, B., Nombela, M.A., Vilas, F., 2000. Geochemistry of Major and Trace Elements in Sediments of the Ria de Vigo (NW Spain): an Assessment of Metal Pollution. Marine Pollution Bulletin 40 (11), 968-980.

Sandgren, P., Snowball, I., 2001. Application of mineral magnetic techniques to paleolimnology, in: Last W.M., Smol J.P. (Eds), Tracking environmental changes using lake sediments: physical and geochemical methods. Physical and Geochemical Methods. Kluwer Academic Publishers, Dordrecht, The Netherlands, pp. 217-238.

Sawai, Y., Jankaew, K., Martin, M.E., Prendergast, A., Choowong, M., Charoentitirat, T., 2009. Diatom assemblages in tsunami deposits associated with the 2004 Indian Ocean tsunami at Phra Thong Island, Thailand. Marine Micropaleontology 73, 70–79.

Schlichting, R., Peterson, C., 2006. Mapped overland distance of paleotsunami: high-velocity inundation in back-barrier wetlands of the central Cascadia margin, USA. The Journal of Geology 114, 577-552.

Schmidt, R., Roth, M., Tessadri, R., Weckstrom, K., 2008. Disentangling late-Holocene climate and land use impacts on an Austrian alpine lake using seasonal temperature anomalies, ice-cover, sedimentology, and pollen tracers. Journal of Paleolimnology 40, 453-469.

Schroeder, J.O., Murray, R.W., Leinen, M., Pflaum, R.C., Janecek, T.R., 1997. Barium in equatorial Pacific carbonate sediment: Terrigenous, oxide, and biogenic associations. Paleoceanography 12, 125-146.

Shennan, I., Long, A.J, Rutherford, M.M., Green, F.M., Innes, J.B., Lloyd, J.M., Zong, Y., Walker, K.J., 1996. Tidal marsh stratigraphy, sea-level change and large earthquakes, I: a 500 years record in Washington, U.S.A. Quaternary Science Reviews 15, 1023-1059.

Shi, S., Dawson, A.G., Smith, D.E., 1995. Coastal sedimentation associated with the December 12th, 1992 tsunami in Flores, Indonesia. Pure and Applied Geophysics 144, 525-536.

Srinivasalu, S., Thangadurai, N., Jonathan, M.P., Armstrong-Altrin, J.S., Ayyamperumal, T., Ram Mohan, V., 2008. Evaluation of trace-metal enrichments from the 26 December 2004 tsunami sediments along the Southeast coast of India. Environmental Geology 53, 1711-1721.

Switzer, A.D., Srinivasalu, S., Thangadurai, N., Mohan, W.R., 2012. Bedding structures in Indian tsunami deposits that provide clues to the dynamics of tsunami inundation. Geological Society, London, Special Publication 361, 61-77.

Szczuciński, W., 2012. The post-depositional changes of the onshore 2004 tsunami deposits on the Andaman Sea coast of Thailand. Natural Hazards 60,115-133.

Szczuciński, W., Niedzielski, P., Rachlewicz, G., Sobzyński, T., Ziola, A., Kowalski, A., Lorenc, S., Siepak, J., 2005. Contamination of tsunami sediments in a coastal zone inundated by the 26 December 2004 tsunami in Thailand. Environmental Geology 49, 321-331.

Szczuciński, W., Niedzielski, P., Kozak, L., Frankowski, M., Ziola, A., Lorenc, S., 2007. Effects of rainy season on mobilization of contaminants from tsunami deposits left in a coastal zone of Thailand by the 26 December 2004 tsunami. Environmental Geology 53, 253-264.

Wagner, J.F., Srisutam, C., 2011. Grain-size and thin section characteristics of tsunami sediments from Thai-Andaman Coast, Thailand. In: Mörner, N.A. (Ed.), The tsunami threat – Research and Technology. InTech, pp. 259-282.

Wassmer, P., Schneider, J.L., Fonfrège, A.V., Lavigne, F., Paris, R., Gomez, G., 2010. Use of anisotropy of magnetic susceptibility (AMS) in the study of tsunami deposits: Application

to the 2004 deposits on the eastern coast of Banda Aceh, North Sumatra, Indonesia. Marine Geology 275, 255-272.

Wedepohl, K.H., Environmental influences on the chemical composition of shales and clays. Physics and Chemistry of the Earth 8, 305-333.

Whelan, F., Kelletat, D., 2005. Boulder deposits on the southern Spanish Atlantic coast: possible evidence for the 1755 AD Lisbon tsunami? Science of Tsunami Hazards 23, 25–38.

Williams, H.F.L., Hutchinson, I., Nelson, A.R., 2005. Multiple sources for late-Holocene tsunamis at Discovery Bay, Washington State, USA. The Holocene 15 (1), 60-73.

Zaragosi, S., Bourillet, J.F., Eynaud, F., Toucanne, S., Denhard, B., Van Toer, A., Lanfumey, V., 2006. The impact of the last European deglaciation on the Bay of Biscay turbidite systems. In: Mulder, T. (Ed.), Geo-Marine Letters, Special Issue, Deep-Sea Turbidite Systems on French Margins 26 (6), 317-330.

CHAPITRE 2 : Tomographie par rayons X – méthodologie et étude de cas : le dépôt de tsunami de 1755 à Los Lances, Andalousie.

Une fois traité le jeu de données initiales (chapitre 1), la thèse s'est déroulée en deux phases successives : (1) mise en place d'un protocole de traitements des données brutes et création d'outils d'analyse dédiés à l'étude des dépôts ; (2) application de la méthodologie dans le cadre de trois études de cas destinées à valider la pertinence des outils et l'intérêt de la technique : a) tsunami de 1755 en Andalousie (chapitres 1 et 2) ; b) tsunami de 1996 dans le Lac Karymskoye au Kamchatka (chapitre 3) ; (c) tsunami Holocène sur la côte ouest de l'Australie (chapitre 4).

Le protocole complet de traitement des données tomographiques est conçu de manière à pouvoir être utilisé pour n'importe quel jeu de données obtenu par X-CT (Annexe 1). Les outils d'analyse créés consistent en une série de trois codes écrits sous Matlab, dédiés aux analyses granulométriques en deux et trois dimensions, à l'étude en trois dimensions de la fabrique sédimentaire d'un échantillon et au comptage de divers types de particules (bioclastes, minéraux lourd, etc.) et sont disponibles en annexe (Annexe 2). Leur utilisation est décrite en détail dans le protocole de traitement. Les aspects purement méthodologiques sont exposés dans l'article suivant, suivis des résultas des analyses structurales, granulométriques et texturales en deux et trois dimensions ainsi que de leurs implications en terme d'interprétation des dépôts. L'étude a été conduite sur les échantillons récupérés en 2010 en Andalousie sur le site de Los Lances (tsunami de 1755) et fait suite à la précédente publication (Cuven et al., Marine Geology, 2013), dont les résultats et les conclusions ont servi de base comparative. Cet article a été soumis à la revue Sedimentology en janvier 2016.

X-ray tomography of tsunami deposits: towards a new depositional model of tsunami deposits

Simon Falvard[1], Raphaël Paris[1]

(1) Laboratoire Magmas et Volcans, Université Blaise Pascal - CNRS - IRD, OPGC, 5 rue Kessler, 63038 Clermont Ferrand

Abstract

X-ray computed microtomography (X-CT) is used to obtain high resolution imagery of a historical tsunami deposit in Andalusia, Spain (1755 Lisbon tsunami). The first part of the paper focuses on the technical potential of the method for characterising grain size distribution, structures, components analysis and sedimentary fabric of unconsolidated sediments at resolutions down to particle scale. The results are compared to data obtained using other techniques such as laser diffraction, anisotropy of magnetic susceptibility (AMS) and X-ray microfluorescence for the same deposits in the previous studies (Cuven et al., 2013). Specific technical details such as sampling, scanning and image processing methods, and further improvements are addressed. The technique holds a great potential for small scale analysis of sedimentary structures, grain size distribution, composition and fabric of fine-grained deposits (medium sands and smaller particles, depending on the resolution of the scans). The use of X-CT provides new insights into the stratigraphy of the deposits and gives access to significantly more detailed view of key sedimentary features such as mudlines, rip-up clasts, crude laminations, convolutions, floating outsized clasts, and contacts between successive units. The analysis of the 1755 tsunami deposits using X-CT allows proposing new hypotheses for the sedimentary processes formingtsunami deposits. Deposition by settling is limited and the section analysed here is dominated by a high shear stress leading to the development of traction carpets, with laminated mudlines corresponding to the basal frictional region of these carpets. The transition from uprush to backwash is marked by vortex resembling Kelvin-Helmoltz instabilities.

Keywords: tsunami deposits; 1755 Lisbon tsunami; X-ray tomography; grain size; sedimentary fabrics; traction carpet

1. Introduction

Since the pioneering works conducted on the study of tsunami deposits in the mid- to late 1980s (e.g. Atwater, 1987; Bourgeois et al., 1988; Dawson et al., 1988), a lot of progress has been done and tsunamis scientists can now rely on a wide variety of methods and criteria to identify and characterize tsunamis deposits (Morton et al., 2007; Chagué-Goff et al., 2011; Goff et al., 2012; Ramírez-Herrera et al. 2012; Cuven et al. 2013). The available methods include many differentindicators, such as sedimentological analysis of grain size and grain sorting (Bondevik et al. 2005; Chagué-Goff et al. 2002; Cuven et al. 2013; Iliev et al. 2005; Jaffe and Gelfenbaum 2007; Minoura et al. 1996; Minoura et al. 1997; Moore et al. 2007; Morton et al. 2008; Naruse et al. 2012; Nishimura and Miyaji 1995; Pilarczyk et al. 2012; Szczuciński et al., 2012a), criteria related to sedimentary structures (e.g. Moore et al., 2007; Morton et al., 2008; Szczuciński et al. , 2012b; Naruse et al. , 2012; Bondevik et al. , 2005; Kilfeather et al., 2007), and sedimentary fabric (Wassmer et al., 2010; Goff et al., 2012; Cuven et al., 2013; Paris et al. 2014; Schneider et al. 2014). Wassmer et al. (2010) and later studies by Cuven et al. (2013) Paris et al. (2014) and Schneider et al. (2014) showed that the measure of anisotropy of magnetic susceptibility (AMS) could give access to useful information about the sedimentary fabric of the tsunami deposits. AMS measurements have been successfully used in several sedimentary environments (e.g. Liu et al., 2001; Park et al., 2000; Rees and Woodall, 1975; Tarling and Hrouda, 1993), but its application to tsunami deposits is recent and still remains rather rare as of now.

Chemical (e.g. Minoura and Nakaya, 1991; Cuven et al., 2013; Goff and Chagué-Goff, 1999; Ramírez-Herrera et al., 2012) and biological proxies such as tests of ostracodes (e.g. Bony et al., 2012; Naruse et al., 2012), molluscs (e.g. Minoura et al., 1996), diatoms (e.g. Dawson, 2007; Ramírez-Herrera et al., 2012; Szczuciński et al., 2012b), foraminifera (e.g. Dominey-Howes et al., 1999; Pilarczyk et al., 2012; Ramírez-Herrera et al., 2012; Bondevik et al., 2005) or nannoliths (e.g. Paris et al. 2010; Szczuciński, et al. 2012b) are used to gain information about the provenance of the sedimentary material displaced by the tsunami and/or to detect chemical markers of salt-water inundation. Mineralogical analysis, especially of heavy minerals (e.g. Switzer et al., 2005; Babu et al., 2007; Jagodziński et al., 2009; 2012),

which includes pyroxenes, amphiboles, zircon, tourmaline, garnet, etc. are also used to trace the source of the sediments (e.g. Jagodziński et al. , 2009; 2012) or to constrain their transport conditions, especially the hydrodynamic characteristics of the flow (Morton et al., 2008; Nichol et al., 2007).

However, the identification and the interpretation of tsunami deposits remain challenging for several reasons. Despite the diversity of available methods, tsunami deposits are not always well-preserved, and bioturbation and erosion can rapidly affect the structure and initial thickness of the deposits (Szczuciński et al. 2007; Paris et al. 2009; Szczuciński 2012c; Cuven et al. 2013). Apart from problems related to preservation, it appears that the majority of the sampling methods does not allow a continuous sampling of the deposits and depends on the interpretation made on the field by the operator (e.g. taking one individual sample for each identified subunit or selecting a step size in terms of depth) (Cuven et al., 2013). This "discretization" of the deposits introduces a bias which in turn will influence the way analyses will be conducted in the lab. Furthermore, most lab analyses are based on destructive methods and/or on bulk samples.

While the above mentioned methods may give good results down to the centimetre scale, it appears that the current set of available proxies does not include methods at the micro-scale with the aim of identifying microstructures, microfabrics and non-destructive grain size analysis. Indeed, Kilfeather et al. (2007) showed that tsunami deposits can have a complex micromorphology, which holds important information about depositional processes. In this paper, the authors test the applicability and robustness of X-ray tomography for better characterising tsunami deposits structures, composition and textures in a continuous way throughout the deposit and at small scale in order to better understand tsunami flow dynamics (e.g. waves number, current direction, flow conditions). The method is applied to sandy deposits formed by the 1755 Lisbon tsunami in Andalusia (southern coast of Spain, Fig. 1).

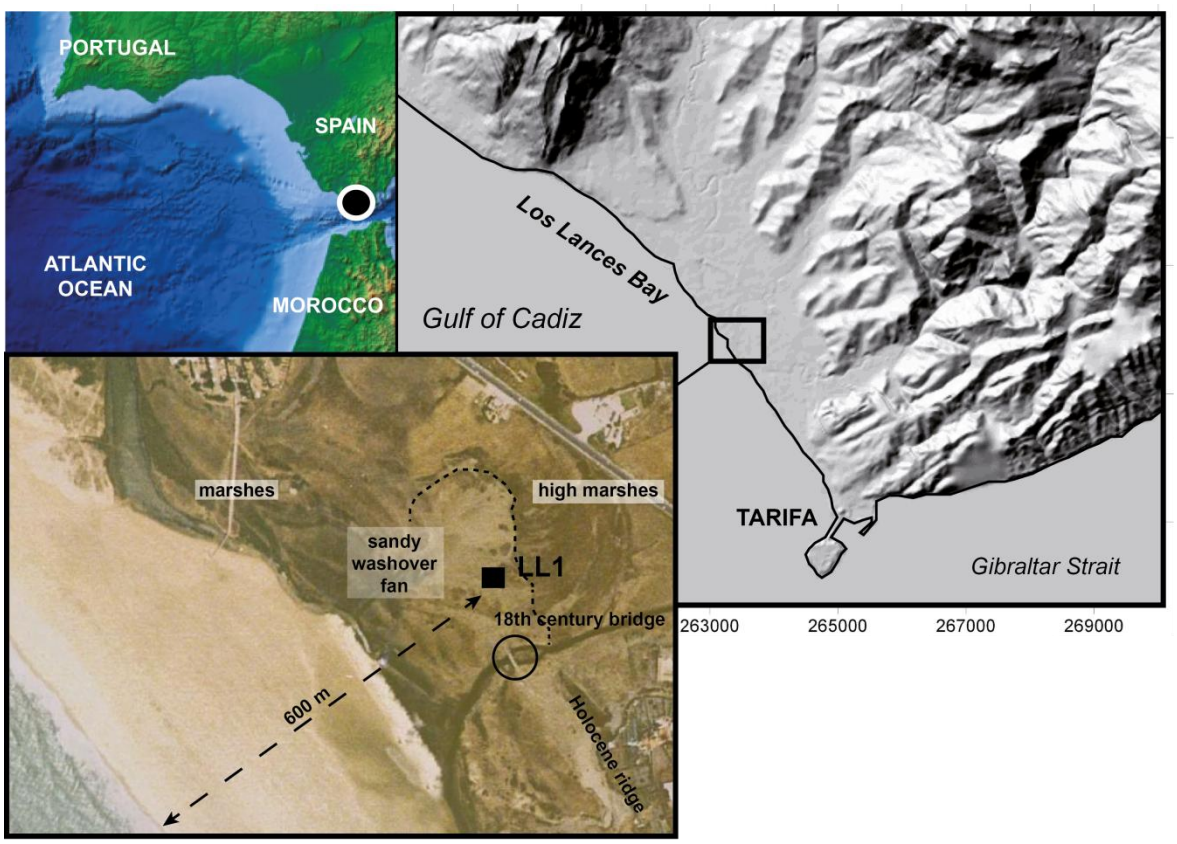

Fig. 1: Location map and satellite view of the study area.
The tsunami samples were retrieved from the 1755 sandy washover fan in Los Lances Bay.
The bridge was partially destroyed by the tsunami (after Cuven et al., 2013).

2. X-ray computed tomography

X-ray computed tomography (X-CT, for X-ray Computed Tomography) is an imaging method that allows the representation of an object (sample) based on its ability to absorb X rays. This technique allows obtaining detailed views of the interior of a sample in three dimensions. The complete description of the X-CT working principles is beyond the scope of this paper, but can be found in the literature (e.g. Ketcham and Carlson, 2001). Several different generations of equipment exist, with different X-ray production and beam focusing systems, but the general working principle remains the same: a beam is generated by an X-ray source that passes through the sample and finally hits an X-ray sensitive surface, typically a CCD camera sensor. This process results in the acquisition of a view, similar to standard radiography. The sample is then rotated at a given angle and scanned again to obtain another view and the process is repeated, until the whole volume has been scanned. The volume is then reconstructed from all the views (Fig 2b), and usually conveniently rendered as a

succession of “slices”, which are 2D images of the sample that correspond to what would be seen if the sample were cut along the plane of the scan (Fig 2a).

This technique already found wide use in the medical domain where X-ray tomography is routinely conducted in hospitals and in the industry where it allows for instance to check mechanical parts for inner defects (cracks, bubbles, unwanted heterogeneities, etc.). It has also been widely used by geologists to study the inner structure, permeability and composition of natural and experimental, consolidated or unconsolidated rock samples by a non-destructive and reproducible approach (e.g. Denison and Carlson 1997; Mees et al. 2003; Ketcham et al. 2005b; Kuper et al. 2007; Zabler et al. 2008; Giachetti et al. 2011). X-ray radiography has been used in a few cases for structural analyses of tsunami deposits (e.g. Bondevik et al. 2005; Choowong et al. 2008). Choowong et al. (2008) showed that X-ray absorption data (X-ray radiography) gives useful insights into sedimentary structures and inferred supercritical flow characteristics from them. The characteristics and advantages of X-CT seem to make it a promising method for a better understanding of tsunami deposits (May et al., 2016) since (1) the analysis is non-destructive and allows the conservation of the samples, (2) the resolution of the images is limited only by the abilities of the equipment, (3) X-CT provides three dimensional views of structures, textures and every physical feature of the samples (grains, fossils, wood, bones, ceramics, etc.).

A lot of different scanning equipments exist nowadays, from small desk-sized tomographs designed for relatively low resolution routine scanning (e.g. for quick control of mechanical parts with resolutions in the order of a few tens of micrometres) to tomography dedicated synchrotron beamlines intended for very high resolution and special scanning conditions where resolution, when scanning operations are conducted under optimal conditions can go down to a few tens of nanometres. The study of microstructures in a sandy to clayey deposit imposes strong constraints and several features must get special attention: (1) since the sediment is mostly fine to very fine grained, the maximum achievable resolution is a major factor and usually, the higher the resolution, the better. The resolution offered by desk sized apparatus is often not high enough and multi-resolution imaging may be useful to be able to easily scout in the whole sample without overwhelming the computer and then access fine structures and particles on a specific area of interest. Multi-scale imaging also allows addressing the problem of poorly sorted sediment which can contain both very fine and rather coarse particles (especially in the case of matrix supported sediment). (2) X-CT imagery depends on the absorption of X-rays by the sample. This absorption is directly linked to the density of the grains and thus to their mineralogical composition (e.g. Ketcham 2005b). This

means that different materials with similar densities (e.g. quartz and feldspars) will have similar shades of grey on the final images, and that very dense (e.g. heavy minerals such as magnetite or titanomagnetite) and very light material (e.g. air or water) will respectively show very clear and very dark shades of grey. Since the composition of tsunami deposits depends on the sediments available and mobilised by the tsunami, they often contain heterogeneous phases, meaning that the scanning equipment must be able to correctly render such differences with as few loss of information as possible.

3. Methods

3.1. Sampling and X-ray scanning

X-CT was performed on samples of the 1755 Lisbon tsunami deposits at Los Lances Bay, southern Spain (Fig. 1). In this area, four washover fans breaching all Holocene ridges, including the Late Medieval ridge, were interpreted as evidence of the 1755 tsunami (Gracia et al., 2006). Reicherter et al. (2010) found tsunami deposits up to 700 m inland (~4 m a.s.l.). According to historical sources (Campos, 1991), the 1755 tsunami waves were 11 m high in Los Lances and the inundation distance reached more than 1.5 km. Cuven et al. (2013) used a combination of sedimentological (grain size, sorting, AMS), micromorphological (X-ray radiography, thin sections) and geochemical analysis (X-ray microfluorescence, ICP-AES) to characterise in detail the different phases of tsunami deposition and flow dynamics.

Sediments have to be sampled in a way that allows at the same time to preserve them and to obtain a sample size which can fit in the selected X-ray device (tomograph). Better results are obtained with cylindrical samples. Even if X-CT can theoretically be conducted on any shape of sample, non-tubular samples scans may be affected by strong artefacts during the reconstruction process (the authors observed a noticeable amount of distortion of the particles after scanning cubic samples). Additionally, while these tubes have to be rigid enough to be pressed into fine grained sediment (medium sand and finer), they should have the thinnest walls possible to facilitate penetration and limit side effects, and they should be as transparent as possible to X-ray light, which excludes the use of tubes made from dense material (e.g. any kind of metal). In addition, the smaller the diameter of the sample, the better the achievable resolution of the scan, but the spatial representativity of the sample has to be taken into account too. These factors led the author to choose carbon fibre tubes with a diameter of

20mm and 1mm thick walls. The 20mm diameter would allow obtaining scans with resolutions of a few micrometres and sampling enough volume to see structures in 3 dimensions, and the 1mm walls thickness was necessary to ensure a sufficient rigidity for tube lengths of up to 25cm, the carbon fibres being easily penetrated even by low energy X-rays. Two carbon fibre tubes were retrieved from the tsunami deposit for X-CT, along with bulk samples for grain size analysis, plastic boxes for thin sections confection and low resolution (100µm) tomography of structures, and two 50cm long half cores (LL1 and a replica, LL1bis). Both tubes cover a span of 34 centimetres, with the first tube covering depths from 29 to 46cm and the second depths from 45 to 63cm. Tube sampling at lower depth was prevented by the water saturation of the sediments which made coring impossible due to an extremely low cohesion. The Los Lances site was selected due to the texture of the tsunami deposits (sandy to clayey units), which were easier to sample correctly for X-CT. Coarser grained, indurated or pure clay deposits would have been more difficult to sample using small diameter rigid tubes because of very low cohesion of the particles or too strong side effects due to very low mechanical strength. The tubes were scanned at the tomography-dedicated beamline ID19 of the ERSF synchrotron (Grenoble, France), with a resolution of 14.652µm/voxel.

3.2. Image processing

Depending on the composition and size of the sample, and the scanning parameters (devices used, resolution, scanning time, beam energy, etc.), X-ray scans have to be processed in order to extract a maximum of data. Some processing steps are mostly used to obtain more user friendly images (e.g. contrast adjustments), which may not be mandatory for the extraction of data but can greatly improve the way the images look to the human eye, helping the operator to discriminate phases (e.g. particles, air, etc.) and structures (Fig. 3). Separation of phases is of particular importance, and noise must be carefully treated prior to further processing. 3D processing allows ensuring that the whole tomogram will be processed as a whole instead of in a slide by slide manner, which would sometimes result in the apparition of artifacts such as artificial “schistosity” introduced by the independent processing of each slide.

3.2.1. Particle-scale analysis in 2D

While having access to the 3D structure of the sample is the main advantage of X-CT, it has a cost in terms of image size (a single tomogram can take up to several gigabytes in size) and the quantity of information contained in the tomogram can be huge (a 2x10cm cylindrical sample of sand can typically contain several hundreds of thousands of particles or more). Separating grains in 3D allows obtaining several useful characteristics (see *4.3. Particles analysis (3D)*), but it is time-consuming and some very fine particles can sometimes not be properly separated from each other or from a matrix with a similar density. Vertical and/or horizontal 2D slices of the tsunami section were obtained using ImageJ, thus allowing analyses in two dimensions. (Fig. 4a). Different vertical sections of the core were selected based on criteria such as image quality, significance, preservation of the structures etc. When resolution of the scan was sufficient, particles were separated from each other and analysed individually using ImageJ's Region of Interest (ROI) manager. Each particle is represented by its assumed intermediate diameter (B-axis) in the form of a straight line drawn across the particle, which is then converted into a ROI. The length of every ROI is measured, together with its coordinates along the core, and represents the assumed intermediate diameter of the particle, in a way resembling what a laser granulometer would do (except that a laser granulometer would assume a spherical grain, whatever its real shape is; Merkus, 2009). The data measured with ImageJ's ROIs are then analysed using two separate Matlab codes written by the authors (see supplementary material):

The first one (*grainmap*) is used to extract a map representing the size of the particles along the sample (Fig. 4b). Grain size is drawn on a map representing the vertical sample slice. This allows a quick and convenient visualization of grain size distribution and structures along the deposit.

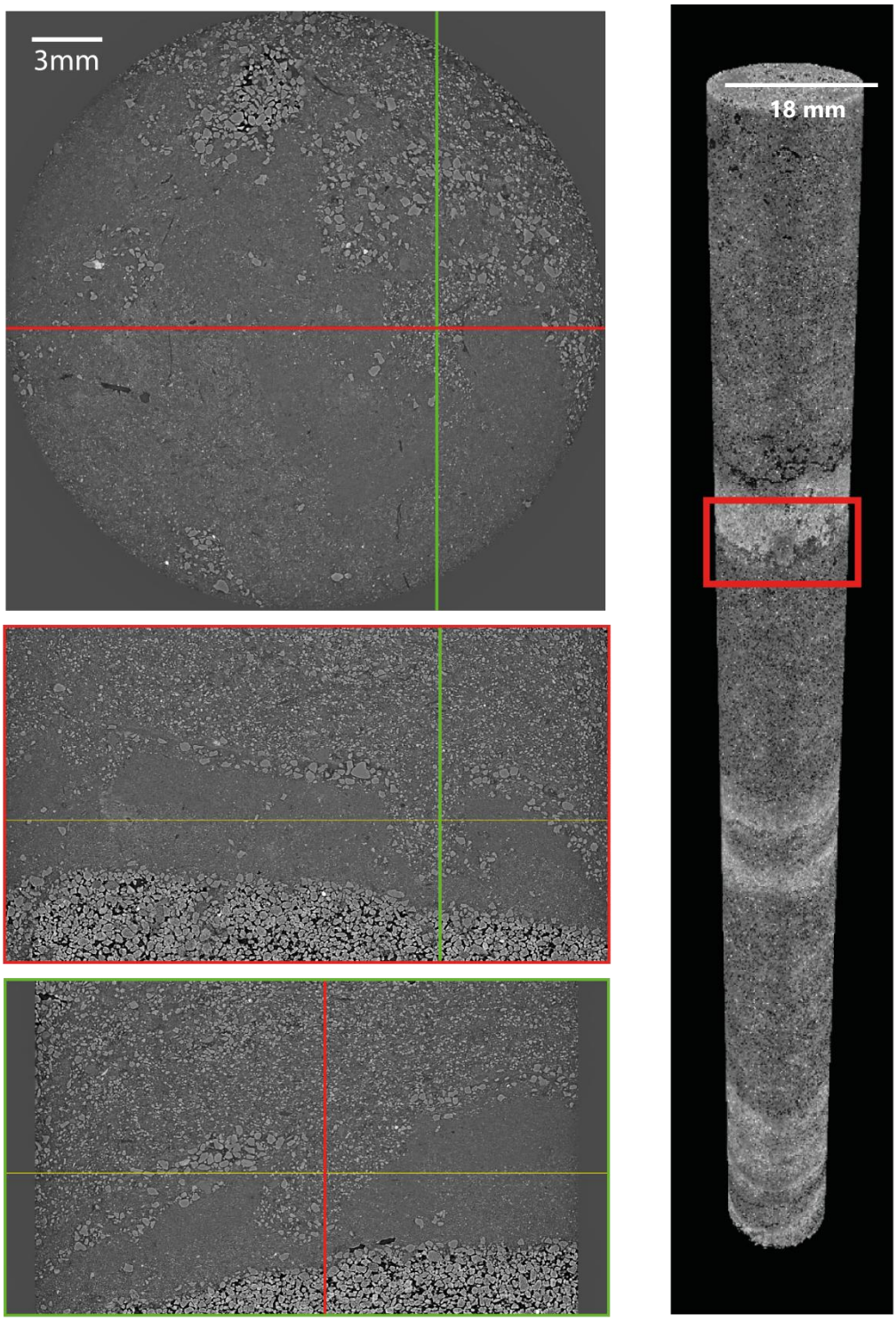

Fig. 2: a – 2D transversal views (slices) of a cylindrical sample of the 1755 tsunami deposit. The sample consists of a 2cm wide carbon fibre tube carefully pressed into the deposit and hermetically sealed to avoid losing water. The grey corners correspond to areas outside the sample (air) and have been given a known and uniform grey value for easier handling. The resolution is 14.652 µm per voxel. The access to the third dimension greatly helps the visualization and understanding of such fine-scale features. The slices are made along an horizontal plan (upper slice), a vertical, N145 azimuth plan (intermediate slice, approximate location represented on figure 2b) and a vertical, N55 azimuth plan (lower slice) b - Three dimensional representation of the same sample, obtained by stacking 10958 slices.

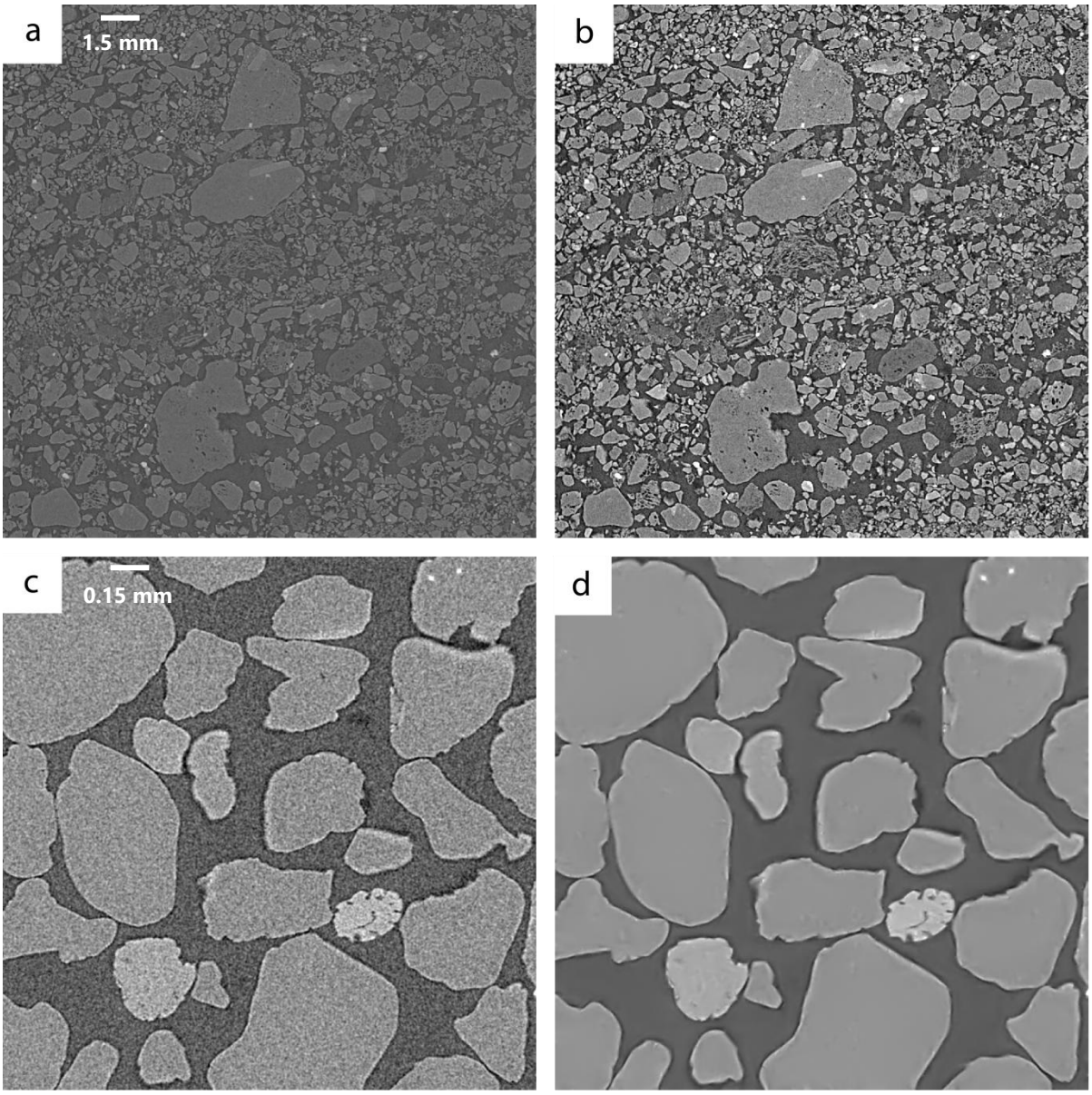

Fig. 3: a - Raw tomographic reconstruction. b - Same reconstruction after contrast improvement using curves in ImageJ. c - In some cases, contrast enhancement of the images can lead to an excessive amount of noise which interferes with grey-value based separation methods. d - Same image after noise treatment made by application of a median filter in ImageJ. Several noise treatment methods are available depending on the context and the amount of noise to be subtracted. A good balance between noise reduction and details conservation must be found and intermediate solution are usually more effective than a heavy noise reduction which can be counterproductive.

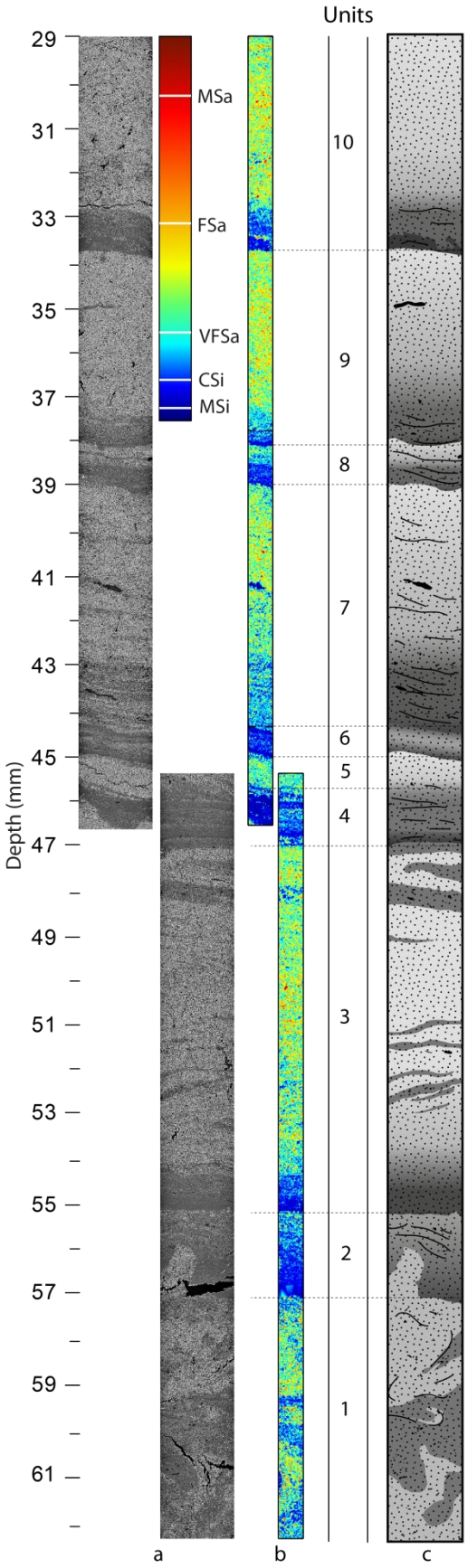

Fig. 4: a - Vertical slices of the two tubes covering the entire tsunami sequence. The contrast has been enhanced for easier reading of the stratigraphy. b - Grain size map of the 5mm wide central strip of the slices, showing very fine grained (mudlines) and coarser grained (fine to medium sand) sublayers, allowing a continuous and precise overview of the grain size distribution along the deposit. The scale is defined according to Wensworth's classification. MSa: medium sand; FSa: fine sand; VFSa: very fine sand; CSi: coarse silt; MSi: medium silt. The finer end of the scale here is limited to medium silts (16 µm), which roughly correspond to the resolution of the scans (14.652 µm). c – Log stratigraphy inferred from the X-CT scans.

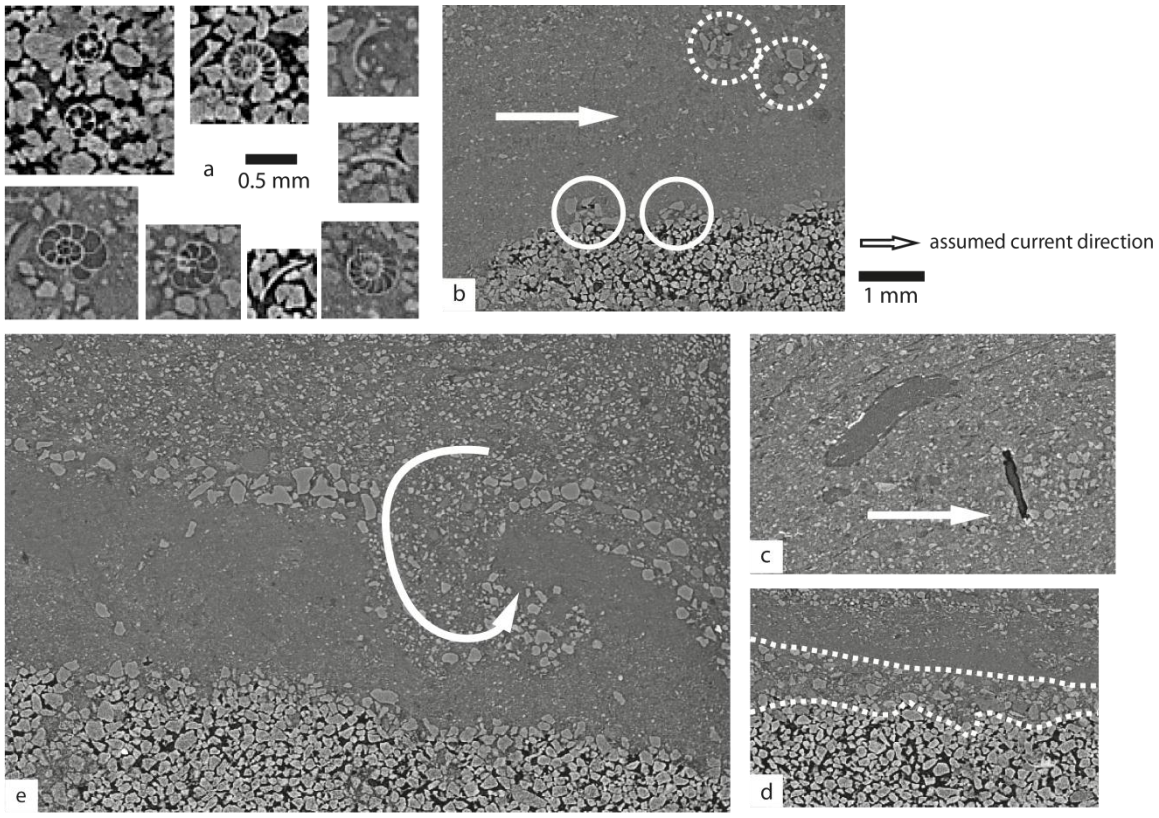

Fig. 5: a - Bioclasts (foraminifer tests) found into the X-CT data. While bioclasts complex shapes usually make them very difficult to separate, they can easily be identified, located and counted on X-CT images. b - Erosive contact with scouring of the underlying particles (full circles) and particles scoured away and imbedded into the over lying unit (dashed circles). c - Tapered rip-up clast in unit 1, revealing important shear stress during the deposition process. d - Between dashed lines: impregnation of the pores of unit 5 by the clay of unit 6. Note the sharp erosive contact between both units. e - Vortex and line of floating outsized clasts at the base of unit 10 (backwash unit).

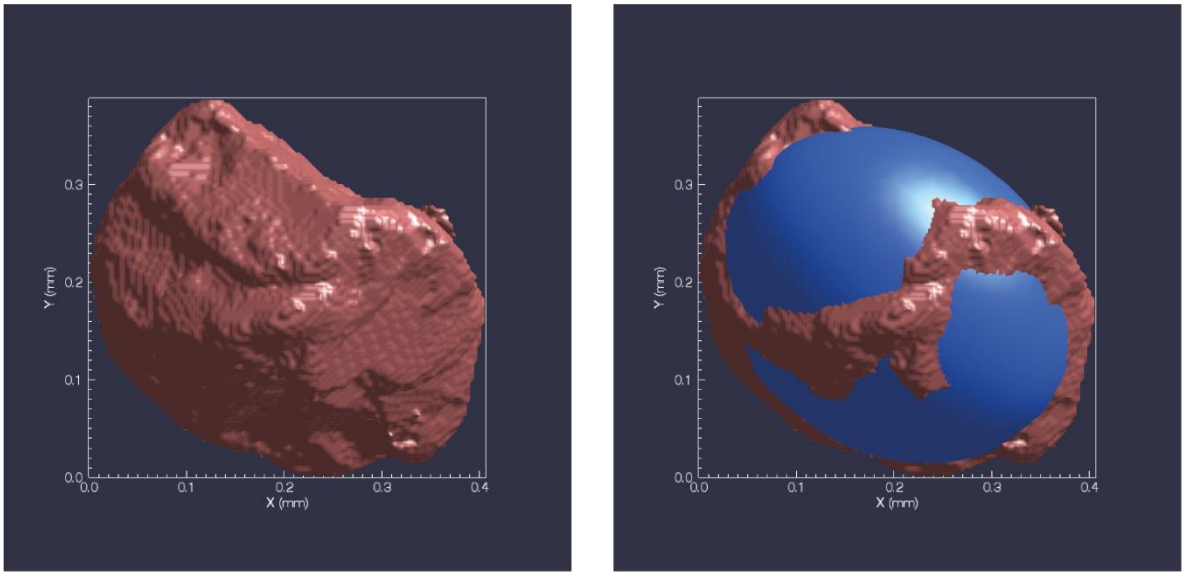

Fig. 6: a - 3D representation of a single grain separated using Blob3D software. b - Same grain represented with its best fit ellipsoid, used to perform the measurements.

The second one (*grainstat*) calculates several parameters widely used in sedimentology: mean grain size, minimum and maximum grain size, number of particles,

standard deviation, kurtosis, skewness, sorting coefficient, D25 and D75 (any percentile can be easily added if needed) are automatically calculated. The operator has to enter a sub sampling step and the code will subsample the dataset and calculate every parameter for each subsample. Results are rendered in the form of text files or graphs representing the calculated values against depth.

These two codes are meant to allow the user to have a general view of the grain size distribution along the core as a whole, and to choose a proper subsampling step or zone of interest instead of having to choose how to subsample directly on the field at the risk of missing small structures or sublayers of interest, or mix unit that might look similar on the field. They are also meant to allow to accurately link grain size distribution with other data such as components analysis (e.g. minerals, bioclasts), fabrics (e.g. anisotropy of magnetic susceptibility), chemistry (e.g. X-ray fluorescence), and structures (discontinuities, erosive contacts, bedforms, bioturbation).

3.2.2. Components analysis

Other proxies accessible with X-CT are related to the composition of the particles in the deposit. The 1755 tsunami deposit studied here is mostly composed of subangular to subrounded quartz grains, together with subrounded orthopyroxenes, numerous marine bioclasts (fragments of gastropod and bivalve shells, benthic foraminifers, diatoms, sponge spicules, rhodophyta calcareous algae, echinoderms), charred woods, and rare heavy minerals (Cuven et al., 2013). Bioclasts were identified by their shape (Fig. 5a) and counted along vertical slices, using the *bioclast* Matlab code (see supplementary material). *Bioclast* works the same way as the *grainstat* code does: bioclasts positions throughout the core are manually recorded using ImageJ's ROI manager, then sorted and plotted by the code, thus representing the quantity of bioclasts along the tsunami section.(In order to ensure a sufficient representativity and unlike other particles, bioclasts should be identified throughout the whole core instead of a single vertical slice, but since separating them from the other particles and the matrix is usually difficult and would be time consuming, only their vertical position is retained and exploited. The *bioclast* code is not meant to analyse bioclasts shapes and orientations.

3.2.3. Particle-scale analysis in 3D

For analysing particles in 3D, the authors used Blob3D (Ketcham 2005b), which is a free to use software dedicated to the study of particles in 3 dimensions. It includes image processing tools that work in 3D and tools dedicated to the segmentation, separation and quantitative analysis of particles (Fig. 6). Depending on the complexity of the sample, particles can be separated fully automatically (if the phase of interest is sparse enough, like for instance dense minerals in loose clay or organic matter). However in the case of grain-supported sediment or even sometimes of densely packed matrix-supported sediment, manual separation of grains may be mandatory. While this may take several hours to several days depending on the size of the sample, the gain in terms of precision usually makes it worth it, if not essential to get usable data. The resolution (14.6 µm per voxel) was sufficient to separate grains, which gave access to the third dimension of space and thus information on the orientations of the particles both in terms of direction (azimuth) and dip. Due to the resolution limit and signal to noise ratio, the fine particles (typically particles finer than very fine sands) were more difficult and sometimes impossible to separate, which led to a lower representation of particles in mudlines and silty pockets. On the other hand, the separation was made more difficult in the section where the sediment had an air matrix (grain supported sands and silts) due to the more important proportion of touching particles. Once particles were separated, several parameters such as particle volume, bounding ellipsoid dimensions (min and max axis), orientation, and grey values (useful to identify different phases) were extracted.

Blob3D measures orientations as the directions of the long and minimum axis of the particle's best-fit ellipsoid and gives them in the form of three direction cosines which can easily be converted into orientations in degrees. Softwares such as Stereo32 (Röller & Trepmann, Ruhr Universität Bochum) or Stereonet (Allmendinger, http://www.geo.cornell.edu/geology/faculty/RWA/programs/stereonet.html) were used to render convenient graphical representations of particles orientations and calculating the eigenvalues (the normalised vector magnitudes) S_1 (longest axis), S_2 (intermediate axis) and S_3 (shortest axis) of the fabric ellipsoid. This ellipsoid thus corresponds to the preferred orientations of the particles extracted from the sample.

Equilateral ternary diagrams (Benn, 1994) were used to describe sedimentary fabrics by calculating and representing a sample's fabric isotropy ($I = S_3/S_1$) and elongation ($E = 1 –$

(S_2/S_1)) (Fig. 7). The three poles of the diagram correspond to an isotropic fabric ($S_1 = S_2 = S_3$; I = 1 and E = 0), a planar girdle shaped fabric ($S_1 = S_2 > S_3$; I = E = 0, which corresponds to an oblate ellipsoid) and a cluster shaped fabric ($S_1 > S_2 > S_3$; I = 0, E = 1, which corresponds to a prolate ellipsoid). Benn (1994) demonstrated that the use of such equilateral ternary diagrams is perfectly suited to describe sedimentary fabrics.

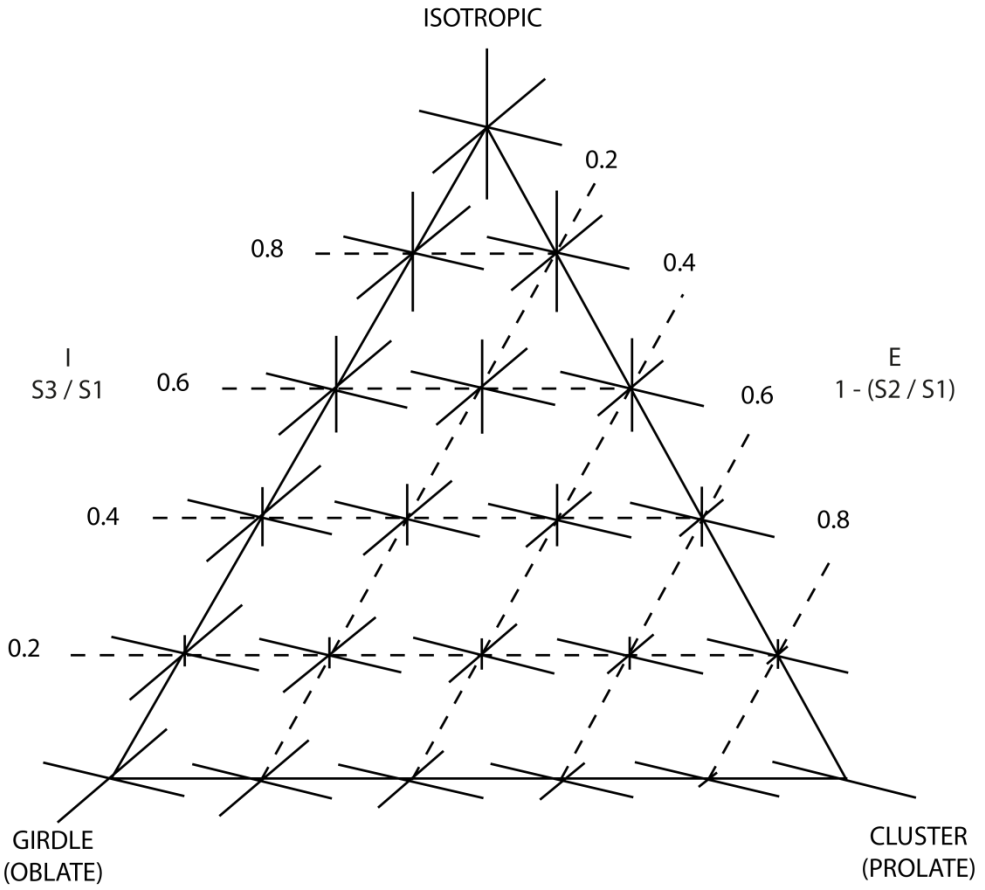

Fig. 7: Benn's triangular diagram, used to represent the fabric shape of the ellipsoid corresponding to the preferential orientations of the particles of a sample. (After Benn, 1994).

4. Results

4.1. Log stratigraphy and grain size distribution (2D)

The grain size mapping obtained using the *grainmap* code allows a quick and straightforward reading of the global grain size distribution (GSD) of the deposit (Fig. 4b), and the structures identified can easily and precisely be linked to GSD trends given by the *grainstat* code. The log stratigraphy is inferred from vertical reslices of the tomographic data of the two tubes, sampled a few tens of centimetres away from LL1bis half core (Cuven et al., 2013). The tsunami deposit as sampled in the carbon fibre tubes is subdivided from base to

top in 10 different units (Fig. 4c), which are summarized in table 1. According to our quantitative analysis of X-CT data, the tsunami deposit is characterised by a poor sorting, fine skewed and leptokurtic grain size distributions, which is consistent with the results obtained by Cuven et al. (2013) with conventional techniques (laser diffraction on bulk samples).

Nevertheless, the data show variations of the values (Fig. 8). It is especially clear that the fine sections of the deposit (i.e. the clayey bases of units 5, 6, 7, 8, 9 and 10) are better sorted and present higher skewness and kurtosis values, which is consistent with a higher concentration of fine particles in the deposit. Higher mean grain size usually translates into lower sorting, skewness and kurtosis throughout the deposit. The finest grained subunits (e.g. the bases of units 2 and 3) also have low sorting values due to the resolution limit of the scans which made the separation of very fine particles difficult. The lower representation of the finest section of these subunits shows in the “number of grains” plot of Fig. 8.

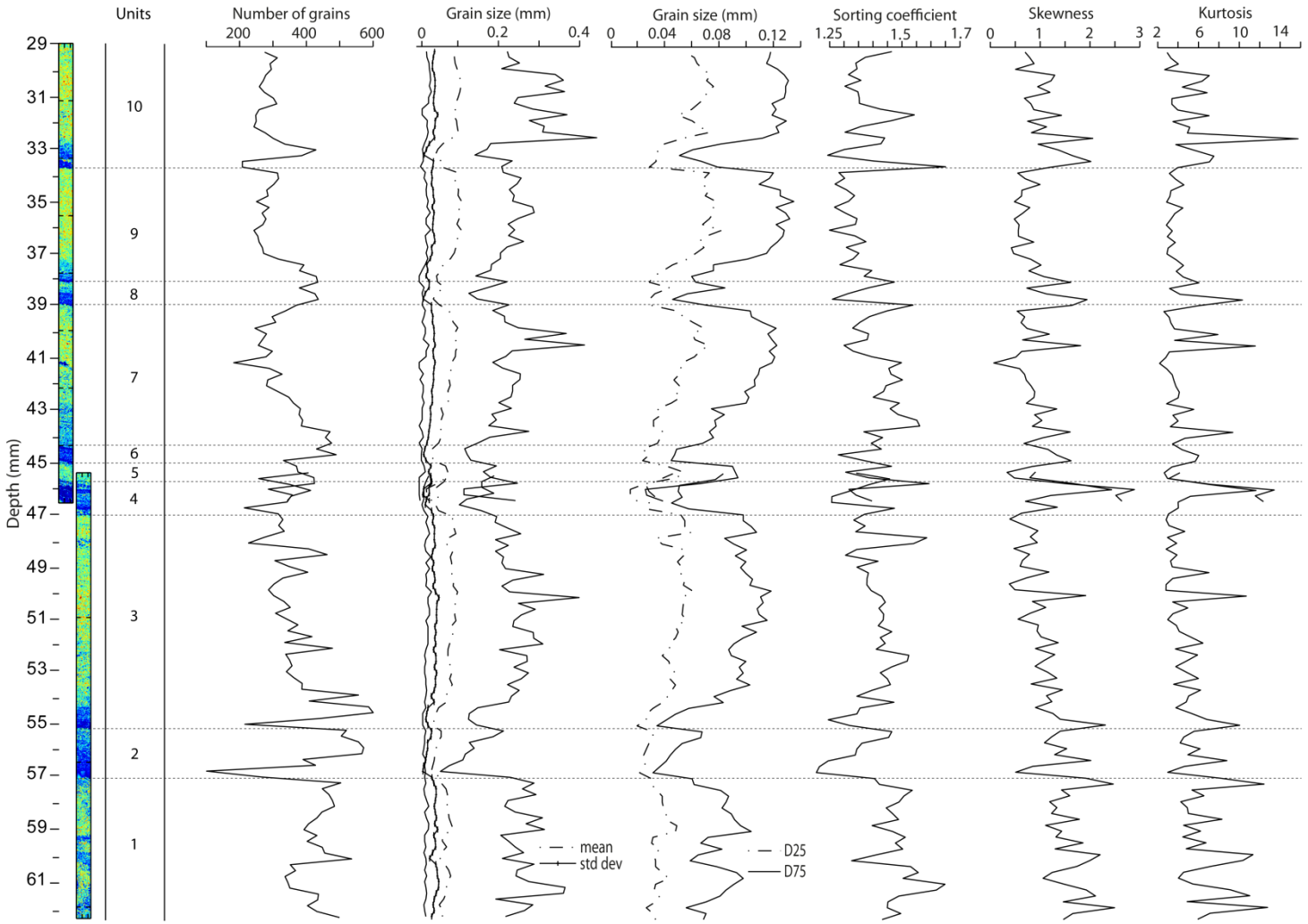

Fig. 8: Results of the calculations made by using the grainmap and grainstat codes. The grain size map has been calculated from the measurement of the B axis of more than 29000 particles. Grain size distribution statistics have been calculated using a 2 mm interval, which allows visualizing small structures while retaining enough particles in each step, ensuring the representativity of the measurements.

Unit	Depth (cm)	Description	Contact with underlying unit	Grading	Intraclasts	Bioclasts	Sorting Skewness Kurtosis	Units from Cuven et al. (2013)
10	33.6-29	Clayey mudline with floating sand grains on top (33.5-33.2), crudely laminated silty clay (33.2-32.5) to very fine sand (32.5-29)	Sharp, erosive base, with infiltration of clay in the underlying unit 9	Inverse grading (33.2-32.5) and no grading (32.5-29)	Numerous intraclasts between 33.2 and 33.5 cm	No bioclasts (33.5-33.2), and small foraminifers and diatoms (33.2-29)	Poorly sorted, strongly fine-skewed, strongly leptokurtik	8 (32.5-29) 7 (33-32.5)
9	38.1-33.6	Laminated silty clay (basal mudline) and massive very fine sand (37-33.5)	Wavy erosive base, scour-and-fill figures	Inverse grading (37.8-36), and no grading (36-33.5)	-	Rare foraminifers		6 (37-33)
8	39-38.1	Crudely laminated silty clay (mudline) turning to very fine sand upward	Wavy, erosive base	Inverse grading	Rare rip-up clasts of soil	Marine bioclasts (foraminifers, shell fragments). Higher bioclasts concentrations in clayey silts levels and pockets.		5 (39.5-37)
7	44.3-39	Laminated clayey sand (44.2-42.5) and laminated very fine sand (42.5-38.9)	Wavy base with sand grains partly embedded in the underlying unit 6	Inverse grading	Numerous rip-up clasts of soil (large and tapered)			4 (44.5-39.5)
6	45-44.3	Banded mudline (clayey silt and very fine sand)	Wavy, erosive base, clay infiltration in underlying unit 5	No grading	Few rip-up clasts of soil (in the laminations)			
5	45.7-45	Unstructured very fine sand	Sharp base	No grading	Few rip-up clasts of soil			3 (48-44.5)
4	47-45.7	Laminated silty clay (mudline) with lines of very fine sand	Sharp, erosive base, clay infiltration in underlying unit 3	No grading, except locally (inverse grading at 46.8-46.6)	-			2 (49-48)
3	55.2-47	Laminated clayey silt (basal mudline) to very fine sand with crude laminations	Sharp, erosive base	No grading (55-54), inverse grading (54-50), normal grading (50-47)	Rip-up clasts of soil (in the laminations)			1 (54-49)
2	57.1-55	Clayey silt. Complex laminations in the upper part	Sharp, erosive base	No grading	Numerous rip-ups clasts of soil			
1	62.5-57.1	Clay and very fine sand (diamicton) with convolutions	(reworked)	No grading	Numerous rip-up clasts of clayey soil			

Table 1: Description of the stratigraphic units.

The stratigraphy of the deposit is summarized in table 1.

1. Unit 1 (minimum 62.5 to 57.1cm) is a poorly sorted diamicton deposit made of clay and very fine sand. Convolution of clay “rich” and clay “poor” pockets can be seen on the grain size map (Fig. 4a). No grain size grading could be detected. Marine bioclasts (mostly foraminifers) are abundant, along with tapered rip-up clasts (Fig. 5c) of low density material (pre-tsunami clayey soil).
2. Unit 2 (57.1 to 55cm) is a poorly sorted clayey silt, with a clayey base, and rip-up clasts of soil. The erosive contact with unit 1 appears sharp despite the presence of desiccation cracks, and the presence of local convolutions reworking fine sand from unit 1. The upper part of unit 2 displays complex crude laminations.
3. Unit 3 (55.2 to 47 cm) is a poorly sorted clayey silt (basal mud layer) to very fine sand with crude oblique laminations (especially between 54 and 51cm). The base is erosional, with grains from unit 2 being scoured away (Fig. 4b). The very fine sand is inversely graded from 54 to 50 cm, and then normally graded from 50 to 47 cm (Fig. 8). A clay-rich horizon of fine sand lies between 48 and 47.7 cm. Foraminifers are found throughout the whole unit, especially in the finest fractions. The laminations are dipping seaward and present a crude alternation of sub-horizontal (angles between 0 and 3°) and tilted (angles between 13 and 20°) laminae.
4. Unit 4 (47 to 45.7cm) is a laminated silty clay (mudline) with lines of very fine to fine sand. Foraminifers are still abundant. An inversely graded subunit can be distinguished in the intermediate part of the unit (46.7-46.2 cm).
5. Unit 5 (45.7 to 45cm) is thin unit of massive very fine sand. Foraminifera and fragments of shells can be found especially near or inside small diffuse clayey pockets.
6. Unit 6 (45 to 44.3cm) is a mudline characterised by its banded structure. Laminations are not well defined, thus producing a complex mixing of alternating clayey silt and very fine sand. Base of unit 6 is fills the pores of unit 5 over a thickness of around 0.5mm (Fig. 5d). A few bioclasts could be detected.
7. Unit 7 (44.3 to 39cm) is generally poorly sorted, inversely graded and laminated, but two subunits can be distinguished: laminated clayey sand from 44 to 42.5 cm and crudely laminated very fine sand from 42.5 to 38.8 cm. The base of unit 7 is wavy and erosive, and contains tapered clayey intraclasts and numerous foraminifers. Laminations have angles between 14 and 22 degrees dipping landward in the lower clayey sand, turning to very crude horizontal laminations in the upper very fine sand.

8. Unit 8 (39 to 38.1cm) consists of a lower laminated silty clay turning to very fine sand (inverse grading). The upper sandy part seems truncated by overlying unit 9.

9. Unit 9 (38.1 to 33.6cm) presents an erosional contact with unit 8 (scour-and-fill structures). Its base consists of a mud layer. The lower silty clay (38-37.2 cm) has numerous tapered intraclasts of clay and progressively turns to a massive deposit of very fine sand (37-33.5 cm), thus defining a trend of inverse grading from 37.8 to 36 cm. It is worth noting that the abundance of marine bioclasts decreases from units 7 to 9 (rare foraminifers being found at depth 34-35 cm).

10. Unit 10 (33.6 to 29 cm) starts with a clayey mudline capped with floating sand grains, followed crudely laminated silty clay (33.2-32.5 cm) and very fine sand (32.5-29 cm). Base is sharp (except small infiltrations of clay and local scour-and fill structures in unit 9) and erosive. The boundary between the basal clay and the laminated silty clay shows a 2.5 mm large vortex affecting the line of floating sand grains. Swirls of sand-to-silt grains in a clayey matrix are wrapped around a roughly North-South axis (Fig. 4e). The upper very fine sand (32.5-29 cm) is crudely laminated at its base (poorly-defined oblique laminations). Bioclasts (foraminifera and diatoms) are quasi absent and particularly small.

4.2. Components analysis (bioclasts)

Marine bioclasts such as foraminifers, shell fragments (gastropods and bivalves), sponge spicules and echinoderms are clearly identified on the X-ray imagery. Cuven et al. (2013) also found diatoms, which could not be detected on the X-CT images due to limited resolution. The distribution of bioclasts along the core, calculated using the *bioclast* code, is represented on Fig. 9.

Moderate bioclasts concentrations are found in units 1 and 2. Bioclasts are present in greater quantities in clayey pockets of unit 1 and the silt-rich part of unit 2. The intermediate part of unit 3 (silty sand) is particularly rich in bioclasts, while the lower (clayey silt) and upper sections (sand) contain less. Clayey and silty pockets in the sand contain numerous bioclasts. All the units up to unit 8 show the same kind of bioclasts distribution: few to very few bioclasts in clay layers (clayey laminae in unit 4, bottom and top of unit 6) and sand sections: upper parts of units 4 and 7). The abundance increases in silty sections (intermediate

part of unit 3, unit 5 and lower part of unit 7) and clayey pockets found throughtout the sand sections, where some of the highest bioclasts concentrations are found (upper parts of units 3 and 7). On the opposite, unit 8 contains a few foraminifera in its silty clay base but almost none in its upper silty sand part. Units 9 and 10 appear to be practically without carbonated bioclasts, with 2 found in unit 9 and 3 in unit 10.

4.3. Sedimentary fabric analysis (3D)

The separation of particles in three dimensions is used for textural analysis. Sedimentary fabric data from the tomographic images sets was acquired in a way that allows direct comparison with the fabric data acquired using anisotropy of magnetic susceptibility by Cuven et al. (2013). X-CT data is subsampled in zones corresponding to AMS cubes retrieved on the half-cores (similar depth, shape and volume). At least 1000 particles were separated in each subsample.

All subsamples except one (54.9 to 57.1cm: unit 2) have isotropy values higher than 0.5 (Fig.10a), corresponding to rather isotropic fabric ellipsoids. Subsamples of units 8 and 9 have the most isotropic shapes (isotropy values between 0.85 and 0.9). All ellipsoids have low to very low values of elongation (oblate shapes) with $E<0.20$, except subsample 9 (59.8 to 62.0cm, unit 1, $E=0.21$). The S1 axes of the ellipsoids are often oriented along NW-SE to E-W directions (Fig.10b), roughly parallel to the shoreline (which is oriented NNW-SSE at Los Lances). Two ellipsoids (subsamples of units 4-5 and 7) display a NE-SW preferential orientation associated with very flat (oblate) ellipsoids. Unit 1 has a NE-SW orientation associated with the most elongated (prolate) ellipsoid which is associated to complex features of convolution.

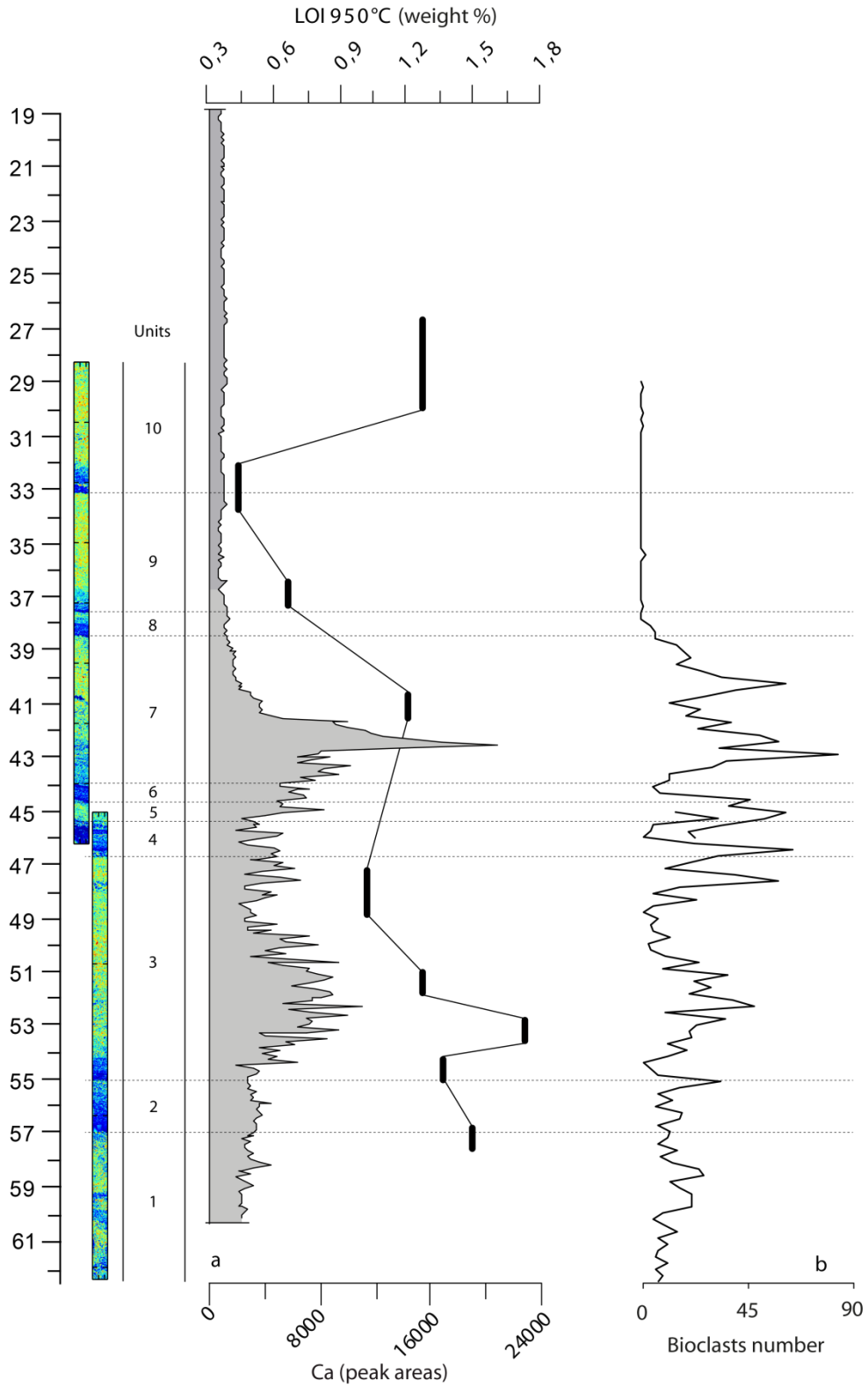

Fig. 9: Representation of the counting of bioclasts along the core, using (a) X-ray fluorescence (grey plot) and loss on ignition (Cuven et al., 2013), and (b) the bioclast code on X-CT images. While bioclasts are not located using three dimensional coordinates in the cores, they have been counted along the whole core instead of just a vertical slice, in order to ensure a good representativity of the data. Representing their quantity along a simple vertical graph allows a more straightforward reading of the data and is precise enough for stratigraphic work.

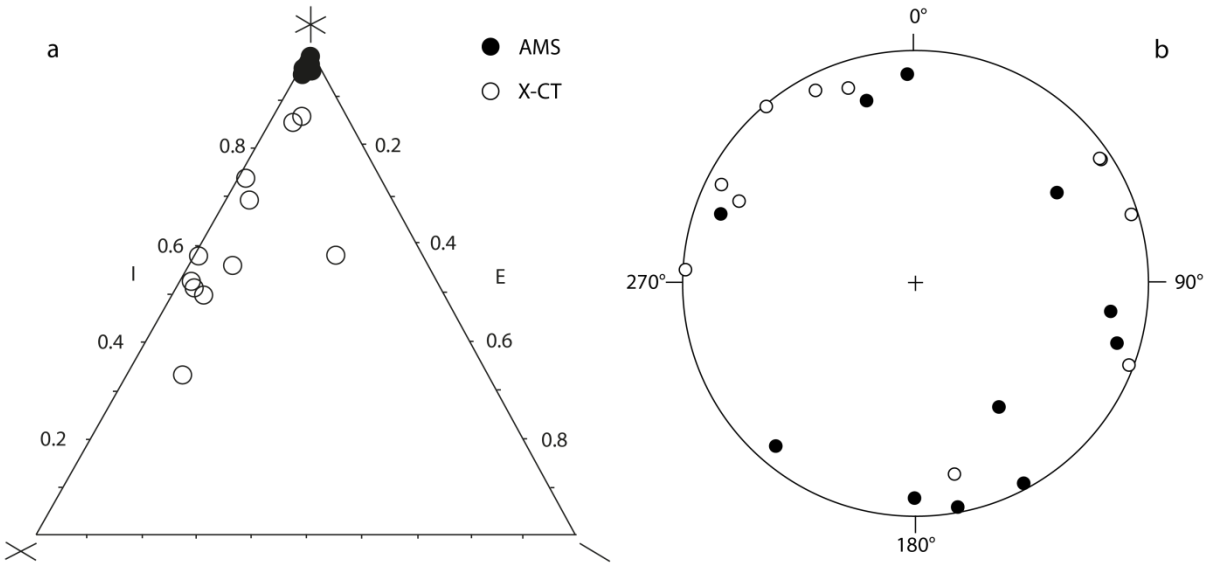

Fig. 10: a – Anisotropies of the ellipsoids of preferential orientations of the particles in each subsample. I: isotropy of the ellipsoid, with I = S3/S1. E: elongation of the ellipsoid, with E = 1 – (S2/S1). The shape of the ellipsoid is represented at each end of the plot : isotropic (top), oblate (low left) and prolate (low right). b – Orientation and dip of the longest axis of each subsample. 1 – See supplementary material for individual representations of the anisotropy of each subsample and for density maps of preferred orientations.

5. Discussion

5.1. X-CT vs other methods

Log stratigraphy and sedimentary structures. Simple visual analysis of the tomograms revealed very fine (millimetric or sub-millimetric) structures such as thin mudlines, mud drapes, clay infiltrations, that were very difficult or even often impossible to see clearly on a half core or in the field. While very fine structures could also be seen using more classical techniques such as the visual analysis of thin sections, the access to the three dimensions of space also made possible a detailed visualization of complex structures such as scour-and-fill and convolutions, which are difficult to interpret when only two dimensions are accessible.

Ten successive units were identified using X-CT data (depth 29 to 62.5 cm along the core). Cuven et al. (2013) previously found 8 different units on the same core (depth 29 to 54 cm). The dark grey silty clay below depth 54 cm was water saturated during sampling and poorly preserved. It was interpreted by Cuven et al. (2013) as a pre-tsunami sediment. However, the structures revealed by X-CT (convolutions, numerous rip-up clasts of clay) suggest that these

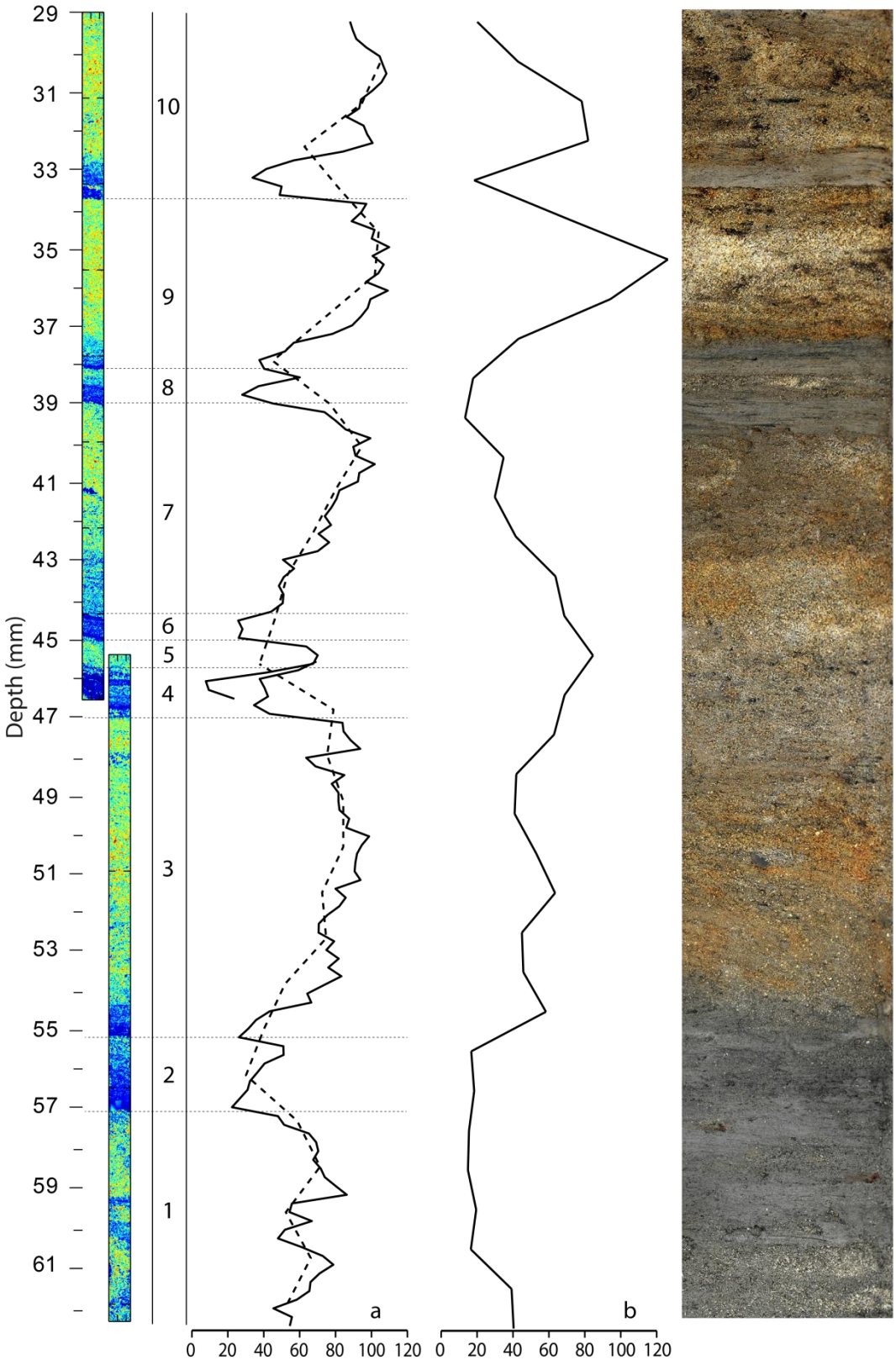

Fig. 11: Comparison of mean grain size data obtained with X- CT (a) using a 10mm step (dashed line) and a 2mm step (full line) and laser diffraction (b, 10mm step). X- CT allows using very fine measurement steps (depending only on the resolution of the scans) and precisely linking structures and subunits to GSD data.

clays correspond indeed to pre-tsunami sediment but considerably reworked by a high-energy turbulent flows. Except a very thin unit of fine clay (unit 6), the stratigraphy presented by Cuven et al. (2013) is roughly consistent with tomographic data. Cuven et al. (2013) considered the mudlines as independent units.

Grain size distribution and vertical grading. Vertical trends of mean grain size and sorting estimated from X-CT and from laser diffraction (data from Cuven et al., 2013) are similar (Fig. 11), except in the lower part of the core where the complex structure of the deposit varies radically over short distances (complex convolutions). However, the resolution of X-CT data (14.6 µm) prevented any analysis of particles finer than coarse silt, thus limiting any quantitative comparison between GSD obtained from laser diffraction and X-CT.

Grading inferred from laser diffraction on bulk samples is incomplete and might lead to misinterpretations, even if manual sampling is realised at a very fine step. For instance, unit 10 was erroneously described as normally graded by Cuven et al. (2013). X-CT data allows detecting trends of inverse grading which were not evidenced by other techniques. Normal grading of tsunami deposits is often reported in the literature, but inverse grading is occasionally described in the lower part of individual tsunami units or in particular topographical settings (e.g. Shi et al., 1995; Bondevik et al., 1997; Minoura et al., 1997; Gelfenbaum and Jaffe, 2003; Hori et al., 2007; Paris et al., 2007; Choowong et al., 2008; Higman and Bourgeois, 2008; Moore et al., 2011; Wagner and Srisutam, 2011; Naruse et al., 2012; Koiwa et al., 2014). X-CT analysis of the 1755 tsunami deposits at Los Lances confirms that there is no fining upwards of the overall sequence, and shows that the successive units are inversely graded or not graded, except for the upper part of unit 3 which is normally graded.

Vertical trends of bioclasts abundance. The vertical distribution of bioclasts inferred from X-CT is compared with Ca concentrations measured by X-ray microfluorescence and loss on ignition at 950°C (Fig. 9) (Cuven et al. 2013). Despite very different steps of analysis (1mm for XRF, 2mm for X-CT and bulk samples for LOI), all techniques give consistent results. The discrepancy between X-CT and XRF, and LOI values in units 9 to 10 (depth 33.5-29 cm) was already interpreted by Cuven et al. (2013) as the effect of resolution of scanning versus size of the bioclasts. As observed on thin sections, there are up to 7% of bioclasts (including diatoms) in subunit 10, but they are smaller than in the other units. The proportion of biogenic Ca might be underestimated by the XRF core scanner due to the small (4mm) width of the X-

ray beam. X-CT data is not affected by this limitation due to the 18mm inner diameter of the carbon fibre tubes and the fact that the whole sample is analysed. Moreover, since bioclasts are manually identified, X-CT can be used even in carbonated sediment, assuming a sufficient resolution of the images. On the other hand, fine bioclasts such as shell fragments can be difficult to distinguish in the X-CT images, leading to a potential loss of information and slightly underestimated content values. This resolution issue is also probably responsible for the apparent absence of diatoms in X-CT data when Cuven et al. (2013) reported their presence in the deposit.

Sedimentary fabric. Fig. 10b shows a comparison between sedimentary fabric inferred from X-CT and from AMS (data from Cuven et al., 2013). X-CT data highlights an important point: the Los Lances deposit contains few heavy minerals, let alone para- and ferromagnetic ones. This low abundance of magnetic particles in the deposit has two consequences: (1) the values of magnetic susceptibility are low (in the order of 10^{-6} SI); (2) the fabric is measured using very sparse particles (or particles finer than the scan resolution of 14.6 µm/voxel. This led the authors question the representativity of such low values of magnetic susceptibility and could explain some of the discrepancies observed between X-CT and AMS data in terms of preferential orientation of the particles. The comparison of the ellipsoid shapes (Fig. 10a) shows that the ellipsoids calculated using X-CT data always have a higher anisotropy than ellipsoids calculated using AMS.

While anisotropy degrees are very different, both techniques give similar results in terms of dominant orientation (roughly NW-SE, i.e. perpendicular to the shoreline, see Fig. 1). Fabric inferred from X-CT thus confirms that the mean orientation of the long axis of the particles in a high-energy current tends to be oriented perpendicular to flow direction (e.g. Rees, 1983; Wassmer et al., 2010; Schneider et al., 2014). However, all but two ellipsoids calculated using X-CT (subsamples 9 and 10, respectively corresponding to units 2 and 1) have isotropic-oblate shapes, which should correspond to deposition of particles by settling, under low-energy flows. This is not compatible with the structural and textural analysis of X-CT imagery, which clearly shows characteristics that are not compatible with settling as a dominant depositional mode (sharp erosive bases, rip-up clasts, crude laminations, convolutions, scour-and-fill figures, inverse grading). The fact that the X-CT subsamples correspond to the AMS in terms of size and shape (due to the need of cross-validation between the two approaches) probably explains this contradiction: the lack of precision of regular ASM cubes (2 cm wide plastic boxes), let no other choice than sampling several

structures together (see supplementary material for detailed sampling depths). The theoretical advantage of X-CT imagery is that it allows the operator to crop regions of interest in the deposit and conduct analyses virtually on a per subunit basis. However, the resolution and rather low contrast of the scans did not allow us to do so for this study since the extraction of enough particles in 3D required to use rather large subsamples. For instance, it was impossible to analyse the fabric developed in the thin laminae of heavy minerals (mostly orthopyroxenes) described by Cuven et al. (2013) above and below the mudlines.

Cheel (2005) shows that particles deposition under oscillating currents or in high particle-concentration mud can result in isotropic or even oblate ellipsoids. Two explanations are given : (1) oscillating currents can lead to the deposition of particles which longest axes may alternatively align perpendicular to the current when the energy of the flow is strong enough, and parallel to the current when the current strength decreases between oscillations. (2) Sediment rich flows may prevent particles from aligning parallel or transversely to the current due to too important interaction between touching grains and lack of space for spatial organization of the particles. In our case, oblate-isotropic ellipsoids are associated with poorly-organized (in terms of fabric) deposits of high energy, sediment-rich current.

Distinguishing uprush and backwash. Sedimentary fabric inferred from X-CT data do not allow attributing a backwash origin for any part of the tsunami deposit. However, Cuven et al. (2013) interpreted unit 10 as the result of the final backwash, all other units being deposited by uprush currents. This unit is characterised by small-size bioclasts, numerous rip-up clasts of soil and wood, renewed traction (inferred from AMS data), higher mud content, lower Si and Ba concentrations, and positive Ca-Al Spearman coefficient of correlation pointing to a dominant continental source. Considering that unit 10 corresponds to the backwash, it is worth mentioning that the textural and structural analysis of X-CT data do not show significant difference from uprush units (Table 1). However, the vortex observed at the base of unit 10 (Fig. 5e) resembles flame features formed by Kelvin-Helmoltz instabilities developed at the interface between two fluids of different velocity and density, as described in other tsunami deposits (Minoura & Nakata, 1994; Schnyder et al., 2005; Matsumoto et al., 2008). The vortex is associated with outsized floating clasts of sand in a clay-silt matrix and its geometry suggests a seaward-oriented flow, i.e. backwash. It should however be noted that the size of the sample is relatively small and may only give us access to a truncated part of the

structures. The possible difference between the observed structures in the tube and the global organisation of the deposit should be kept in mind.

5.2. Limitations and advantages of the technique

Limitations.

The logs rendered by the *grainmap* code do not represent a total grain size distribution and the colours are calculated by interpolating values between the centre of the particles, which are represented by a single point and not by their actual size. These logs shall therefore only be used for qualitative description. The resolution of the image is a key factor since it limits the lower representable grain size and will thus determine the size of the particles which could be quantitatively analysed. But since resolutions of a few micrometres or even a few hundreds of nanometres can nowadays be achieved depending on the size of the sample, the limitations linked to resolution can be addressed in several cases, especially if small scale samples can be retrieved.

As previously said, the grain number graph is not meant to be used for statistical analysis but only to keep an eye on the representativity of the subsampling, since grains smaller than the resolution limit of the scans cannot be separated, hence the noticeable drops in grain quantities shown in some mudlines. This limitation should be kept in mind when comparing subsamples that exhibit very different mean grain sizes, especially with the ones whose mean grain size is close to the resolution limit.

In addition, the separation process of particles in 3D can be complex and very time consuming, making the acquisition of quantitative 3D data fastidious for large samples. However, the development of automated separation techniques could help overcoming this inconvenience (Carr et al., 2015).

Advantages

Tomography is most suitable for small scale measurements, with for instance other techniques such as laser diffraction and AMS measurements being useful for analysing a whole deposit and/or area with numerous pluri-millimetre/centimetre scaled samples in a quicker and more convenient way, and tomography based grain size analysis and fabric measurement adding precision for smaller scale structures/units study. An advantage of the fabric analysis with X-CT is that it takes every particle into account with no regard to magnetism. This allows running an analysis on a sample which is poor or depleted in para- or ferromagnetic mineral. This technique also addresses the problem raised by Rees (1965)) of potential false preferred orientations introduced by touching grains of high magnetic susceptibility in highly magnetic samples.

The *grainstat* code allows quantitative analysis of the particles and can be modified depending on user's needs (additional measurements of any kind can easily be added to the code) in order to obtain the most comprehensive dataset. Since the measurements are based on the same kind of data as the *grainmap* code, an equal care to the scans resolution shall also be taken, but the fact that both codes use the same data file allows directly linking structures and particles characteristics. This is very important, especially when dealing with very fine structures (e.g. mudlines or fine sand laminations) where the characteristics of the deposit can vary very abruptly.

The use of the three codes thus allows a comprehensive description of the log along the deposit using the same sample to extract the data. This makes comparisons of different parameters easier and more consistent than comparing data obtained from samples collected with different methods.

3D analysis of the particles of unconsolidated sediments has two major interests: (1) grain size distribution measurement, as in 2D, except that 3D measurement take the whole particle into account and is given as a volume and an aspect ratio instead of a "grain size" which is supposed to represent the intermediate diameter of an ellipsoidal particle. (2) The access to the third dimension allows measuring the precise orientation of each particle (measurement of the direction and dip of the longest axis of the particle's ellipsoid), which in turn allows documenting sedimentary fabric parameters in a way similar to measurements of anisotropy of magnetic susceptibility or serial sectioning analysis.

5.3 Towards a new depositional model of tsunami deposits

A key parameter for understanding processes of transport and accumulation of sediments by a tsunami is the high shear stress generated at the offshore-to-onshore transition, where the oscillatory long wave turns to a combined oscillatory – unidirectional flow. Flow regime of a tsunami inland ranges from subcritical to supercritical conditions, with Froude numbers between 0.7 and 2 (e.g. Matsutomi et al., 2011). This is attested by the diversity of bedforms observed in tsunami deposits: current ripples formed during oscillatory and combined flow, plane to low-angle bedding (both landward and seaward-inclined), low-angle trough cross-bedding and wedge-shaped cross-bedding, convolute beddings and flames, hummocky cross stratification, and antidunes (Fujiwara et al., 2000; Takashimizu & Masuda, 2000; Nanayama & Shigeno, 2006; Fujiwara & Kamataki, 2007; Choowong et al., 2008; Matsumoto et al., 2008, 2010; Nanayama et al., 2011; Fujiwara & Tanigawa, 2014; Koiwa et al., 2014, Switzer et al., 2012). The most frequent bedforms observed in tsunami deposits are plane to low-angle laminations. Grain size analyses and sedimentary fabric inferred from AMS suggest that tractive shearing is important if not predominant in the formation of some tsunami deposits (e.g. Le Roux & Vargas, 2005; Paris et al., 2007; Moore et al., 2011; Cuven et al., 2013; Schneider et al., 2014).

The analysis of the 1755 tsunami deposits at Los Lances through X-CT allows proposing new hypotheses for building a depositional model of tsunami deposits in which traction carpets (Hiscott & Middleton, 1980; Lowe, 1982; Sohn, 1997) plays an important role.The formation of traction carpets in tsunami deposits was already inferred by Moore et al. (2011), Jagodziński et al. (2012) and Schneider et al. (2014).

The majority of the successive units composing the tsunami deposit studied here are crudely laminated and the contacts between these units are erosive. Unit 1 differs from the other units since it represents the initial uprush on dry land of a supercritical flow causing extensive erosion of the substrate, as evidenced by the absence of well-defined structure except complex convolutions, and numerous rip-up clasts of greyish mud (pre-tsunami marsh deposits).

The other units are characterised by plane to oblique (low-angle) laminations of the lower-to-upper flow regime transition (Fr ~1). These laminations are often very crude and

poorly-defined, except in units 3 and 7 (Fig. 4 and Table 1). Laminations in unit 3 are dipping seaward, with alternating very low (<3°) and low angles (13-20°), indicating transitional conditions between upper plane bed and downstream-migrating in-phase waves. Laminations dipping 14 to 22° landward in the lower part of unit 7 (clayey sand) can be interpreted as long-length dunes of the lower flow regime, followed by a return to upper plane beds in the upper part of the unit (very fine sands). Crude laminations in the tsunami deposit are associated to small-scale (mm scale) variations of grain size and sorting, as described by Cheel and Middleton in laminated sandstones (1986), but they are not systematically associated with a unit-scale vertical grading of the grain size (Fig.8). The non-uniform distribution of particles and development of upper plane bed horizontal lamination in a tsunami deposit could be controlled by flow unsteadiness (e.g. pulses) and variations of sediment supply, migration of low bedforms, and variations of grain size reflecting different sources of sediment, as observed for turbulent density-stratified flows such as high-density turbidity currents and pyroclastic flows (e.g. Lowe 1982; Postma et al., 1983; Valentine, 1987; Cartigny et al., 2013).

The important role of shear stress and traction is also supported by the unexpected results obtained on the mudlines, which are usually interpreted as short-lived settling periods of the finest grain size fractions. However analysis of X-ray imagery reveals that the mudlines are not graded, poorly sorted, and crudely laminated. The contact between the mudlines and underlying units is always erosive and seem to correspond to the beginning of a deposition phase (Fig. 5b). These observations make sense if we consider that the base of a tsunami wave is characterised by a high shear stress and a high concentration of particles. Mudlines would then represent the frictional fine-grained region (typically clay to clayey silt) of an erosive traction carpet or shear carpet. Intense shear stress is also evidenced by tapered intraclasts (rip-up clasts of soil and mud) in units 1 and 7 (Fig. 5c).

Each new wave is a new sediment supply mixing coastal sands (beach, dune) and mud from the marsh, with a probable partial reworking of previously deposited units. Mud is mostly confined to the basal frictional region of the flow, while sand is drifted toward a collisional zone of least dispersive stress and lower sediment concentration (as described in other traction carpets: Sohn, 1997; Cartigny et al., 2013). Inverse grading is often preserved in this collisional region (e.g. units 7 and 9). In friction-dominated zones such as the mudlines, grain size segregation is hampered by high particle concentration and shear stress, forming

ungraded but laminated deposits. It is worth noting that the tsunami deposit studied here is relatively fine-grained (from clays to fine sands), thus limiting the generation of dispersive pressure and inverse grading. Normal grading observed at the top of unit 3 indicates a dilute flow overlying the traction-dominated flow. This phase is absent from the other units, probably because it was short-lived and immediately eroded by a following wave.

The base of unit 10, which is interpreted by Cuven et al. (2013) as a backwash unit, also displays a well-developped traction carpet. Vortex described as Kelvin-Helmoltz instabilities are formed at the boundary between two zones of contrasted shear stress, velocity and particle concentration (Fig. 5e). Outsized floating clasts are also concentrated at this interface, which is consistent with the so-called Z-shaped velocity profile of traction carpets (Lowe, 1982).

6. Conclusions and perspectives

X-ray microtomography is a powerful tool for investigating complex unconsolidated sediments such as tsunami deposits in a non-destructive way, allowing the visualization of structures that no other technique would have preserved intact in three dimensions. The technique also gives the ability to obtain quantitative data on parameters that find a wide use in tsunami deposits studies, such as grain size distribution and sedimentary fabric. X-CT provides new insights into the inner organisation of a tsunami deposit, both in terms of structure, but also on sedimentary features such as mudlines, rip-up clasts, crude laminations, convolutions, floating outsized clasts, and contacts between successive units. This approach lead us to propose new hypotheses for interpreting tsunami deposits, which are here dominated by a high shear stress leading to the development of traction carpets, with laminated mudlines corresponding to the basal frictional region of these carpets. This conceptual model needs to be validated by X-CT analyses on other tsunami deposits. More attention must be paid on the sedimentary facies related to bed friction in tsunami deposits, because the thickness of the bottom boundary layer and the bed shear stress increase as the tsunami approaches the coast. This is a fundamental mechanism for understanding the transport of sediments by tsunami and clue for determining the magnitude of a tsunami from its deposits.

With the constant improvements of tomographic techniques (better resolutions and signal-to-noise ratios), image processing and accessibility of equipments, one can expect X-CT to become easier to perform on geological samples with complex and fine-scale structures and textures. A reliable method for automatic segmentation would be very useful to get consistent results from one sample to another in a minimum amount of time, manual segmentation being time consuming. The combination of the lowering of scan times, better resolution and faster processing will make exhaustive study of a sedimentary sequence easier and faster. Further developments of X-CT for the study of tsunami deposits would include comprehensive analysis of the components and distribution of specific populations, such as heavy minerals, woods, and bioclasts (including characterisation of different types of bioclasts from their geometry). As stated above, the relatively small size of the samples limits the spatial representativity of the study and the spatial interpretation. X-CT analysis of several cores along longitudinal and lateral transect would ensure a better coverage and help characterising the spatial variability and landward evolution of the tsunami deposit. Studies of other well documented deposits should also be conducted to complete the cross-validation process of the technique. Furthermore, while this technique could be used on other kind of fine grained deposits such as tempestites.

Acknowledgments

This study was funded by the Conseil Régional d'Auvergne, project TSUNAMIX, and by the French National Research Agency, project ANR-08-RISKNAT MAREMOTI. The authors are particularly grateful to Stéphanie Cuven (PalGeoSed), Marine Tridon and Yannick Guéhenneux (LMV, Clermont-Ferrand), Paul Tafforeau and Elodie Boller (ID 19 ESRF, Grenoble). Adam Switzer and Witold Szczuciński are thanked for their detailed and constructive comments. This is ClerVolc Laboratory of Excellence contribution number *XXX*.

References

Atwater, B. F, 1987. Evidence for Great Holocene Earthquakes along the Outer Coast of Washington State. Science 236, pp. 942-944.

Babu, N., Suresh Babu, D. S., Mohan Das, P. N, 2007. Impact of Tsunami on Texture and Mineralogy of a Major Placer Deposit in Southwest Coast of India. Environmental Geology 52 (1), 71-80.

Benn, D., 1994. Fabric Shape and the Interpretation of Sedimentary Fabric Data. Journal of Sedimentary Research 64 (4a), 910-915.

Bondevik, S., Svendsen, J.I., Mangerud, J., 1997. Tsunami sedimentary facies deposited by the Storegga tsunami in shallow marine basins and coastal lakes, western Norway. Sedimentology 44, 1115-1131.

Bondevik, S., Mangerud, J., Dawson, S., Dawson, A., Lohne, Ø., 2005. Evidence for three North Sea tsunamis at the Shetland Islands between 8000 and 1500 years ago. Quaternary Science Reviews 24 (14-15), 1757-1575.

Bony, G., Marriner, N., Morhange, C., Kaniewski, D., Perinçek, D., 2012. A high-energy deposit in the Byzantine harbour of Yenikapı, Istanbul (Turkey). Quaternary International 266, 117-130.

Bourgeois, J., Hansen, T.A., Wiberg, P.L., Kauffman, E.G., 1988. A Tsunami Deposit at the Cretaceous-Tertiary Boundary in Texas. Science 241, 567-570.

Carr, S., Diggens, L., Groves, J., O'Sullivan, C., Marsland, R., 2015. Visualising, segmenting and analysing heterogenous glacigenic sediments using 3D x-ray CT. EGU Genral Assembly 2015, Geophysical Research Abstracts vol. 17.

Cartigny, M.J.B., Eggenhuisen, J.T., Hansen, E.W.M., Postma, G., 2013. Concentration-dependent flow stratification in experimental high-density turbidity currents and their relevance to turbidite facies models. Journal of Sedimentary Research 83 (12), 1046-1064.

Chagué-Goff, C., Dawson, S., Goff, J. R., Zachariasen, J., Berryman, K. R., Garnett, D. L., Waldron, H. M., Mildenhall., D. C., 2002. A tsunami (ca. 6300 years BP) and other

Holocene environmental changes, northern Hawke's Bay, New Zealand. Sedimentary Geology 150 (1), 89-102.

Chagué-Goff, C., Schneider, J.-L., Goff, J.R, Dominey-Howes, D., Strotz, L., 2011. Expanding the proxy toolkit to help identify past events — Lessons from the 2004 Indian Ocean Tsunami and the 2009 South Pacific Tsunami. Earth-Science Reviews 107 (1–2), 107-122.

Cheel, R.J., 2005. Introduction to Clastic Sedimentology (Notes for a University level, second year, half-credit course in clastic sedimentology).

Cheel, R.J., Middleton, G.V., 1986. Horizontal lamination formed under upper flow regime plane bed conditions. Journal of Geology 94, 489-504.

Choowong, M., Murakoshi, N., Hisada, K.-I., Charoentitirat, T., Charusiri, P., Phantuwongraj, S., Wongkok, P., 2008. Flow Conditions of the 2004 Indian Ocean Tsunami in Thailand, Inferred from Capping Bedforms and Sedimentary Structures. Terra Nova 20 (2), 141-149.

Cnudde, V., Boone, M.N., 2013. High-resolution X-ray computed tomography in geosciences: a review of the current technology and applications. Earth Science Reviews 123, 1-17.

Cuven, S., Paris, R., Falvard, S., Miot-Noirault, E., Benbakkar, M., Schneider, J.-L., Billy, I., 2013. High-resolution analysis of a tsunami deposit: Case-study from the 1755 Lisbon tsunami in southwestern Spain. Marine Geology 337, 98-111.

Dawson, A.G., Long, D., Smith, D.E., 1988. The Storegga Slides: Evidence from eastern Scotland for a possible tsunami. Marine Geology 82 (3–4), 271-276.

Dawson, S., 2007. Diatom biostratigraphy of tsunami deposits: Examples from the 1998 Papua New Guinea tsunami. Sedimentary Geology 200 (3-4), 328-335.

Denison, C., Carlson, W. D., 1997. Three-Dimensional Quantitative Textural Analysis of Metamorphic Rocks Using High-Resolution Computed X-Ray Tomography: Part II. Application to Natural Samples. Journal of Metamorphic Geology 15 (1), 45-57.

Dominey-Howes, D., Dawson, A., Smith, D., 1999. Late Holocene Coastal Tectonics at Falasarna, Western Crete: A Sedimentary Study. Geological Society, London, Special Publications 146 (1), 343-352.

Fujiwara, O., Masuda, F., Sakai, T., Irizuki, T., Fuse, K., 2000. Tsunami deposits in Holocene bay mud in southern Kanto region, Pacific coast of central Japan. Sedimentary Geology 135, 219-230.

Fujiwara, O., Kamataki, T., 2007. Identification of tsunami deposits considering the tsunami waveform: An example of subaqueous tsunami deposits in Holocene shallow bay on southern Boso Peninsula, Central Japan. Sedimentary Geology 200 (3-4), 295-313.

Fujiwara, O., Tanigawa, K., 2014. Bedforms record the flow conditions of the 2011 Tohoku-Oki tsunami on the Sendai Plain, northeast Japan. Marine Geology 358, 79-88.

Gelfenbaum, G., Jaffe, B., 2003. Erosion and sedimentation from the 17 July, 1998 Papua New Guinea tsunami. Pure and Applied Geophysics 160, 1969-1999.

Giachetti, T., Burgisser, A., Arbaret, L., Druitt, T. H., Kelfoun, K., 2011. Quantitative textural analysis of Vulcanian pyroclasts (Montserrat) using multi-scale X-ray computed microtomography: comparison with results from 2D image analysis. Bulletin of Volcanology 73 (9), 1295-1309.

Goff, J.R., Chagué-Goff, C., 1999. A late Holocene record of environmental changes from coastal wetlands: Abel Tasman National Park, New Zealand. Quaternary International 56 (1), 39-51.

Goff, J.R., Chagué-Goff, C., Nichol, S., Jaffe, B., Dominey-Howes, D., 2012. Progress in palaeotsunami research. Sedimentary Geology 243–244, 70-88.

Gracia, I.J., Alonso, C., Benavente, J., Anfuso, G., Del Rio, L., 2006. The different coastal records of the 1755 tsunami waves along the south Atlantic Spanish Coast. Zeitschrift für Geomorphologie, Supplementbände 146, 195–220.

Higman, B., Bourgeois, J., 2008. Deposits oft he 1992 Nicaragua tsunami. In: Shiki, T., Tsuji, Y., Yamazaki, T., Minoura, K. (Eds.), Tsunamiites – features and implications. Elsevier, pp. 81-103.

Hiscott, R.N., Middleton, G.V., 1980. Fabric of coarse deep-water sandstones Tourelle Formation, Quebec, Canada. Journal of Sedimentary Petrology 50 (3), 703-721.

Hiscott, R.N., 1994. Traction-Carpet Stratification in Turbidites-Fact or Fiction? Journal of Sedimentary Research, section A: Sedimentary Petrology and Processes 64A (2), 204-208.

Hori, K., Kuzumoto, R., Hirouchi, D., Umitsu, M., Janjirawuttikul, N., Patanakanog, B., 2007. Horizontal and vertical variations of 2004 Indian tsunami deposits: an example of two transects along the western coast of Thailand. Marine Geology 239, 163-172.

Iliev, A. Ya., Kaistrenko, V.M., Gretskaya, E.V., Tikhonchuk, E.A., Razjigaeva, N.G., Grebennikova, T.A., Ganzey, L.A., Kharlamov, A.A., 2005. Holocene tsunami traces on Kunashir Island, Kurile subduction zone. In : Satake, K. (Ed.), Tsunamis: Case Studies and Recent Developments. Springer, 171-192.

Jaffe, B., Gelfenbaum, G., 2007. A simple model for calculating tsunami flow speed from tsunami deposits. Sedimentary Geology 200 (3-4), 347-361.

Jagodziński, R., Sternal, B., Szczuciński, W., Lorenc, S., 2009. Heavy minerals in 2004 tsunami deposits on Kho Khao Island, Thailand. Polish Journal of Environmental Studies 18 (1), 103-110.

Jagodziński, R., Sternal, B., Szczuciński, W., Chagué-Goff, C., Sugawara, D., 2012. Heavy minerals in the 2011 Tohoku-oki tsunami deposits—insights into sediment sources and hydrodynamics. Sedimentary Geology 282, 57-64.

Ketcham, R.A., Carlson, W.D., 2001. Acquisition, optimization and interpretation of X-ray computed tomographic imagery: applications to the geosciences. Computers & Geosciences 27 (4), 381-400.

Ketcham, R.A., 2005a. Computational methods for quantitative analysis of three-dimensional features in geological specimens. Geosphere 1 (1), 32-41.

Ketcham, R.A., 2005b. Three-dimensional grain fabric measurements using high-resolution X-ray computed tomography. Journal of Structural Geology 27 (7), 1217-1228.

Ketcham, R.A., Meth, C., Hirsch, D.M., Carlson, W.D., 2005. Improved methods for quantitative analysis of three-dimensional porphyroblastic textures. Geosphere 1 (1), 42-59. Kilfeather, A.A., Blackford, J.J., van der Meer, J.J.M., 2007. Micromorphological Analysis of Coastal Sediments from Willapa Bay, Washington, USA: A Technique for Analysing Inferred Tsunami Deposits. Pure and Applied Geophysics 164 (2-3), 509-525.

Koiwa, N., Kasai, M., Kataoka, S., Isono, T., 2014. Examination of relation with tsunami behavior reconstructed from on-site sequence photographs, topography, and sedimentary deposits from the 2011 Tohoku-oki tsunami on the Kamikita Plain, Japan. Marine Geology 358, 107-119.

Kuper, K.E., Zedgenizov, D.A., Ragozin, A.L., Shatsky, V.S., Porosev, V.V., Zolotarev, K.V., Babichev, E.A., Ivanov., S.A., 2007. Three-dimensional distribution of minerals in diamondiferous eclogites, obtained by the method of high-resolution X-ray computed tomography. Nuclear Instruments and Methods in Physics Research Section A: Accelerators, Spectrometers, Detectors and Associated Equipment 575 (1-2), 255-258.

Le Roux, J. P. Vargas, G., 2005. Hydraulic behaviour of tsunami backflows: insights from their modern and ancient deposits, Environmental Geology 49, 65– 75.

Liu, B., Saito, Y., Yamazaki, T., Abdeldayem, A., Oda, H., Hori, K., Zhao, Q., 2001. Paleocurrent analysis for the Late Pleistocene–Holocene incised-valley fill of the Yangtze delta, China by using anisotropy of magnetic susceptibility data. Marine Geology 176 (1–4), 175-189.

Lowe, D.R., 1982. Sediment gravity flows: II depositional models with special reference to the deposits of high-density turbidity currents. Journal of Sedimentary Petrology 52 (1), 279-297.

Matsumoto, D., Naruse, H., Fujino, S., Surphawajruksakul, A., Jarupongsakul, T., Sakakura, N., Murayama, M., 2008. Truncated flame structures within a deposit of the Indian Ocean Tsunami: evidence of syn-sedimentary deformation. Sedimentology 55 (6), 1559-1570.

Matsumoto, D., Shimamoto, T., Hirose, T., Gunatilake, J., Wickramasooriya, A., DeLile, J., Rathnayake, C., Ranasooriya, J., Murayama, M., 2010. Thickness and grain-size distribution of the 2004 Indian Ocean tsunami deposits in Periya Kalapuwa Lagoon, eastern Sri Lanka. Sedimentary Geology 230 (3-4), 95-104.

Matsutomi, H., Okamoto, K., Harada, K., 2010. Inundation flow velocity of tsunami inland and its practical use. Proceedings of the 32nd Conference on Coastal Engineering, Shanghai, China, 2010.

May, S.M., Falvard, S., Norpoth, M., Pint, A., Brill, D., Engel, M., Scheffers, A., Dierick, M., Paris, R., Squire, P., Brückner, H., 2015. A mid-Holocene candidate tsunami deposit from the NW Cape (Western Australia). Sedimentary Geology.

Mees, F., Swennen, R., Geet, M.V., Jacobs, P., 2003. Applications of X-ray computed tomography in the geosciences. In: Mees, F., Swennen, R., Geet, M.V., Jacobs, P. (Eds),

Applications of X-ray computed tomography in the geosciences. Geological Society, London, Special Publications 215 (1), 1-6.

Merkus, H.G., 2009. Particle Size Measurements: Fundamentals, Practice, Quality. Springer Science & Business Media.

Minoura, K., Gusiakov, V.G., Kurbatov, A., Takeuti, S., Svendsen, J.I., Bondevik, S., Oda, T., 1996. Tsunami sedimentation associated with the 1923 Kamchatka earthquake. Sedimentary Geology 106 (1–2), 145-154.

Minoura, K., Imamura, F., Takahashi, T., Shuto, N., 1997. Sequence of Sedimentation Processes Caused by the 1992 Flores Tsunami: Evidence from Babi Island. Geology 25 (6), 523-526.

Minoura, K., Nakaya, S., 1991. Traces of Tsunami Preserved in Inter-Tidal Lacustrine and Marsh Deposits: Some Examples from Northeast Japan. Journal of Geology 99 (2), 265-287.

Minoura, K. and Nakata, T., 1994. Discovery of an ancient tsunami deposit in coastal sequence of southwest Japan: verification of a large historic tsunami. Island Arc, 3, 66–72.

Moore, A.L., McAdoo, B.G., Ruffman, A., 2007. Landward fining from multiple sources in a sand sheet deposited by the 1929 Grand Banks tsunami, Newfoundland. Sedimentary Geology 200 (3–4), 336-346.

Moore, A., Goff, J., McAdoo, B.G., Fritz, H.M., Gusman, A., Kalligeris, N., Kalsum, K., Susanto, A., Suteja, D., Synolakis, C.E., 2011. Sedimentary deposits from the 17 July 2006 Western Java tsunami, Indonesia: use of grain size analyses to assess tsunami flow depth, speed, and traction carpet characteristics. Pure and Applied Geophysics 167 (11), 1951-1961.

Morton, R.A., Gelfenbaum, G., Jaffe, B., 2007. Physical criteria for distinguishing sandy tsunami and storm deposits using modern examples. Sedimentary Geology 200 (3-4), 184-207.

Morton, R.A., Goff, J.R., Nichol, S.L., 2008. Hydrodynamic implications of textural trends in sand deposits of the 2004 tsunami in Sri Lanka. Sedimentary Geology 207, 56-64.

Nanayama, F., Shigeno, K., 2006. Inflow and outflow facies from the 1993 tsunami in southwest Hokkaido. Sedimentary Geology 187 (3-4), 139-158.

Nanayama, F., Shigeno, K., Shitaoka, Y., Furukawa, R., 2011. Geological study of unsual tsunami deposits in the Kuril subduction zone for mitigation of tsunami disasters. In: Mörner, N.-A. (Ed), The tsunami threat - Research and Technology. InTech, 283-298.

Naruse, H., Arai, K., Matsumoto, D., Takahashi, H., Yamashita, S., Tanaka, G., Murayama, M., 2012. Sedimentary features observed in the tsunami deposits at Rikuzentakata City. Sedimentary Geology 282, 199-215.

Nichol, S.L., Goff, J.R., Devoy, R.J.N., Chagué-Goff, C., Hayward, B., James, I., 2007. Lagoon subsidence and tsunami on the West Coast of New Zealand. Sedimentary Geology 200 (3-4), 248-262.

Nishimura, Y., Miyaji, N., 1995. Tsunami deposits from the 1993 southwest Hokkaido earthquake and the 1640 Hokkaido Komagatake eruption, northern Japan. Pure and Applied geophysics 144 (3-4), 719-733.

Paris, R., Cachão, M., Fournier, J., Voldoire, O., 2010. Nannoliths Abundance and Distribution in Tsunami Deposits: Example from the December 26, 2004 Tsunami in Lhok Nga (northwest Sumatra, Indonesia). Géomorphologie : Relief, Processus, Environnement 1, 109-118.

Paris, R., Lavigne, F., Wassmer, P., Sartohadi, J., 2007. Coastal sedimentation associated with the December 26, 2004 in Lhok Nga, west Banda Aceh (Sumatra, Indonesia). Marine Geology 238, 93-106.

Paris, R., Wassmer, P., Sartohadi, J., Lavigne, F., Barthomeuf, B., Desgages, E., Grancher, D., 2009. Tsunamis as geomorphic crises: Lessons from the December 26, 2004 tsunami in Lhok Nga, West Banda Aceh (Sumatra, Indonesia). Geomorphology 104 (1–2), 59-72.

Paris, R., Switzer, A.D., Belousova, M., Belousov, A., Ontowirjo, B., Whelley, P.L., Ulvrova, M., 2014. Volcanic Tsunami: A Review of Source Mechanisms, Past Events and Hazards in Southeast Asia (Indonesia, Philippines, Papua New Guinea). Natural Hazards 70 (1), 447-470.

Park, C.K., Doh S.J., Suk, D.W., Kim, K.H., 2000. Sedimentary fabric on deep-sea sediments from KODOS area in the eastern Pacific. Marine Geology 171 (1–4), 115-26.

Pilarczyk, J.E., Horton, B.P., Witter, R.C., Vane, C.H., Chagué-Goff, C., Goff, J., 2012. Sedimentary and foraminiferal evidence of the 2011 Tōhoku-oki tsunami on the Sendai coastal plain, Japan. Sedimentary Geology 282, 78-89.

Postma, G., Roep, T.B., Ruegg, G.H.J., 1983. Sandy-gravelly mass-flow deposits in an ice-marginal lake (Saalian, Leuvenumsche Beek Valley, Veluwe, the Netherlands), with emphasis on plug-flow deposits. Sedimentary Geology 34 (1), 59-82.

Ramírez-Herrera, M.T., Lagos, M., Hutchinson, I., Kostoglodov, V., Machain, M.L., Caballero, M., Goguitchaichvili, A., 2012. Extreme wave deposits on the Pacific coast of Mexico: Tsunamis or storms? — A multi-proxy approach. Geomorphology 139–140, 360-371.

Rees, A.I., 1965. The Use of Anisotropy of Magnetic Susceptibility in the Estimation of Sedimentary Fabric1. Sedimentology 4 (4), 257-271.

Rees, A.I., Woodall, W.A., 1975. The magnetic fabric of some laboratory-deposited sediments. Earth and Planetary Science Letters 25 (2), 121-130.

Rees, A.I., 1983. Experiments on the production of transverse grain alignment in a sheared dispersion. Sedimentology 30 (3), 437-448

Reicherter, K., Vonberg, D., Koster, B., Fernández-Steeger, T., Grützner, C., Mathes-Schmidt, M., 2010. The sedimentary inventory of the 1755 Lisbon tsunami along the southern Gulf of Cádiz (southwestern Spain). Zeitschrift für Geomorphologie 54, Suppl. 3, 147-173.

Schneider, J.-L., Chagué-Goff, C., Bouchez, J.-L., Goff, J., Sugawara, D., Goto, K., Jaffe, B., Richmond, B., 2014. Using Magnetic Fabric to Reconstruct the Dynamics of Tsunami Deposition on the Sendai Plain, Japan — The 2011 Tohoku-Oki Tsunami. Marine Geology 358, 89-106.

Schnyder, J., Baudin, F., Deconinck, J.-F., 2005. A possible tsunami deposit around the Jurassic-Cretaceous boundary in the Boulonnais area (northern France). Sedimentary Geology 177, 209–227.

Shi, S., Dawson, A.G., Smith, D.E., 1995. Coastal sedimentation associated with the December 12th, 1992 tsunami in Flores, Indonesia. Pure and Applied Geophysics 144, 525-536.

Sohn, Y.K., 1997. On traction-carpet sedimentation. Journal of Sedimentary Research, Section A: Sedimentary Petrology and Processes 67 (3), 502-509.

Srinivasalu, S., Jonathan, M.P., Thangadurai, N., Ram-Mohan, V., 2009. A study on pre- and post-tsunami shallow deposits off SE coast of India from the 2004 Indian Ocean tsunami: a geochemical approach. Natural Hazards 52 (2), 391-401.

Switzer, A.D., Pucillo, K., Haredy R.A., Jones, B.G., Bryant, E.A., 2005. Sea Level, Storm, or Tsunami: Enigmatic Sand Sheet Deposits in a Sheltered Coastal Embayment from Southeastern New South Wales, Australia. Journal of Coastal Research 214, 655-663.

Switzer, A., Srinivasalu, S., Thangadurai, N., Mohan, W.R., 2012. Bedding structures in Indian tsunami deposits that provide clues to the dynamics of tsunami inundation. Geological Society, London, Special Publication 361, 61-77.

Szczuciński, W., Niedzielski, P., Kozak, L., Frankowski, M., Zioła, A., Lorenc, S., 2007. Effects of Rainy Season on Mobilization of Contaminants from Tsunami Deposits Left in a Coastal Zone of Thailand by the 26 December 2004 Tsunami. Environmental Geology 53 (2), 253-264.

Szczuciński, W., Rachlewicz, G., Chaimanee, N., Saisuttichai, D., Tepsuwan, T., Lorenc, S., 2012a. 26 December 2004 Tsunami Deposits Left in Areas of Various Tsunami Run up in Coastal Zone of Thailand. Earth, Planets and Space 64 (10), 843-858.

Szczuciński, W., Kokociński, M., Rzeszewski, M., Chagué-Goff, C., Cachão, M., Goto, K., Sugawara, D., 2012b. Sediment sources and sedimentation processes of 2011 Tohoku-oki tsunami deposits on the Sendai Plain, Japan — Insights from diatoms, nannoliths and grain size distribution. Sedimentary Geology 282, 40-56.

Szczuciński, W., 2012c. The Post-Depositional Changes of the Onshore 2004 Tsunami Deposits on the Andaman Sea Coast of Thailand. Natural Hazards 60 (1), 115-133.

Takashimizu, Y., Masuda, F., 2000. Depositional facies and sedimentary successions of earthquake-induced tsunami deposits in Upper Pleistocene incised valley fills, central Japan. sedimentary Geology 135, 231-239.

Tarling, D., Hrouda, F., 1993. The Magnetic Anisotropy of Rocks. Chapman and Hall, London.

Valentine, G.A., 1987. Stratified flow in pyroclastic surges. Bulletin of Volcanology 49 (4), 616-630.

Wagner, J.F., Srisutam, C., 2011. Grain-size and thin section characteristics of tsunami sediments from Thai-Andaman Coast, Thailand. In: Mörner, N.A. (Ed.), The tsunami threat – Research and Technology. InTech, pp. 259-282.

Wassmer, P., Schneider, J.-L., Fonfrège, A.V., Lavigne, F., Paris, R., Gomez, C., 2010. Use of anisotropy of magnetic susceptibility (AMS) in the study of tsunami deposits: Application to the 2004 deposits on the eastern coast of Banda Aceh, North Sumatra, Indonesia. Marine Geology 275 (1–4), 255-272.

Zabler, S., Rack, A., Manke, I., Thermann, K., Tiedemann, J., Harthill, N., Riesemeier, H.. 2008. High-resolution tomography of cracks, voids and micro-structure in greywacke and limestone. Journal of Structural Geology 30 (7), 876-887.

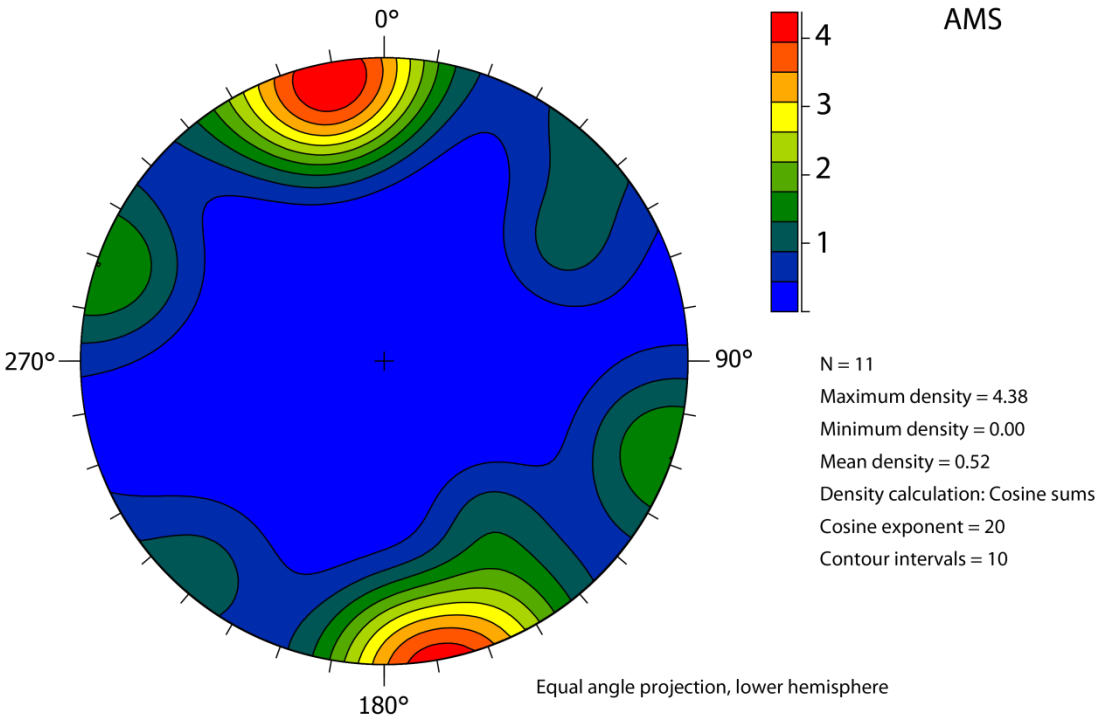

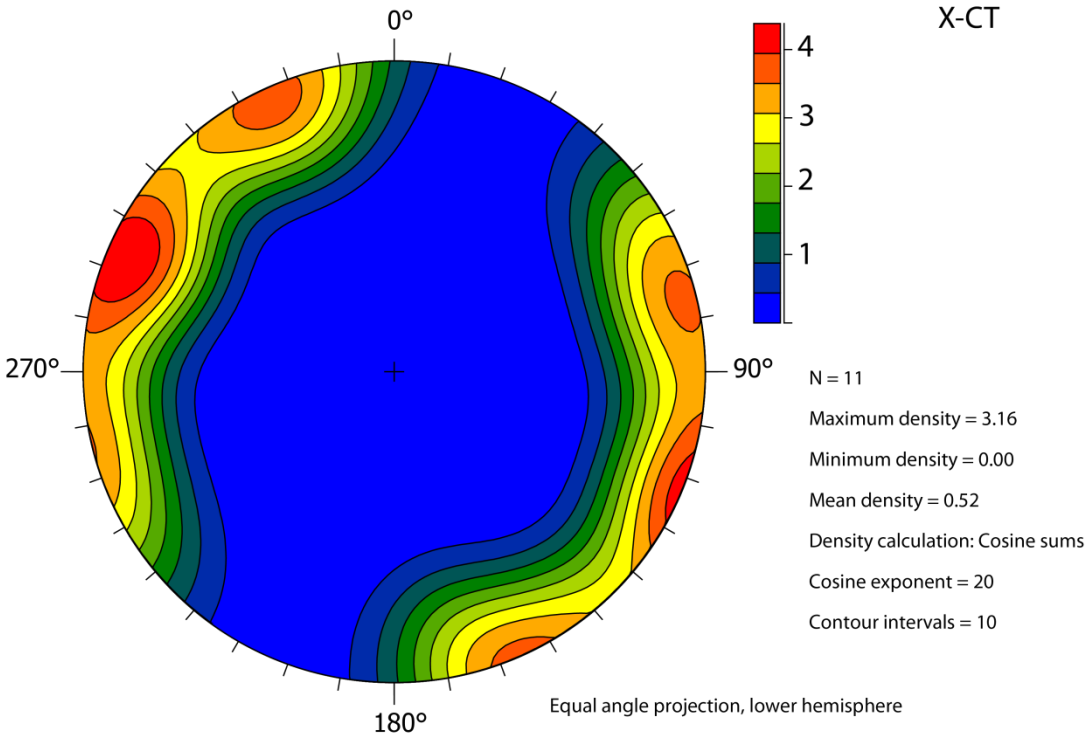

Supplementary data 1: Density maps of the preferred orientations of grains in the deposit, measured using AMS (upper) and X-CT (lower)

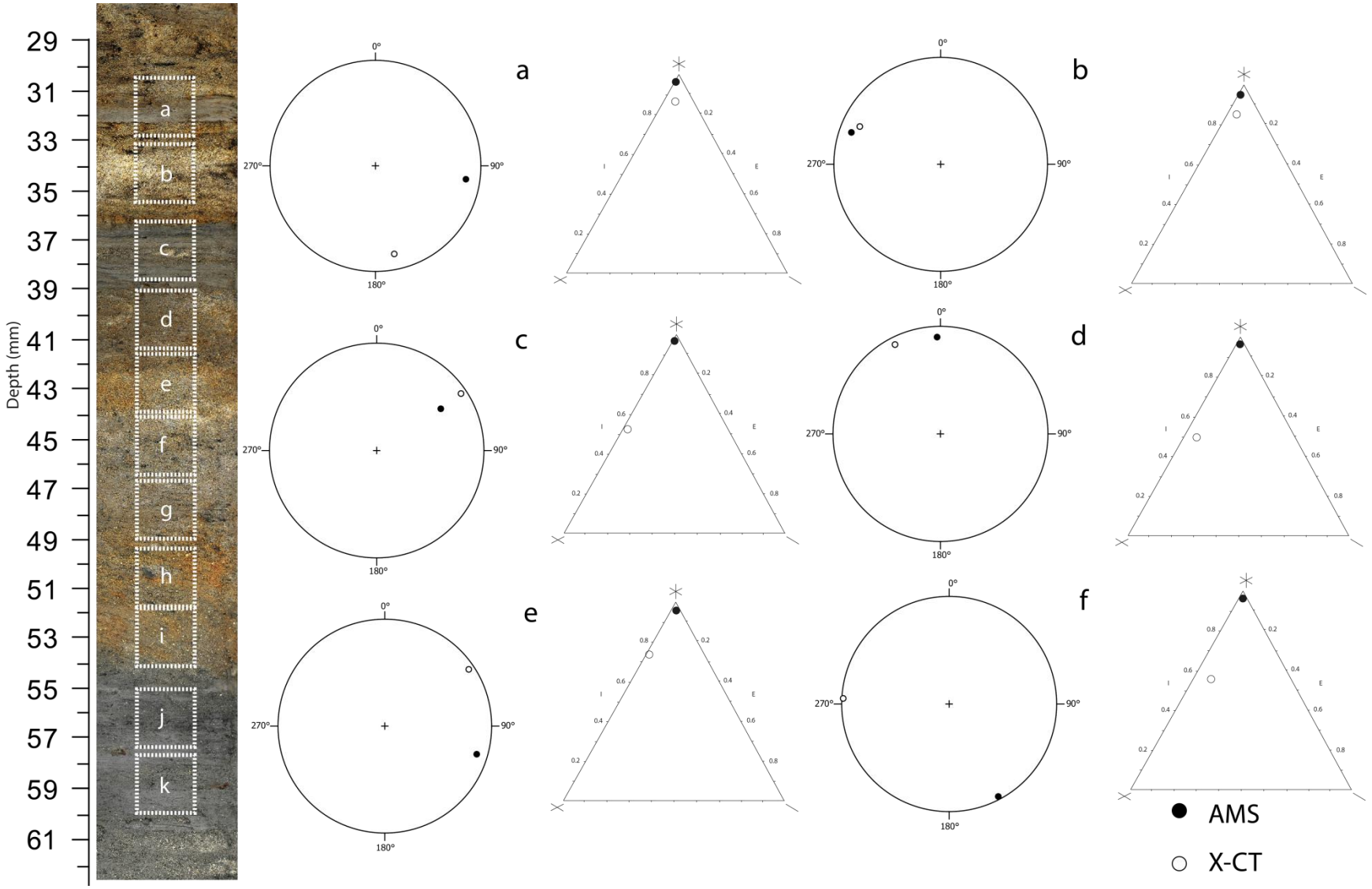
Depth (mm)
29
31
33
35
37
39
41
43
45
47
49
51
53
55
57
59
61
a
b
c
d
e
f
g
h
i
j
k
0°
90°
180°
270°
I
E
AMS
X-CT

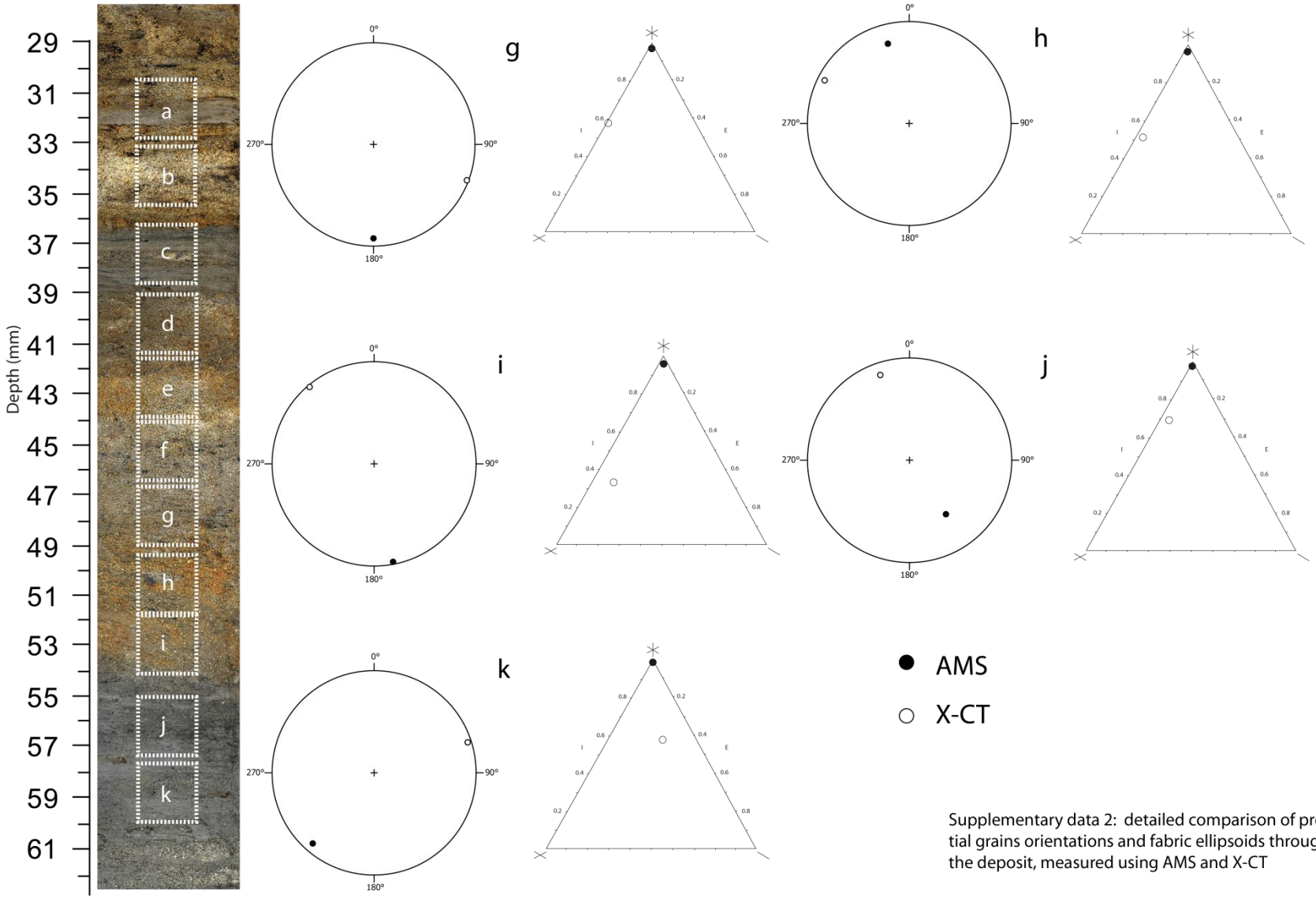

Supplementary data 2: detailed comparison of preferential grains orientations and fabric ellipsoids throughout the deposit, measured using AMS and X-CT

CHAPITRE 3 : Etude de cas – Analyse des minéraux lourds sur un transect de dépôts de tsunami - 1996 Lac Karymskoye, Kamchatka, Russie.

La tomographie par rayons X étant basée sur le principe de la détection des variations d'absorbance de l'échantillon, elle constitue un outil particulièrement adapté pour l'analyse de particules de densité particulière, comme c'est le cas des minéraux lourds. Les études d'abondance des minéraux lourds au sein de dépôts de tsunamis tendent à se multiplier mais se basent la plupart du temps sur des échantillonnages discrets en sachets (*bulk*) ou des descriptions *in situ* dans le cas de minéraux facilement identifiables (typiquement des minéraux sombres comme par exemple des oxydes métalliques, des pyroxènes, des amphiboles…), et outre les techniques de comptage sous loupe binoculaire ou sur lame sous microscope pétrographique ou MEB, il n'existe actuellement pas d'autre technique analytique quantitative permettant de les étudier.

L'article suivant présente l'étude de la distribution des minéraux lourds contenus dans les dépôts d'un tsunamis mis en place sur les rives du lac Karymskoye lors d'une éruption phréatomagmatique en janvier 1996 (étude menée dans le cadre de l'ANR VITESSS). L'origine volcanique du matériel sédimentaire déposé explique les importantes proportions de minéraux lourds (en particulier oxydes métalliques, olivine et clinopyroxènes) qu'il contient et en fait un excellent candidat pour évaluer l'apport de la tomographie par rayons X à l'étude des minéraux lourds dans les dépôts de tsunamis. La majeure partie des minéraux lourds provenant de clastes juvéniles basaltiques de l'éruption en cours, cette étude permet aussi de voir comment cette population juvénile est incorporée aux dépôts de tsunami et comment on peut en tirer des hypothèses sur les mécanismes sources de tsunami dans ce contexte particulier.

Ce troisième chapitre est présenté sous la forme d'un article qui sera prochainement soumis.

Structure and distribution of heavy minerals in tsunami deposits inferred from X-ray tomography – case of the 1996 volcanic tsunami in Karymskoye Lake, Kamchatka.

Simon Falvard[1], Raphaël Paris[1], Marina Belousova[2], Alexander Belousov[2], Thomas Giachetti[3], Stéphanie Cuven[4]

[1] Laboratoire Magmas et Volcans, Université Blaise Pascal - CNRS - IRD, OPGC, 5 rue Kessler, 63038 Clermont Ferrand

[2] Institute of Volcanology and Seismology, Petropavlosk - Kamchatsky, Russia

[3] Department of Geological Sciences, University of Oregon, Eugene, USA

[4] PalGeoSed and IODP-France, 14 Av. Edouard Belin, 31400, Toulouse, France

---

Introduction

Heavy minerals in clastic sediments and sedimentary rocks are commonly used to study diagenesis, weathering processes, sediment provenance, depositional processes, and paleoenvironmental reconstructions (e.g. Dill, 1998; Mange & Wright, 2007). Heavy minerals are often reported in tsunami deposits (e.g. Switzer et al., 2005, 2012; Bahlburg & Weiss, 2006; Szczuciński et al., 2006; Babu et al., 2007; Morton et al., 2007, 2008; Narayana et al., 2007; Higman and Bourgeois, 2008; Srinivasalu et al., 2008; Jagodziński et al., 2009, 2012; Moore et al., 2011; Costa et al., 2015). Babu et al. (2007) and Jagodziński et al. (2009) estimated higher concentration of heavy minerals in tsunami and post-tsunami sediments, compared to pre-tsunami sediments. Heavy minerals described in recent tsunami deposits are likely concentrated in pockets or laminae (e.g. Morton et al., 2007; Higman and Bourgeois, 2008; Srinivasalu et al., 2008; Jagodziński et al., 2012; Switzer et al., 2012). Jagodziński et al. (2009) noted that higher mica concentrations occurred towards the upper part of the 2004 tsunami deposits in Thailand, with mica flakes found more commonly in the finest-grained sediment samples. However, the 2011 Tohoku-oki tsunami deposits in Sendai, which are particularly rich in heavy minerals, show no different assemblage compared to other pre-tsunami sediments and no vertical trends with a 1cm-interval sampling (Jagodziński et al., 2012). This predominance of local sediments (beach, dune, soil) upon offshore sediments is

confirmed by the rarity of marine bioclasts in the 2011 tsunami deposits at Sendai (Pilarcyk et al., 2012; Szczuciński et al., 2012).

The concentration and distribution of heavy minerals in tsunami deposits is mostly source-dependent, but they are promising indicators of sediment provenance and flow dynamics. Cuven et al. (2013) concluded that "further investigations are needed to improve understanding of the spatial distribution of different populations of grains, in terms of density and shape, and their relationship to sediment sorting in tsunami deposits". In this paper, X-ray tomography is used for identifying heavy minerals and characterising their spatial distribution in tsunami deposits. The 1996 tsunami in Karymskoye Lake (Kamchatka, Eastern Siberia, Russia) is a good candidate because the heavy mineral population is mostly provided by the volcanic eruption that generated the tsunami.

1996 eruption and tsunamis in Karymskoye Lake

Karymskoye Lake fills the late Pleistocene Akademii Nauk caldera belonging to the Eastern Volcanic Belt of Kamchatka Peninsula. The lake is 4 km across, with steep flanks and a flat bottom at 60-70 m deep (Fig. 1). The ~0.5 km³ of fresh water is fed by several streams and hot springs, and drained by the Karymskaya River to the North (Belousov & Belousova, 2001). The post-caldera volcanic history is poorly documented and apparently limited to scoria cones, maars and tuff rings in the northern part of the lake (Belousov et al., 1997). Eruptive vents are aligned along a North-South fault linking the Akademii Nauk caldera to Karymsky stratovolcano, one of the most active volcanoes in Kamchatka.

After a strong earthquake on January 1st, 1996, there was an intense seismic swarm and two basaltic eruptions started simultaneously from Karymskoy Lake and from the central vent of Karymsky volcano on January 2nd (Muravyev et al., 1998). Surtseyan type phreatomagmatic activity formed a new tuff-ring attached to the northern flank of the lake. The ice sheet covering the lake might have prevented the generation of waves during the first stages of the eruption. Pyroclastic base surges damaged bushes as far as 1.3 km from the vent, at elevations up to 150 m above the level of the lake (Belousov & Belousova, 2001). Ash fall deposits extend mostly to the southeast, with a thickness decreasing from 5 cm to 1 cm. Large ballistic blocks of juvenile magma (basaltic bombs), hydrothermally rocks and rhyodacitic pumice were ejected either during an initial vent-clearing or final explosion (Grib, 1998; Belousov & Belousova, 2001). Tsunamis generated by underwater explosions were observed during helicopter flight and periodically triggered debris flows in the Karymskaya River

(Muravyev et al., 1998). Belousov & Belousova (2001) described the effects of the tsunamis on the shores of the lake, and Belousov et al. (2000) estimated wave runups. The values of runup decrease with the distance from the source, i.e. the eruptive vent, with a maximum runup of 19 m on the northwestern shore (< 1 km from the vent) and a minimum runup of 1.8 m on the southeastern shore (3 km from the vent). Boulders up to 1.3 m^3 were transported from their initial location up to 60 m inland. Soil erosion by successive tsunamis formed talus up to 2-3 m high all around the lake, except on the southern rocky shore. Sediment reworking by tsunami waves left new beaches up to 50 m wide and sandy patches on terraces behind the talus (Fig. 2). These tsunami deposits are often more than 1 m thick on the beach, but less than 30 cm on the terraces and gentle slopes. The limit of inundation can be traced by drift wood and rounded pumice lapilli (coming from old rhyolitic pyroclastic deposits of the caldera).

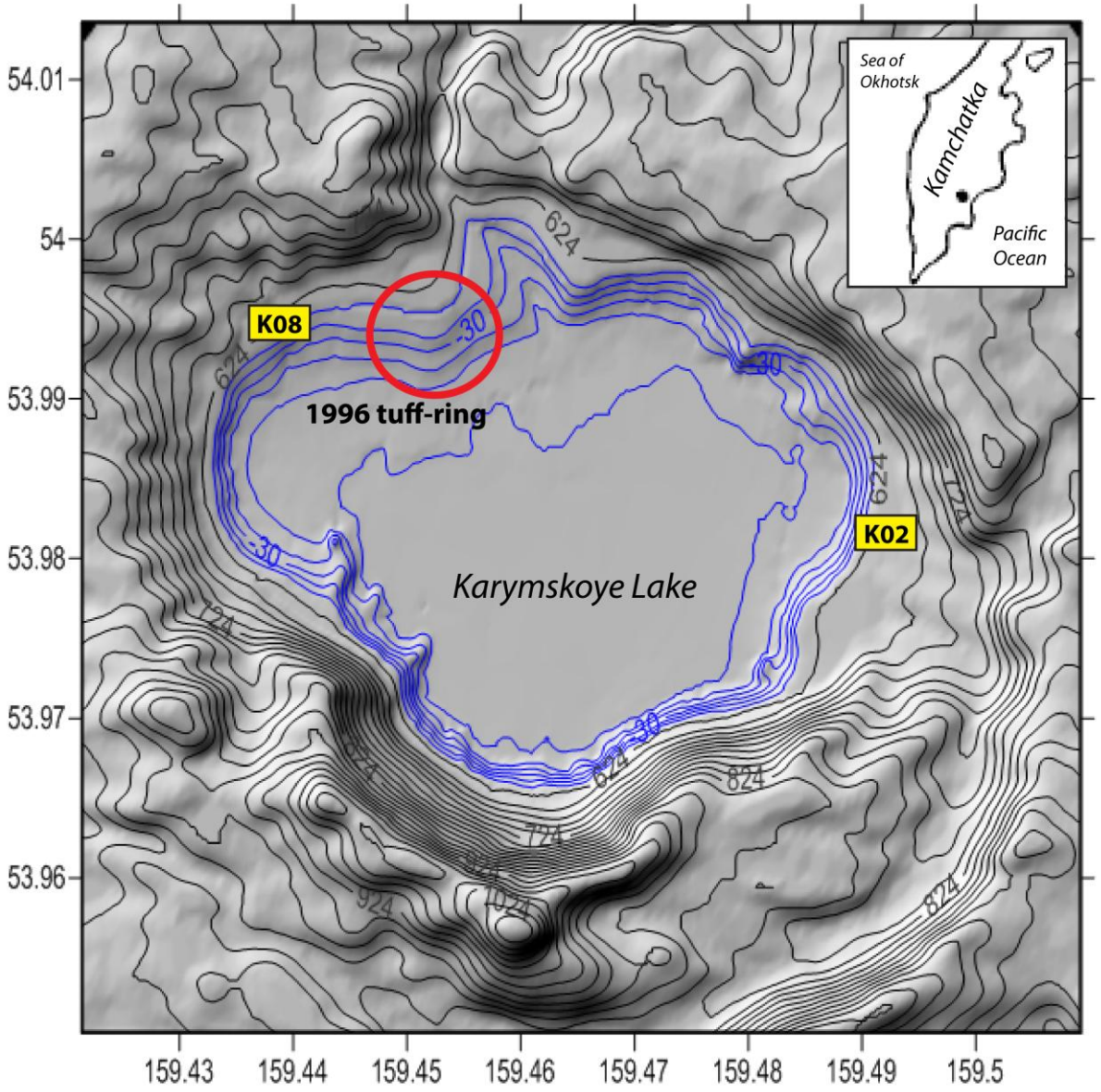

Fig. 1 – Location map of Karymskoye Lake, Kamchatka Peninsula, Russia. Bathymetric contours are in meters below the surface of the lake (624 m a.s.l.). Red circle indicates the tuff-ring formed during the 1996 eruption.

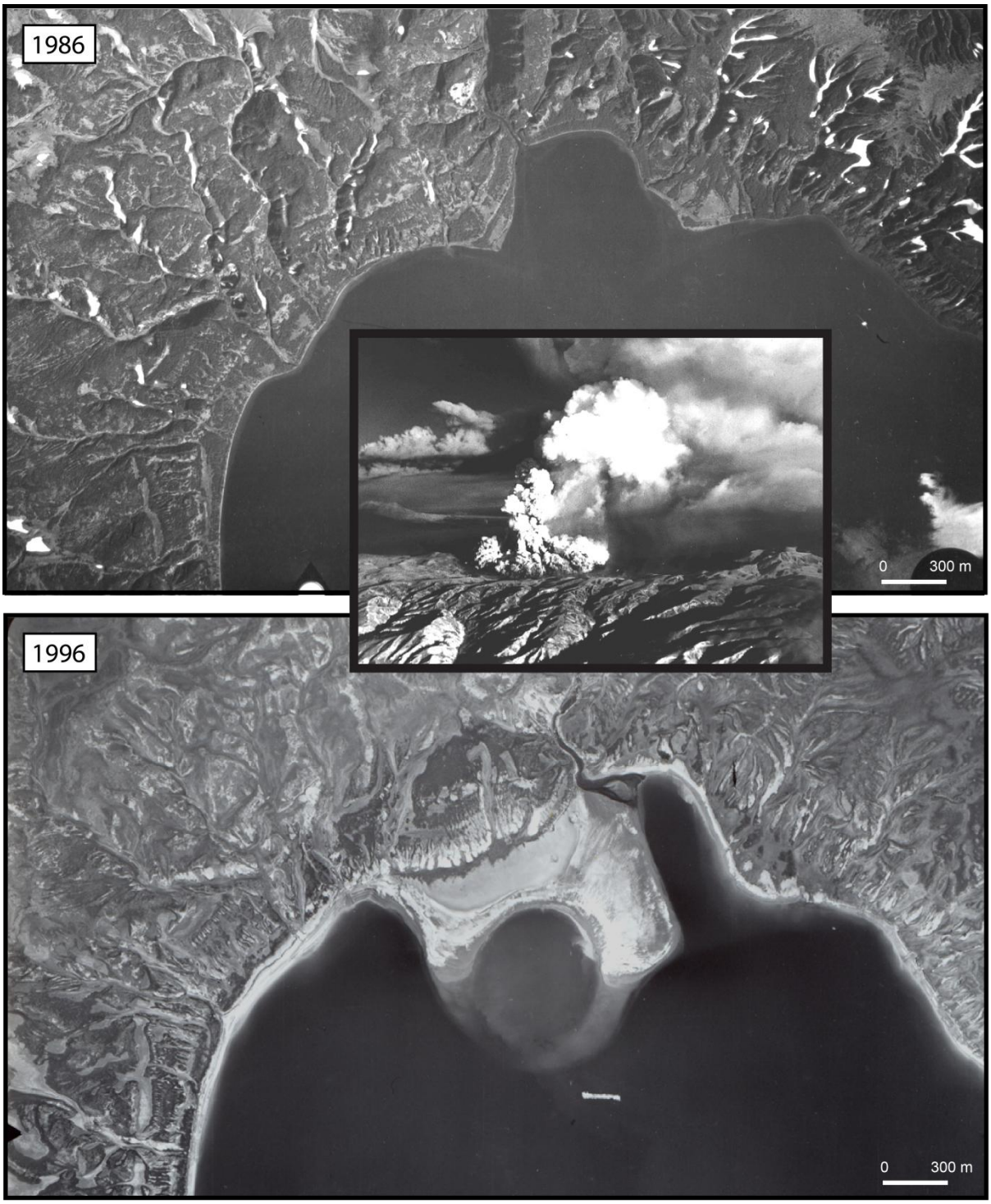

Fig. 2 – Effects of the 1996 eruption and tsunamis on the northern shore of Lake Karymskoye. Note formation of a new tuff-ring with an inner diameter of 500 m, extensive destruction of the vegetation (bush) and erosion of the shoreline, formation of new beaches, and slope erosion near the eruptive vent. Modified from Paris (2015). Photograph courtesy of Ya. D. Muravyev.

Fig. 3 – Example of sampling at site K02-9 (eastern shore of the lake). Bulk sampling of the 1996 tsunami deposit (K02-9A to K02-9D) and pre-tsunami sediments (K02-9E). The tsunami deposit is also sampled using carbon tubes (cores for X-ray tomography) and plastic boxes (for thin sections). Note the 20 cm-large rip-up clast of white ash at the base of the tsunami deposit.

Methods

Survey on the shores of Karymskoye Lake (Kamchatka, Russia) was carried out in August 2009. Tsunami deposits were retrieved in plastic boxes (blocks) and carbon tubes (cores), thus preserving their structure (Fig. 3). Bulk samples were collected along trenches for grain size analysis (laser diffraction) and composition (binocular). Thin-sections were made for each box sample using dehydration by water-acetone-epoxy-exchange, and analysed with a SEM (JEOL JSM-5910, Laboratoire Magmas & Volcans, Clermont-Ferrand, France). Chemical analyses were performed on dehydrated blocks of sediments using an Avaatech X-ray Fluorescence (XRF) core scanner (EPOC laboratory, Bordeaux). High-resolution chemical element variations were captured at the sediment surface every 500 µm with a ionization energy of 10 kv.

X-ray computed tomography (X-CT) of the tsunami sediments in carbon tubes was realised using (1) an Explore CT-120 GE Healthcare (INSERM Clermont-Ferrand) at a resolution of 50 µm per voxel, and (2) the ESRF beamline ID19 (Grenoble, France) at a resolution of 15 µm per voxel (one sample only: K02-9). X-CT is an analytical technique based on the absorption of X-rays by the sample (Hounsfield, 1962). This means that particles of different densities will appear in the images in different shades of grey. Due to their high density, heavy minerals appear in very bright grey to white tones on the X-CT images, which allowed to easily separating them from the other particles by using a simple threshold value. Particles with grey values corresponding to the heavy minerals (241 to 255 on an 8-bit image histogram) were turned white and particles and matrix of lower density were turned black. The choice of the threshold value was validated by determination of the minerals on thin sections of the same areas. The position of each heavy mineral in the core was then automatically measured and saved. Heavy minerals abundances along the cores were calculated using a 1mm subsampling step with a Matlab code (see Falvard & Paris, submitted, for more details). The higher resolution of scans performed at ESRF ID19 (15 µm per voxel) allowed measuring the intermediate diameter of each particle along a vertical slice of the sample, plotting a map of the grain size distribution and measuring GSD parameters (using Matlab codes proposed by Falvard & Paris, submitted).

For this study, we focus on 9 trenches along a 25 m long transect on the eastern shore of the lake (Fig. 4). Transect is oriented N135°, i.e. perpendicular to the shoreline. The first ten meters of the transect (trenches K02-8 and K02-9) correspond to the new beach formed during the 1996 eruption and tsunamis. The shores of the lake were vegetated by alder bush

before the tsunami. Trench K02-7 is on a gentle slope break between the beach and a terrace. The other trenches (K02-1 to K02-6) are located on this terrace that is 1-2 m above the level of the lake (624 m a.s.l.). Roots or coarse clasts prevented sampling K02-8, K02-5 and K02-6 in carbon tubes. Dehydrated blocks and thin sections were prepared for samples K02-9 (upper 10 cm only) and K02-8. Results obtained on the eastern shore of the lake are compared with a proximal section on the western shore (K08), at 1 km from the source of the tsunamis, i.e. the eruptive vent (Fig. 1).

Results

Belousov et al. (2000) measured runups between 1.8 and 2.4 m on the eastern shore of the lake. Low topography of this area favoured penetration of tsunami waves inland, up to 100 m, even if the wave heights were small compared to the other shores. Preserved thickness of the 1996 tsunami deposits progressively decreases landward, from 43 cm on the beach (K02-9) to 3 cm at 30 m from the shoreline (K02-6). This landward thinning is associated to landward fining of the mean grain size, but the tsunami deposits are internally structured in subunits with different characteristics. The contact with the underlying soil and riverbed sediments is always erosive. Rip-up clasts of soil and white compacted ash are frequent (Fig. 3).

Thickest section K02-9 displays 4 subunits (A-D). Basal unit (K02-9D) is a massive 23 cm thick dark medium sand with > 50% of fresh pyroclasts of basaltic lava and crystals (plagioclases, olivines and clinopyroxenes) from the 1996 eruption. Texture of the 1996 basaltic pyroclasts ranges from poorly to highly vesiculated, with occasional veins of rhyolite (Grib, 1998; Belousov & Belousova, 2001). Most frequent texture found in the K02 sections is blocky and poorly vesiculated. The presence of rip-up clasts of soil at the base of the subunit and crude laminations observed on X-CT excludes primary fallout deposition. Subunit KO2-9D has high concentrations of heavy minerals (olivines, clinopyroxenes and oxydes), with two pulses at > 1500 heavy minerals per mm (Fig. 5).

Second subunit 9C scours subunit 9D and a 20 cm-large rip-up clasts of white ash marks the contact (Fig. 3). Subunits 9C, 9B and 9A are all laminated: horizontal to weakly oblique laminae of coarse silt to fine sands in 9C, crudely laminated fine to coarse sands in 9B, and cross-laminae of very fine to medium sands in 9A (Fig. 6 and 7). Similar laminations are observed on section K02-8. Compared to the dark sand of basal subunit 9D, the other subunits have less 1996 juveniles (< 40 %) and less heavy minerals (< 700 per mm), but more pumice (> 20 %) and rare diatoms in subunit 9A. The distribution of pumice clasts in the tsunami deposits is not homogenous. Sublayers or lines enriched in pumices (40-90 %) coinciding with peaks of Si/Ca were identified on thin sections and X-CT (Fig. 8). Here, the concentration of heavy minerals (X-CT) is not grain-size dependent and correlates with peaks of Fe/Al and Ca/Al, which represent respectively higher concentrations of oxydes and olivines, and clinopyroxenes (Fig. 6).

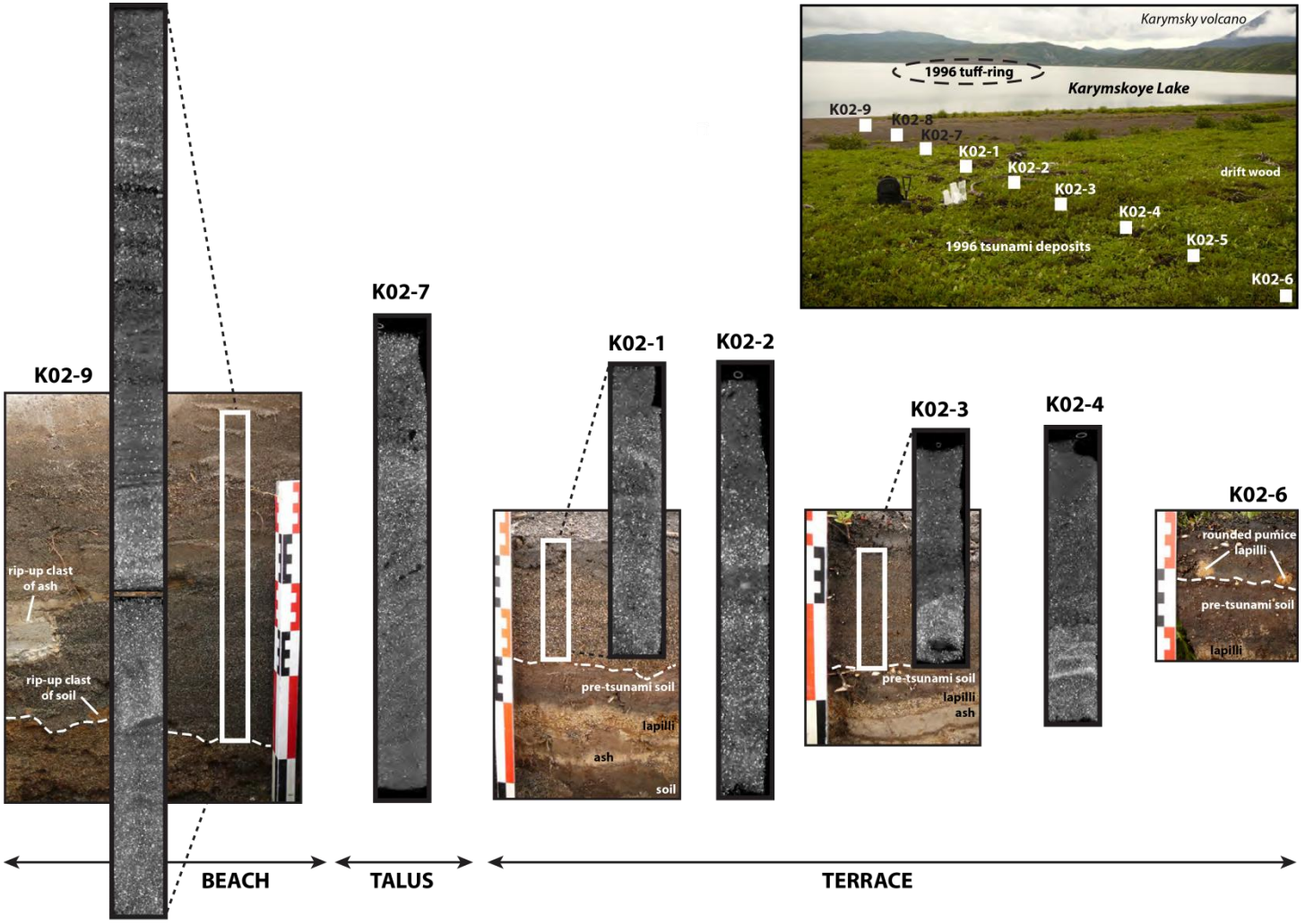

Fig. 4 – Longitudinal transect in the 1996 tsunami deposit on the eastern shore of Karymskoye Lake. The tsunami was generated by underwater explosions from the tuff-ring (dotted circle). X-ray tomography was performed on 6 core samples.

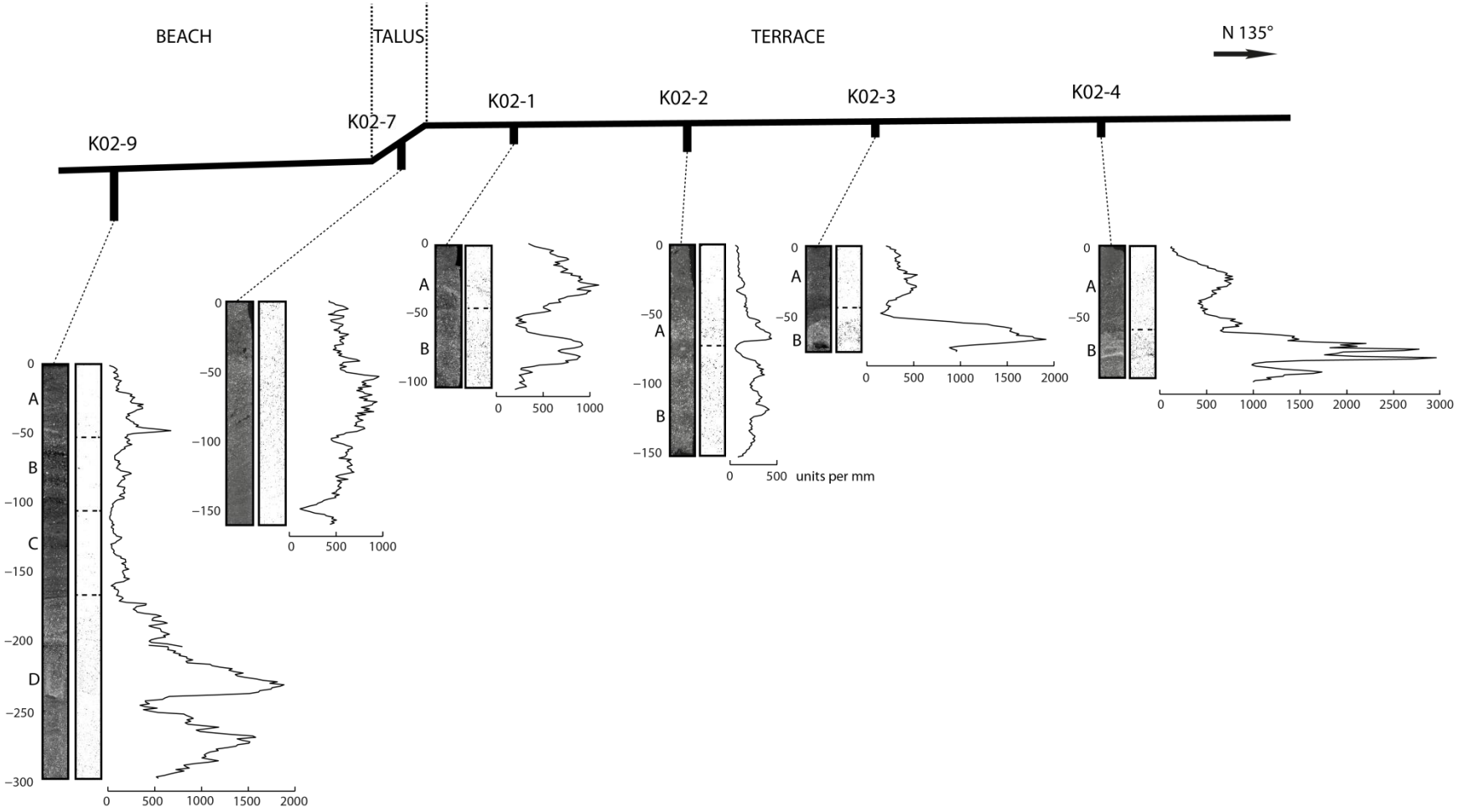

Fig. 5 – Image mapping and concentration of heavy minerals (units: number of minerals per mm) inferred from X-CT on cores of tsunami deposits. See figure 4 for location of the sections.

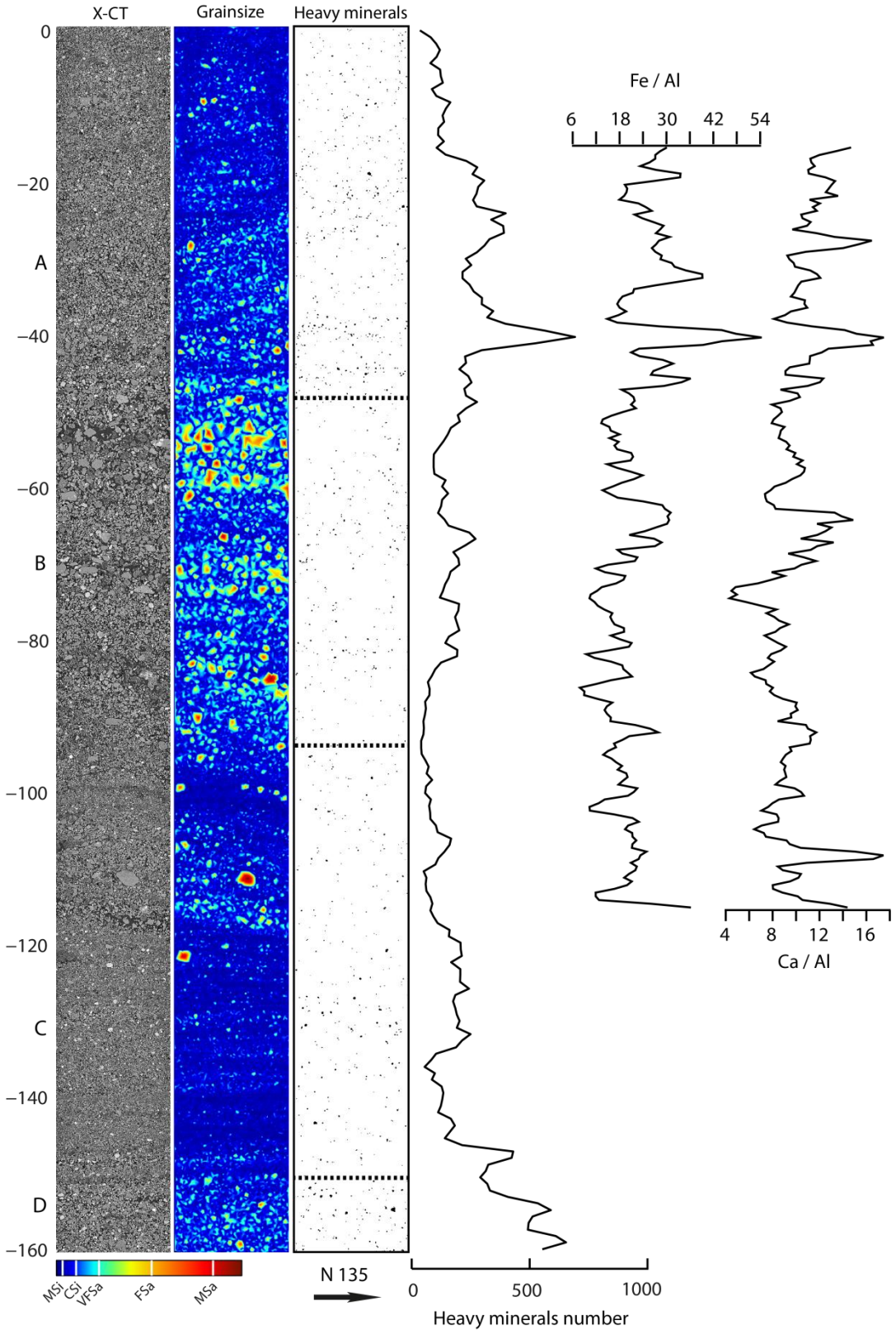

Fig. 6 – Concentration of heavy minerals (X-CT, units per mm) compared to grain size (image analysis of X-CT), and major element chemistry (XRF) of the upper part of section K02-9 (subunits A, B and C). The Fe/Al and Ca/Al profiles represent respectively higher concentrations of oxydes + olivines, and clinopyroxenes.

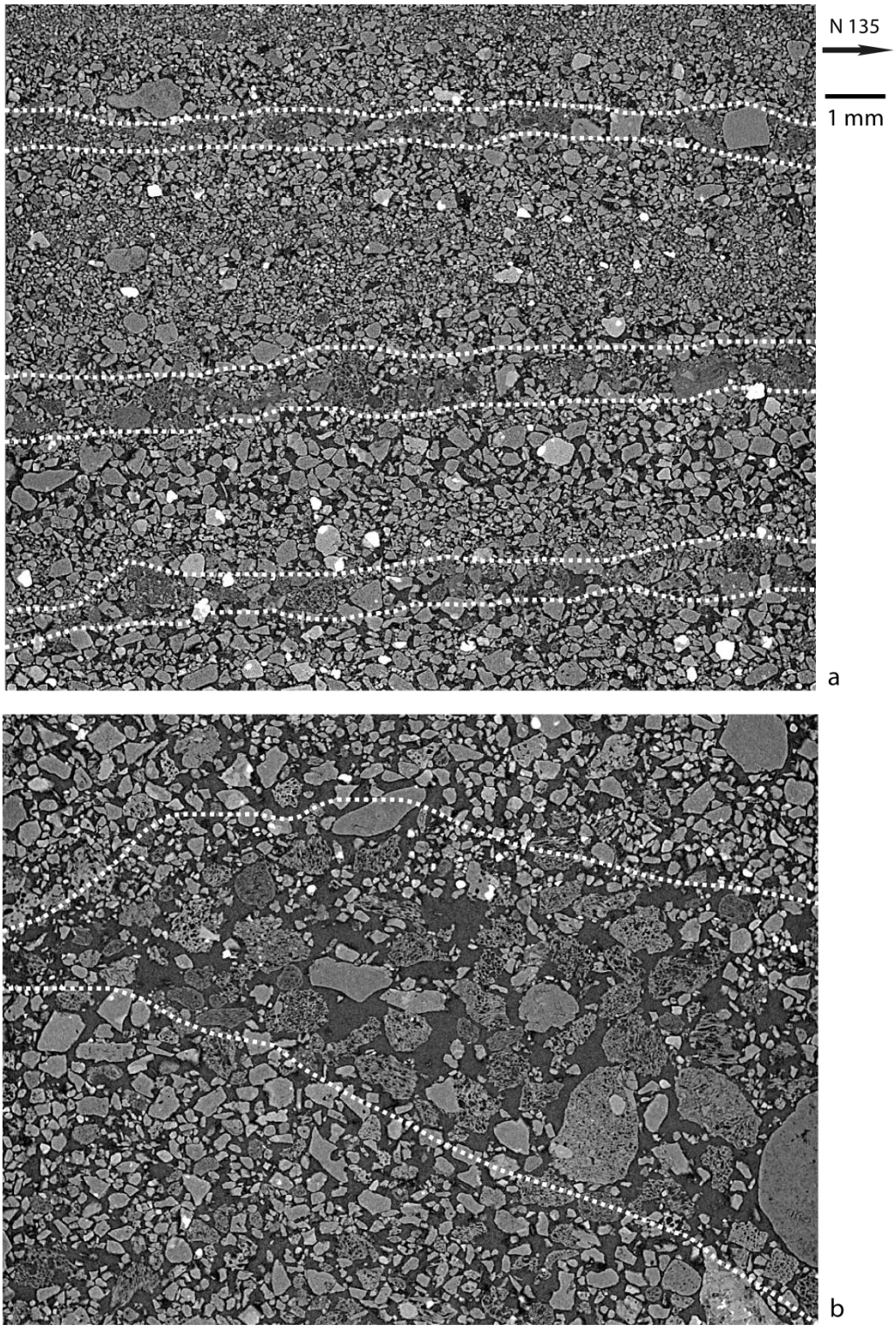

Fig. 7 : Cropped views of K02-9 sample scanned at ESRF. The resolution is 15 micrometre/voxel. The heavy mineral appear in bright white and are very easy to identify throughout the deposit. a - subhorizontal laminations in the intermediate part of the deposit (subunit C). Almost invisible to the naked eye, they appear clearly on the scans due to the low density of pumices intercalated between sand grains. b - Landward plunging stratification in the upper part of the deposit (subunit A), mostly composed of coarse pumices (notice the typical vesiculation inside the grains) and large volumes of air matrix between layers of finer sands and silts.

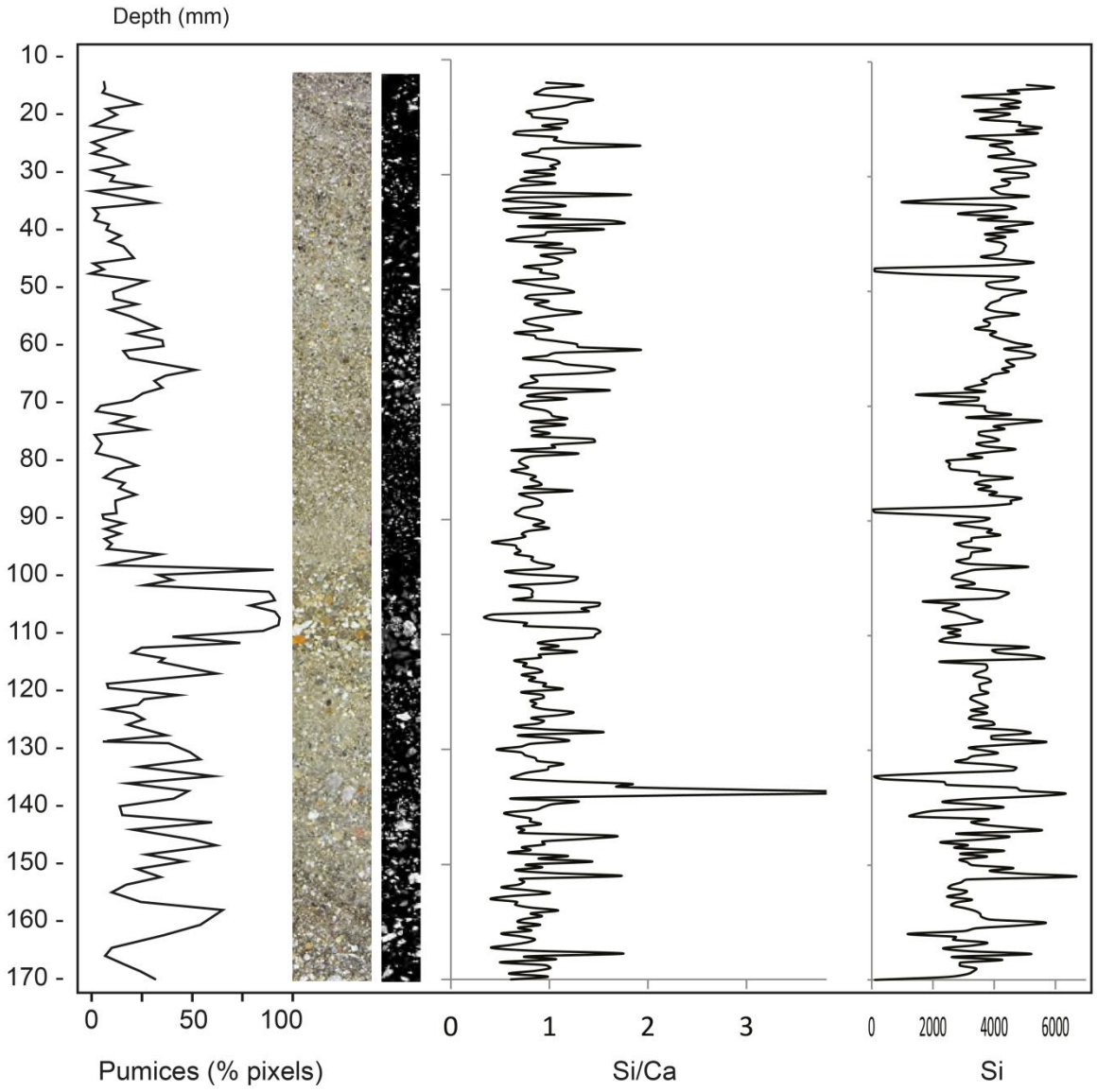

Fig. 8 – Distribution of pumices estimated from image analysis of thin sections at the SEM and Si/Ca profile inferred from XRF scan of dehydrated block (sample K02-8).

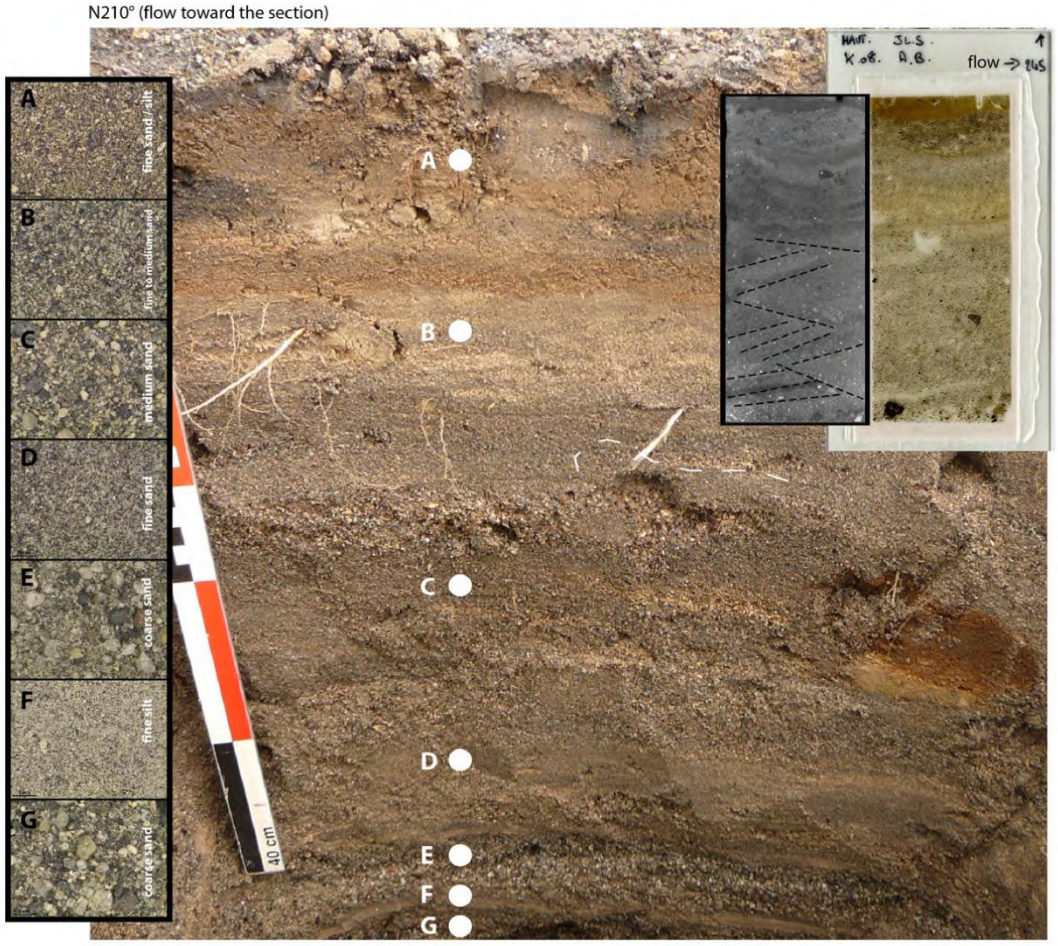

Fig. 9 – Overview of section K08 (western shore of the lake). The 1996 tsunami deposit represents the entire thickness trenched and is organised in distinct subunits, which are all laminated (except subunit K08-E and lenses of coarse sand in K08-C). Note the rip-up clasts of soil and ash on the right side and the backset cross-laminae in subunit K08-B (X-CT).

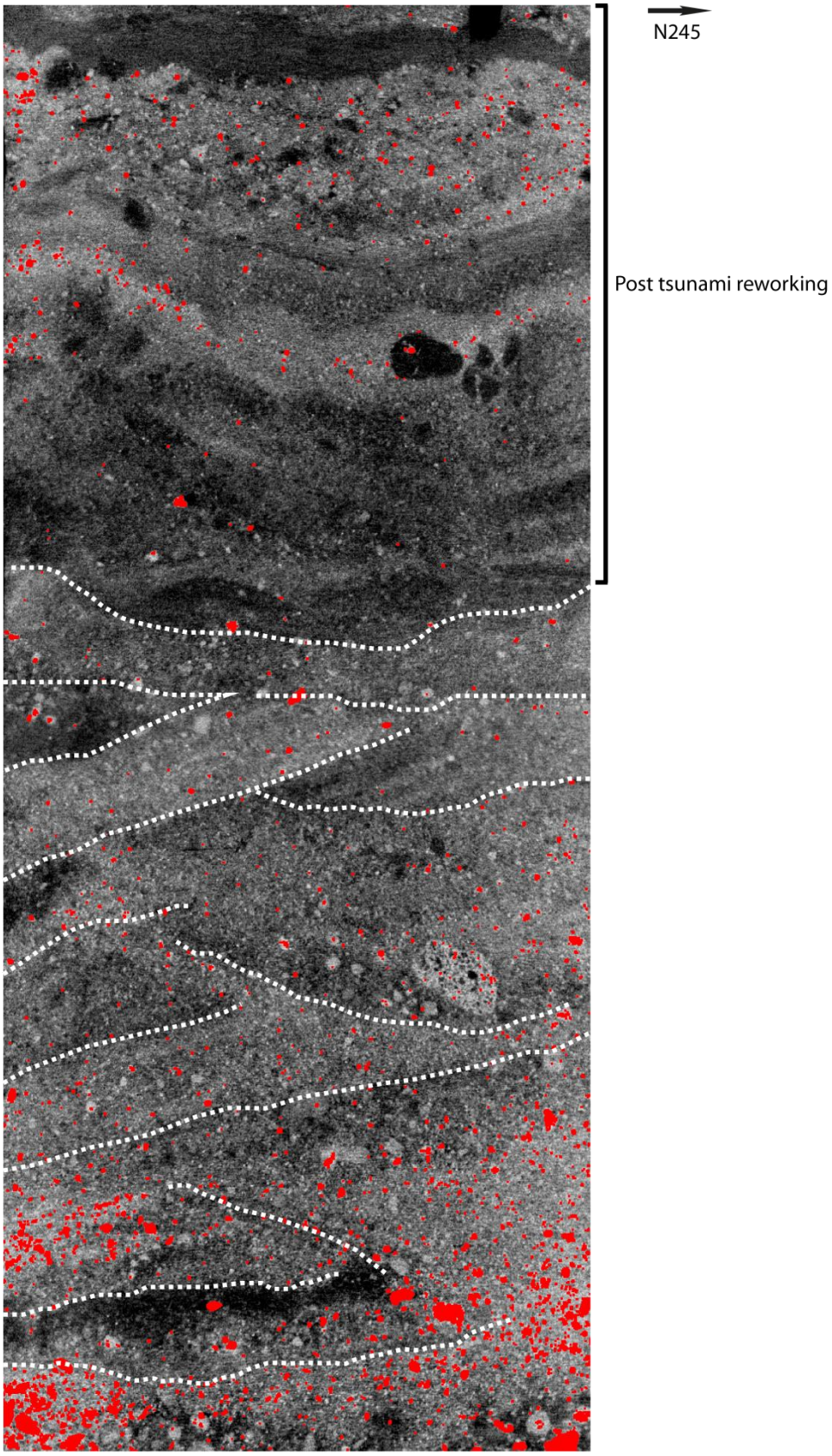

Fig. 10 – Heavy minerals (in red) and cross-bedded laminae of the upper part of the K08 section, western shore of the lake.

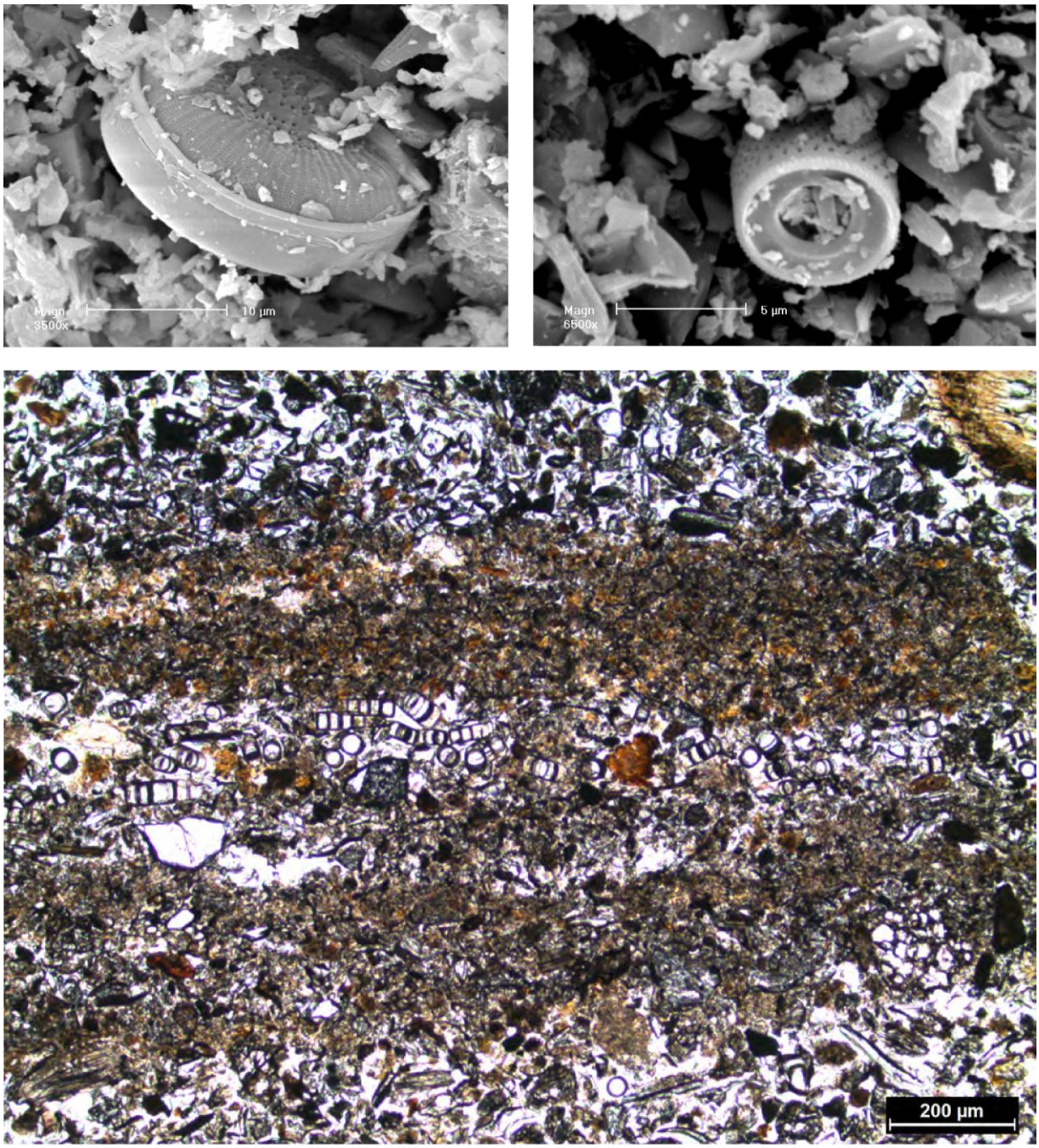

Fig. 11 - Diatoms in tsunami sample K08 viewed at the SEM and in thin sections. The distribution of diatoms in the 1996 tsunami deposits is not random, and fine-grained sub-layers or lines enriched in diatoms can be seen at the base of coarser subunits.

Despite its small size and smooth morphology, the talus between the beach and the terrace (Fig. 4) affected the depositional processes, as evidenced by the structure and texture of tsunami deposits attached to the slope. There are no subunits longer visible on section K02-7, which is obliquely laminated and inversely graded from very fine sand at the base to medium sand at the top. Inverse grading is coupled with an upward increase of the concentration of heavy minerals (Fig. 5). Lamination is dipping downward, the angle being similar to the topography of the talus.

Located at the foot of the talus, section K02-1 is poorly organised and no internal structure and vertical grading could be detected on the field. However, X-CT allows distinguishing two successive pulses of medium-to-coarse sand particularly rich in heavy minerals, separated by a horizontal laminae of very fine sands with less heavy minerals (at -5 cm on fig. 5). Same structure is found on the following sections (K02-2 to K02-6), with lower concentrations of heavy minerals at K02-2 (< 500 per mm) and higher concentrations at the base of sections K02-3 and K02-4 (> 1500 per mm). High concentrations of heavy minerals are associated to high proportions (> 50 %) of juvenile material from the 1996 eruption such as basaltic pyroclasts and phenocrysts of plagioclase, olivine, and clinopyroxene.

Similar stratigraphy was found on other trenches located along the eastern shore of the lake. In this area, terraces higher than 2 m systematically prevented the deposition of sediments by tsunami waves further inland. When tsunami deposits are constrained to the new beach, their thickness often increases landward until the talus of the terrace.

High terraces or steep slopes of the western side also limited inundation and deposition to the beach, where the 1996 tsunami deposits are particularly thick (commonly > 50 cm). Belousov et al. (2000) reported wave runups higher than 5 m in this area (note that the maximum values of runup are controversial because located in areas also affected by pyroclastic surges). Due to a different topographic setting and closer distance to the source, the structure of the 1996 tsunami sequence is different. Section K08 displays a complex succession of laminated sands and silts characterised by abrupt variations of grain size (Fig. 9). The base of the tsunami deposit is unclear and more than 7 subunits can be distinguished. Low-resolution X-CT on a dehydrated block allows identifying cross-laminae in the upper part of the sequence (subunit K08-B on fig. 9). This cross-bedding is not associated to any particular distribution of heavy minerals (Fig. 10). Deposits sampled along the western shore of the lake are particularly rich in diatoms. The distribution of diatoms is not random, and fine-grained sub-layers or lines enriched in diatoms can be seen at the base of coarser subunits (Fig. 11). Although being located at 1 km from the eruptive vent and near the limit of

pyroclastic surges, 1996 tsunami deposits of the western shore have always less than 30 % of juvenile clasts from the 1996 eruption.

Discussion

X-CT proved to be a useful technique to detect heavy minerals in the deposit, with measured abundances ranging from several dozens to 3000 units per millimetre in the samples (Fig. 5), and despite a limited resolution (50 µm for INSERM scans). Comparing grain size data and heavy mineral abundances in the upper part of K02-9 (Fig. 6) shows that the distribution of heavy minerals along the deposit is not random and not grain size dependent. Subunits enriched in heavy minerals are clearly evidenced by the X-CT data. These remarks are also valid for the pumice clasts (Fig. 8), whose behaviour in water waves is probably different from heavy minerals (except micas in a certain extent due to their flaky shapes, but none were found in these deposits). However, heavy minerals in the 1996 tsunami deposits are never distributed along thin laminae, as often described in other tsunami deposits (e.g. Morton et al., 2007; Higman and Bourgeois, 2008; Srinivasalu et al., 2008; Jagodziński et al., 2012; Switzer et al., 2012).

Distribution of heavy minerals together with the structure and texture of the tsunami deposits of the lower trenches, i.e. forming the new beach (e.g. K02-9 and K08), suggest that multiple tsunamis were produced during the volcanic eruption. It is worth reminding that most of the explosions were not tsunamigenic, as they simply produced a single, near-vertical, column-like jet of gas and pyroclasts that collapsed back into the lake, thus generating a subtle base surge (Belousov & Belousova, 2001). Strongest observed explosions started with a rapidly rising (~3 s), smooth-surfaced bulbous mass of gas and pyroclasts expanding within a shell of water up to 450 m high. This mass then became unstable and was pierced by cypressoid jets of pyroclasts with gas and water. Simultaneously, a bore-like elevation of the water surface started to propagate radially at about 20–40 $m.s^{-1}$ thus forming a tsunami in the lake (Muravyev et al., 1998; Belousov & Belousova, 2001). This description represents the mature stage of the eruption, and there are no observations available for the initial and final stages.

Initial stage of volcanic activity started at a water depth of 45-50 m, but the depth of fragmentation is not known. First explosions occurred as the surface of the lake was still covered by a 1m-thick icecap and they could not generate tsunamis. The products of these initial explosions were trapped under the icecap and deposited on the bottom and flanks of the

lake. During a transitional stage, the eruption progressively broke the ice surface and fallout pyroclasts started to accumulate on ice rafts. We can postulate that the first tsunamis pushed ice rafts with pyroclasts on the shores plus reworked pyroclasts accumulated on the flanks of the lake following the initial explosions. For areas which were not affected by important pyroclastic fallout (e.g. less than 3 cm of ash on the eastern shore), this hypothesis could explain the high proportion of juvenile material (and heavy minerals) in the thick basal subunit of tsunami deposits (Figs 3).

The two peaks of heavy minerals in subunit K02-9D highlights two successive pulses or waves (Fig. 5). This is concordant with the typical scenario of wave trains generated by underwater explosions. Indeed, the expansion, rise and gravitational collapse of a water crater produced by an explosion typically generate two successive bores followed by a number of smaller undulations propagating radially from the source (Paris, 2015). Note that this source mechanism slightly differs from the shallower explosions described by Muravyev et al. (1998) and Belousov & Belousova (2001) during the mature stage of the eruption. Two-peak distribution of heavy minerals is also clear on sections located on the terrace of the eastern shore (Fig. 5: sections K02-1 to K02-4). This transect-scale correlation means that a major tsunami consisting of two main waves occurred at a transitional stage of the eruption (not observed) and inundated the terrace up to 100 m inland on the eastern shore of the lake. The term transitional is used because it corresponds to the end of the initial non-tsunamigenic stage with the lake covered by ice, and the onset of the observed mature stage of activity (as observed during helicopter flights (Muravyev et al., 1998).

This scenario contradicts the interpretation of Belousov & Belousova (2001) who argued that the largest tsunamis occurred at the end of the eruption. However, it is difficult to imagine how explosions might have generated large waves when the tuff ring was already well developed and thus water depth reduced (compared to the previous stages of eruption). Magma-water interactions during phreatomagmatic eruptions are complex and their physics is controlled by water depth, geometry of the vent and magma-water interface, transfer of thermal energy, processes of intermingling and mixing between magma and water, metastability of superheated water, and quantity of gas in the ascending magma (Kokelaar, 1986; Wohletz, 1986; Morrissey et al., 2010). Violent steam explosions of eruptions forming maars and tuff rings, as occurred at Taal in 1965 and Karymskoye in 1996, are potentially more tsunamigenic than Surtseyan and other emergent volcanic activities (Paris, 2015).

After the largest one, other tsunamis impacted the shores of the lake, leaving multi-bedded deposits (e.g. K08) whose distribution is limited to the beach (< 1.50 m above the

level of the lake). These second-phase tsunami deposits are less rich in heavy minerals (Fig. 5). Orientation of the laminations in the upper part of section K02-9 (Fig. 6 and 7) indicates transitions from upper plane beds (horizontal lamination) to low-angle beds dipping landward (dunes). Capping subunits are often cross-bedded (Fig. 6 and 10), with either backset orientation if we consider that it was deposited by an uprush flow of the upper regime (antidunes), or foreset orientation if it corresponds to a final backwash or drainout of the lake.

Conclusion

X-CT helped evidencing the structure and characterising the distribution of heavy minerals in the 1996 tsunami deposits. In this case study, the source of the heavy minerals was controlled by the volcanic eruption that generated the tsunamis. A new scenario of the events is proposed:

(1) Accumulation of juvenile basaltic pyroclasts (main source of heavy minerals) in the lake, under the icecap, during the initial stage of the eruption. No tsunamis.

(2) Transitional stage corresponding to strong emergent explosions in a partially frozen lake. Major tsunami pushes ice rafts to the shores and leaves tsunami deposits rich in juvenile material up to the terraces. Runup values measured by Belousov et al. (2000) might represent this tsunami. One of the vent-clearing phreatic explosions which ejected blocks of country rocks up to 3 m diameter at distances of up to 1.3 km (Belousov & Belousova, 2001) could be the source of this major tsunami.

(3) Mature stage observed during helicopter flights (Muravyew et al. (1998) consisting in successive phreatomagmatic explosions, some which being tsunamigenic. Magnitude of the tsunamis generated during this phase is lower than the previous one (no deposition on the terraces). Tsunami deposits representing this phase have lower abundance of heavy minerals, although being contemporaneous with ash fallout.

(4) Dam break at the head of the Karymskaya River and drainout of the lake 5 months after the end of the eruption, reworking the surface of the tsunami deposits and tuff-ring (ripples mentioned by Belousov & Belousova, 2001).

This study confirms that X-CT is a powerful technique for characterising tsunami deposits (Falvard & Paris, submitted), and takes advantage of the particularity of tsunami deposits related to a phreatomagmatic eruption. Our interpretation of the sedimentary sequences provides another evidence of volcanic eruption reconstructed using its tsunami

record (Paris et al., 2014), and a coupled eruption-tsunami scenario that could be used for defining hazard scenarios in other volcanic lakes.

Acknowledgments

This study was funded by the Conseil Régional d'Auvergne, project TSUNAMIX, and by the French National Research Agency, project ANR 08-JCJC-0042 VITESSS (Volcano-Induced Tsunamis: Sedimentary Signature and numerical Simulation). The authors are particularly grateful to Elisabeth Miot-Noirault (INSERM, Clermont-Ferrand), Paul Tafforeau and Elodie Boller (ID 19 ESRF, Grenoble), Isabelle Billy (EPOC CNRS, Bordeaux), and all participants of the survey to Karymskoye Lake. This is ClerVolc Laboratory of Excellence contribution number XXX.

References

Babu, N., Babu, D., Das, P., 2007. Impact of tsunami on texture and mineralogy of a major placer deposit in southwest coast of India. Environmental Geology 52, 71-80.

Bahlburg, H., Weiss, R., 2006. Sedimentology of the December 26, 2004 Sumatra tsunami deposits in eastern India (Tamil Nadu) and Kenya. International Journal of Earth Sciences 96 (6), 1195-1209.

Belousov, A., Belousova, M., Muravyev, Y., 1997. Holocene eruptions in Akademiya Nauk caldera and the age of Karymsky stratovolcano, Kamchatka. Transactions of the Russian Academy of Sciences, Earth Sciences Section 335, 653-657.

Belousov, A., Voight, B., Belousova, M., Muravyev, Y.D., 2000. Tsunamis generated by subaquatic volcanic explosions: unique data from 1996 eruption in Karymskoye lake, Kamchatka, Russia. Pure and Applied Geophysics 157, 1135–1143.

Belousov, A., Belousova, M., 2001. Eruptive process, effects and deposits of the 1996 and ancient basaltic phreatomagmatic eruptions in Karymskoye lake, Kamchatka, Russia. In: White, J., Riggs, N. (eds.) Volcaniclastic Sedimentation in Lacustrine Settings. Blackwell, International Association of Sedimentologists Special Publications, 30, 235–260.

Chagué-Goff, C., Schneider, J.L., Goff, J.R., Dominey-Howes, D., Strotz, L., 2011. Expanding the proxy toolkit to help identify past events – Lessons from the 2004 Indian

Ocean Tsunami and the 2009 South Pacific Tsunami. Earth-Science Reviews 107, 107-122.

Cheel, R.J., 1984. Heavy mineral shadows, a new sedimentary structure formed under upper flow regime conditions: its directional and hydraulic significance. Journal of Sedimentary Petrology 54, 1173-1180.

Costa, P.J.M., Andrade, C., Cascalho, J., Dawson, A.G., Freitas, M.C., Paris, R., Dawson, S., 2015. Onshore tsunami sediment transport mechanisms inferred from heavy mineral assemblages. The Holocene 25 (5), 795-809.

Cuven, S., Paris, R., Falvard, S., Miot-Noirault, E., Benbakkar, M., Schneider, J.-L., Billy, I., 2013. High-resolution analysis of a tsunami deposit: Case-study from the 1755 Lisbon tsunami in southwestern Spain. Marine Geology 337, 98-111.

Dill, H.G., 1998. A review of heavy minerals in clastic sediments with case studies from the alluvial-fan through the nearshore-marine environments. Earth-Science Reviews 45, 103-132.

Falvard, S., Paris, R., 2016. X-ray tomography of tsunami deposits: towards a new depositional model of tsunami deposits. Submitted to Sedimentology.

Grib, E.N., Petrology of ejecta

Higman, B., Bourgeois, J., 2008. Deposits of the 1992 Nicaragua tsunami. In: Shiki, T., Tsuji, Y., Yamazaki, T., Minoura, K. (Eds.), Tsunamiites – features and implications. Elsevier, pp. 81-103.

Hounsfield, G.N., 1962. Computerized transverse axial scanning (tomography): Part 1. Description of system. British Journal of Radiology 46 (552), 1016-1022.

Jagodziński, R., Sternal, B., Szczuciński, W., Lorenc, S., 2009. Heavy minerals in 2004 tsunami deposits on Kho Khao Island, Thailand. Polish Journal of Environmental Studies 18, 103–110.

Jagodziński, R., Sternal, B., Szczuciński, W., Chagué-Goff, C., Sugawara, D., 2012. Heavy minerals in the 2011 Tohoku-oki tsunami deposits – insights into sediment sources and hydrodynamics. Sedimentary Geology 282, 57-64.

Mange, M.A., Wright, D.T. (eds.), 2007. Heavy minerals in use. Developments in Sedimentology 58, Elsevier, 1283 p.

Moore, A., Goff, J., McAdoo, B.G., Fritz, H.M., Gusman, A., Kalligeris, N., Kalsum, K., Susanto, A., Suteja, D., Synolakis, C.E., 2011. Sedimentary deposits from the 17 July 2006 Western Java tsunami, Indonesia: use of grain size analyses to assess tsunami flow

depth, speed, and traction carpet characteristics. Pure and Applied Geophysics 167 (11), 1951-1961.

Morton, R.A., Gelfenbaum, G., Jaffe, B.E., 2007. Physical criteria for distinguishing sandy tsunami and storm deposits using modern examples. Sedimentary Geology 200, (3-4), 184-207.

Morton, R.A., Goff, J.R., Nichol, S.L., 2008. Hydrodynamic implications of textural trends in sand deposits of the 2004 tsunami in Sri Lanka. Sedimentary Geology 207 (1-4), 56-64.

Muravyev, Y.D., Fedotov, S.A., Budnikov, V.A., Ozerov, A.Y., Magus'kin, M.A., Dvigalo, V.N., Andreyev, V.I., Ivanov, V.V., Kartasheva, L.A., Markov, I.A., 1998. Volcanic activity in the Karymsky center in 1996: summit eruption at Karymsky and phreatomagmatic eruption in the Akademii Nauk caldera. Volcanology and Seismology 19, 567-604.

Narayana, A.C., Tatavarti, R., Shinu, N., Subeer, A., 2007. Tsunami of December 26, 2004 on the southwest coast of India: post-tsunami geomorphic and sediment characteristics. Marine Geology 242, 155-168.

Paris, R., Wassmer, P., Lavigne, F., Belousov, A., Belousova, M., Iskandarsyah, Y., Benbakkar, M., Ontowirjo, B., Mazzoni, N., 2014. Coupling eruption and tsunami records: the Krakatau 1883 case-study, Indonesia. Bulletin of Volcanology 76, 814.

Paris, R., 2015. Source mechanisms of volcanic tsunamis. Philosophical Transactions of the Royal Society A 373, 20140380.

Pilarcyk, J.E., Horton, B.P., Witter, R.C., Vane, C.H., Chagué-Goff, C., Goff, J., 2012. Sedimentary and foraminiferal evidence of the 2011 Tohoku-oki tsunami on the Sendai coastal plain, Japan. Sedimentary Geology 282, 78-89.

Srinivasalu, S., Thangadurai, N., Jonathan, M.P., Armstrong-Altrin, J.S., Ayyamperumal, T., Ram Mohan, V., 2008. Evaluation of trace-metal enrichments from the 26 December 2004 tsunami sediments along the Southeast coast of India. Environmental Geology 53, 1711-1721.

Switzer, A., Pucillo, K., Haredy, R., Jones, B., Bryant, E., 2005. Sea level, storm, or tsunami: enigmatic sand sheet deposits in a sheltered coastal embayment from southeastern New South Wales, Australia. Journal of Coastal Research 21, 655-663.

Switzer, A., Srinivasalu, S., Thangadurai, N., Mohan, W.R., 2012. Bedding structures in Indian tsunami deposits that provide clues to the dynamics of tsunami inundation. Geological Society, London, Special Publication 361, 61-77.

Szczuciński, W., Chaimanee, N., Niedzielski, P., Rachlewicz, G., Saisuttichai, D., Tepsuwan, T., Lorenc, S., Siepak, J., 2006. Environmental and geological impacts of the 26 December 2004 tsunami in coastal zone of Thailand – overview of short and long-term effects. Polish Journal of Environmental Studies 15 (5), 793-810.

Szczuciński, W., Kokociński, M., Rzeszewski, M., Chagué-Goff, C., Cachao, M., Goto, K., Sugawara, D., 2012. Sediment sources and sedimentation processes of 2011 Tohoku-oki tsunami deposits on the Sendai Plain, Japan – insights from diatoms, nannoliths and grain size distribution. Sedimentary Geology 282, 40-56.

Torsvik, T., Paris, R., Didenkulova, I., Pelinovsky, E., Belousov, A., Belousova, M., 2010. Numerical simulation of explosive tsunami wave generation and propagation in Karymskoye Lake, Russia. Natural Hazards and Earth System Sciences 10 (11), 2359-2369.

Ulvrová, M., Paris, R., Kelfoun, K., Nomikou, P., 2014. Numerical simulations of tsunami generated by underwater volcanic explosions at Karymskoye Lake (Kamchatka, Russia) and Kolumbo volcano (Aegean Sea, Greece). Natural Hazards and Earth System Sciences 14, 401-412.

CHAPITRE 4 : Identification d'un paléotsunami et caractérisation de la fabrique sédimentaire par tomographie aux rayons X (Ouest Australie).

L'une des problématiques liée aux paléotsunamis consiste a pouvoir clairement les identifier et caractériser leurs dépôts. La tomographie par rayons X présente l'intérêt de permettre à la fois des analyses structurales et texturales sur les mêmes échantillons, mais également de pouvoir être réalisée sur virtuellement n'importe quel type d'échantillon solide, les limites étant seulement imposées par l'équipement à disposition pour l'acquisition des images.

Dans le cadre de cette étude conduite par Simon Matthias May, des carottes en tube PVC de 6 cm de diamètre ont été récupérées à Ninety Mile Beach (ouest de l'Australie) et scannées à l'Université de Ghent (Belgique), à une résolution de 50µm par voxel (scannées où ?). Leur analyse nous a permis d'obtenir non seulement des données structurales précises mais également des données quantitatives concernant la fabrique sédimentaire, qui nous ont

permis de mettre en avant des phénomènes de semelles de traction au sein du dépôt et de renforcer l'hypothèse d'un dépôt mis en place par un tsunami.

Cette étude démontre l'intérêt de la tomographie par rayons X pour les études structurales et texturales, y compris dans le cadre de sédiments difficilement échantillonnables (granularité élevée, mauvais tri, cohésion limitée) et difficilement analysables (résolution limitée par le diamètre relativement important des carottes).

Cet article, fruit d'une collaboration naissante avec les collègues de Cologne sera publié dans Sedimentary Geology (*in press,* accepté fin 2015). C'est aussi un premier élément de valorisation de notre expérience en tomographie aux rayons X.

A mid-Holocene candidate tsunami deposit from the NW Cape (Western Australia)

Simon Matthias May*[1], Simon Falvard[2], Maike Norpoth[1], Anna Pint[1], Dominik Brill[1], Max Engel[1], Anja Scheffers[3], Manuel Dierick[4], Raphaël Paris[2], Peter Squire[3], Helmut Brückner[1]

[1]Institute of Geography, University of Cologne, Albertus-Magnus-Platz, 50923 Cologne, Germany

[2]Laboratoire Magmas et Volcans, Université Blaise Pascal – CNRS – IRD, OPGC, 5 rue Kessler, 63038 Clermont-Ferrand, France

[3]Southern Cross GeoScience, Southern Cross University, PO Box 157, Lismore NSW 2480, Australia

[4]Department of Physics and Astronomy, Centre for X-ray Tomography, Ghent University, Proeftuinstraat 86, 9000 Ghent, Belgium

*corresponding author, mays@uni-koeln.de

ABSTRACT

Although extreme-wave events are frequent along the northwestern coast of Western Australia and tsunamis in 1994 and 2006 induced considerable coastal flooding locally, robust stratigraphical evidence of prehistoric tropical cyclones and tsunamis from this area is lacking. Based on the analyses of X-ray computed microtomography (µCT) of oriented sediment cores, multi-proxy sediment and microfaunal analyses, optically stimulated luminescence (OSL) and ^{14}C-AMS dating, this study presents detailed investigations on an allochthonous sand layer of marine origin found in a back-barrier depression on the NW Cape Range peninsula. The event layer consists of material from the adjacent beach and dune, fines and thins inland, and was traced up to ~400 m onshore. Although a cyclone-induced origin cannot entirely be ruled out, the particular architecture and fabric of the sediment, rip-up clasts and three subunits point to deposition by a tsunami. As such, it represents the first stratigraphical evidence of a prehistoric, mid-Holocene tsunami in NW Western Australia. It

was OSL-dated to 5400-4300 years ago, thus postdating the regional mid-Holocene sea-level highstand.

Keywords: Palaeotsunami deposit; sediment fabric; X-ray microtomography; optically stimulated luminescence

1. *INTRODUCTION*

The NW coast of Western Australia is impacted by 1–2 tropical cyclones per year, and ten tsunamis have been recorded since 1858, including those following the 1883 Krakatoa eruption and the earthquakes off the coast of Indonesia in 1977, 1994 and 2006 (Goff and Chagué-Goff, 2014). Although observations during these tsunamis are rather sporadic, wave heights of ~6 m (Cape Leveque) and a run-up of ~8 m Australian Height Datum (AHD) (Shelter Bay, Shark Bay) occurred during the 1977 Sumba and 2006 Java tsunamis, respectively (Prendergast and Brown, 2011; Goff and Chagué-Goff, 2014). At the North West Cape, the 1994 Java tsunami overwashed the dune barrier at Baudin (Fig. 1), 3.6 km S of the study area. Inundation extended up to 300 m inland, and a run-up of ~7 m AHD was inferred (Gregson and van Reeken, 1998). In addition, tropical cyclones cause extensive coastal flooding. As one of the most powerful cyclones in Australia's historical record, category 5 tropical cyclone Vance (March 18th–22nd, 1999) resulted in water levels of ~7 m above event tide in the Exmouth Gulf (Nott and Hubbert, 2005). However, little is known about the geological imprint of historical (Prendergast and Brown, 2011; May et al., 2015a) and prehistorical extreme-wave events in northwestern Western Australia. So far, prehistorical tsunamis or storms were inferred from corals or large molluscs in washover deposits and dunes up to 1 km inland, or from marine organisms attached to wave-emplaced boulders (Scheffers et al., 2008, and references therein). These findings lack stratigraphic contexts, and uncertainties related to radiocarbon dating of reworked marine organisms (May et al., 2015a) or where the marine palaeo-reservoir effect may bias the inferred chronologies.

This paper provides, for the first time, detailed stratigraphic evidence of a prehistoric extreme-wave event from northwestern Western Australia. Based on multi-proxy sediment and microfaunal analyses, optically stimulated luminescence (OSL) and ^{14}C-dating, an

allochthonous sand layer of marine origin was identified in a mud-filled back-barrier depression at the NW coast of the Cape Range peninsula. As a novel approach in the context of tsunami deposits, X-ray computed microtomography (µCT) scans of oriented cores reveal characteristic sediment fabrics, which have been described from modern (Wassmer et al., 2010) and historical (Cuven et al., 2013) tsunami deposits but are rarely preserved in palaeotsunami deposits. We discuss the origin of the event layer against the background of its sedimentary characteristics and the local sedimentary environment.

2. PHYSICAL SETTING

Investigations were carried out in the low-lying back-barrier zone at Ninety Mile Beach access (21°50'28.03"S, 114°2'54.06"E), located in the northwestern part of the NW Cape (Western Australia). The site comprises a circular mudflat some 200 m from the sea, and slightly elevated low and open shrublands (Fig. 1). A dune belt of ~5 m AHD separates the site from the Ningaloo Reef, the local producer of bioclastic skeletal fragments. Heavy winds, sustained rainfall and severe flooding are mainly related to tropical cyclones during summer. The post-glacial marine transgression approached its maximum at ~7000–6000 years BP, when the formation of the Ningaloo Reef off the NW Cape had just started (Collins et al., 2003). A relative sea-level (RSL) highstand of 1–2 m above present level followed by a marine regression is documented for several coastal sections of Western Australia (Lewis et al., 2013; Engel et al., 2015) and is also assumed for the NW Cape.

The continuously falling RSL resulted in low sedimentation rates in coastal settings since c. 5000 years, impeding the accumulation of sediment archives suitable for storing palaeo-wave events (Nott, 2004). However, although its deposits have not yet been presented, the 1994 Java tsunami explicitly showed that considerable flooding of near-coast sediment archives may occur (Gregson and van Reeken, 1998), and palaeotsunami and palaeocyclone deposits may be stored in topographical lows.

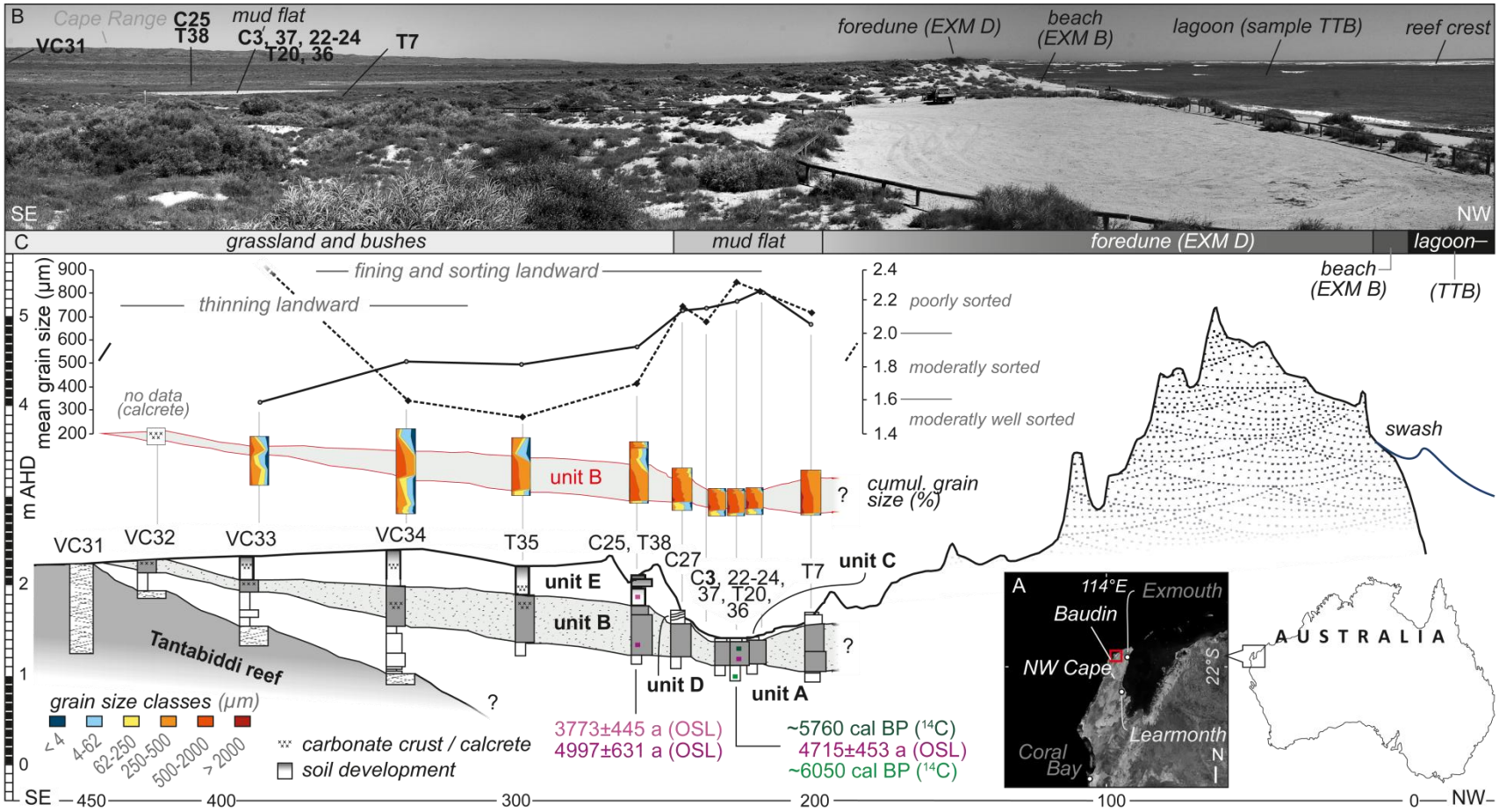

Fig. 1. (A) Overview of NW Western Australia [based on NASA Worldview data (NASA EOSDIS)]. Study site is marked by a red frame. (B) Panorama photo of study site (Ninety Mile Beach access) as seen from the top of the foredune (view towards SW). Location of sampling sites along the ~400 m long shore-perpendicular sediment transect (Fig. 1C) as well as of the modern samples are depicted. (C) Sediment transect with landward thinning and fining of unit B, and grain size distribution of cores/trenches.

3. METHODS

3.1 Sedimentary analyses

Samples were taken from cores and trenches at 16 locations along a shore-perpendicular transect crossing a circular mudflat (Fig. 1) at Ninety Mile Beach access, c. 200 m from the coast. The stratigraphical transect comprises trenches T7, T20 and T35, T36 and 38, percussion cores VC31–34 and push cores C3 (master core; Fig. 2), 22–25, 27 and 37. Percussion cores were taken using an Atlas Copco Cobra Pro percussion corer and probes of 6 cm in diameter. Push cores were taken by pushing plastic tubes also with a diameter of 6 cm into the sediment by hand. Cores and trenches reached depths between 50 and 150 cm below surface (b.s.), and sediment recovery amounted to a minimum of 90 % during coring. The distance between sampling sites was between 5 and 50 m. Percussion cores and trenches were photographically documented and significant facies were sampled. Push cores were opened and sampled in the lab in steps of 0.5–1 cm. Elevation of the cores and profiles were measured using a Topcon HiPer Pro differential global positioning system (DGPS) with an altimetric accuracy of ~2 cm. Elevations given in AHD (Australian Height Datum) are based DGPS measurements using the on static mode and AUSPOS post-processing. Modern samples were taken from the present beach (EXM B), the dune (EXM D) and the lagoon some 450 m off the beach (i.e., the Holocene reef platform, TTB).

The coarse- and fine-grained fractions (>2 mm and <2 mm) were separated using a 2 mm sieve and weighed; percentage of the gravel fraction (>2 mm) is separately illustrated for master core C3. The air-dried fine-grained fraction was carefully hand-pestled for particle disaggregation. Grain size distribution of the fine-grained fraction was measured using a Beckman Coulter LS 13320 laser particle analyzer (<2 mm). Samples were pre-treated with H_2O_2 (30%) to remove organic carbon and 0.5 N $Na_4P_2O_7$ (55.7 g/l) for aggregate dispersion. Statistical measures were calculated after Folk and Ward (1957) using the GRADISTAT software (Blott and Pye, 2001). In order to determine sedimentary environments and sediment source areas, microfaunal analyses (foraminifers, ostracods) were carried out for samples of master core C3 and for the modern samples. Samples (10 cm^3) were pre-treated with H_2O_2 (30%) for dispersion and sieved to isolate fractions of >100 and <100 μm. The microfaunal content was investigated under a binocular microscope and quantitatively recorded. A minimum of ~300 (foraminifers) and ~100 (ostracods) specimens per sample were counted where possible. We distinguished reworked and non-reworked foraminifers based on the

degree of fragmentation and abrasion/rounding. For determination taxa and ecological preferences, Yassini and Jones (1995), Hayward et al. (1999), De Deckker and Yokoyama (2009), and Karanovic (2012) were used.

Principal component analysis (PCA) was carried out using the PAST software (Hammer et al., 2001) for samples of master core C3 (Fig. 3). For PCA, the grain size parameters mean, sorting, skewness and kurtosis as well as the percentage of microfaunal contents were included. Spearman's rank correlation coefficient was used to avoid autocorrelations.

We interpreted µCT scans of an oriented push core (C37) in order to infer information about sediment fabric as well as flow directions and characteristics. Scans were performed at HECTOR, a custom-built CT scanner setup at UGCT (Centre For X-ray Tomography, Ghent University, Belgium) (cf., Masschaele et al., 2013). The CT scanner was specifically designed for multidisciplinary CT applications and is built around a 240kV X-RAY WorX microfocus source (XWT 240-SE) and a Perkin-Elmer flat panel detector (1620 CN3 CS). Based on the sample size and composition, optimal scanner settings were determined to be 220kV tube voltage, 50W beam power and 1 mm of aluminum filtration to reduce beam hardening while preserving a sufficiently high signal-to-noise ratio. A total of 2000 projections was recorded, with a 1-second exposure per projection. The isotropic voxel pitch of the reconstructed volume was 50 µm. The tomographic datasets were reconstructed using the Octopus software package, and the reconstructed 3D volumes were rendered using the visualization software package VGStudio MAX. Visual interpretation was performed using myVGL 2.1 software.

In addition, quantification of sediment fabrics such as the orientation and dip of the longest axes of particles and particle shape measurements (Figs. 4, 5) was performed using ImageJ, Blob3D (Ketcham, 2005) and Stereo32 (Röler and Trepmann, 2013) software. Three sections of the reconstructed core (lower parts of subunit I and II) were chosen for subsampling and sediment fabric analyses. The original scans (images) were cropped and oriented towards the north using ImageJ software. Subsequent processing included adjustments of brightness and contrast as well as corrections of the signal-to-noise ratio in order to extract larger particles and remove smaller ones from the images. Subsamples were extracted from the whole dataset and transferred into Blob3D. Subsample I (basal layer of unit B; base of subunit I, trc; cf., Fig. 4) included 360 images, subsample II (lower to middle part of subunit I) 500 images, and subsample III (lower part of subunit 2) 400 images. The

grayscale images were converted into a binary image and the threshold value between black and white was determined to 172. Subsequently, particle correction and separation was done by using the "remove islands" and "remove holes" function of Blob3D and, finally, manually with the separation module of Blob3D. Analyses were stopped when a total of at least 300 particles per sample were measured. Finally, the shape of the ellipsoidal particles was calculated using Stereo32 for each subsample using the major axes of particles extracted in Blob3D. Particle isotropy (*I*) and elongation (*E*) are based on eigenvectors S1 (max), S2 (intermediate) and S3 (min), calculated using Stereo32 software.

3.2 Dating techniques

Three OSL (optically stimulated luminescence) samples were taken from trenches T36 (T36 OSL 1, 15 cm b.s.) and T38 (T38 OSL 1; 36 and 70 cm b.s.). OSL dating was performed at the Cologne Luminescence Lab (CLL; Institute of Geography, University of Cologne). To estimate environmental dose rates (Table 1), assessment of U, Th and K concentrations by means of high-resolution gamma spectrometry and measurement of in situ water contents were performed on grab samples of the material within a 30-cm radius around the dated sample. In case of T36 OSL 1, where the sampled layer has a thickness of only 30 cm, an additional dose rate sample was taken from the mudflat below and considered in the calculation of the total dose rate. In addition, the contribution of the cosmic dose rate was calculated on the basis of geographical position, altitude above sea level, and thickness and density of the sediment overburden (Prescott and Hutton, 1994). Comparison of the decay activities of different nuclides within the ^{238}U and ^{232}Th chains reveals disequilibria in the range of 12–22% for the ^{232}Th chain and 5–15% for the ^{238}U chain. For the final luminescence ages these disequilibria are insignificant compared to 1-sigma uncertainties of about 10%, since the related age differences are significantly smaller, as already documented (e.g., Olley et al., 1996).

sample	**depth** b.s. [m]	**water** [%]	**U** [ppm]	**activities U-chain** [Bq/kg]	**RDE** [%]	**Th** [ppm]	**activities Th-chain** [Bq/kg]	**RDE** [%]	**K** [%]	**dose rate** [Gy/ka]
T36 OSL1	0.15	12±5	1.06±0.09	Pb 214: 13.6±0.36 Bi 214: 13.3±0.26	10	0.43±0.04	Th 228: 1.7±0.10 Ac 228: 2.2±0.36 Tl 208:1.9±0.24	12	0.12±0.00	0.55±0.06
T36 basal mud	0.35	63±5	0.48±0.03			0.49±07			0.17±0.00	
T38 OSL 1	0.36	10±5	1.32±0.06	Pb 214: 16.3±0.25 Bi 214: 17.5±1.95	5	1.03±0.17	Th 228: 3.9±0.11 Ac 228: 4.3±0.34 Tl 208: 5.4±0.28	18	0.22±0.01	0.57±0.09

T38 OSL 2	0.70	7±5	1.06±0.14	Pb 214: 12.8±0.21 Bi 214: 13.5±0.25	15	0.36±0.08	Th 228: 1.3±0.09 Ac 228: 1.7±0.34 Tl 208: 1.7±0.21	22	0.12±0.00	0.74±0.10

Table 1. Dosimetry data. Notes: depth b.s. – sampling depth below surface, water – *in-situ* water content, U – uranium, Th – thorium, K – potassium, RDE – radioactive disequilibria. OSL dating was carried out in the Cologne Luminescence Lab (CLL).

sample	**labcode**	**$N_{(acc/meas)}$**	**OD** [%]	**skewness**	**age model**	**burial dose** [Gy]	**age** [ka]
T36 OSL1	C-L3514	42/45	16.1	0.6	CAM	2.57±0.14	4715±453
T38 OSL 1	C-L3515	37/48	25.9	-0.22	CAM	2.83±0.26	3773±445
T38 OSL 2	C-L3516	45/48	16.3	1.8	CAM	2.79±0.16	4997±631

Table 2. Burial doses and luminescence ages. Notes: $N_{acc/meas}$ – number of accepted *versus* measured aliquots, OD – over-dispersion, CAM – central age model (Galbraith et al., 1999). OSL dating was carried out in the Cologne Luminescence Lab (CLL). The weighted mean age of unit B is 4833 ± 549 a.

Sample	Depth (m b.s.)	Lab. no.	Sample description	$\delta^{13}C$ (ppm)	^{14}C age (BP)	1σ max-min (cal BP)	2σ max-min (cal BP)
C 3/4 PR	0.46	UGAMS10492	unid. plant remains	-25.3	5290 ± 25	6169-5934	6177-5922
C 3/7 M	0.15	UGAMS10493	mollusc test	1.4	5390 ± 30	*5828-5715	*5865-5664

Table 3. ^{14}C-AMS dating results. Notes: unid. plant remains – unidentified plant remains; unid. m. fragments – unidentified mollusc fragments. Lab. no. – Laboratory number, UGAMS = Center for Applied Isotope Studies, University of Georgia (USA). All ages were calibrated using CALIB 7.0 software and the calibration datasets of Reimer et al. (2013; mollusc samples) and Hogg et al. (2013; plant samples). * – corrected for a local marine reservoir effect with $\Delta R = 65 \pm 18$ (O'Connor et al., 2010).

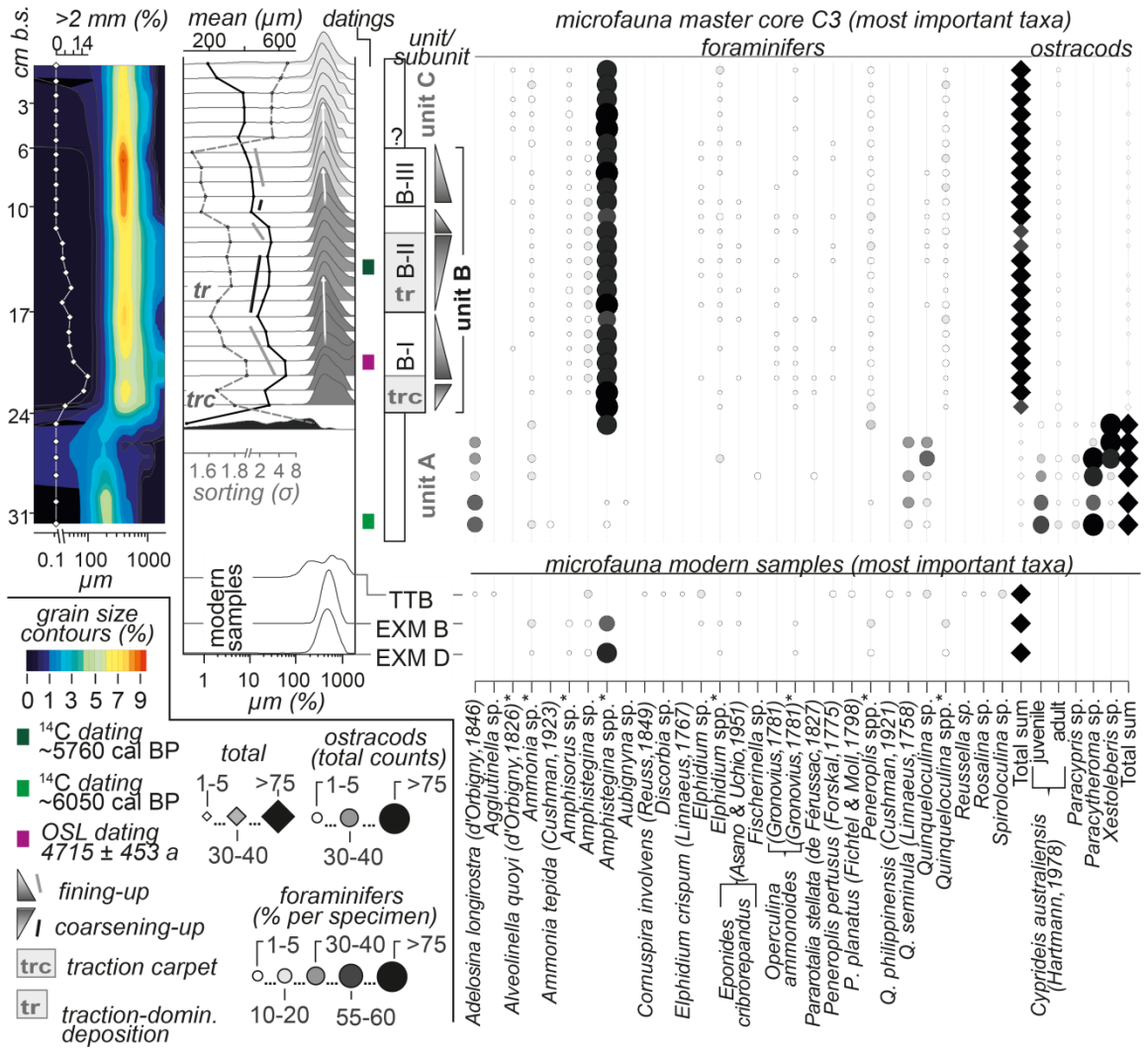

Fig. 2. Sediment characteristics, granulometry and microfaunal data of master core C3 and the modern samples. * – reworked (fragmented/rounded); b.s. – below surface.

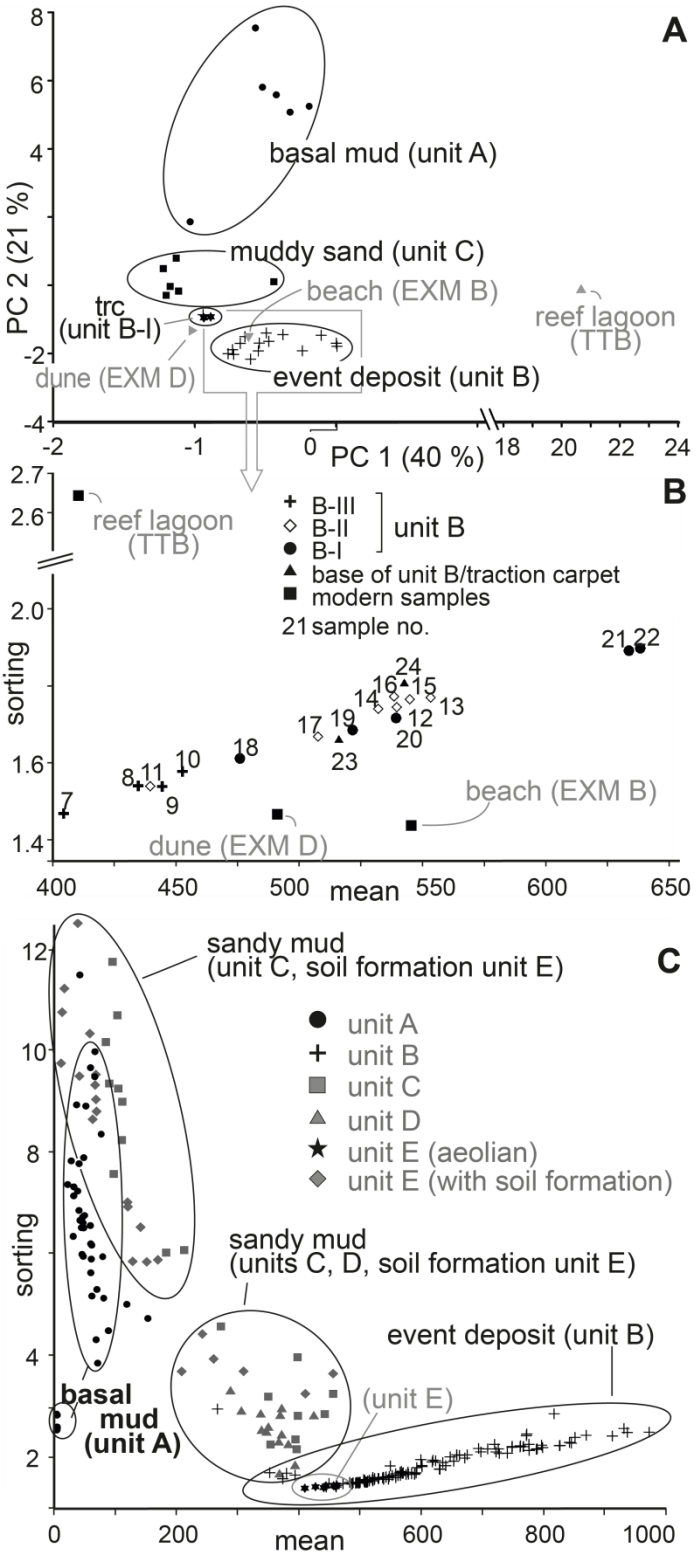

Fig. 3. (A) PCA results show clustering of sedimentary units. Unit B separates from other units and has the same characteristics as the modern beach and dune. (B) Negative correlation of mean grain size and sorting for samples from unit B in C3. For top of subunits B-I and B-III (fining- and sorting-up) this trend is parallel to sample depth (sample no.). (C) Relation of mean grain size and sorting for all samples from sampling sites T7, C22–25, C27, T35 and VC34. Event unit B clearly separates from basal unit A and subsequent units C, D and E. A negative correlation of mean grain size and sorting is also visible.

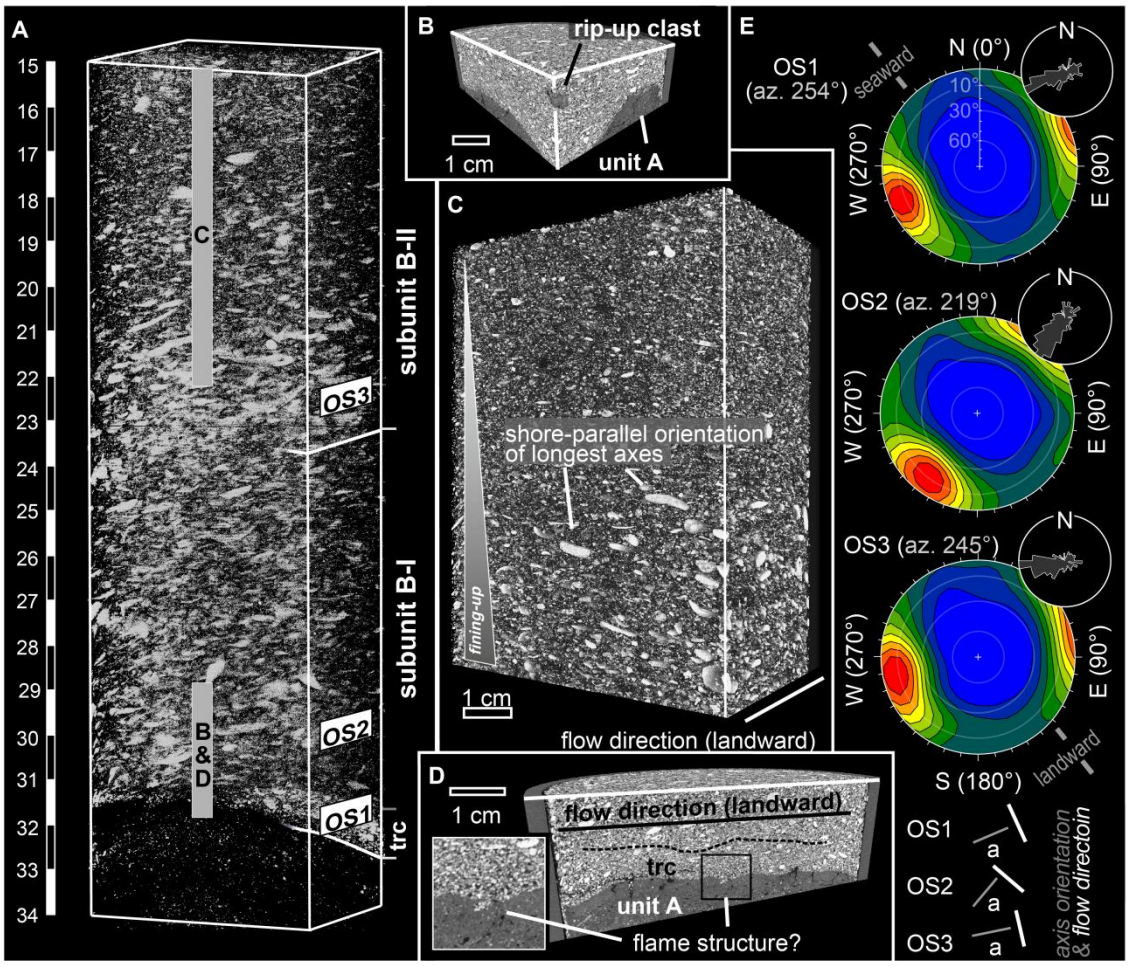

Fig. 4. µCT scans of core C37. (A) Similar to C3, subunits are present in unit B of C37. Sediment fabric (particle orientation) and normal grading are visible. (B) Rip-up clasts in subunit B-I. (C) Fining-up and fabric of subunit B-II. (D) Traction carpet (?) at the base of subunit B-I and flame structures at the boundary between units A and B. (E) Dominant (shore-parallel) orientation and dip of longest particle axes at the base of subunits B-I and B-II; flow direction is perpendicular (landward) (OS1-3, Fig. 4A). az. – azimuth.

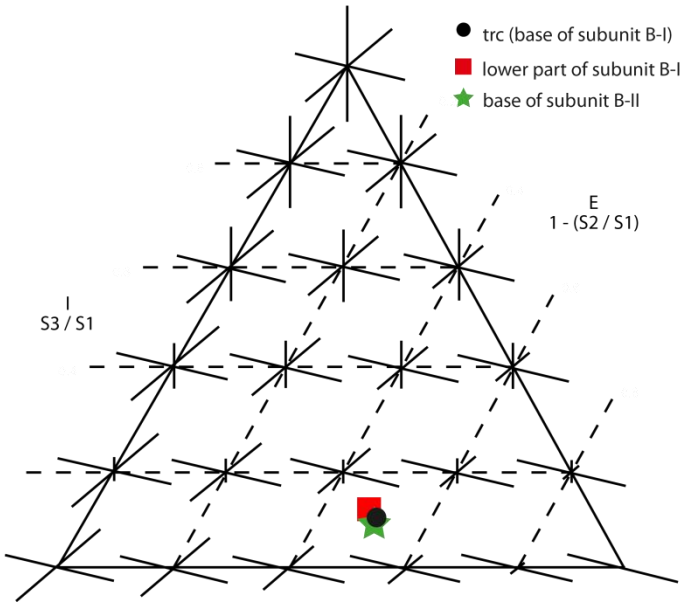

Fig. 5. Shape of the ellipsoids calculated from the orientations (longest axis) of the particles separated for each subsample using the shape triangle diagram of Benn (1994). Particle isotropy (I) and elongation (E) are calculated using the eigenvectors of the ellipsoids, S1 (max eigenvalue), S2 (intermediate) and S3 (min); see Benn (1994) for details. The eigenvalues have been calculated using Stereo32 software. All subsamples exhibit a rather prolate shape, which supports the idea of a traction-based transportation mode of the particles.

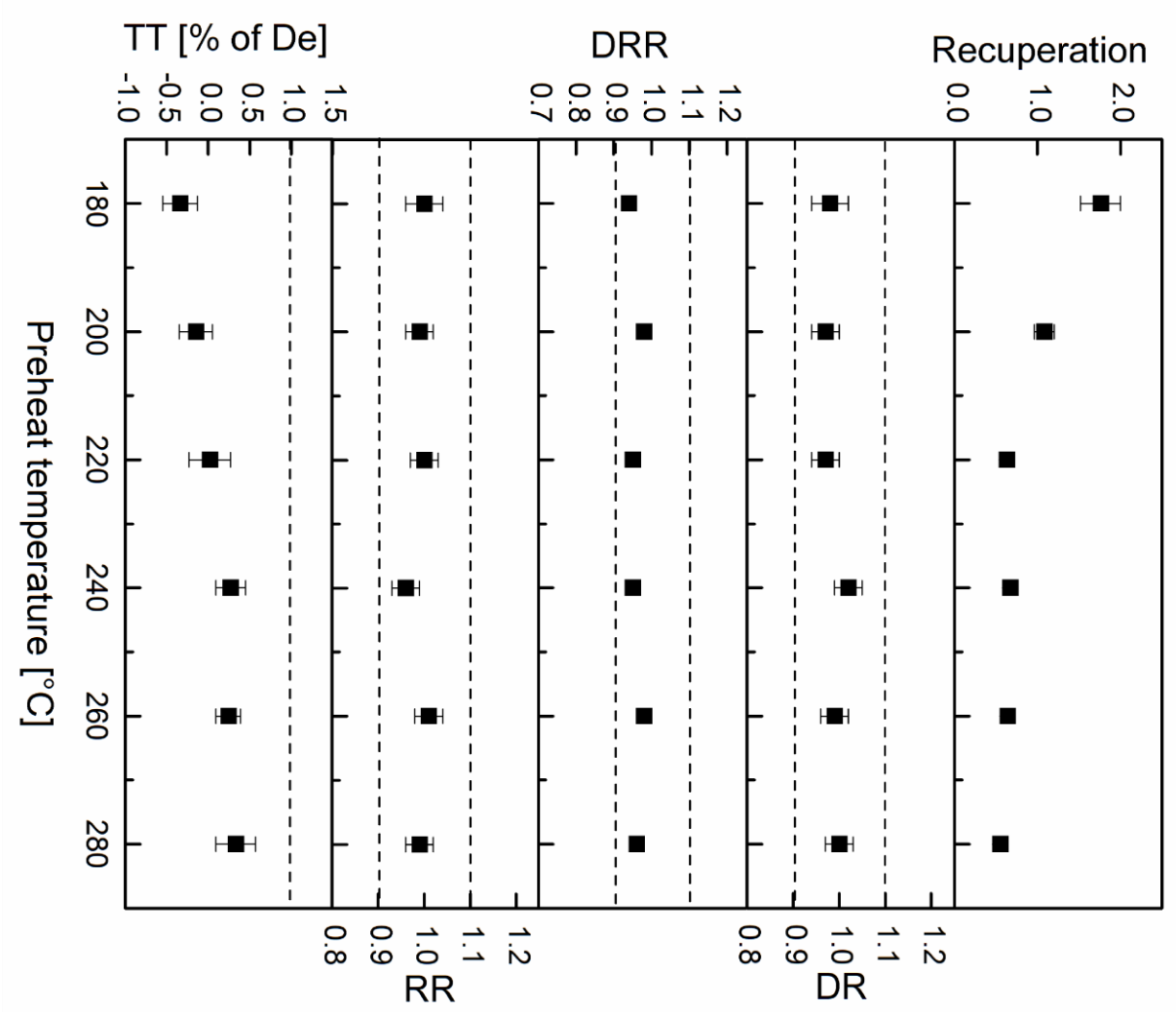

Fig. 6. Results of preheat-plateau and dose-recovery test performed on T36 OSL1 (n = 4 per temperature interval). Since no significant temperature dependency of dose values is visible, a preheat temperature of 200 °C was selected.

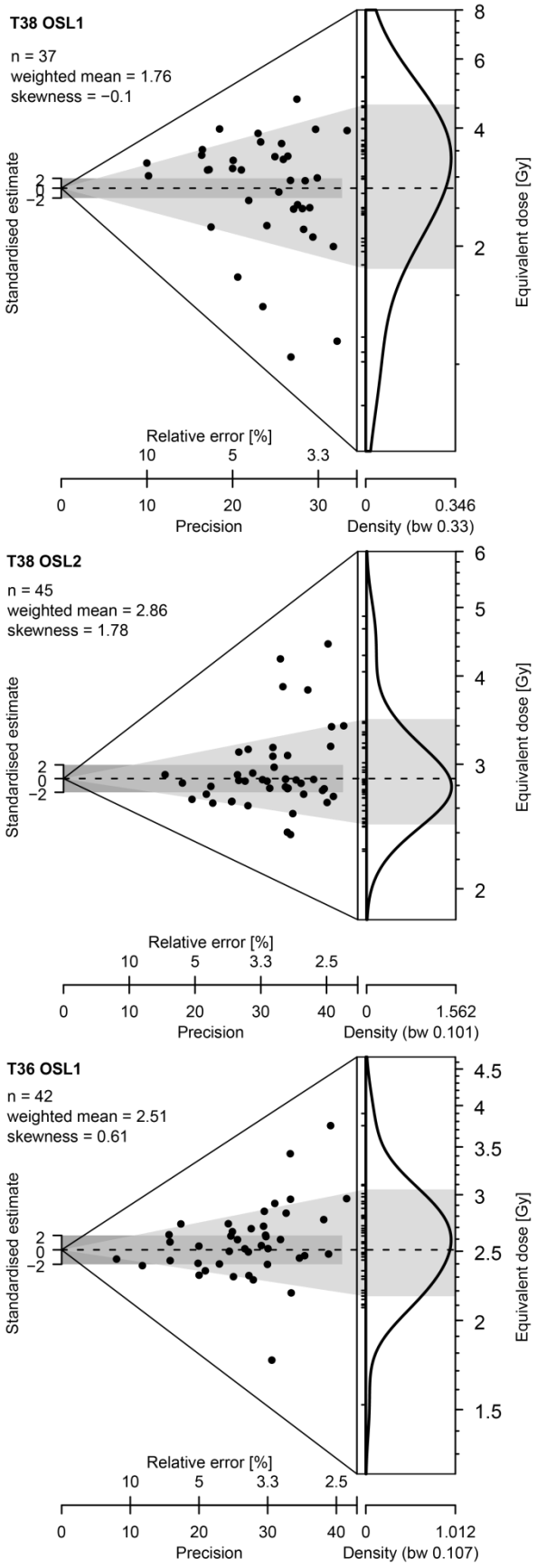

Fig. 7. Abanico plots of De distributions (Dietze et al., 2014) for samples from trenches T36 (T36 OSL 1) and T38 (T38 OSL 1 and 2). All samples show approximately normally distributed dose values. Hence, the burial doses were calculated using the central age model (dark grey bars).

Samples for burial dose determination were collected in opaque aluminium tubes and processed under subdued red light. Samples were sieved to fractions of 150–200 mm and chemically pre-treated with HCl, H_2O_2, sodium oxalate and HF to remove carbonates, organics, clay and the alpha-affected rim of the grains. Pure quartz was extracted by heavy liquid separation with densities of 2.62 and 2.68 g/cm^3. Small 1-mm aliquots of quartz were measured on Risø TL/OSL devices with $^{90}Sr/^{90}Y$ beta sources delivering ~0.08 to 0.15 Gy/s at the sample position. Signals were stimulated by means of blue LEDs for 40 s and a Hoya U340 filter (7.5 mm) was used for signal detection.

Equivalent dose measurements followed the SAR protocol of Murray and Wintle (2003). Since combined a dose-recovery-preheat-plateau and thermal transfer test (measurement of four aliquots per temperature interval after bleaching by blue LEDs for 100 s at room temperature) exemplarily performed on T36 OSL 1 showed no dose-dependence for temperatures between 180 and 280 °C (transfer of charge <0.5% of natural D_e and dose-recovery values of 0.94–0.98), a preheat temperature of 200 °C was selected for all D_e measurements (Fig. 6). The general suitability of the applied SAR protocol for the samples was verified by (i) dose recovery tests with measured to given dose ratios of 0.94–0.98 that revealed reproducibility; (ii) linear-modulated luminescence (with linearly increasing stimulation energy over a measurement interval of 3600 s) which demonstrates the dominance of an easily bleachable fast component (photon-ionisation cross section of $1.6–1.8x10^{-17}$) comparable to the one described by Singarayer and Bailey (2003); and (iii) constant $D_e(t)$ plots that point to thermally stable signals (Bailey, 2003).

Out of 48 measured aliquots per sample, between 37 and 45 aliquots passed the SAR acceptance criteria in respect of recycling ratio (0.9–1.1), recuperation (<5% of D_e), depletion ratio (0.9–1.1), and signal to background ratio (>3) and could be considered for the calculation of burial doses. Due to the approximately normally distributed (skewness <2) and moderately scatted (overdispersion of 16–25%) D_e distributions (Fig. 7), all samples were assumed to be well bleached and, in consequence, the central age model (CAM) of Galbraith et al. (1999) was used for burial dose calculation. The respective dose values, statistical characteristics of the D_e distributions, and ages for each sample are summarised in Table 2.

A mollusc and a plant remain were dated by ^{14}C (Table 3). The mollusc test has been transported prior to deposition. ^{14}C-ages were corrected for a marine reservoir effect of ΔR =

65±18 where necessary (O'Connor et al., 2010) and calibrated using CALIB 7.0 software (Hogg et al, 2013; Reimer et al., 2013) (Table 3).

4. SEDIMENTOLOGY

4.1 Trench-scale grain size and microfaunal characteristics

At the base of C3, laminated sandy mud (31–24 cm b.s., Figs. 2, 3) shows layers of one to few mm thickness and mean grain size values between 4 and ~100 µm. The foraminiferal assemblage (Fig. 2) is mainly composed of well-preserved individuals of *Adelosina longirostra, Quinqueloculina seminula* and *Quinqueloculina* sp. Juvenile and adult *Cyprideis australiensis, Paracypris* sp., *Paracytheroma* sp., *Xestoleberis* sp. compose the ostracod assemblage.

Unconformably overlying is coarse to medium sand with abundant foraminifers, shell debris and well-rounded gravel (24–6 cm b.s., unit B). A medium sand layer (24–22 cm b.s.; base of subunit B-I) comprises the bottom section. Coarse sand and gravel contents increase from 22–20 cm b.s. and decrease between 20–17 cm b.s (top of subunit B-I). Between 17–11 cm b.s., massive sand and gravel was found, coarsening-up at 17–12 cm b.s. and fining-up at 12–11 cm b.s. (subunit B-II). The sediment lacks any gravel component and is fining-up at 10–6 cm b.s. (subunit B-III).

Samples from unit B cluster based on the PCA and the sorting/mean grain size ratio (Fig. 3). Granulometric characteristics are similar to the beach and dune (EXM B and D), although the latter are slightly better sorted (Figs. 2, 3). Reefal sediments (TTB) are poorly sorted and show increased mud contents (Fig. 2).

Reworked (i.e., fragmented/rounded) *Amphistegina* spp. (60–90%) and other inner shelf taxa dominate the foraminiferal assemblages of EXM B and D as well as unit B (Figs. 2, 3A). Sample TTB has a higher diversity and is dominated by less or non-reworked individuals of inner shelf taxa (Fig. 2), which are also present in lower abundance in sections of unit B and samples EXM B and D. Fresh individuals of *Peneroplis pertusus* are only found in unit B and TTB. While samples EXM B and D are void of ostracods (Fig. 2), several adult specimens of *C. australiensis* are present in unit B.

Mean grain size again increases until 2 cm b.s., before fining-up from 2–0 cm b.s. A higher mud content is evident in the uppermost 6 cm (unit C), and a thin mud drape overlies the sand sequence.

4.2 Sediment fabric in µCT scans

Similar to unit B in C3, at least two subunits with a distinct orientation of coarser shell and gravel components and graded bedding are visible in the µCT scans of oriented core C37 (Figs. 1, 4). However, in C37, subunit B-II is fining-up (Fig. 4C). For the base of subunits B-I and B-II (OS1-3 in Fig. 4A,E), the longest axes of the mainly prolate coarse particles (Fig. 5) exhibit a distinct shore-parallel orientation (SW-NE to WSW-ENE) with a dominant dip of ~6-9° both towards SW and NE. Well-rounded, 15 cm-large Pleistocene reef rock clasts floating in unit B were found in T20 (Fig. 8). Micro-cavities (~0.5 cm) disrupt the sharp erosive boundary to unit A, resembling flame structures (Fig. 4C,D).

Mud clasts floating in the sandy to gravelly matrix were identified in subunit B-I (Figs. 4B, 8). The (palaeo-)surface of the underlying mud is overlain by a ~1 cm-thick layer of medium to coarse sand with lower amounts of shell fragments and gravel (Fig. 4D), analogous to the base of unit B in C3 (base of subunit B-I; Fig. 2).

4.3 Transect-scale sediment characteristics and chronology

The sand sheet of unit B was detected in trenches (T) and further cores (VC, C) along the entire transect, except for the most landward core VC31 (Fig. 1). It thins and fines landwards and is partly cemented in VC32–34 and T35. The basal ~1 cm-thick layer of medium to coarse sand with reduced contents of larger mollusc fragments and gravel (base of subunit B-I; Figs. 2, 4C–E) varies in thickness; it was not found in the landward cores. While unit B is overlain by unit C in the cores from the mudflat, it is followed by laminated sandy mud (unit D, C27) and well-sorted fine sand (unit E, C25) landwards. In the latter core, unit E gradually changes to muddy fine sand in its upper part (50-0 cm b.s.). Landwards of VC32, the weathered Pleistocene reef rock emerges at the surface; VC31 penetrated deeply weathered cemented sand and red loam.

Based on the weighted mean of two OSL ages from T36 and T38 [4715±453 years, 4997±631 years], unit B was deposited 4833±549 years ago (Tables 1, 2; Figs. 6, 7). This is in agreement with the ^{14}C-age of a bivalve shell from unit B in C3 (5582–5757 cal years BP) at 9 cm b.s. (Table 3), giving a maximum age for the sand sheet. Plant remains from unit A yielded an age of 5922–6177 cal years BP at 46 cm b.s. The well-sorted fine sand of unit E in T38 (36 cm b.s.) gives an age of 3773±445 years.

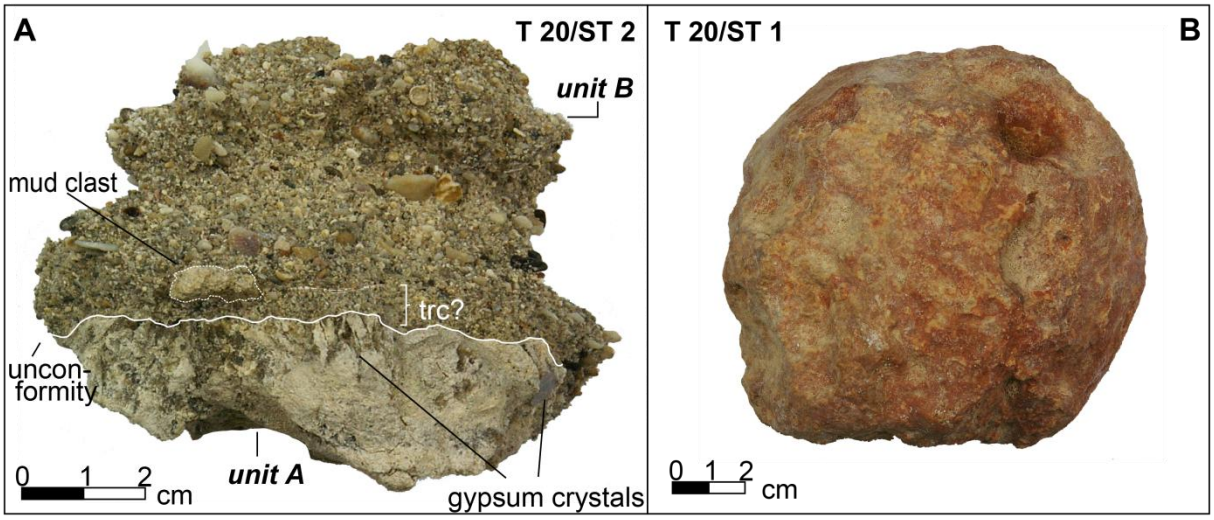

Fig. 8. (A) Photo of cemented section found in T20 illustrating sediment composition; subunit I directly following basal mud unit A contains a rip-up clast and is indicated by a 1–2 cm-thick basal layer, interpreted as traction carpet deposits. (B) In T20, well-rounded cobble-sized fragments of Pleistocene sedimentary rocks were found floating in the sandy matrix of unit B.

5. DATA INTERPRETATION AND DISCUSSION

5.1 Sediment source and origin of unit B

While the foraminiferal assemblage of unit A, dominated by inner shelf species *A. longirostra*, *Q. seminula* and *Quinqueloculina* sp., suggests inter- to subtidal lagoonal conditions, juvenile *C. australiensis* (preferring sandy substrate), *Paracytheroma* sp. (preferring organic-rich mud), *Paracypris* sp. and *Xestoleberis* sp. indicate a protected marginal-marine palaeoenvironment with salinity fluctuations and temporarily hypersaline conditions (e.g,, Yassini and Jones 1995), probably a semi-enclosed lagoon (Table 4). These conditions persisted until ~6050 cal BP or later.

The inverse grading in the basal (B-I, B-II) and normal grading in the upper (B-I, B-III) part of its subunits (Figs. 1, 2), the distinct fining and thinning landward pattern, and the

erosive boundary to underlying mudflat sediments point to an event-induced origin of unit B (e.g., Morton et al., 2007). Although a suite of diagnostic characteristics for the identification of palaeotsunami (and palaeostorm) deposits has been discussed in the aftermath of the tsunamis in 2004 (Dec 26th, Indian Ocean Tsunami), 2010 (Feb 27th, Chile Tsunami) and 2011 (Mar 11th, Tohoku-oki Tsunami, Japan) (e.g., Morton et al., 2007; Paris et al., 2010; Szczuciński et al., 2012), the detection and differentiation of storm and tsunami deposits is still associated with a number of challenges, including site-specific sediment characteristics, an archive-specific preservation potential, or post-depositional changes (e.g., Szczuciński, 2012). However, tsunamis tend to generate extensive sand sheets, generally fining inland and upwards, and comprising distinct subunits as well as an erosive lower contact. They often contain rip-up clasts of reworked material, and sediment fabrics may reflect palaeo-current directions (Paris et al., 2010). While storm deposits may produce similar trench-scale sediment characteristics (Morton et al., 2007), they generally tend to be more narrow and thick, and thin landward rather abruptly on a transect scale (Paris et al., 2010).

All mentioned tsunami characteristics are found in unit B, why we tentatively conclude that it was deposited by a tsunami 5400-4300 years ago. However, Supertyphoon Haiyan on the Philippines recently demonstrated that powerful tropical cyclones may result in coastal flooding with tsunami-similar hydrodynamic characteristics, where infragravity waves with periods of > 1 min are caused by non-linear wave interactions with shallow reef platforms (May et al., 2015b; Roeber and Bricker, 2015; Shimozono et al., 2015). In these cases, pulses of sustained (i.e. > 1 min) landward-directed coastal flooding may reach flow velocities of >5 m/s, which is in the range of those inferred for recent major tsunamis at the coast (Fritz et al., 2006, 2012). Since wave-reef interactions and the generation of infragravity waves at our study site cannot be excluded, a storm generation of unit B cannot entirely be ruled out.

The sediment source of the candidate tsunami deposit is predominantly the beach and dune directly NW of the transect based on unit B's similarities in granulometry, microfaunal composition and taphonomy (Figs. 2, 3), which reflects conditions at the sediment source and is hardly modified by tsunami transport (Szczuciński et al., 2012). Well-preserved individuals of *Elphidium* sp., *Amphistegina* sp. and *Eponides cribrorepandus*, and some species found only in the modern sample TTB (*P. pertusus*) indicate a minor component from the reef

lagoon (Table 4). Some individuals of *Pararotalia stellata* as well as *Quinqueloculina* spp. suggest the entrainment of material eroded from unit A.

5.2 Implications on hydrodynamic conditions and depositional processes

The orientation of particles deposited from suspension or traction is preserved when current velocities are sufficiently high. A flow-perpendicular orientation of the longest axes of (ellipsoidal) particles, as observed in unit B (SW-NE to WSW-ENE, Fig. 4E), is typical for bedload transport by rolling or sliding in strong and highly concentrated currents (Wassmer et al., 2010; Schneider et al., 2014) and indicates flow directions towards the SE. Inverse grading, observed at the base of subunits B-I and B-II, is associated with traction carpets (trc) and dominant bedload transport (tr; Figs. 2–4) at the base of tsunami deposits from the 2006 Java Tsunami and the 2011 Tohoku-oki Tsunami, where finer but dense sediment grains settle in a highly concentrated, collision-dominated flow (Moore et al., 2011; Szczuciński et al., 2012). In addition, the flame structures between units A and B indicate run-up-associated, synsedimentary deformation and truncation of basal strata (i.e., unit A) (Matsumoto et al., 2008) due to high-velocity unidirectional (landward) flow generating strong shear stress.

The poor sorting of basal layers can be attributed to the presence of a coarser fraction (>700 µm), which causes the bimodal or close to bimodal grain size distribution of, for example, the lower samples of subunits B-I and B-II (Figs. 2, 3). The correlation between mean grain size and sorting and the fining-upward trend may suggest a change in deposition from bedload to suspension within a decelerating flow particularly in subunits B-I and B-III (Moore et al., 2011) (Fig. 2). While sediment particles in subunit B-II of C3 may have almost entirely been deposited by traction, flow deceleration may be inferred at the top of this subunit at C37 (Fig. 4C).

We tentatively interpret the deposit to represent three major waves of one tsunami, with the base of subunits (Figs. 2, 4) representing initial high-velocity inundation pulses. In addition, sediments at its base show a trend towards better sorting between C27 and T35, before mud contents within unit B cause very poor sorting in VC33. Decelerating flow velocities during deposition of unit B and dominant deposition from suspension are inferred for the landward section of the transect (Moore et al., 2011).

5.3 Comparison with regional event data and RSL change

Previous studies found major far-field tsunamis of similar age from geologic evidence in the northern Indian Ocean (e.g., Jackson et al., 2014). However, the regional tsunami history and numerical models suggest that the strongest events affecting Western Australia arise from earthquakes along the Java and Sumbawa segments of the Sunda megathrust (Burbidge et al., 2008). While a correlation of these palaeoevents with the one presented here seems equivocal, it is remarkable that age clusters of corals attached to wave-emplaced boulders at the NW Cape and of shells found in dunes in SW Exmouth Gulf (Scheffers et al., 2008, and references therein) coincide with the age of unit B.

A RSL ~1 m higher than at present at the time of the tsunami and a continuous RSL fall since then (Lewis et al., 2013) involved low sedimentation rates during the mid- to late Holocene (Nott, 2004). While the only thin sediment cover on top of unit B and the accumulation of units C and D seem to reflect continuous deflation and episodic mud flat deposition in the back-barrier area, the well-sorted sand of unit E in the landward cores/trenches is of aeolian origin, with deposition until at least 3773±445 years ago (T38 OSL 1). Since then, soil formation took place, leading to the evolution of carbonate crusts in most of the landward cores.

6. CONCLUSIONS

Based on the analyses of µCT scans of oriented cores, multi-proxy sediment and microfaunal analyses, this study presents the first stratigraphic evidence of a prehistoric extreme-wave event, most likely a palaeotsunami, from the NW part of Western Australia. The candidate tsunami deposit was OSL-dated to 5400-4300 years ago.

Although rarely described from palaeotsunami deposits, the good preservation of sedimentary characteristics and sediment fabric allow for inferring hydrodynamic characteristics of the event. Up to three subunits were detected within the deposit, characterized by typical inverse (bottom part) and normal (top part) grading. The qualitative and quantitative analysis of µCT scans, as exemplified in this study, represents a novel

approach to deduce sediment fabrics of palaeoevent deposits. Particle orientations inferred from the µCT scans reveal that the subunits were deposited due to landward flow directions during three run-up phases of the event inducing high shear velocities at the beginning and decelerating flow conditions at the end. Despite low sedimentation rates during the last ~5000 years, our results show that geological archives along the Ningaloo Reef are capable of remarkably well preserving traces of extreme-wave events.

ACKNOWLEDGMENTS

Funding by Deutsche Forschungsgemeinschaft (DFG, MA 5768/1-1) and Australian Research Council (ARC, Future Fellowship FT0990910) is gratefully acknowledged. The research was kindly permitted and supported by Ann Preest, the local elders and aboriginal communities of Exmouth, and the Department of Environment and Conservation (Perth/Exmouth).

REFERENCES

Abu-Zied, R.H., Keatings, K., Flower, R.J., Leng, M.J., 2011. Benthic Foraminifera and their stable isotope composition in sediment cores from Lake Qarun, Egypt: changes in water salinity during the past ~500 years. Journal of Paleolimnology 45, 167–182.

Bailey, R.M., 2003. The use of measurement-time dependent single-aliquot equivalent-dose estimates from quartz in the identification of incomplete signal resetting. Radiation Measurements 37, 673–683.

Benn, D., 1994. Fabric Shape and the Interpretation of Sedimentary Fabric Data. Journal of Sedimentary Research 64, 910–915.

Blott, S.J., Pye, K., 2001. GRADISTAT: a grain size distribution and statistics package for the analysis of unconsolidated sediments. Earth Surface Processes and Landforms 26, 1237–1248.

Burbidge, D., Cummins, P.R., Mleczko, R., Thio, H.K., 2008. A probabilistic tsunami hazard assessment for Western Australia. Pure and Applied Geophysics 165, 2059–2088.

Collins, L.B., Rong Zhu, Z., Wyrwoll, K.-H., Eisenhauer, A., 2003. Late Quaternary structure and development of the northern Ningaloo Reef, Australia. Sedimentary Geology 159, 81–94.

Cuven, S., Paris, R., Falvard, S., Miot-Noirault, E., Benbakkar, M., Schneider, J.-L., Billy, I., 2013. High-resolution analysis of a tsunami deposit: Case-study from the 1755 Lisbon tsunami in southwestern Spain. Marine Geology 337, 98–111.

De Deckker, P., Yokoyama, Y., 2009. Micropalaeontological evidence for Late Quaternary sea-level changes in Bonaparte Gulf, Australia. Global and Planetary Change 66, 85–92.

Debenay, J.-P., Bénéteau, E., Zhang, J., Stouff, V., Geslin, E., Redois, F., Fernandez-Gonzalez, M., 1998. Ammonia beccarii and Ammonia tepida (Foraminifera): morphofunctional arguments for their distinction. Marine Micropaleontology 34, 235–244.

Dietze, M., Kreuzer, S., Burow, C., Fuchs, M., Fischer, M., Schmidt, C., 2015. The abanico plot: visualising chronometric data with individual standard errors. Quaternary Geochronology, doi:10.1016/j.quageo.2015.09.003.

Engel, M., Brückner, H., Pint, A., Wellbrock, K., Ginau, A., Voss, P., Grottker, M., Klasen, N., Frenzel, P., 2011. The early Holocene humid period in NW Saudi Arabia – Sediments, microfossils and palaeo-hydrological modelling. Quaternary International 266, 131–141.

Engel, M., May, S.M., Scheffers, A., Squire, P., Pint, A., Kelletat, D., Brückner, H., 2015. Prograded foredunes of Western Australia's macro-tidal coast – implications for Holocene sea-level change and high-energy wave impacts. Earth Surface Processes and Landforms 40, 726–740.

Folk, R.L., Ward, W.C., 1957. Brazos River Bar: a study in the significance of grain size parameters. Journal of Sedimentary Petrology 27, 3–26.

Fritz, H.M., Borrero, J.C., Synolakis, C.E., Yoo, J., 2006. 2004 Indian Ocean tsunami flow velocity measurements from survivor videos. Geophysical Research Letters 33, L24605, doi: 10.1029/2006GL026784.

Fritz, H.M., Phillips, D.A., Okayasu, A., Shimozono, T., Liu, H., Mohammed, F., Skanavis, V., Synolakis, C.E., Takahashi, T., 2012. The 2011 Japan tsunami current velocity measurements

from survivor videos at Kesennuma Bay using LiDAR. Geophysical Research Letters 39, L00G23, doi: 10.1029/2011GL050686.

Galbraith, R.F., Roberts, R.G., Laslett, G.M., Yoshida, H., Olley, J.M., 1999. Optical dating of single and multiple grains of quartz from Jinmium rock shelter, northern Australia: Part I, Experimental design and statistical models. Archaeometry 41, 339–364.

Goff, J., Chagué-Goff, C., 2014. The Australian tsunami database: A review. Progress in Physical Geography 38, 218–240.

Gregson, P.J., van Reeken, I.A., 1998. Tsunami observations in Western Australia. In: Woodroffe, C.D. (Ed.), Maritime Natural Hazards in the Indian Ocean. Wollongong Papers on Maritime Policy 6, University of Wollongong, Australia, pp. 131–145.

Hammer, Ø., Harper, D.A.T., Ryan, P.D., 2001. PAST: Paleontological statistics software package for education and data analysis. Palaeontologica Electronica 4, article 4.

Hayward, B.W., Grenfell, H.R., Reid, C.M., Hayward, K.A., 1999. Recent New Zealand shallow-water benthic Foraminifera: Taxonomy, ecologic distribution, biogeography, and use in palaeoenvironmental assessments. Lower Hutt, New Zealand, Institute of Geological and Nuclear Sciences Monograph 21, 258 pp.

Hogg, A.G., Hua, Q., Blackwell, P.G., Niu, M., Buck, C.E., Guilderson, T.P., Heaton, T.J., Palmer, J.G., Reimer, P.J., Reimer, R.W., Turney, C.S.M., Zimmerman, S.R.H., 2013. SHCal13 Southern Hemisphere Calibration, 0–50,000 Years cal BP. Radiocarbon 55, 1889–1903.

Jackson, K.L., Eberli, G.P., Amelung, F., McFadden, M.A., Moore, A.L., Rankey, E.C., Jayasena, H.A.H., 2014. Holocene Indian Ocean tsunami history in Sri Lanka. Geology 42, 859–862.

Karanovic, I., 2012. Recent fresh water Ostracods of the World. Crustacea, Ostracoda, Podocopida. Springer, Berlin/Heidelberg, 610 pp.

Ketcham, R.A., 2005. Computational methods for quantitative analysis of three-dimensional features in geological specimens. Geosphere 1, 32–41.

Lewis, S.E., Sloss, C.R., Murray-Wallace, C.V., Woodroffe, C.D., Smithers, S.G., 2013. Post-glacial sea-level changes around the Australian margin: a review. Quaternary Science Reviews 74, 115–138.

Masschaele, B., Dierick, M., Van Loo, D., Boone, M.N., Brabant, L., Pauwels, E., Cnudde, V., Van Hoorebeke, L., 2013. HECTOR: A 240kV micro-CT setup optimized for research. Journal of Physics: Conference Series 463, article 012012, doi: 10.1088/1742-6596/463/1/012012.

Matsumoto, D., Naruse, H., Fujino, S., Surpharwajruksakul, A., Jarupongsakul, T., Sakakura, N., Murayama, M., 2008. Truncated flame structures within a deposit of the Indian Ocean Tsunami: evidence of syn-sedimentary deformation. Sedimentology 55, 1559–1570.

May, S.M., Brill, D., Engel, M., Scheffers, A., Pint, A., Opitz, S., Wennrich, V., Squire, P., Kelletat, D., Brückner, H., 2015a. Traces of historical tropical cyclones and tsunamis in the Ashburton Delta (NW Australia). Sedimentology 62, 1546–1572.

May, S.M., Engel, M., Brill, D., Cuadra, C., Lagmay, A.M.F., Santiago, J., Suarez, J.K., Reyes, M., Brückner, H., 2015b. Block and boulder transport in Eastern Samar Philippines during Supertyphoon Haiyan. Earth Surface Dynamics Discussions 3, 739-771.

Moore, A., Goff, J., McAdoo, B., Fritz, H., Gusman, A., Kalligeris, N., Kalsum, K., Susanto, A., Suteja, D., Synolakis, C., 2011. Sedimentary Deposits from the 17 July 2006 Western Java Tsunami, Indonesia: Use of Grain Size Analyses to Assess Tsunami Flow Depth, Speed, and Traction Carpet Characteristics. Pure and Applied Geophysics 168, 1951–1961.

Morton, R.A., Gelfenbaum, G., Jaffe, B.E., 2007. Physical criteria for distinguishing sandy tsunami and storm deposits using modern examples. Sedimentary Geology 200, 184–207.

Murray, A.S., Wintle, A.G., 2003. The single aliquot regenerative dose protocol: potential for improvements in reliability. Radiation Measurements 37, 377–381.

Murray, J.W., 2006. Ecology and Applications of Benthic Foraminifera. Cambridge University Press, Cambridge, 440 pp.

Nott, J., 2004. Palaeotempestology: the study of prehistoric tropical cyclones – a review and implications for hazard assessment. Environmental International 30, 433–447.

Nott, J., Hubbert, G., 2005. Comparisons between topographically surveyed debris lines and modelled inundation levels from severe tropical cyclones Vance and Chris, and their geomorphic impact on the sand coast. Australian Meteorological Magazine 54, 187–196.

O'Connor, S., Ulm, S., Fallon, S.J., Barham, A., Loch, I., 2010. Pre-bomb marine reservoir variability in the Kimberley region, Western Australia. Radiocarbon 52, 1158–1165.

Olley, J.M., Murray, A., Roberts, R.G., 1996. The effects of disequilibria in the uranium and thorium decay chains on burial dose rates in fluvial sediments. Quaternary Science Reviews 15, 751–760.

Paris, R., Fournier, J., Poizot, E., Etienne, S., Morin, J., Lavigne, F., Wassmer, P., 2010. Boulder and fine sediment transport and deposition by the 2004 tsunami in Lhok Nga (western Banda Aceh, Sumatra, Indonesia): A coupled offshore-onshore model. Marine Geology 268, 43–54.

Pint, A., Frenzel, P., Fuhrmann, R., Scharf, B., Wennrich, V., 2012. Distribution of Cyprideis torosa (Ostracoda) in quaternary athalassic sediments in germany and its application for palaeoecological reconstructions. International Review of Hydrobiology 97, 330–335.

Prendergast, A., Brown, N., 2012. Far-field impact and coastal sedimentation associated with the 2006 Java tsunami in West Australia. Natural Hazards 60, 69–79.

Prescott, J.R., Hutton, J.T., 1994. Cosmic ray contributions to dose rates for luminescence and ESR dating: large depths and long-term time variations. Radiation Measurements 23, 497-500.

Reeves, J.M., 2004. The use of Ostracoda in the palaeoenvironmental reconstruction of the Gulf of Carpentaria, Australia, from the last interglacial to present. PhD thesis, School of Earth and Environmental Sciences, University of Wollongong, 477 pp.

Reimer, P.J., Bard, E., Bayliss, A., Beck, J.W., Blackwell, P.G., Ramsey, C.B., Buck, C.E., Cheng, H., Edwards, R.L., Friedrich, M., Grootes, P.M., Guilderson, T.P., Haflidason, H., Hajdas, I., Hatté, C., Heaton, T.J., Hoffmann, D.L., Hogg, A.G., Hughen, K.A., Kaiser, K.F., Kromer, B., Manning, S.W., Niu, M., Reimer, R.W., Richards, D.A., Scott, E.M., Southon, J.R., Staff, R.A., Turney, C.S.M., van der Plicht, J., 2013. IntCal13 and Marine13 Radiocarbon Age Calibration Curves 0–50,000 Years cal BP. Radiocarbon 55, 1869–1887.

Roeber, V., Bricker, J., 2015. Destructive tsunami-like wave generated by surf beat over a coral reef during Typhoon Haiyan. Nature Communications 6, 7854, doi: 10.1038/ncomms8854.

Röler, K., Trepmann, C., 2013. Software for geoscientists: Stereo32 and StereoNett. Institut für Geologie – Ruhr University Bochum, Bochum, Germany. http://www.ruhr-uni-bochum.de/hardrock/downloads.html.

Scheffers, S.R., Scheffers, A., Kelletat, D., Bryant, E.A., 2008. The Holocene paleo-tsunami history of West Australia. Earth and Planetary Science Letters 270, 137–146.

Schneider, J.-L., Chagué-Goff, C., Bouchez, J.-L., Goff, J., Sugawara, D., Goto, K., Jaffe, B., Richmond, B., 2014. Using magnetic fabric to reconstruct the dynamics of tsunami deposition on the Sendai Plain, Japan — The 2011 Tohoku-oki tsunami. Marine Geology 358, 89–106.

Singarayer, J.S., Bailey, R.M., 2003. Further investigations of the quartz optically stimulated luminescence components using linear modulation. Radiation Measurements 37, 451–458.

Shimozono, T., Tajima, Y., Kennedy, A. B., Nobuoka, H., Sasaki, J., Sato, S., 2015. Combined infragravity wave and sea-swell runup over fringing reefs by super typhoon Haiyan. Journal of Geophysical Research - Oceans 120, 4463–4486.

Szczuciński, W., 2012. The post-depositional changes of the onshore 2004 tsunami deposits on the Andaman Sea coast of Thailand. Natural Hazards 60, 115–133.

Szczuciński, W., Kokociński, M., Rzeszewski, M., Chagué-Goff, C., Cachão, M., Goto, K., Sugawara, D., 2012. Sediment sources and sedimentation processes of 2011 Tohoku-oki tsunami deposits on the Sendai Plain, Japan – Insights from diatoms, nannoliths and grain size distribution. Sedimentary Geology 282, 40–56.

Wassmer, P., Schneider, J.-L., Fonfrège, A.-V., Lavigne, F., Paris, R., Gomez, C., 2010. Use of anisotropy of magnetic susceptibility (AMS) in the study of tsunami deposits: Application to the 2004 deposits on the eastern coast of Banda Aceh, North Sumatra, Indonesia. Marine Geology 275, 255–272.

Yassini, I., Jones, B.G., 1995. Recent Foraminiferida and Ostracoda from estuarine and shelf environments on the southeastern coast of Australia. University of Wollongong Press, Wollongong, 484 pp.

CONCLUSION

La tomographie par rayons X s'est révélée au cours de cette thèse être un outil extrêmement utile dans le cadre d'études structurales et texturales, tant à des échelles centimétriques qu'infra-millimétriques. L'absence de logiciels dédiés aux études sédimentologiques en deux et trois dimensions a pu être compensée par l'écriture de codes Matlab simples d'utilisation et facilement adaptables par l'utilisateur. Couplés aux logiciels existants (en particulier ImageJ et Blob3D), ils se sont révélés efficaces dans toutes les situations et avec tous les types d'images. Si les temps de traitement nécessaires dans le cas où les particules doivent être séparées manuellement sont longs et peuvent atteindre plusieurs heures voire plusieurs jours (cas du chapitre 2), l'intégralité du processus de traitement peut ne prendre que quelques dizaines de minutes lorsqu'une séparation automatique des particules peut être effectuée (cas du chapitre 3).

La confrontation des résultats issus de la tomographie par rayons X avec les résultats obtenus au moyen des techniques dites « conventionnelles » (chapitres 1 et 2) et de simples observations de terrain (chapitre 4) a prouvé la capacité de la technique à fournir des données pertinentes. De plus, la résolution très supérieure permise par l'X-CT par rapport aux techniques conventionnelles a permis de remettre en question des théories jusqu'à présent admises, en particulier en ce qui concerne l'organisation des dépôts à l'échelle millimétrique et infra-millimétrique, et les implications dynamiques que cette organisation représente.

En effet, la mise en évidence de contacts très érosifs et de figures typiques d'écoulements très turbulents associés aux mudlines est totalement incompatible avec les théories classiques qui associent mudlines et sédimentation lente (décantation) censée intervenir entre les phases d'*uprush* et de *backwash* (ce dont nous doutions au préalable…). Nous avons ainsi démontré la prépondérance d'un transport par traction avec éventuellement le développement de semelles (cas du tsunami de 1755). La visualisation à haute résolution et en trois dimensions de la structuration interne des dépôts s'est révélé être un outil indispensable pour accéder à ce type de données, et le fait de pouvoir associer à partir du même échantillon et de la même technique analytique données structurales et texturales a permis une interprétation particulièrement fiable, ce que ne permettent pas les autres techniques.

Les deux limites essentielles rencontrées au cours des différentes études de cas, à savoir la résolution des images et leur rapport signal sur bruit (qui conditionne immédiatement les possibilités de séparation des différentes phases en se basant sur leurs valeurs de gris) n'ont pas entravé outre mesure l'obtention de résultats pertinents. De plus, ces limites ne tiennent qu'aux caractéristiques techniques des appareils disponibles et pourraient être repoussées en utilisant des échantillons de taille inférieure (*cf.* infra), des temps d'acquisition plus longs et/ou des paramètres d'analyse optimisés. Des tests effectués récemment auprès de constructeurs ont permis d'obtenir, avec des échantillons tubulaires similaires à ceux utilisés pour cette thèse, des images à bons rapport signal/bruit dont les résolutions sont proches du micromètre. La diminution du diamètre interne des tubes permettrait un gain encore supérieur en résolution, moyennant une perte de représentativité spatiale des échantillons.

Les échantillons de forme tubulaire en fibres de carbones se sont révélés globalement adaptés, en permettant en particulier d'allier polyvalence quant aux sédiments prélevables et aux épaisseurs échantillonnables, rigidité parfaite et très bonne transparence aux rayons X, tout en conservant une représentativité spatiale permettant la lecture des structures dans les trois dimensions. Cependant, le prélèvement d'échantillons très peu cohérents (par exemple sables grossiers, sédiments secs et/ou indurés) ou mécaniquement très peu résistants (épaisses couches argileuses) s'est parfois révélé problématique. Des essais préliminaires d'imprégnation à l'air libre des sédiments grossiers par une résine polyester insaturée diluée ont été conduits et pourraient se révéler très efficaces. Pour l'échantillonnage de sédiments très meubles, la diminution de l'épaisseur des parois du tube (environ 1 mm pour les tubes en fibres de carbone) permettrait de diminuer au maximum les effets de bord, moyennant une perte probable de rigidité (l'opacité des tubes métalliques aux rayons X les rend impropres à l'échantillonnage).

L'obtention de données de meilleure résolution et au contraste optimisé permettrait non seulement de faciliter la séparation des particules, ce qui se traduirait par un gain de temps non négligeable, mais également d'étudier les fractions les plus fines des dépôts, en particulier les silts très fins voire les argiles, tant du point de vue textural (fabrique sédimentaire de sous unités fines) que structural, en particulier par l'étude des *mudlines* dont

les positions et l'organisation dans les dépôts du tsunami de 1755 laissent entrevoir des mécanismes de mise en place beaucoup plus complexes que la simple décantation (*cf.* Chapitre 2). La microtomographie par rayons X démontre ainsi un fort potentiel pour permettre des avancées significatives dans la compréhension des dépôts de tsunamis et vient efficacement compléter le panel de méthodes et marqueurs dédiés à leur étude.

ANNEXES

Annexe 1 : Traitement des scans, extraction et traitement des données.

- Fichiers de base : Tomogrammes 2D en coupe transverse (scans horizontaux) :

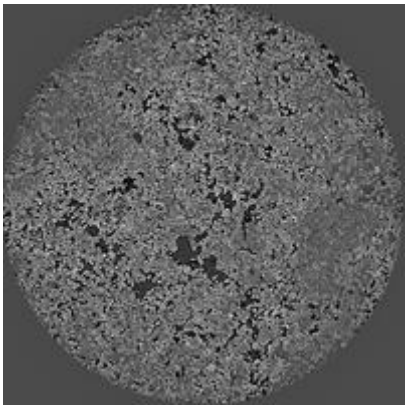

- Logiciels nécessaires :
  - ImageJ (ou Fiji) équipé du plugin 'A Trous' wavelet filter (http://rsbweb.nih.gov/ij/plugins/a-trous-wavelet-filter.html)
  - Excel (ou tableur compatible avec les fichiers xls)
  - Matlab (testé avec la version R2011a)
  - Blob3D (http://www.ctlab.geo.utexas.edu/software/)
  - Stereonet (http://www.geo.cornell.edu/geology/faculty/RWA/programs/stereonet.html) ou équivalent
  - Eventuellement : Photoshop (et le module Camera Raw) et PAST (traçage des histogrammes et des courbes plus simple que sous Excel)
- Fichiers de traitement :
  - *macro_atrous.ijm* : traitement du bruit via ImageJ
  - *colormapcartograins.map* : échelle de couleurs pour carto des grains via Matlab
  - *grainmap.m* : cartographie des tailles de grains via Matlab
  - *grainstat.m* : calcul des nombres de grains, diamètres mini, maxi, moyens, écart-type, kurtosis, skewness, D25, D75 et indice de tri des grains via Matlab
  - *bioclast.m* : comptage de particules en sein des échantillons (pas forcément des bioclastes, le code marche pour n'importe quel type de particule).

Optimisation des images : ajustement des contrastes et traitement du bruit

L'ajustement des contrastes peut se faire avec n'importe quel logiciel de traitement d'image conventionnel ou spécialisé (Photoshop, Gimp, Photofiltre, ImageJ, etc.). Il aide à la lecture de l'image mais ne change pas grand-chose pour la séparation des grains par les logiciels : les modifications de contraste ne peuvent pas séparer 2 pixels de même valeur, et plus le contraste est poussé, plus le bruit numérique devient visible.

Le réglage du contraste doit être fait en prêtant particulièrement attention aux extrémités de l'histogramme : les pertes de données par saturation des blancs ou des noirs ne sont pas compensables une fois l'image enregistrée.

Pour le bruit, pas de méthode miracle, mais 2 options semblent plus efficaces :

- Avec **Photoshop** : module **Camera Raw**. L'algorithme de traitement du bruit est très efficace pour corriger le bruit fin tout en conservant les contours, mais on n'a aucune info sur son fonctionnement précis (probablement à base de filtre médian). Sur des particules fines (quelques pixels de côté) l'atténuation des contours devient non négligeable -> à tester au cas par cas.

- Avec **ImageJ** : Utilisation du **plugin 'A Trous' wavelet filter** (Marchal & Mutterer), intégré dans une macro pour le traitement par lot (fichier '***macro_atrous.ijm***'). La ligne 10 du code permet de régler l'intensité du filtre (k1 à k5 : coefficients de transformation de niveau croissant [traitement du bruit de plus en plus « grossier » en plusieurs « phases », k1 à k5, d'intensité réglable]. Le réglage de base à k1 = 2,5 et k2, k3, k4, k5 = 0 convient pour des scans types ESRF/LL1 (grains très petits, jointifs, à faible contraste).

  Pour **éditer les valeurs de k**: ImageJ : *Plugins > Macros > Edit…*

  Utilisation :

  - *Plugins > Macros > Run…*
  - Première boîte de dialogue **:** sélection du dossier contenant les images à traiter (la macro encode automatiquement les fichiers en 8 bits).
  - Deuxième boîte de dialogue : sélection du format de sortie (recommandé : TIFF).
  - Troisième boîte de dialogue : sélection du dossier de sortie.

2D : Séparation et mesure du diamètre intermédiaire des grains

La séparation des grains en 2 dimensions est effectuée entièrement manuellement via ImageJ. Pour obtenir des données de tailles de grains en fonction de la profondeur d'échantillonnage il est nécessaire de passer d'une représentation de l'échantillon en coupes transversales (« horizontales ») à une représentation en coupes sagittales (« verticales ») en utilisant la fonction *reslice* d'ImageJ (*Image > Stacks >Reslice[/] …*).

Il est évidemment indispensable de renseigner l'échelle de l'image, en mm par pixel (*Analyse > Set scale*) avant de procéder aux mesures.

L'opération consiste à assigner à chaque grain identifié une zone d'intérêt (*ROI – Region Of Interest*. Appuyer sur T une fois le tracé effectué pour lui attribuer une ROI) sous la forme d'un trait représentant l'hypothétique diamètre intermédiaire de son ellipsoïde.

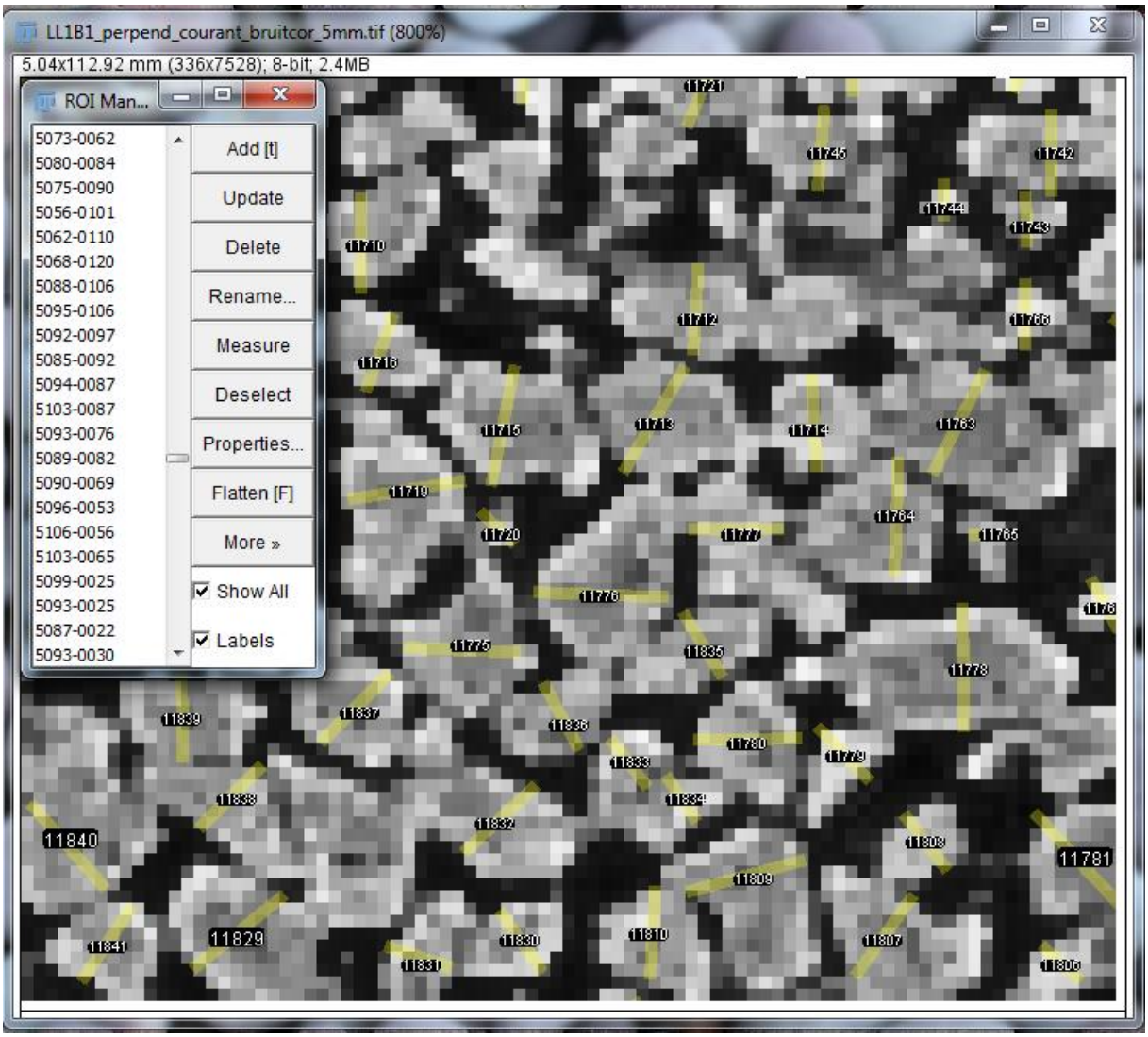

Figure 1 : Diamètres intermédiaires tracés sous ImageJ, et fenêtre de gestion des ROIs (chaque ROI est identifiée dans le tableau par ses coordonnées en y et x en pixels, et par un numéro unique (attribué suivant l'ordre de traçage) sur l'image.

Une fois tous les grains individualisés, la récupération de leurs coordonnées et de leur diamètre se fait en plusieurs étapes :

- Dans *Analyse* > *Set measurements*, cocher la case '*Display label'*
- Dans le ROI manager, sélectionner les lignes correspondant aux grains à mesurer et cliquer sur '*Measure*'
- ImageJ rend un fichier à 4 colonnes (numéro|Label|Angle|Length) à enregistrer au format .xls (enregistrer en .txt via ImageJ puis changer en .xls en modifiant le nom du fichier)
- Dans Excel, supprimer la première colonne et la colonne *Angle*

- La colonne *Label* contient des lignes de type ‘Nomdufichier.extensiondufichier:coordonnéeY-coordonnéeX’ (par exemple : *LL1B1_perpend_courant_bruitcor_5mm.tif:5073-0062*). En utilisant la fonction ‘Remplacer’ d’Excel, remplacer toute la partie ‘nomdufichier.extensiondufichier:’ par un espace, et remplacer le tiret entre Y et X par un espace. (avec l’exemple précédent on obtient : *5073 0062. En cas de dysfonctionnement de la commande, remplacer le tiret par 2 espaces successifs*)
- Sauvegarder le fichier au format .txt
- Dans Excel, créer un nouveau classeur et importer les données du .txt :
  Données > *A partir du texte* > sélectionner le fichier .txt puis
  Fichier délimité > *séparateurs : tabulation et virgule* > *Importer*
- On obtient un tableau à 3 colonnes Y, X, Z (Z : longueur de segment *Length*).
- Supprimer les en-têtes (première ligne) et intervertir les colonnes Y et X pour obtenir un tableau X, Y, Z.
- Dans le fichier brut, **les coordonnées X Y des grains sont données en nombres de pixels depuis l’origine** (ex : 0062 | 5073 : 62 px en X et 5073 en Y depuis le coin supérieur gauche de l’image.). Pour les convertir en millimètres, il suffit de multiplier ces valeurs par la résolution en mm des scans (p.ex. si les scans ont une résolution de 15µm, on a : Y(mm) = Y(px)*0.015).
- Pour rendre le fichier utilisable par les 2 codes matlab (carto des grains et mesures quantitative), les valeurs de Y doivent être inversées (valeurs négatives). Les données doivent être classées par Y décroissant (penser à étendre la sélection quand Excel le propose pour ajuster automatiquement les positions des X et Z correspondants).
- Enregistrer le tableau sous la forme d’un fichier .txt.

2D : cartographie des tailles de grains

Fichiers requis : fichier .txt de coordonnées de type X Y Z (triées par Y croissant décroissant : Ymax en première valeur, Y min en dernière valeur, avec des **valeurs de Y négatives**), fichier *grainmap.m* et fichier *colormapcartograins.map*.

Placer de préférence les 3 fichiers dans le même dossier (simplifie d'éventuels problèmes de chemins avec Matlab), lancer le code ('*Run*' ou taper sur F5) et suivre les instructions. Le code rend une carte des tailles de grains, représentées par des niveaux de couleur du bleu profond au rouge sombre (une sorte de MNT avec des diamètres au lieu d'altitudes), accompagnée d'une légende graduée suivant les classes de tailles de grains définies par Wentworth (1922).

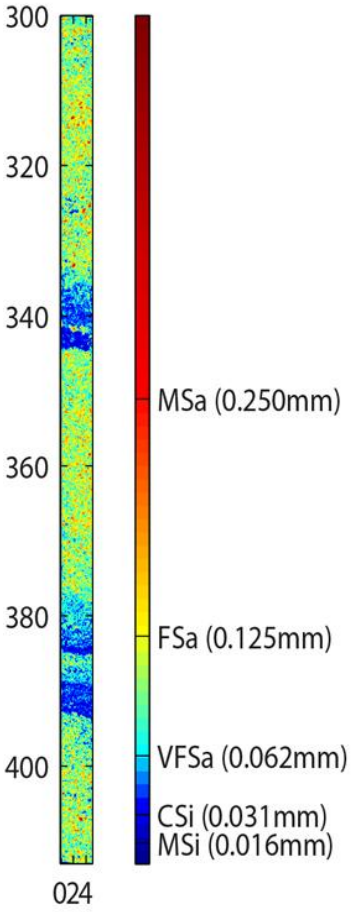

Cette carte n'est à utiliser que pour un travail descriptif/qualitatif, les gradients de couleur entre les grains ne sont dus qu'à l'interpolation réalisée par Matlab, chaque grain n'étant pas représenté à l'échelle mais en tant que point unique (deux grains jointif devraient se traduire par deux surfaces de couleur unie et un passage franc d'une couleur à une autre ce qui n'est pas le cas : Matlab associe chaque valeur de diamètre à un point unique et ne peut donc pas savoir si les grains sont jointifs ou non, d'où les gradients de couleur).

Remarques / limites :

- Le pas de calcul est fixé de base à 0.015mm (lignes 12 et 13 du code), distance correspondant à la limite de résolution des scans ESRF des tubes LL1B1 et LL1B2, utilisés pour écrire le code. Ce pas est à adapter au cas par cas suivant les besoins et la résolution des images.
- Ligne 15 : le *griddata* est réalisé linéairement (*'linear'*) pour des raisons de compromis entre précision, temps de calcul et fiabilité des résultats.
- La figure peut être enregistrée, le format .EPS permet l'obtention d'une image vectorielle utilisable sous Illustrator ou équivalent.
- L'échelle de Wentworth est logarithmique mais Matlab ne permet d'afficher les *colorbars* que suivant des valeurs linéaires, d'où l'apparence inhabituelle de la colorbar.
- La *colormap* a été définie manuellement dans le *Colormap editor* de Matlab. Les curseurs ont été positionnés le long d'une échelle colorimétrique ne comportant que 64 entrées, d'où un manque de précision non négligeable pour les fractions fines (p.ex. le diamètre correspondant à la limite basse des silts moyen (MSi) est de 0.016mm, hors l'échelle ne

propose que les valeurs 0.019 ou 0.012mm. Le diamètre correspondant à la limite basse des silts fins (FSi) est de 0.008mm hors l'échelle ne propose que les valeurs 0.012 ou 0.005). L'impact visuel n'est pas énorme mais ce système rend la carte impropre à d'éventuelles applications quantitatives (pas d'alternative trouvée pour l'instant).

2D : mesures quantitatives, statistiques

Fichiers requis : fichier .txt de type X Y Z (exactement le même qu'avec grainmap), fichiers *grainstat.m.*

Placer de préférence les 3 fichiers dans le même dossier (simplifie d'éventuels problèmes de chemins avec Matlab), lancer le code ('*Run*' ou taper sur F5) et suivre les instructions. Le code mesure/calcule, sur toute l'épaisseur de l'échantillon et dans chaque intervalle entré par l'utilisateur :

- Le nombre de grains,
- Le diamètre du grain le plus fin,
- Le diamètre du plus gros grain,
- Le diamètre moyen de l'intégralité des grains,
- L'écart type correspondant,
- La profondeur moyenne du sous-échantillon,
- Les percentiles D25 et D75 (diamètres passants pour 25 et 75% des grains),
- Le coefficient de tri (sorting coefficient SO),
- Les coefficients d'aplatissement (kurtosis) et de dissymétrie (skewness).

Les résultats des mesures/calculs sont rendus sous la forme de 6 graphiques (ordonnée : profondeur, abscisse : variable considérée). Ces graphiques peuvent être enregistrés (*File> save as*) soit dans un format matriciel (.jpeg, .tiff, .bmp, etc.) soit dans un format vectoriel (.eps p.ex.).

Les valeurs de tailles de grains sont enregistrées par le code dans une matrice nommée '*valz'*. Cette matrice a une taille semi arbitraire : son nombre de colonnes dépend uniquement du pas de sous échantillonnage et est automatiquement adapté par le code (chaque boucle de calcul crée une nouvelle colonne). La matrice a un nombre de lignes fixé à 700 lignes (mesure rendue nécessaire par l'impossibilité d'ajouter progressivement à une matrice des colonnes de

taille différente). Chaque colonne créée est donc intégralement remplie de zéros, avant que ces zéros ne soient le cas échéant remplacés par des valeurs de tailles de grains. Si un ou plusieurs sous échantillons contient plus de 700 valeurs de tailles de grains, la dimension des colonnes doit être adaptée. Cette opération se fait au niveau de la ligne N°23 du code : '*valz = zeros(***700***,1);*' en changeant la valeur '700' par la valeur désirée.

La **matrice des valeurs de tailles de grains vs profondeur** peut être **enregistrée au format .txt** en tapant la ligne suivante dans la fenêtre de commande de Matlab : '*save('cheminudossier\nomdufichier.txt', 'valz', '-ascii');*'. Cette manipulation est surtout utile pour représenter graphiquement les tailles de grains vs profondeur des sous échantillons, sous la forme d'histogrammes en particulier. Le logiciel PAST3 intègre une fonction de traçage d'histogramme simple, performante et beaucoup plus simple à manipuler qu'un code Matlab.

Avant d'être importées dans PAST3, les données doivent être mises en forme (Matlab enregistre les nombre au format scientifique, colonnes séparées par des espaces) via Excel ou équivalent. Les données sont de type nombre, à 3 décimales. La **première ligne de chaque colonne** contient la **profondeur moyenne du sous échantillon**. A cause du système de calcul du code, les colonnes sont classées de gauche à droite par ordre croissant (donc par ordre de profondeurs décroissantes, les valeurs étant négatives !).

Les données calculées pour chaque pas de sous échantillonnage peuvent également être toutes enregistrées dans le même fichier texte en utilisant la même ligne de commande que précédemment et en remplaçant la variable *'valz'* par la variable *'resultats'*. Le fichier texte obtenu correspond à un tableau de données contenant 11 colonnes représentant respectivement : profondeur moyenne du sous échantillon, nombre de grains, diamètre mini, diamètre maxi, diamètre moyen, écart type, kurtosis, skewness, D25, D75, coefficient de tri. Les données sont rangées par ordre de profondeur décroissante. Les colonnes ne possèdent pas d'en-tête (contrairement aux données de taille de grains).

Les **percentiles** sont fixés arbitrairement à 25 et 75%. Si ces valeurs doivent être adaptées, il suffit de modifier en conséquence les valeurs des lignes 45 et 67 écrites sous forme '*nomdevariable = valeur du percentile*'. Seule la valeur du percentile doit être changée, le nom de variable n'influe pas la valeur du résultat. La ligne N°167 permet d'adapter les labels du graphique associé en remplaçant 'D25' et 'D75' par les valeurs adaptées.

La **matrice contenant les résultats des calculs effectués** peut également **être enregistrée** via le même processus, en remplaçant dans la ligne de code le terme *'valz'* par le terme '*resultats'*. La matrice ne contiendra que les résultats des calculs, sans en tête (les grandeurs mesurées dans chaque colonne peuvent être retrouvées à partir de la ligne 186 du code).

3D : fabrique sédimentaire

Fichiers requis : scans de base. Dans le cas d'un échantillon tubulaire, pour simplifier l'analyse, il vaut mieux recadrer chaque scan en format carré de manière à éliminer les zones « vides » (zones hors échantillon). Cette manipulation entraîne la perte des grains périphériques de l'échantillon, qui sont de toute façon plus ou moins remaniés lors de la mise en place du tube. Si les scans doivent être conservés en l'état et si nécessaire, Blob3D permet d'attribuer une valeur de gris donnée aux zones de vide des scans en entrant le rayon de l'échantillon

La séparation des grains en 3D se fait via Blob3D. Le logiciel propose un traitement en 3 temps :

- Préparation des fichiers (phase de segmentation des particules)
- Séparation des particules
- Extraction des données

La préparation des fichiers ne doit surtout pas être négligée. Un seuillage précis des données est impératif pour obtenir des données représentatives (et dans le cas de particules fines impératif pour ne serait-ce que pouvoir les séparer !). La gestion des valeurs de seuil pour binariser les images, et les manipulations type suppression d'îles et de trous (cf. notice de Blob3D) se fait au cas par cas, aucune recette type ne fonctionne à tous les coups. Il vaut cependant mieux « éroder » un peu les grains avec le filtre « remove islands » afin de faciliter leur séparation durant la deuxième phase. La perte de précision en termes de volume et d'orientation est généralement négligeable. Le logiciel propose plusieurs filtres de traitement du bruit et du contraste, mais ImageJ et Photoshop proposent des outils plus simples à mettre en œuvre.

Dans le cas où les traitements en 2D de Photoshop ou ImageJ entraîneraient l'apparition d'artefacts (schistosité artificielle à cause de l'empilement d'images traitées indépendamment les unes des autres, en particulier), Les filtre de traitement de Blob3D

permettent un traitement en 3 dimensions. Dans la plupart des cas un traitement du bruit via un calcul de médiane (Median smoothing) permet un traitement satisfaisant tout en altérant peu les contours des grains.

Durant la phase de séparation des grains, **le logiciel ne peut pas séparer plus de 254 grains à la fois**, ce qui oblige à travailler sur de petites sections d'échantillon (régler en conséquence le nombre maximal de voxels à traiter à la fois dans les préférences du logiciel). Si les grains sont trop petits pour être efficacement séparés avec les commandes erode/dilate (la commande d'érosion agit sur une épaisseur fixe, seul le nombre d'itérations peut être ajusté), il vaut mieux agrandir les images puis recommencer le processus sur les images agrandies (en pensant à corriger la résolution de l'image en conséquence dans la fenêtre adaptée lors de l'importation dans Blob3D !).

Après séparation et extraction des données, Blob3D permet l'export au format xls. Il est recommandé d'extraire la variable « *side contact* » et de supprimer dans Excel (ou équivalent) toutes les lignes pour lesquelles cette valeur vaut 1 (si la valeur vaut 0, le grain est intact, si elle vaut 1, il est tronqué par le bord de l'échantillon).

Extraction des orientations des grains : L'orientation des particules est mesurée par Blob3D et rendue sous forme de cosinus directeurs par rapport aux axes X, Y et Z (colonnes '*Max Axis X*', '*Max Axis Y*' et '*Max Axis Z*'). Les valeurs d'azimut et pendage de chaque particule peuvent être calculées :

Pendage = arcsin(MaxAxisZ) à convertir en degrés, ce qui donne sous Excel :

- **= DEGRES(ASIN(MaxAxisZ))**

Azimut : θ = arctan[cos(MaxAxisX)/cos(MaxAxisY)] (sous Excel : =DEGRES(ATAN(α/β)) Avec α = MaxAxisX et β = MaxAxisY . On obtient une valeur de θ comprise entre ±90°. L'orientation des cosinus directeurs sur X et Y permet de convertir cette valeur sur 360° : si MaxAxis X et MaxAxis Y sont positifs, L'azimut est correct. Si MaxAxisY < 0, l'Azimut est égal à θ + 180°. Si MaxAxisX < 0 et MaxAxisY > 0, l'Azimut est égal à θ + 360°. On peut effectuer ce calcul via une double fonction SI dans Excel :

- **= SI (β<=0 ; 180+θ ; SI(α>=0 ; θ ; 360+ θ))**

L'application de ces formules à chaque particule permet d'obtenir un tableau à deux colonnes d'azimuts en pendages. Pour exploiter ces données avec Stereonett (Stereo32) il faut ajouter pour chaque grain une troisième colonne remplie de « L » afin d'indiquer au logiciel

que chaque couple azimut/pendage correspond à une ligne (et non à un plan), puis enregistrer le tableau au format .txt (séparation par tabulation), qui peut être importé directement dans Stereo32 pour analyse.

Représentation de la fabrique sédimentaire : utilisation du diagramme ternaire de Benn (1994) : diagramme triangulaire basé sur la mesure des valeurs propres normalisées (eigenvalues) de l'ellipsoide correspondant aux orientations préférentielles des particules. Les valeurs propres S1, S2 et S3 (axes max, int et min de l'ellipsoide) sont calculées via Stereo32 (ou Stereonet). Correspondance des pôles du diagramme :

- Fabrique isotrope (S1 = S2 = S3, I = 1 et E = 0) ;
- Fabrique planaire (S1 = S2 > S3, I = E = 0) ;
- Fabrique linéaire (S1 > S2 > S3, I = 0 et E = 1) ;

Avec :

- I (Isotropie) = S3/S1 ;
- E (Elongation) = 1 – (S2/S1)

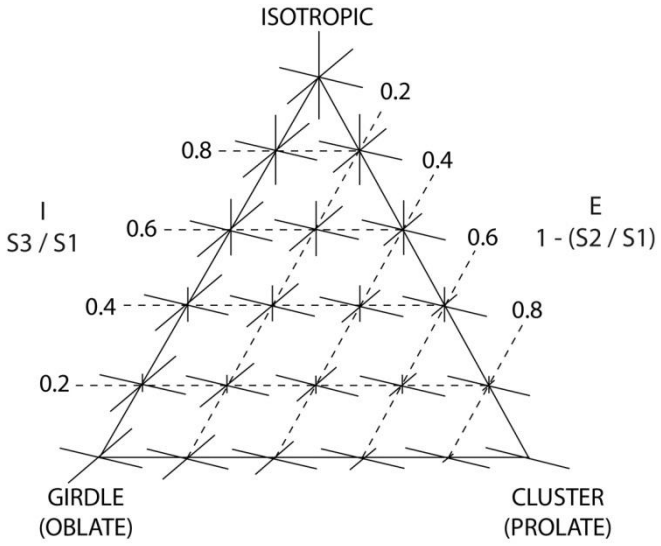

1D : comptage des bioclastes

Le comptage des bioclastes est effectué en 3D (sur slices transversaux) pour s'assurer d'une représentativité suffisante (généralement pas assez de bioclastes sur un reslice longitudinal unique). La méthodologie est la même que pour la cartographie des grains : chaque bioclaste est identifié par une ROI linéaire. Le traitement du fichier de valeurs rendu par ImageJ se fait exactement de la même manière, afin d'obtenir un fichier texte contenant une colonne X, une colonne Y et une colonne Z (dont la valeur n'a aucune importance. Le code n'effectue qu'un simple comptage, les dimensions des particules ne sont pas prises en compte).

Le comptage est effectué par une version simplifiée du code *grainstat* : seule la section de comptage des particules est conservée, l'utilisation du code se fait selon la même marche à suivre : lancement du code, sélection du fichier de données, entrée du pas de sous échantillonnage, récupération des résultats sous la forme d'un graphe, et valeurs enregistrables au format texte.

Annexe 2 : codes

Macro Filtre à trous (ImageJ) :

```
input = getDirectory("source directory");  //sélection du dossier source
format = getFormat(); //sélection du format de sortie
output = getDirectory ("output destination"); //sélection du dossier de sortie
list = getFileList(input); //création de la liste de fichiers à partir du contenu du dossier source
setBatchMode(true);
for (i=0; i<list.length; i++) { //en partant de i=0 et tant que i<nb total de fichiers, on ajoute 1 au numero du fichier (i++= list.length+1)
	showProgress(i+1, list.length); //évolution de la barre de progrès en fonction de i+1 par rapport à la longueur totale de la liste
	open(input+list[i]); //ouvre le fichier correspond au numero i de la liste, du dossier d'entrée

run("8-bit");
run("A trous filter", "k1=2.5 k2=0 k3=0 k4=0 k5=0 non std=1"); //application du filtre
saveAs(format, output+list[i]); //sauvegarde au format sélectionné, au numero i de la liste dans le dossier de sortie
}



function getFormat() {
	formats = newArray("TIFF", "8-bit TIFF", "JPEG", "GIF", "PNG", "PMG", "BMP", "FITS", "Text Image", "ZIP", "Raw"); //crée un tableau de formats
	Dialog.create("Batch Convert"); //crée une boite de dialogue nommée "batch convert"
	Dialog.addChoice("Convert to:", formats, "TIFF"); //crée une liste de choix de formats. format de base : TIFF
	Dialog.show(); //affiche la boite
	return Dialog.getChoice(); //entre le choix sélectionné
}
```

Grainmap :

```
clear all
close all
clc

loadname = uigetfile; %fichier texte xyz, champs séparés par des
tabulations
M = load(loadname);
x = M(:,1); %x = valeurs de toutes les lignes (":") de la première colonne
(",1")
y = M(:,2);
z = M(:,3);
xmin = round(min(x));
ymin = round(min(y));
xmax = round(max(x));
ymax = round(max(y));
XI = xmin:0.015:xmax; %valeurs de XI : de la valeur min de x à son max, par
pas de 0.015mm
YI = ymin:0.015:ymax;
[X,Y] = meshgrid(XI,YI); %création de la matrice [Y,Y] avec les valeurs des
vecteurs XI et YI
ZI = griddata(x,y,z,X,Y,'linear'); %calcul des valeurs ZI sur la matrice
[X,Y], à partir des valeurs x,y,z d'origine
a = figure; %création d'une nouvelle figure, appelée 'a'
imagesc(xmin:xmax,ymin:ymax,ZI); %carto de ZI sur l'espace de min (x et y)
à max(x et y, en utilisant l'intégralité de la colormap (pas de couleurs
non attribuées)
axis image; % axes x et y de l'image à la même échelle, délimités à
l'emprise de la figure
load('colormapcartograins','mycmap'); %chargement de la colormap
'colormapcartograins', attribution à la variable 'mycmap'
set(a,'Colormap',mycmap); % attribution de colormapcartograins à la figure
a en tant que Colormap
set(gca,'YDir','normal'); % on inverse le sens de tracé des données en Y
(imagesc les inverse de base, en réinversant on les remet "à l'endroit",
avec les profondeurs les plus faibles (valeurs les plus élevées) en haut)
colorbar('YTick',[0.016 0.031 0.062 0.125 0.250 0.500], 'YTickLabel', {'MSi
(0.016mm)','CSi (0.031mm)','VFSa (0.062mm)','FSa (0.125mm)','MSa
(0.250mm)','CSa (0.500mm)'});
%ajouts de repères selon l'axe y de la colorbar à des valeurs données, et
attribution de labels
```

Grainstat :

```
clear all
close all
clc

%%%%%%%%%% Accès aux fichiers et définition des variables de base %%%%%%%%%

loadname = uigetfile; %chargement d'un fichier texte yz, champs séparés
%par des tabulations, y : profondeur (valeurs négatives décroissantes), z
%: diamètre du grain
M = load(loadname);
prompt = 'Measurement interval (mm)'; %ligne de caractères à afficher dans
la boîte de dialogue (ligne 9)
answer = inputdlg(prompt); %ouverture d'une boite de dialogue pour
l'obtention du pas de mesure
% !! ENTRER UNE VALEUR POSITIVE !!
pas = str2double (answer{1}); %conversion des caractères entrés en valeur
numérique
y = M(:,2); %y = valeurs de toutes les lignes (":") de la deuxième colonne
(",2")
ymax = max(y); %valeur max de y
ymin = min(y); %valeur min de y
zmaxI = size (M,1); %valeur max de z : nombre de lignes total de la matrice
M -> zmaxI = numéro de la dernière ligne de la liste
ycalc = ymin+pas; %valeur maxi de y dans l'intervalle de calcul (borne
basse + pas de calcul)
ycalcmin = ymin; %valeur mini de y au cours du calcul : borne basse de
l'intervalle de calcul (borne haute : ycalcmin + pas). On débute avec la
plus petite valeur de y (la plus grande profondeur)
k = 1; %compteur pour la création de la matrice de résultats (cf. lignes
42-43)
valz = zeros(700,1);

%%%%%%%%%%%%%%%%%%%% Début des calculs %%%%%%%%%%%%%%%%%%%%%%%%%%%%%%%%%%

for yb = ymin:pas:ymax; %le calcul se déroule de ymin à ymax par incréments
de valeur "pas"
    ymes = y (y<ycalc & y>=ycalcmin); %ensemble des valeurs de y sur
l'intervalle de calcul (ymes rassemble toutes les valeurs de y<ycalc à
y>=ycalcmin)
    ynum = numel(ymes); %nombre d'éléments dans ymes (=nb de lignes de la
matrice correspondant à ymes : nb de grains pris en compte)
    zminI = zmaxI-ynum; %valeur mini de z (N° de ligne dans la matrice, pas
la valeur de la variable !): valeur maxI - nombre de grains

    if  zminI <= 0; %si l'indice de zminI est inférieur à 0 (dans le cas où
l'intervalle entre zmaxI et la première ligne de la matrice soit inférieur
à ynum)...
        break %...on arrête tout pour éviter de lancer une boucle sur un
intervalle incomplet
    end

    z = M(zminI:1:zmaxI,3); %z = valeurs de diamètres de grains prises en
compte : de la ligne N° zmaxI-ynum à la ligne zmaxI
    znum = numel(z); %nombre de lignes de z prises en compte (=nombre réel
de grains mesurés)
    zmin = min(z); %mesure du diamètre mini
    zmax = max(z); %mesure du diamètre maxi
```

```
    zmoy = mean(z); %mesure du diamètre moyen
    zstd = std(z); %mesure de l'écart type
    profmoy = yb+pas/2; %profondeur moyenne

    %%%% calcul D25 et D75 %%%%
    dpercent25 = 25; %définition du percentile;
    zperc = sort (z); %classement des valeurs de z par ordre croissant
    w25 = dpercent25 / 100; % wX = X/100
    resultd25 = w25*znum; % resultdX : fraction en %, fois le nombre
d'éléments de la série : ici la valeur associée à 25% du total
    [N,D] = rat(resultd25); %définition d'un numérateur (N) et dénominateur
(D) pour représenter resultd25 sous forme d'une fraction

    if  isequal(D,1),              % k*Nx is an integer, add 0.5
        resultd25 = resultd25 + 0.5;
    else                           % round up
        resultd25 = round(resultd25);
    end

    [T,R] = strtok(num2str(resultd25),'.'); %on transforme la ligne de
caractères de resultd25 en 2 jetons T et R, séparés par le caractère '.'

    if strcmp(R,'.5'), % si la ligne de caractère de R est '.5'
        D25 = mean(zperc(resultd25 -0.5 : resultd25 + 0.5)); %D25 est la
moyenne des deux valeurs encadrantes
    else
        D25 = zperc(resultd25); %sinon D25 = valeur associée à resultd25
dans la série zperc
    end

    %%%% D75 %%%%

    dpercent75 = 75;
    w75 = dpercent75 / 100;
    resultd75 = w75*znum;
    [N,D] = rat(resultd75);

    if  isequal(D,1),
        resultd75 = resultd75 + 0.5;
    else
        resultd75 = round(resultd75);
    end

    [T,R] = strtok(num2str(resultd75),'.');

    if strcmp(R,'.5'),
        D75 = mean(zperc(resultd75 - 0.5 : resultd75 + 0.5));
    else
        D75 = zperc(resultd75);
    end

    %%%% sorting coefficient %%%%

    SO = sqrt(D75/D25);

    %%%% kurtosis %%%%
    zzmoy = z - zmoy;
    numkurt = (1/znum) * sum ((zzmoy).^4); %numérateur du kurtosis
    denkurt = (1/znum) * sum ((zzmoy).^2); %denominateur du kurtosis
```

```
    zkurt = numkurt / denkurt^2; %kurtosis
    %%%% skewness %%%%%%%%
    numskew = (1/znum) * sum ((zzmoy).^3); %numérateur du skewness
    denskew = (1/znum) * sum ((zzmoy).^2); %denominateur du skewness
    zskew = numskew / denskew^(3/2); %skewness

    %%%%%%%%

    znumad = znum+1; %on ajoute 1 à la valeur de znum pour pouvoir inscrire
toutes les valeurs de z dans valz malgré le décalage d'une ligne pour
l'intitulé (cf infra)
    valz(2:znumad,k) = z; %la colonne k de la matrice valz prend les
valeurs de z, pour les lignes 2 à znumad
    if yb > ymin; %si yb > ymin
       valz(1,k) = yb - (pas/2); %la première ligne de la colonne k de la
matrice valz prend la valeur de yb - pas/2 -> intitulé de la ligne ->
profondeur moyenne du sous échantillon
    else valz(1,k) = yb; %sinon la première ligne de la colonne k prend la
valeur de yb
    end

    resultats(k,:) = [profmoy znum zmin zmax zmoy zstd zkurt zskew D25 D75
SO]; %les résultats des calculs sont rangés en ligne dans la matrice
"resultats". Une ligne = une itération du calcul, une colonne = une
variable
    k = k+1; %incrémentation de la valeur de k : au prochain calcul une
ligne sera ajoutée à la matrice "resultats" pour ne pas écraser les mesures
précédentes

    if  ycalc < ymax ; %Si la valeur max de calcul est < à la valeur max de
y...
        ycalcmin = ycalcmin+pas; %...la valeur mini de calcul devient
l'ancienne valeur maxi...
        ycalc = ycalcmin+pas; %...la valeur maxi devient la nouvelle valeur
mini + le pas de calcul...
        zmaxI = zminI; %...et l'indice maxi de z devient l'ancienne valeur
minI
    end

    clear ymes %effacement de la variable ymes (pour réallocation de la
mémoire sur un bloc de taille suffisante lors de la prochaine itération :
utile car la taille de ymes peut changer énormément d'une itération à
l'autre)

end

%%%%%%%%%%%%%%%%%%%%%%%% Fin des calculs %%%%%%%%%%%%%%%%%%%%%%%%%%%%%%%%

%%%%%%%%%%%%%%%%%%%%%%%% Rendu graphique %%%%%%%%%%%%%%%%%%%%%%%%%%%%%%%%

profmoy = resultats(:,1); %On va chercher
znum = resultats(:,2); %les resultats
zmin = resultats(:,3); %dans les colonnes
zmax = resultats(:,4); %correspondantes
zmoy = resultats(:,5); %de la matrice
zstd = resultats(:,6); %"resultats"
zkurt = resultats(:,7);
zskew = resultats (:,8);
D25 = resultats (:,9);
D75 = resultats (:,10);
```

```
SO = resultats (:,11);

figure;
plot (znum,profmoy,'-m+','MarkerSize',3); %graphe znum vs profondeur, trait
plein magenta, dots en +
xlabel('Number of grains');
ylabel('Depth (mm)');

figure; %représentation des tailles de grains
plot (zmoy,profmoy,'-rp','MarkerSize',6); %graphe zmoy vs profondeur, trait
plein rouge, dots en pentagones
hold on; %pour tracer tous les graphes sur la même figure. placé après le
premier plot au cas où on veuille tracer en semilog
plot (zmin,profmoy,'-b.','MarkerSize',6); %graphe zmin vs profondeur, trait
plein bleu, dots en .
plot (zmax,profmoy,'-.k.','MarkerSize',6); %graphe zmax vs profondeur,
tirets-points noir, dots en .
plot (zstd,profmoy,'-go','Markersize',6); %graphe ecart-type vs profondeur,
trait plein vert, dots en o

xlabel('Grain size (mm)');
ylabel('Depth (mm)');
legend ('mean','min','max','std dev');
hold off

figure; %représentation des D25 et D75
plot (D25, profmoy, '-bo');
hold on;
plot (D75, profmoy, '-rp');
xlabel('Grain size (mm)');
ylabel('Depth (mm)');
legend ('D25','D75');

figure; %représentation du Sorting Index
plot (SO, profmoy, '-');
xlabel ('Sorting coefficient');
ylabel('Depth (mm)');

figure; %représentation du kurtosis
plot (zkurt,profmoy,'-r.')
xlabel ('Kurtosis');
ylabel ('Depth (mm)');

figure; %représentation du skewness
plot (zskew,profmoy,'-b.');
xlabel ('Skewness')
ylabel ('Depth (mm)');
```

Bioclast :

```
% This code has to be run on a .txt file consisting of three columns, the
% first and third ones being respectively the X and Z coordinates of the
% clast, the second one its Y coordinate given in millimetre, using
negative values (negative altitude for depth).
% The data have to be sorted in descending order of depth (top to bottom)

clear all
close all
clc


loadname = uigetfile;
M = load(loadname);
prompt = 'Measurement interval (mm)';
answer = inputdlg(prompt);
pas = str2double (answer{1});
y = M(:,2);
ymax = max(y);
ymin = min(y);
zmaxI = size (M,1);
ycalc = ymin+pas;
ycalcmin = ymin;
k = 1;
valz = zeros(1000,1);



for yb = ymin:pas:ymax;
    ymes = y (y<ycalc & y>=ycalcmin);
    ynum = numel(ymes);
    zminI = zmaxI-ynum;

    if  zminI <= 0;
        break
    end

    z = M(zminI:1:zmaxI,3);
    znum = numel(z);
    zmin = min(z);
    zmax = max(z);
    zmoy = mean(z);
    zstd = std(z);
    profmoy = yb+pas/2;

    resultats(k,:) = [profmoy znum];
    k = k+1;

    if  ycalc < ymax ;
        ycalcmin = ycalcmin+pas;
        ycalc = ycalcmin+pas;
        zmaxI = zminI;
    end

    clear ymes


end
```

```
profmoy = resultats(:,1);
znum = resultats(:,2);


figure;
plot (znum,profmoy,'-k');
xlabel('Bioclasts number');
ylabel('Depth (mm)');
```